Development of vascularised human brain cell co-cultures to improve translation in Alzheimer's disease drug discovery

Samuel David Lane

A thesis submitted to fulfil the requirements for the degree of Doctor of Philosophy

Faculty of Science
School of Chemistry
The University of Sydney

Primary Supervisor:	Prof. Michael Kassiou
Secondary Supervisor:	Dr. Eryn Werry
Industry Supervisor:	Dr. Martin Engel

Statement of Originality

I certify that to the best of my knowledge, this thesis contains no material previously published by any other person except where due acknowledgement has been made. This thesis has not been submitted for any degree or other purposes.

Section 2.18 and 3.2.8 was completed with the assistance of Dr Cesar Moreno (University of Sydney, NSW, Australia).

Section 4.2.1.2 was completed with the assistance of Dr Thomas Grundy, Dr Alexander Volkerling and Dr Martin Engel (Inventia Life Science Operations Pty Ltd., NSW, Australia).

Other than the sections mentioned above, I certify that the intellectual content of this thesis is the product solely of my own work and that all the assistance received in preparing this thesis and sources have been acknowledged.

Samuel Lane 27/2/2025

Acknowledgements

First and foremost, I want to express an impossibly deep gratitude to Eryn. I don't imagine I'll ever have the good fortune to work with anyone else as dedicated and understanding as you. Your ability to inspire curiosity, rigour, and kindness in all those who enter your orbit is *very*, *very* special. Thank you for believing in me when I doubted, and thank you for journeying with me on only-vaguely-relevant tangents about ethics and AI. Your mentorship during this process has taught me much more than science. To MK, thank you for steering the ship with your keen insight and trademark cheek. Your expertise and foresight got this project off the ground, and your trust in me gave me an amazing space to develop as a scientist and person. Thank you.

To my incredible labmates. Mike, you legend, thank you for riding the trials and tribulations of stem cell bioprinting with me. Our work relationship and friendship was always awesomely synergistic—here's hoping we end up solving problems together again. Ali, Sasha, Andre and Beau it's been a pleasure working closely with you all for so long now. I'm really excited to see what is next for all of you, I know it will be amazing. Gigi, Kim, Tom and Zakh, you have all helped develop our lab into such a fun environment over the past couple of years. Thank you for making the lab a place of warmth, even in the damp G08 corridors. Shout-out to previous lab members Damo, Erick, Kiyan, Anneliese and Elijah, whose contributions and camaraderie during their time still resonate. Working alongside such a diverse and talented group has been a privilege. To the chemistry team - while your science isn't championed in this body of work, you are a pillar of our lab as a whole. Thank you for your technical expertise and friendly chats.

To technical teams that made all of my research possible, the G08 (and A12) teams—Keith, Trudy, Maggie, Scott, Laurence—thank you for your steadfast support and for always being ready to troubleshoot. Neftali, Su and Kathy from my SMM and Cytometry, you guys are legends, and your imaging wizardry has been critical to the success of this project.

Martin, thank you for making the time to mentor me amongst the busy job of running a successful biotech company. Our catch-ups helped me expand my perspective on industry research and inspired me to think big. Thanks also to Alex, Tom, and Behnaz from the Inventia team for your innovation, enthusiasm, and easy-going-but-professional communication. Collaborating with you has been one of the highlights of this research journey, and your contributions have enhanced both my work, and my overall outlook on the science and technology industry.

To my family, Mum and Dad, your support, tangible and intangible, have been the foundation of everything I’ve achieved. Thank you for fostering my curiosity and resilience from an early age. Will and Soph, thank you for being a grounding force and reminding me of joys beyond the lab. Your encouragement has been a source of strength, and your humour has kept me smiling through tough days.

Sesame, thank you for being an excellent WFH companion, your gentle headbutts were a treasured reminder to pause and breathe. To my beautiful wife, Seonaid. You have borne a huge load as consequence of the challenges I’ve faced over the last few years. This document, and my (relative) sanity, would have been lost a couple of years ago if it weren’t for you. There aren’t good enough words, so I’ll just say thank you, I love you. To Finlay, I love you so much already. Thanks for helping with my final push to get this done. The next chapter in my life is about you guys.

While this thesis bears my name, it is a testament to the collective effort, generosity and empathy of so many, and I am deeply grateful for all of you.

Author Attribution Statement

Chapter 3 contains data published in the *Journal of Neuroinflammation* as:

Sullivan, MA, **Lane, SD**, McKenzie, A.D.J. et al. iPSC-derived PSEN2 (N141I) astrocytes and microglia exhibit a primed inflammatory phenotype. J Neuroinflammation 21, 7 (2024). https://doi.org/10.1186/s12974-023-02951-2

I designed and performed some experiments, collected and analysed some data and wrote parts of the manuscript.

Chapter 4 contains data published in the *Journal of Biotechnology and Bioengneering* as:

Sullivan MA, **Lane S**, Volkerling A, Engel M, Werry EL, Kassiou M. Three-dimensional bioprinting of stem cell-derived central nervous system cells enables astrocyte growth, vasculogenesis, and enhances neural differentiation/function. Biotechnol Bioeng. 2023 Oct;120(10):3079-3091. doi: 10.1002/bit.28470.

I designed and performed some experiments, collected and analysed some data and wrote parts of the manuscript.

This research reported in this thesis was supported by a NSW Health Industry Partnership Scholarship and a Research Training Program scholarship.

As supervisor for the candidature upon which this thesis is based, I can confirm that the authorship attribution statements above are correct.

Michael Kassiou 28/02/2025 Samuel Lane 28/2/2025

Abstract

Alzheimer's disease (AD) is a devastating neurodegenerative disorder, characterized by cognitive decline and neuropathology involving amyloid β (Aβ), tau pathology and widespread neuroinflammation. Among these, neurovascular deficits represent an underappreciated yet critical component of AD pathology. These deficits are driven by complex interactions between proteinopathy, neuroinflammation, and cellular dysfunction at the neurovascular unit, a dynamic interface between multiple brain cell types. Understanding how these processes disrupt neurovascular function is essential for uncovering the mechanisms underlying AD. However, current AD models rely on non-representative mutations, simplistic 2D monocellular cultures, and animal models that fail to fully recapitulate the complex interactions at the neurovascular unit, limiting their relevance to the human disease and their utility in high-throughput drug discovery. This thesis aims to address these gaps by leveraging induced pluripotent stem cells (iPSCs) and bioprinting technologies to create physiologically relevant, scalable neurovascular models for studying AD pathology. A novel methodology is developed for reliably bioprinting fragile iPSC-derived brain microvascular endothelial-like cells (iBMECs), and is used to examine the pathological impact of Aβ deposition, neuroinflammatory stimuli and endothelial barrier dysfunction.

In Chapter 3, we differentiate and characterise iPSC-derived endothelial cells, pericytes, and astrocytes in classical 2D culture. Functional analyses reveal that iBMECs exhibit enhanced barrier properties compared to common *in vitro* alternatives, while iBMECs and iPSC-derived pericyte-like cells (iPericytes) demonstrate distinct protein secretion profiles and involving inflammatory priming and vascular maintenance. Their limited functional response to known pathological triggers presents an opportunity for further exploration of factors influencing iPSC-derived neurovascular function. In Chapter 4, the potential of 3D bioprinting to produce biomimetic neurovascular architecture is explored. Using CMECs and iBMECs, we optimise media conditions and develop a Rho-associated coiled-coil kinase (ROCK) inhibition protocol that supports iBMEC survival and function in bioprinted constructs. Tricultures combining endothelial cells, pericytes, and astrocytes are also bioprinted, exhibiting robust multicellular organization reminiscent of *in vivo* neurovascular structures, while posing questions surrounding appropriate culture conditions for iPSC-derived tricultures. In Chapter 5, we investigate the response of monocultured 3D iBMEC constructs to inflammatory stimuli, including lipopolysaccharides derived from *E. coli* and *P. gingivalis*, alongside various lengths of Aβ monomers. These experiments reveal important differences in VE cadherin expression between CMEC and iBMECs under longitudinal 3D culture, *in vivo*-reminiscent Aβ deposition phenotypes, and resistance to LPS-induced modulation of these phenotypes. This platform provide a foundation for further investigating how inflammatory and amyloidogenic insults might synergistically impair endothelial function.

This thesis demonstrates the successful differentiation and functional characterization of iPSC-derived neurovascular cell types, the development of an innovative 3D bioprinting framework for monoculture and triculture neurovascular models, and the application of these systems to dissect AD-relevant neurovascular interactions. This platform serves as a rich foundation for future physiologically-relevant, scalable platforms for investigating neurovascular disease pathology and facilitating efficient drug discovery efforts.

List of Abbreviations

AD	Alzheimer's disease
ADRC	Alzheimer's Disease Research Center
AM	Astrocyte Medium
ANOVA	Analysis of variance
APOE	Apolipoprotein E
APP	Amyloid precursor protein
AQP4	Aquaporin-4
BBB	Blood-brain barrier
bFGF	Basic fibroblast growth factor
BM	Basement membrane
BMECs	Brain microvascular endothelial cells
CAA	Cerebral amyloid angiopathy
Cas9-gRNA	CRISPR-associated protein 9 guide RNA
CD	Cluster of differentiation
CI	Cell index
CM	CMEC medium
CMECs	Cerebral microvascular endothelial cells
CNS	Central nervous system
CO2	Carbon dioxide
CRISPR	Clustered regularly interspaced short palindromic repeats
DAPI	4′,6-diamidino-2-phenylindole
DKK-1	Dickkopf-related protein 1
DMEM	Dulbecco's modified eagle medium
DNA	Deoxyribonucleic acid
DSB	Double-stranded break
ecLPS	Lipopolysaccharide from *Escherichia coli*
ECM	Extracellular matrix
EDTA	Ethylenediaminetetraacetic acid
EF-1a	Elongation factor-1 alpha
EGF	Epidermal growth factor
ELISA	Enzyme-linked immunosorbent assay
EM	Endothelial medium
EMMPRIN	Extracellular matrix metalloproteinase inducer
ENA-78	Epithelial-derived neutrophil activator-78
EpCAM	Epithelial cell adhesion molecule
EthD	Ethidium homodimer-1
EVOM	Electrical voltohmmeter

fAD	Familial Alzheimer's disease
FBS	Fetal bovine eerum
FDA	Food and Drug Administration
FGF	Fibroblast growth gactor
GDF-15	Growth differentiation factor 15
GelMA	Gelatin methacrylate
GFAP	Glial fibrillary acidic protein
GLUT-1	Glucose transporter 1
GM-CSF	Granulocyte-macrophage colony-stimulating factor
gRNA	Guide RNA
GRO	Growth-regulated oncogene
HBMEC	Human brain microvascular endothelial cells
HBVP	Human brain vascular pericyte
HDR	Homology-directed repair
HEK293	Human embryonic kidney 293 cells
HEPES	4-(2-hydroxyethyl)-1-piperazineethanesulfonic acid
hESFM	Human endothelial serum-free medium
HUVEC	Human umbilical vein endothelial cells
iBMEC	Induced pluripotent stem cell-derived brain microvascular endothelial cell
ICAM-1	Intercellular adhesion molecule 1
IFN	Interferon
IGF	Insulin-like growth factor
IGFBP	Insulin-like growth factor binding protein
IL	Interleukin
ILS	Inventia Life Sciences
iNPC	induced pluripotent stem cell-derived neural progenitor cells
iPSC	Induced pluripotent stem cell
KLF4	Krüppel-like factor 4
LAT1	L-type amino acid transporter 1
LDL	Low-density lipoprotein
LDLR	Low-density lipoprotein receptor
LPS	Lipopolysaccharide
LRP1	Lipoprotein receptor-related protein 1
MAP	Microtubule-associated protein
MAPT	Microtubule-associated protein tau
MBP	Myelin basic protein
MCI	Mild cognitive impairment
MCP-1	Monocyte chemoattractant protein-1

MDR1	Multidrug resistance protein 1
MeOH	Methanol
MFSD2A	Major facilitator superfamily domain containing 2A
MIF	Macrophage migration inhibitory factor
MMP	Matrix metalloproteinase
MRI	Magnetic resonance imaging
mRNA	Messenger RNA
MYC	Myelocytomatosis oncogene
NG2	Neuron-glial antigen 2
NH4OH	Ammonium hydroxide
NHEJ	Non-homologous end joining
NMDA	N-methyl-D-aspartate
nNOS	Neuronal nitric oxide synthase
NPCs	Neural precursor cells
OCT3/4	Octamer-binding transcription factor 3/4
PAM	Protospacer-adjacent motif
PAX6	Paired box protein Pax-6
PBS	Phosphate-buffered saline
PBST	Phosphate-buffered saline with tween-20
PCR	Polymerase chain reaction
PDGF-AA	Platelet-derived growth factor
PDGFR	Platelet-derived growth factor receptor
PECAM-1	Platelet endothelial cell adhesion molecule-1
PEG	Polyethylene glycol
PET	Positron emission tomography
pgLPS	Lipopolysaccharide from *Porphyromonas gingivalis*
PLVAP	Plasmalemma vesicle-associated protein
PSD95	Postsynaptic density protein 95
PSEN1	Presenilin 1
PSEN2	Presenilin 2
RA	Retinoic acid
RAGE	Receptor for advanced glycation end products
RBP4	Retinol-binding protein 4
RFU	Raw Fluorescence Units
RGD	Arginine-Glycine-Aspartic Acid
RNA	Ribonucleic acid
ROCKi	Rho-associated protein kinase inhibitor
RT	Room temperature
RTCA	Real-time cell analysis

sAD	Sporadic Alzheimer's disease
SD	Standard deviation
SDF-1	Stromal cell-derived factor 1
SMA	Smooth muscle actin
SNP	Single nucleotide polymorphism
SOX2	SRY-Box Transcription Factor 2
SV40	Simian virus 40
TEER	Transendothelial electrical resistance
TFF3	Trefoil factor 3
TFR1	Transferrin receptor 1
TGA	Therapeutic Goods Administration
TLR4	Toll-like receptor 4
TNF	Tumor necrosis factor
TREM2	Triggering receptor expressed on myeloid cells 2
VCAM-1	Vascular cell adhesion molecule 1
VE Cadherin	Vascular endothelial cadherin
VEGF	Vascular endothelial growth factor
YIGSR	Tyrosine-Isoleucine-Glycine-Serine-Arginine
ZO-1	Zonula occludens-1

Table of Contents

Chapter 1: Introduction

Chapter 2: Methods

Chapter 3: Validation and optimisation of 2D iPSC-derived vascular cell cultures

Chapter 4: Development of 3D, Rastrum-bioprinted vascular cultures

Chapter 5: Amyloid β and lipopolysaccharide treatment of 3D, bioprinted endothelial monocultures

Chapter 6: Discussion

List of Figures & Tables

List of Tables

Chapter 1: Introduction

1.1 The neurovasculature

The brain is the most energy-intensive organ in the human body, consuming a fifth of the body's glucose and oxygen, and containing around 650 km of blood vessels to deliver this energy to its entire volume (Zlokovic, 2011b, Zlokovic and Apuzzo, 1998). Nutrients, immune regulators, oxygen and metabolites are shuttled through the vasculature in the form of blood. This is pumped using pressure generated in the heart, and specialised contractile cells surrounding the vascular endothelium (Hall et al., 2014a). From the periphery, penetrating arteries enter the brain through the meninges, narrowing into arterioles, which further branch into capillary beds specialised for the meticulously controlled transfer of molecules (Villabona-Rueda et al., 2019). These capillary beds then branch into larger post-capillary venules, then into even larger veins, which exit the brain to clear CO_2 and metabolic waste products at the lungs and kidneys, respectively (Iliff et al., 2012b).

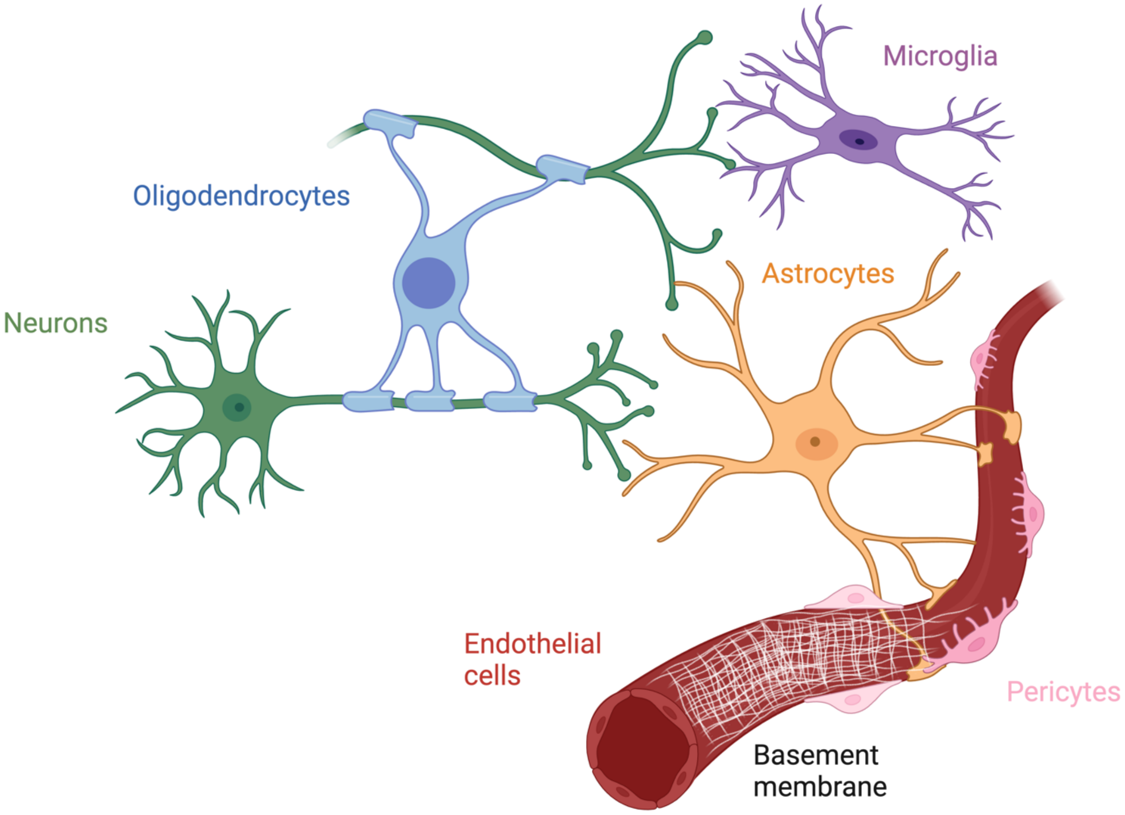

Figure 1.1: Components of the neurovascular unit. Created in Biorender (https://BioRender.com)

The hallmark feature of neurovasculature is the presence of an exceptionally tight barrier between its luminal and abluminal side, which is not seen in the periphery (Blanchette and Daneman, 2015). Although the endothelium is the first line of defence against blood-derived substances, a complex interplay between most brain cell types ensures that the BBB maintains its integrity and responds appropriately to changes in its local microenvironment. A typical section of brain parenchyma contains six main cell types: neurons, astrocytes, microglia, oligodendrocytes, endothelial cells and pericytes, plus components of the extracellular matrix (ECM), which comprise the vascular basement membrane (BM) and give structure to the parenchymal extracellular space (Figure 1.1). To understand the neurovascular unit and its role in vascular brain disorders, examining the cellular roles of endothelial cells, pericytes, astrocytes and the BM is integral.

1.1.1 Cellular Roles in the neurovascular unit

1.1.1.1 Endothelial cells

The brain endothelium is a single cell layer, separating the brain parenchyma from the bloodstream though an intricate vascular network. In the arterioles and capillaries of the brain, this layer of endothelial cells are non-fenestrated, and possess an impressive ability to constrain molecule transfer in order to protect the parenchyma from substances present in the bloodstream (Zhao et al., 2015). Compared to the endothelial cells in arteries and veins, these brain microvascular endothelial cells (BMECs) display a unique, tight junction-mediated barrier that is highly selective to ions, proteins, and other solutes – this is the blood-brain barrier (BBB) (Sweeney et al., 2018) (Figure 1.2).

Regardless of the surrounding tissue type, endothelial cells adhere to each other through adherens junctions, comprised of homophilic interactions between vascular endothelial cadherin (VE cadherin) proteins, and regulated by Platelet endothelial cell adhesion molecule-1 PECAM-1 (Biswas et al., 2006, Privratsky and Newman, 2014). The cadherins also participate in downstream signalling cascades via proteins bound to the cytoplasmic tail (Dejana and Orsenigo, 2013). PECAM-1 plays a role in leukocyte transmigration across the endothelium and contributes to the mechanotransduction that senses blood flow changes and adjusts cellular responses (Marin et al., 2012).

In addition to adherens junctions, brain microvasculature, also includes tight junctions, which effectively conjoin two adjacent membranes (Furuse, 2010). This feature polarises the endothelial cell into a luminal (blood-facing) and abluminal (parenchyma-facing) side, and limits the paracellular passage of molecules as small as monatomic ions (Chen et al., 2014, Beaufort et al., 2013). Notable components of tight junctions are claudins, occludin, zonula occludens, and junctional adhesion molecules. Claudins form the backbone of tight junction strands by establishing size- and charge-selective pores that regulate paracellular ion permeability (Furuse et al., 1998, Amasheh et al., 2002). Occludin tightly modulates tight junction stability and barrier function, though its absence does not disrupt barrier formation, suggesting an important regulatory role in barrier permeability (Saitou et al., 2000, Itallie et al., 2010, Siddiqui et al., 2015). Zonula occluden-1 (ZO-1) anchors these tight junction proteins to the intracellular cytoskeletons. ZO-1 and Claudin 5, although imperative for tight junction function, do not seem to confer similarly low permeability when expressed in the periphery, suggesting an adjunct role for other assisting proteins/molecules expressed only in the CNS) (Schuetz et al., 2005).

In addition to the junctional regulation of paracellular permeability (movement between cells, through tight junctions), there are a number of properties of CNS endothelial cells that restrict transcellular permeability (movement through cells, across both apical and basal membranes) (Figure 1.2). Peripheral vascular endothelial cells may have fenestrae (pores through the cell body which allow transcellular passage of substances), whereas BMECs are always non-fenestrated (Ueno et al., 2024, Braet and Wisse, 2002). Additionally, rates of caveolae-mediated transcytosis, a mechanism by which plasma membrane vesicles can transport solutes and proteins from one side of a cell to the other, are significantly reduced in CNS endothelial cells relative to peripheral (Lutz et al., 2017, Andreone et al., 2017). Caveolin-1, restricts BBB transcytosis by stabilizing caveolae, modulating their transport dynamics, and contributing to angiogenesis by regulating VEGF signalling pathways (Zhao et al., 2010, Wu et al., 2013). Upstream of caveolin-1, upregulation of major facilitator superfamily domain-containing protein 2 (MFSD2A) and downregulation of plasmalemma vesicle-associated protein (PLVAP) regulates the existence of caveolar-rich domains, thus reducing the levels of vesicular transport in these cells (Chow and Gu, 2017).

Leukocyte adhesion molecules are expressed on endothelial cell surfaces to bind white blood cells and allow their entry into tissues for immune surveillance. In the brain, immune regulation of this kind predominantly occurs at barriers of reduced tightness, like the blood-cerebrospinal fluid barrier, where activated memory T-cells can cross the more permissive barrier to monitor for pathogens without compromising BBB integrity (Wewer et al., 2011, Ransohoff et al., 2003). At the BBB, endothelial cells express low levels of leukocyte adhesion molecules, restricting the passage of leukocytes (Piccio et al., 2002).

To assist the correct filtering of molecules from the blood to the brain, a suite of transporters are expressed on endothelial cells in a cell-polarised manner (Figure 1.2). Efflux transporters use the hydrolysis of adenosine triphosphate to remove molecules from the endothelial cytoplasm against their concentration gradient, crossing the luminal membrane into the blood (Kastin et al., 2002). The most studied of these include P-glycoprotein (P-gp or MDR1) and breast cancer resistance protein. P-gp, which transports a wide range of substrates has been implicated in Alzheimer's disease (AD) pathology, where its reduced activity may impact BBB integrity and function (Montagne et al., 2017). Other important transporters are more specific, and ensure that integral molecules are granted passage across the BBB. GLUT-1 is the primary glucose transporter at the BBB expressed primarily on the abluminal membrane (but also on the luminal membrane), enabling glucose uptake critical for neuronal energy metabolism. GLUT-1 deficiency is associated with impaired cognitive function and neurodevelopmental disorders (Suls et al., 2008, Bélanger et al., 2005). Among others, MFSD2A transports fatty acids (in addition to its role in caveolae dynamics) and L-type amino acid transporter 1 (LAT1) transports amino acids (Zhao et al., 2020, Fukumoto et al., 2013). While vesicular transport across the cell is inhibited in the CNS, some transporters, like the transferrin receptor (TFR1) and low-density lipoprotein (LDL) receptors, exist to allow receptor-mediated vesicular transport. LDLRs mediate the uptake of cholesterol-rich lipoproteins, vital for maintaining neural cell membrane integrity and myelin formation (Mok et al., 2023). A related protein, lipoprotein receptor related protein-1 (LRP1), is a transporter with high-affinity binding to lipoproteins and other substrates, facilitating their transcytosis out of the parenchyma (Pflanzner et al., 2011).

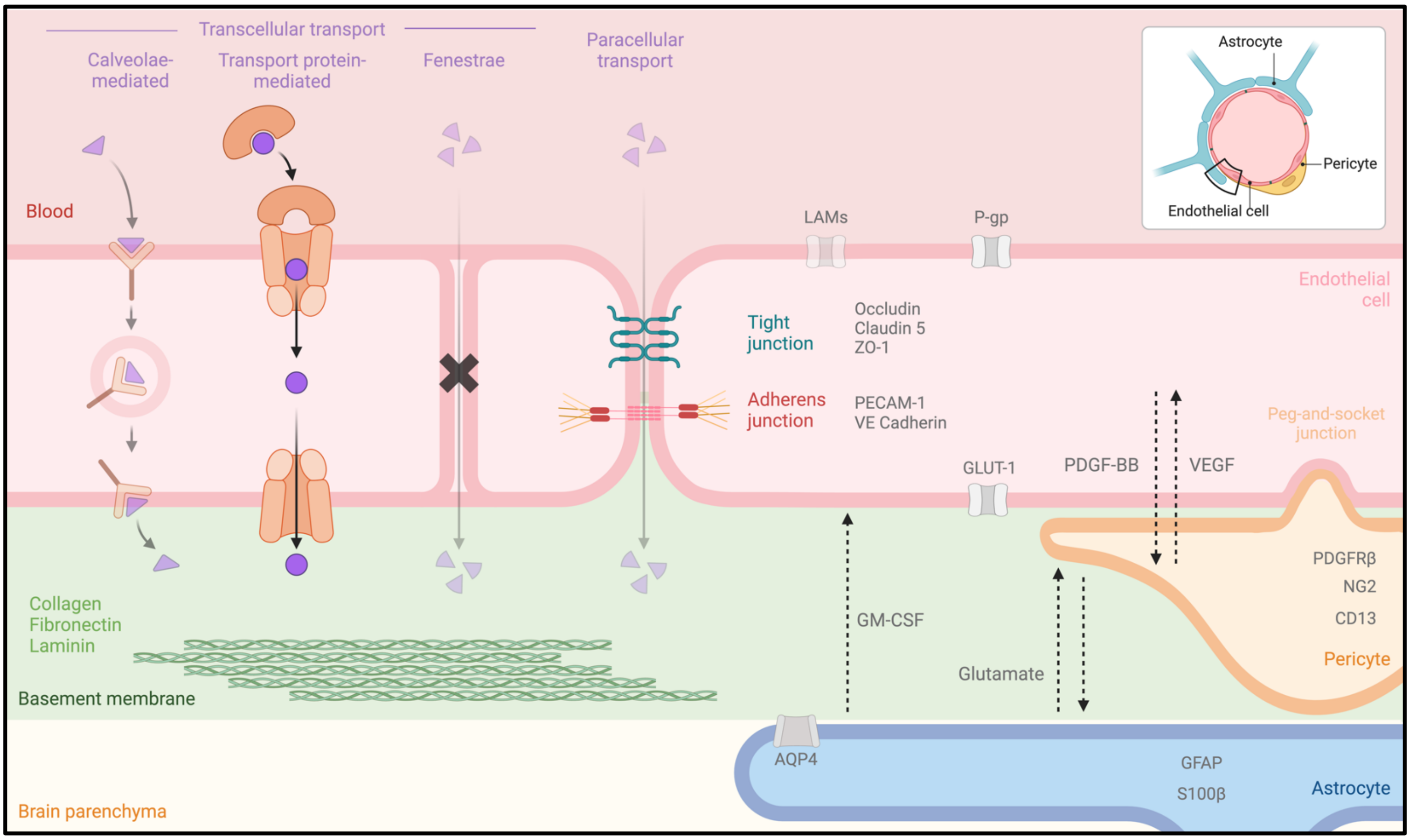

Figure 1.2: Junctions, transport and communication at the tripartite neurovascular unit. Created in Biorender (https://BioRender.com), with significant modifications to the template from Delrose (2024). Black cross denotes the lack of fenestrae in brain microvascular endothelial cells. Abbreviations: AQP4: Aquaporin 4, CD13: Cluster of Differentiation 13, GM-CSF: Granulocyte-macrophage Colony-Stimulating Factor, GFAP: Glial Fibrillary Acidic Protein, GLUT-1: Glucose Transporter 1, LAMs: Leukocyte-Adhesion Molecules, NG2: Neural/Glial Antigen 2, P-gp: P-glycoprotein, PDGF-BB: Platelet-Derived Growth Factor-BB, PDGFRβ: Platelet-Derived Growth Factor Receptor β, PECAM-1: Platelet Endothelial Cell Adhesion Molecule-1, S100β: S100 Calcium-Binding Protein β, VE cadherin: Vascular Endothelial Cadherin, VEGF: Vascular Endothelial Growth Factor, ZO-1: Zonula Occludens-1.

1.1.1.2 Pericytes

The brain endothelium is closely associated with pericytes, a mural cell type embedded in the BM surrounding capillaries, post-capillary venules and terminal arterioles (with scarcer numbers in the periphery). They are closely related to smooth muscle cells which are found in the larger arteries and veins, and express more α-smooth muscle actin (α-SMA) (Yamazaki and Mukouyama, 2018). Pericytes are distinguished from similar cell types by the simultaneous presence of platelet-derived growth factor receptor β (PDGFRβ), alanyl aminopeptidase (CD13), and neuron-glial antigen 2 (NG2) (Winkler et al., 2010, Özen et al., 2014, Armulik et al., 2011b). Endothelial cell-pericyte interactions are strengthened by physical "peg-and-socket" junctions between the cells (Figure 1.2). These connections are formed by a mix of junctional proteins and connexin-43 channels which allow for direct transfer of ions, metabolites and messengers (Bobbie et al., 2010, Monickaraj et al., 2018). Pericytes incompletely cover the abluminal surface of microvascular walls, however still play a number of roles in the proper functioning of the BBB (Sims, 1986).

One major function of pericytes is regulation of blood flow through capillary modulation (Nikolakopoulou et al., 2019, Uemura et al., 2020). Pericyte expression of contractile proteins such as α–SMA purportedly allows pericytes to control vascular diameter at the capillary level of the vascular tree (Peppiatt et al., 2006). In this study, glutamate exposure leads to pericyte relaxation and capillary dilation (Hall et al., 2014b). This notion has been contested however, by experiments showing that capillary dilation occurs independently of pericyte contractility, suggesting alternative mechanisms for blood flow regulation in capillaries (Hill et al., 2015, Attrill et al., 2019). While neurovascular coupling is predominantly carried out by astrocytes, pericytes also help synchronise local blood flow to neuronal activity, allowing efficient oxygen and nutrient delivery to active brain regions (Attwell et al., 2010).

Additionally, pericytes are involved in the regulation of angiogenesis and wound healing by secreting growth factors like VEGF, which stimulate endothelial cell proliferation and vessel maturation, especially after injury (Dulmovits and Herman, 2012). Low levels of adhesion molecules ICAM-1 and VCAM-1 in pericytes, are upregulated upon exposure to inflammatory cytokines, involved in lysosomal degradation during pericyte phagocytosis (Allt and Lawrenson, 2001, Özen et al., 2014).

Another key role of pericytes is the release a multitude of structural proteins that comprise the BM and ECM, proteins like collagen IV, laminin, and fibronectin to maintain this important acellular component of the neurovascular unit (Shimizu et al., 2011, Sakhneny et al., 2021, Lauridsen et al., 2017). Finally, pericytes facilitate the appropriate envelopment of the cerebrovasculature by astrocyte end-feet, forming the next important component of the BBB (Armulik et al., 2010).

1.1.1.3 Astrocytes

Astrocytes, named for their stellate morphology at homeostasis, are glial cells that perform numerous key roles in the neurovascular unit. Astrocytes are interconnected through gap junctions formed by connexin proteins, enabling ion and small molecule exchange across astrocyte networks to maintain homeostasis and synchronize activity within the neurovascular unit (Bennett et al., 2003, Nagy and Rash, 2000). Their processes extend to envelop a number of entities including the cerebrovasculature, nodes of Ranvier and synapses, providing trophic and metabolic support through the recycling of neurotransmitters, such as glutamate and gamma-aminobutyric acid (GABA), and antioxidant support (Mahmoud et al., 2019). Astrocytic end-feet, found at the end of astrocyte branches, envelop approximately 99% of the cerebrovasculature, anchoring to the abluminal side of the BM and acting as physical and immunological barrier between the bloodstream and the parenchyma (Mathiisen et al., 2010) (Figure 1.2). The anchoring mechanism occurs via the interaction between astrocytic dystrophin-dystroglycan complexes, with agrin protein in the BM (Ruggieri et al., 2019). The association with BM agrin by end-feet, elicits the upregulation of the water channel aquaporin-4 (AQP4), and organises them into a specialised structure: orthogonal arrays of intramembranous particles (Landis and Reese, 1974). These proteins help facilitate the exchange of potassium ions and water across the astrocytic membrane, a mechanism which underlies a central role of the astrocyte - neurovascular coupling or functional hyperemia.

Astrocytes also play a large role in functional communication to other cells in the neurovascular unit, allowing regulation of the BBB. While the brain requires large amounts of energy, it has little capacity to store energy, thus local increases in cerebral blood flow are used to deliver energy to areas that need it most. Astrocytes facilitate this by relaying vasoactive signals from neuronal synapses to their end-feet, which are in contact with blood vessels, enabling targeted blood flow adjustments (Attwell and Laughlin, 2001). Astrocytes also play significant roles in paracrine signalling, releasing hedgehog agonists that regulate low levels of leukocyte adhesion molecule expression on mature endothelial cells and exert anti-inflammatory effects (Alvarez et al., 2011). Inflammatory responses at the blood-brain barrier (BBB) are further moderated by astrocyte-derived granulocyte-macrophage colony-stimulating factor (GM-CSF) and retinoic acid, which support BBB integrity and reduce inflammation (Mizee et al., 2014, Spampinato et al., 2015). Astrocytes also participate in active communication with pericytes, and indeed the brains of Huntington's disease mice have been shown to display low pericyte coverage of vessels, due to the inflammatory response of dysfunctional astrocytes (Hsiao et al., 2015). Astrocyte-released interleukin (IL)-6 has been shown to modulate BBB permeability during inflammatory events, while glial cell line-derived neurotrophic factor (GDNF) and basic fibroblast growth factor (bFGF) support BBB integrity by promoting endothelial cell survival and reinforcing tight junctions within the neurovascular unit (Bell et al., 2012, Igarashi et al., 1999). Astrocytes are important for the glymphatic system, where AQP4 channels facilitate cerebrospinal fluid influx into the brain parenchyma, aiding in the clearance of interstitial solutes, a process critical for homeostasis and protection against neurodegeneration (Iliff et al., 2012a, Mestre et al., 2018).

1.1.1.4 Basement membrane

While not a cell type, the BM and ECM provide fundamental structural and functional support to the cellular portion of the neurovascular unit. The broader ECM is a macromolecular network consisting of polysaccharides and proteins, occupying around 20% of the total brain volume (Syková and Nicholson, 2008). The composition of this network varies with respect to the needs of its immediate environment, allowing cell adhesion to be tuned to perineuronal, perisynaptic and perivascular microenvironments (Lendvai et al., 2011). The native ECM surrounding neurovasculature is the BM, a thick structure composed of collagen IV, fibronectin, laminins, heparan sulfate proteoglycans and entactins. These molecules are largely secreted by pericytes, but also by endothelial cells, astrocytes and neurons (Thomsen et al., 2017). In the BM, adhesion occurs through integrin-mediated binding to matrix proteins, along with interactions with other receptors like dystroglycan and CD44 (Wright et al., 2012). In the wider ECM, adhesion occurs via integrin and proteoglycan interactions, but is more variable due to diverse ECM components that allow for dynamic cell attachment and migration (Pathak and Kumar, 2011). The macromolecules of the ECM also provide trophic support, and and contribute to the regulation of cell behaviour by presenting growth factors and mechanical cues that influence cellular proliferation, differentiation, and migration (Humphrey et al., 2014, Nune et al., 2014). Fibronectin is a glycoprotein that mainly binds to cellular integrin receptors to anchor them to the ECM (Takahashi et al., 2007b). Collagen IV is integral for the basal lamina specifically, being the basis for the sheet like structure of BMs as opposed to other ECMs (Boudko et al., 2018). Laminins, a family of glycoproteins with multiple subtypes, are essential for basement membrane stability and play a key role in cellular signalling, supporting structural integrity and directing cellular functions such as adhesion, migration, and differentiation (Hohenester, 2019, Li et al., 2020).

At the post-capillary venule level, the BM can be described as two separate membranes, an endothelial BM, comprising a4 and a5 laminin subtypes, and a parenchymal BM, secreted by astrocytes, comprising a1 and a2 subtypes (Hallmann et al., 2005). This disparity in laminin subtype distribution informs specialised function which allows T-cell infiltration into the perivascular space but restricts its entry to the parenchyma through laminin a5 in the parenchymal BM (Sixt et al., 2001). Matrix metalloproteases (MMPs), enzymes which degrade ECM proteins, play a dual role in the neurovascular unit by facilitating leukocyte migration and remodelling of the ECM (Candelario-Jalil et al., 2009, Zhao et al., 2019). However, dysregulation of MMPs has been linked to neuroinflammatory processes and BBB disruption in Alzheimer’s disease, where elevated MMP activity contributes to pathological protein accumulation and neuronal damage (Dore-Duffy and Cleary, 2011). Other key components of the matrix include: agrin, perlecan, glycosaminoglycans and osteonectin (Hallmann et al., 2005). All of these components act as substrates for dystroglycans or integrin receptors, and their interaction underlies the adherence of BBB cells to the BM (Baeten and Akassoglou, 2011). Integrin receptors, are crucial for anchoring cells to the BM and transmitting signals that regulate cellular responses like survival, proliferation, and migration, making them essential to BBB structural stability and function (Halder et al., 2023, Izawa et al., 2017).

1.1.1.5 Other cells

In addition to the principal components of the neurovascular unit, other parenchymal cell types maintain significant communication and physical connections with the neurovascular unit. Neurons are the key functional unit of the brain. Due to their specialised electrical properties, they allow the synchronised integration of electrical information, which ultimately endows the range of abilities characteristic of brains (Maki et al., 2013). Neural dendrites receive stimulation from other neurons, which moves towards the soma through the propagation of an electrochemical gradient along the cell wall. Once stimulation at the soma reaches a threshold, a large electrochemical action potential is propagated towards synaptic terminals where neurotransmitters are released from vesicles into the synaptic cleft, to be received at a post-synaptic terminal for signal transduction (King et al., 2015). Other transmitters like nitric oxide, diffuse freely across cell membranes, with their release tightly coupled to neuronal activity. The vasodilation-inducing abilities of nitric oxide, contribute to the role of neurons in neurovascular coupling and the regulation of local cerebral perfusion (Zhu et al., 2016).

Oligodendrocytes are glia that provide insulation of axons by enveloping their exterior in a myelin sheath comprised of lipids, and proteins such as myelin basic protein (MBP) (Baumann and Pham-Dinh, 2001). Oligodendrocytes contain a cell body, from which many branches extend towards neurons, enveloping a portion of the axon, leaving a space of uncovered axon (called a node of Ranvier) between it and the next sheath. At the neuron, these nodes contain a high concentration of ion channels, allowing for highly efficient transduction, through saltatory propagation (Brivio et al., 2017). In addition to this, oligodendrocytes also provide paracrine signalling releasing molecules such as brain-derived neurotrophic factor and IGF-1, which support neuronal health, modulate vascular function, contributing to the overall homeostasis and resilience of the neurovascular unit (Nave and Werner, 2014).

Microglia are the resident immune cells in the brain, and are key to the maintenance of proper brain function and response to pathogens or waste. In homeostasis, microglia survey the surrounding microenvironment with a highly ramified morphology, scavenging for unhealthy/dead cells, unnecessary synapses, protein aggregates and debris, whilst responding to chemical signals in order to direct their movement and phenotype (Liu et al., 2023). In the past, it was thought that once activated microglia transform into a classical, pro-inflammatory, M1-like phenotype, encompassing pro-inflammatory cytokine excretion (e.g TNF-α, IL-6 and IL-1β) and phagocytotic activity. The opposing M2-like state signified an anti-inflammatory phenotype focused on the resolution of inflammation, initiation of tissue reconstruction, restoration of homeostasis and anti-inflammatory cytokine release (e.g. IL-10) (Orihuela et al., 2016, Lier et al., 2021). However, it is now clear that microglial phenotypes exist on a more expansive spectrum of cellular behaviour and morphology, where elements of phenotypic categories exist in combination. Here, modern transcriptomics provides more granular phenotypic signatures exemplified by the so-called “disease-associated microglia” (Deczkowska et al., 2018, Keren-Shaul et al., 2017). Microglia modulate vascular permeability and contribute to inflammation and tissue repair at the BBB, with evidence also suggesting important physical interactions mediated by “capillary-associated microglia” (Zrzavy et al., 2017, Bisht et al., 2021). Chronic microglial activation has been suggested to be a key driver of disorders that involve protein accumulation (Heneka et al., 2015, Lv et al., 2024, Jäntti et al., 2022).

1.2 Alzheimer's Disease

1.2.1 Background

Neurodegenerative diseases are some of the most pernicious disorders to commonly affect humans. These disorders act, through varied mechanisms, to degrade the structure and function of the central and peripheral nervous systems. The majority of central neurodegenerative diseases result in a collection of symptoms, termed dementia, involving impairments in memory, behaviour and other cognitive functions, subsequently impairing daily life (Raz et al., 2016). The most common dementia is AD, which has a pathology defined by neuroinflammation, the build-up of extracellular amyloid β (Aβ), and the presence of intracellular neurofibrillary tangles consisting of hyperphosphorylated tau protein (WHO, 2015). Due to an aging world population, the World Health Organisation expects a tripling of AD incidence by 2050, resulting in global costs approaching 2 trillion USD by 2030 (WHO, 2015, Alzheimer's Association, 2023).

1.2.2 Epidemiology & pathology

Pathologically, AD is often categorised into familial AD (fAD) and sporadic AD (sAD). fAD describes when the disease directly results from certain causative genetic mutations, in genes such as the amyloid precursor protein (*APP*) or presenilin 1 and 2 (*PSEN1*, *PSEN2*). Over 99% of AD patients do not carry these disease causing-mutations, and for these sAD patients, the cause of the disorder is due to unclear interactions between the patient's genetics and environmental factors (Eratne et al., 2018, Masters et al., 2015). The largest genetic risk factor for sAD is the ε4 allele of Apolipoprotein E (APOE4). Apolipoproteins are proteins involved in fat metabolism via their function as stabilisers and signalling centres within lipoprotein assemblies, that transport fats through blood plasma or extracellular spaces (Mahley et al., 1984, Wang and Eckel, 2014). The APOE protein has three human isoforms, APOE2, APOE3 and APOE4, that display an 8%, 78% and 14% respective allele frequency in the general population (Raber et al., 2004). Although small differences exist, allele frequencies are comparable across Caucasian, African-American, Japanese and Hispanic ethnicities (Farrer et al., 1997). APOE3 is used as a baseline as it is the most common allele, with APOE4 representing an increased risk of AD, and APOE2 being protective against AD.

Strikingly, homozygous APOE4 carriers are 15 times more likely to have AD than homozygous APOE3 carriers, while APOE2 homozygotes are 40% less likely (Farrer et al., 1997). Due to this strong association to the AD phenotype, investigating the mechanistic link to AD pathogenesis is a fascinating and growing avenue of research. While *APP*- and *PSEN*-driven AD produces an earlier onset AD, *APOE4*-driven AD commonly results in a later onset, with the average age of onset approximately 20 years higher than the *APP*- and *PSEN*-driven disease (Raulin et al., 2022, Ryman et al., 2014). Although some other clinical differences are observed (e.g. *PSEN1* mutations can cause motor dysfunction, some *APP* variants can drive hemorrhagic strokes), pathology and clinical features between *APP*-, *PSEN*- and *APOE*- driven AD are largely comparable (de Kort et al., 2023, Jih et al., 2025, Pillai et al., 2021).

While age is the most significant environmental risk factor for AD (Masters et al., 2015), the importance of other factors like brain trauma (Livingston et al., 2017), sex (Riedel et al., 2016b), cardiovascular health (Wanleenuwat et al., 2019), education (Ngandu et al., 2007, Karp et al., 2004), social engagement (Penninkilampi et al., 2018) and mental health (Kuring et al., 2020) are becoming increasingly apparent. Similarly, chronic periodontic infection, specifically with *Porphyromonas gingivalis*, is becoming recognised as a significant risk factor for AD. The presence of periodontitis is associated with increase in AD-associated cognitive decline, in an observational and case-control study (Holmer et al., 2018, Ide et al., 2016). While there is a rich body of evidence supporting associations between AD and *P. gingivalis,* especially through the systemic inflammation induced by its virulence factors, evidence of direct causal relationships are hindered due to measurement differences between studies (Elwishahy et al., 2021).

While risk factors can be identified, effective diagnosis has remained challenging primarily due to the protracted pre-clinical disease phase, where neurodegeneration begins 20-30 years before symptom presentation (Davies et al., 1988). Clinical diagnosis is often inferred from antemortem clinical symptoms such as functional changes in memory, cognition and behaviour (McKhann et al., 2011), however clinical overlap with other dementias hinders diagnostic accuracy. Advances in cerebrospinal fluid biomarkers and PET imaging of Aβ and tau have boosted diagnostic accuracy (Walhovd et al., 2010), however full confirmation of the disease still requires post-mortem neuropathological analysis (McKhann et al., 2011).

Investigation into the pathological entities that underly AD have unravelled a deeply complex set of mechanisms that cluster around two pathological proteins: Aβ and tau (Glenner and Wong, 1984, Weingarten et al., 1975). In addition to these two proteins, neuroinflammation, a third hallmark of the disease, is often included to encompass the key role of immune dysregulation in AD progression (Thakur et al., 2023, Krstic and Knuesel, 2013). In addition to widespread parenchymal pathology, significant alterations are observed in the neurovascular system, impairing protein clearance that further exacerbates neuroinflammation (Zlokovic, 2011b, Kisler et al., 2017). Disentangling the interaction between genetic and environmental risk factors is key to understanding AD, and designing effective therapies (Bertram and Tanzi, 2009).

1.2.3 Amyloid β

Amyloids are misfolded protein aggregates, containing a cross-β structure, that are associated with a large number of disease states (Sunde et al., 1997). Aβ is a subset of this class, including monomeric peptides from 37-49 amino acids in length, which can form numerous soluble oligomer states, and aggregate to form larger insoluble plaques (Haass et al., 1992). These peptides arise from APP, an integral membrane protein, which is fragmented by secretase proteins (formed by presenilin subunits encoded by *PSEN1* and *PSEN2* genes). Cleavage by these proteins under physiological conditions generates non-pathological fragments, however, when *APP* is cleaved by β-secretase (encoded by beta-site amyloid precursor protein cleaving enzyme 1, *BACE1*), soluble sAPPβ is released, leaving a fragment (C99) that can be cleaved by gamma-secretase to form pathological Aβ peptides (Kojro and Fahrenholz, 2005). These pathological peptides are generally found in 2 lengths in the brain: $A\beta_{40}$ and $A\beta_{42}$ (although other forms are found), with $A\beta_{40}$ observed more commonly in soluble fractions, while $A\beta_{42}$ is more common in insoluble plaques (Jan et al., 2008). The ratio of $A\beta_{42}/A\beta_{40}$ has been proposed as a more informative way of measuring pathogenic Aβ as this ratio is higher in AD patients, and $A\beta_{42}$ is more susceptible to oligomerisation (Kwak et al., 2020, Sengupta et al., 2016). Soluble oligomeric Aβ occurs when monomers become misfolded, and aggregate together to form unstable oligomers (Larson and Lesné, 2011). Alternatively, plaque development begins with fibrillogenesis, where amyloid monomers attach to each other to form oligomers. These oligomers can further aggregate to become elongated, insoluble fibrils, organised into repeating β-strand structures that confer resistance to proteolytic cleavage (Walsh and Selkoe, 2007). These insoluble fibrillar structures deposit as plaques in the extracellular space, which have been shown to harbour a plethora of other molecules such as lipids (like cholesterol), nucleic acids, carbohydrates and other proteins (including APOE) (Stewart and Radford, 2017). While an active area of research, consensus remains that oligomers represent a more pathologically-relevant species than plaques (Cline et al., 2018, Selkoe and Hardy, 2016).

1.2.4 Tau

Tau is a microtubule-associated protein (MAP), that maintains cytoskeletal microtubule stability, and is highly expressed in the axons of neurons (Binder et al., 1985, Weingarten et al., 1975). During normal functioning, interactions with tubulin promote microtubule assembly and stability, having varied effects depending on the isoforms available and the protein's phosphorylation state (Cleveland et al., 1977, Johnson and Stoothoff, 2004). At homeostasis, tau is natively unfolded and highly soluble, allowing its phosphorylation sites to be highly accessible to enzymes (Mandelkow and Mandelkow, 2012).

Irregular or excessive phosphorylation of the tau protein (e.g. by dysregulation of kinases and phosphatases) can prompt a variety of pathomechanisms. Examples of this include: mislocalisation of tau (Decker et al., 2015, Tai et al., 2014); detachment of tau from the microtubule, inducing microtubule disassembly (Nachman et al., 2020); prevention of tau passage into the nucleus, inhibiting its DNA-protective properties (Sultan et al., 2011) and tau aggregation (Jouanne et al., 2017, Guo et al., 2017). The mechanisms of tau aggregation remain an active area of investigation, although a nucleation-elongation mechanism has been suggested, in which an initial oligomeric nucleus is created, onto which tau units are polymerised to form long fibrils, eventually leading to complex neurofibrillary tangles (von Bergen et al., 2000, Wang and Mandelkow, 2016). Tau can then spread in a prion-like manner, where oligomers are transported out of the cell, to 'seed' new tau pathology in neighbouring cells (Holmes and Diamond, 2014).

Accumulation of neurofibrillary tangles (and soluble tau species) trigger a number of pathogenic pathways, including neuronal degradation, endoplasmic reticulum stress and synapse loss (Abisambra et al., 2013, Fox et al., 2011, DeTure and Dickson, 2019). Tau-mediated synaptic dysfunction and mitochondrial impairment have been shown to amplify Aβ-induced neuronal dysfunction, and have even been suggested to be necessary for Aβ-mediated neurotoxicity (Zempel et al., 2010, Forner et al., 2017). AD-tauopathy contributes to BBB disruption through modulation of endothelial permeability and pericyte functions, enabling passage of neurotoxic compounds and immune cells causing neuroinflammation (Sweeney et al., 2018). Emerging research also highlights the potential for tau-targeting therapies to also mitigate Aβ toxicity and neuroinflammation, making tau a critical focal point in efforts to develop disease-modifying treatments for AD (Ng et al., 2022, Shi et al., 2019).

1.2.5 Neuroinflammation

Emerging evidence underscores the role of neuroinflammatory processes and systemic factors, including innate immune gene variants and chronic infections, as pivotal contributors to AD risk. The centrality of the neuroinflammatory response to AD pathogenesis was highlighted by innate immune genes revealed to be associated with AD incidence by genome wide association studies, and further corroborated by a swathe of experimental work investigating relevant functional components of those genes, especially triggering receptor expressed on myeloid cells 2 (TREM2: a regulator of microglial inflammation and phagocytosis) (Harold et al., 2009, Lambert et al., 2009).

Constituents of chronic periodontic infection such as *P. gingivalis*-derived gingipains and polysaccharides, are found in human AD brain specimens, and play key roles in neuroinflammation and cognitive decline (Poole et al., 2013, Dominy et al., 2019). Lipopolysaccharides from *P. gingivalis* (pgLPS) have been identified in the cerebrospinal fluid and hippocampi of patients with AD, and activate microglia, and exacerbate tau and Aβ pathology in preclinical models (Liu et al., 2024). Infection provokes the downregulation of major facilitator superfamily domain containing 2a (Mfsd2a) expression, which may contribute to increased barrier permeability in rats, and an *in vitro* BBB model (Lei et al., 2023). These authors also demonstrated that *P. gingivalis* was able to pass through their rat and *in vitro* BBB models. Although no viable bacteria have been found in human brains, suggesting that molecules like gingipains and pgLPS may be transported by other mechanisms from the peripheral infection (Liu et al., 2024).

Neuroinflammation in AD represents a self-perpetuating cycle, where exogenous inflammatory triggers and proteinopathies synergize to exacerbate neuronal damage and vascular dysfunction. It is thought that exogenous inflammatory stimuli acts to increase AD-risk, while developing proteinopathy acts to magnify neuroinflammation, creating a vicious cycle. Exogenous factors such as smoking, poor diet, pathogens, peripheral infections and chronic stress can promote an increasingly damaging, pro-inflammatory milieu at early stages of the disease (Paolillo et al., 2023). Early neuroinflammation is known to provide a ripe environment for tau aggregation and seeding, but also for amyloid deposition in the parenchyma and vasculature, which further exacerbates local inflammation (Arnaud et al., 2007, Arnaud et al., 2009, Chabrier et al., 2012). Tau interacts with microglia, astrocytes, and pericytes, triggering an inflammatory response that propagates neurodegeneration (Montalbano et al., 2022). Similarly, Aβ deposition can cause activation of microglia, astrocytes, and pericytes, inducing a neurotoxic environment that promotes further Aβ accumulation and neuronal damage (Chabrier et al., 2012). In the neurovascular unit, cerebral amyloid deposition causes vascular dysfunction, BBB disruption, and perivascular inflammation, impairing glymphatic clearance in a way that worsens Aβ burden and entrenches dysfunctional neuroinflammatory environments (Kress et al., 2014, Zlokovic, 2011a). Neuroinflammation has been shown to be a dominant mechanism at the later stages of the disease, with widespread cortical atrophy, white matter damage, and neuronal network dysfunction occurring in more widespread brain areas, and also occurring independent of Aβ and tau pathology (Bélarbi et al., 2012, Leng et al., 2022).

1.2.6 Neurovascular deficits

Neurovascular dysfunction stands as a critical, underappreciated hallmark of AD (summarised in Figure 1.3), with cerebral amyloid angiopathy (CAA) being its most striking manifestation (Pantelakis, 1954). While parenchymal Aβ can cause considerable damage, In CAA, amyloid deposits accumulate within the neurovasculature, causing profound barrier dysfunction (Wisniewski et al., 1997). This pathology is distinct from AD, however is often viewed as an accompanying symptom considering the intertwined pathologies and how often they are observed in comorbidity (Cordonnier and van der Flier, 2011). Estimates of the prevalence of cerebral amyloid angiopathy in AD range from 70% to 98%, decidedly increased from rates in the general population (Biffi and Greenberg, 2011). CAA typically presents as Aβ deposits in the small arteries and capillaries of the cortex and leptomeninges. These deposits are predominantly composed of $A\beta_{40}$, contrasting to the $A\beta_{42}$ found parenchymally (Herzig et al., 2004, Herzig et al., 2006). This results in microaneurysms, reduced vessel diameter and perivascular microhaemorrhage, which can subsequently cause BBB leakage and dysregulation of perivascular drainage pathways (Vinters et al., 1994, Vinters, 1987, Mandybur, 1986, Zekry et al., 2003). A quarter of AD patients show severe CAA, while half of those who die from CAA-related haemorrhages also show neuropathological AD (Jellinger, 2002, Ellis et al., 1996). Additionally, microbleeds are observed in AD patients more than any other dementia (Cordonnier et al., 2006). While not observed in all AD patients, research implicating the presence of CAA with higher impairment in AD patients underscores its pathological significance (Pfeifer et al., 2002, Neuropathology Group of the MRC CFAS, 2001). Extravasation of blood-derived molecules like albumin, immunoglobulins and prothrombin have been observed, associating to various amyloid forms, in the microvascular portions of post-mortem AD brains (Wisniewski and Kozlowski, 1982, Wisniewski et al., 1997), with prothrombin levels positively correlated with the Braak staging of the patient (Zipser et al., 2007). Aberrant endothelial tight junction expression and localisation are also observed in post-mortem brain samples, mice models, and *in vitro* following exposure to pathogenic amyloids (Carrano et al., 2012, Kook et al., 2012, Marco and Skaper, 2006).

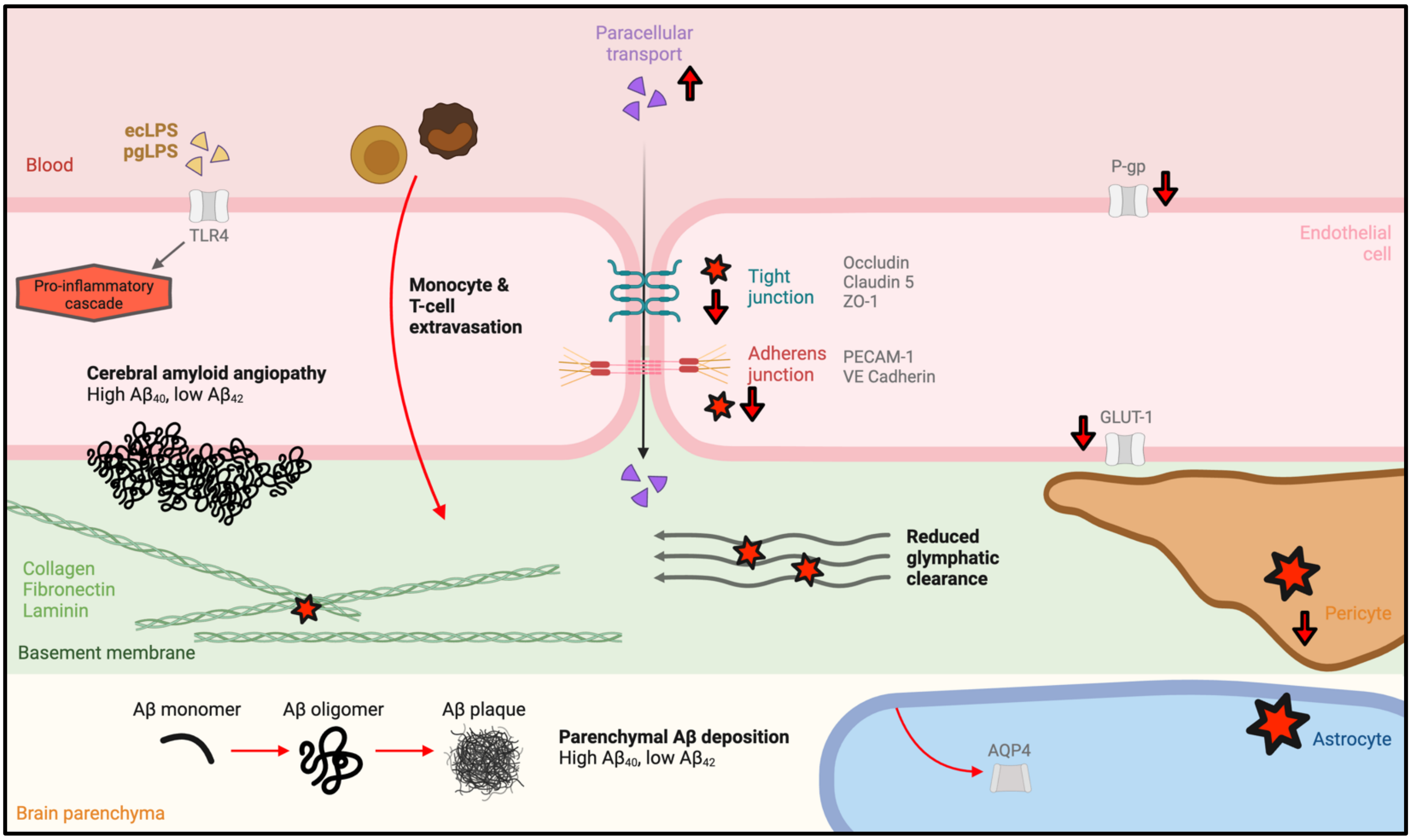

Figure 1.3: Alzheimer's disease-related pathology at the neurovascular unit. Key pathological hallmarks include: Loss and disruption of junctional proteins, Increased paracellular permeability, reduction in transporter (GLUT-1) expression, bacterial endotoxins interacting with TLR4 to induce degradation and loss of pericytes, activation of astrocytes, mislocalisation of AQP4, increased parenchymal Aβ deposition, cerebral

amyloid angiopathy, P-gp dysfunction, reduced glymphatic clearance, disrupted basement membrane proteins. Created in Biorender (https://BioRender.com), with significant modifications to the template from Delrose (2024). Abbreviations: Aβ: Amyloid β, AQP4: Aquaporin 4, ecLPS: lipopolysaccharide from *E. coli*, GLUT-1: Glucose Transporter 1, P-gp: P-glycoprotein, PECAM-1: Platelet Endothelial Cell Adhesion Molecule-1, pgLPS: lipopolysaccharide from *P. gingivalis*, TLR4: Toll-like Receptor 4, VE cadherin: Vascular Endothelial Cadherin, VEGF: Vascular Endothelial Growth Factor, ZO-1: Zonula Occludens-1.

A key early feature of Alzheimer's pathology is the breakdown of the BBB, driven in part by dysfunctional endothelial transporter biology. Studies note reduced expression of the BBB glucose transporter, GLUT-1, in AD patients and mouse models, where it can result in microvascular degeneration, reduced tight junction protein expression, accelerated Aβ pathology and extravasation of blood components (Harik, 1992, Horwood and Davies, 1994, Mooradian et al., 1997, Merlini et al., 2011, Hooijmans et al., 2007, Winkler et al., 2015). Using magnetic resonance imaging (MRI), an age-dependent breakdown of the hippocampal BBB was shown to occur in living AD and MCI patients as opposed to healthy controls, and this breakdown correlated with measures of pericyte injury (Montagne et al., 2015). Efflux transporters like LRP1 have the ability to actively transport Aβ out of the parenchyma, and its expression is reduced in AD patients, which has been shown to interrupt Aβ clearance in an inducible LRP1 deletion mouse model (Shibata et al., 2000, Deane et al., 2004, Storck et al., 2016). Recently, it was shown in mice that LRP1 loss results in activation of the cyclophilin A–MMP-9 pathway, causing tight junction loss and barrier dysfunction that could be rescued by cyclophilin A inhibition (Nikolakopoulou et al., 2021). Expression of the P-gp transporter is reduced surrounding Aβ plaques, and degraded by $A\beta_{40}$, which has been shown to impair adequate Aβ clearance (Park et al., 2014, Hartz et al., 2016, Cirrito et al., 2005).

Chronic neuroinflammatory states brought on by neurovascular exposure to infections, contribute to neuronal apoptosis and cognitive decline in AD (Charoensaensuk et al., 2021). Pro-inflammatory cascades elicited by bacterial substituents such as LPS, and gingipains from *P. gingivalis*, can promote vascular Aβ accumulation through the endothelial upregulation of receptor for advanced glycation end products (RAGE) (Zeng et al., 2020). Mechanistically, pgLPS activates TLR4 signalling, driving release of pro-inflammatory cytokines like IL-6 and CCL2, via the NF-κB pathway, further amplifying cytokine production and endothelial dysfunction

(Kim et al., 2023, Xie et al., 2020, Sato et al., 2021). pgLPS exposure also impairs tight junction protein expression, leading to increased permeability in human vascular endothelial cells, a key feature of BBB breakdown in AD (Zhang et al., 2013). Infection with *Escherichia coli* and its isoform of LPS (ecLPS) also generates a TLR4-mediated pro-inflammatory neurovascular environment, that can exacerbate AD-related neuroinflammation (Zhan et al., 2016). While ecLPS is most commonly used in neuroinflammatory modelling due to its strong response, P. gingivalis may be more relevant for AD (Qiu et al., 2021).

Neurovascular implications in AD also involve significant pericyte dysfunction. At homeostasis, pericytes can influence glymphatic flow by modulating the expression and localisation of water channels on astrocytes, through the PDGF-BB signalling pathway (Simon et al., 2022). This glymphatic pathway is the main mechanism of removing waste from the CNS, thus representing a critical protective function of pericytes. APOE4 carriers and AD patients harbour pericytes with disorganised ultrastructural features, that cover less of the vasculature, which can impair the waste clearance function of these cells (Sengillo et al., 2013b, Halliday et al., 2015, Farkas and Luiten, 2001, Baloyannis and Baloyannis, 2012). Accumulation of AD-related proteinopathy is seen in human and rodent AD brains, and pericytes subsequently upregulate LRP1 and other receptors such as the low density lipoprotein receptor (LDLR) (Zenaro et al., 2017, Ma et al., 2018). The capillaries of AD patients are constricted by pericytes, lowering cerebral blood flow (Nortley et al., 2019) and reduced pericyte coverage of the neurovasculature is observed in AD brains, correlating with barrier disruption, causing accelerated parenchymal and vascular amyloid deposition, and impairing clearance of $A\beta_{40}$ and $A\beta_{42}$ (Sengillo et al., 2013a, Sagare et al., 2013).

Astrocyte dysfunction plays another crucial role in the neurovascular impairments associated with AD. AD patient brains express aberrant levels of astrocytic GFAP and AQP4, also showing a mislocalisation of AQP4 (diffuse rather than predominantly at perivascular endfeet) that correlates with Braak stage and Aβ pathology (Wilcock et al., 2009, Zeppenfeld et al., 2017, Yang et al., 2011). This aberrant astrocytic AQP4 phenotype also impairs the cerebrospinal fluid-mediated clearance of toxic solutes (including Aβ) from the interstitial fluid through the drainage pathways (Iliff et al., 2012b). Before widespread Aβ burden, mice harbouring the Swedish and Arctic *APP* mutations exhibit increased astrogliosis, coupled with increased vascular laminin deposition. In areas flanking CAA and parenchymal Aβ, astrocytes retract their endfeet leading to neurovascular uncoupling, and barrier dysfunction (Merlini et al., 2011).

Neurovascular components also interact with tau pathology, and other risk factors like APOE4. Mice expressing a mutant tau isoform show dysfunctional neurovascular coupling that precedes cognitive impairment and neurofibrillary tangle pathology (Park et al., 2020). This dysfunction involves a decoupling of postsynaptic density 95 (PSD95) and neuronal nitric oxide synthase (nNOS), reducing vasodilatory nitric oxide release and impairing vasodilation. In addition to cellular effects, the acellular BM also undergoes thickening in AD brain capillaries, and a range of BM proteins are overexpressed in subclinical and clinical AD patients (Farkas and Luiten, 2001, Lepelletier et al., 2017). APOE4 genotype is also a risk factor for CAA, and has been shown to affect the binding of Aβ with laminin, which is involved in Aβ clearance through the perivascular pathway (Howe et al., 2020).

While recent years have seen an increase in focus on the neurovascular influence on AD pathology, there are still gaps in our understanding. The mechanisms by which *P. gingivalis* and its endotoxins modulate vascular inflammation cascades remain poorly understood, particularly in the context of their differential effects compared to other bacterial endotoxins. Additionally, the potential synergy between bacterial-induced neuroinflammation and isoform-specific Aβ deposition phenotypes has not been systematically investigated. The lack of physiologically relevant *in vitro* models capable of capturing these complex host-pathogen interactions limits our ability to study them in controlled, human-relevant contexts.

1.2.7 Treatment

While the hallmarks of the disease have been heavily researched, there are still many unanswered questions, and no widely accepted disease-modifying treatment available to patients (Gauthier et al., 2016). Over 3300 clinical trials have taken place to develop therapies for AD, yet only a few have gain approval by the United States Food and Drug Administration (FDA) or the Australian Therapeutic Goods Administration (TGA) (Xiao and Zhang, 2024, Cummings et al., 2024). Besides the recent flurry of anti-Aβ antibody therapies, all of these are symptomatic therapies that do nothing to alter the disease course. These therapies are: memantine, donepezil, rivastigmine, and galantamine (Yiannopoulou and Papageorgiou, 2020). Memantine is an NMDA receptor antagonist, the only therapy with positive effects at later stages of the disease, offering some improvements in global function by reducing glutamate-induced ion flux (Tricco et al., 2018, Matsunaga et al., 2015). The other three drugs are acetylcholinesterase inhibitors, which slow the onset of cognitive symptoms but only during earlier stages of the disease course (Kumar et al., 2015). Aside from pharmacological intervention, other non-disease-modifying strategies for AD management include: cognitive behavioural therapy, exercise, music therapy and environmental management e.g. clear communication, pleasurable activities and simplification of routines (Na et al., 2019, Atri, 2019).

The last few years have seen an influx of anti-Aβ monoclonal antibody therapies. While aducanumab, lecanemab and donanemab have received FDA approval, many challenges remain before we can confidently combat this disease (Ramanan and Day, 2023, Li et al., 2023a). Aducanumab showed disputable reductions in cognitive decline, and was discontinued after the United States Medicare system refused to cover the therapy, citing a low standard of proof upheld by the FDA (Dyer, 2024). Subsequently, both lecanemab and donanemab elicited a significant reduction of Aβ-load in most patients. In the case of lecanemab, patients also showed reductions in tau pathology and some slowing of cognitive decline (approximately 25% slower cognitive decline over the 18 month trial). In the TRAILBLAZER-ALZ 2 trial investigating donanemab, patients saw an average 29% reduction in cognitive decline in patients with at least intermediate tau pathology, and evidence of considerable amyloid clearance (Sims et al., 2023).

The effectiveness of these drugs, especially compared to their risk profiles, has been hotly debated, with many pointing out that slim effect sizes and conditional efficacy sharply limit the clinical significance of these therapies (Høilund-Carlsen et al., 2024). A wide range of consequences further highlight the need for continued development, including the high prevalence of cerebral edema and microhemorrhages (termed amyloid-related imaging abnormalities), contraindication with anticoagulant medications, increased risks for APOE4 carriers, excessive financial costs and the health risks and logistical challenges of regular infusion frequencies. It has also been postulated that reductions in amyloid-PET signal may be reflective of therapy-related tissue damage, rather than true disease modification (Høilund-Carlsen et al., 2024).

While a formidable body of research has interrogated cellular pathology in AD, we are still left with a noticeable lack of viable disease-modifying treatments. A key reason for this is the lack of *in vivo* and *in vitro* models that accurately recapitulate AD pathology, crippling the effectiveness of therapeutic discovery efforts (Liu et al., 2019, Pound and Ritskes-Hoitinga, 2018, McGraw et al., 2017). Particularly, the absence of neurovascular components in these models, and the limited recognition of the neurovascular unit's role in Alzheimer's disease pathogenesis, hinders understanding of multicellular pathomechanisms (Zlokovic, 2011a). To complement *in vivo* models of CNS disorders, there is a pressing need for advanced *in vitro* models that faithfully integrate the multicellular pathology and 3D microenvironment essential for accurately capturing disease mechanisms and informing therapeutic discovery.

1.3 Alzheimer's disease modelling

1.3.1 In vivo models

In order to efficiently model and screen drugs for CNS diseases like Alzheimer's disease, it is important to use models that accurately and reliably recapitulate the human disease, including incorporation of the neurovascular unit (Table 1.1). Ethical issues preventing invasive human (or non-human primate) experiments combined with the lack of effective, non-invasive imaging tools, force researchers to use other non-human animals to test the efficacy of drugs intended to treat the disease in humans (Drummond and Wisniewski, 2017). While some research is conducted using invertebrates like worms (*Caenorhabditis elegans)*, flies (*Drosophila melanogaster)* or zebrafish (*Danio rerio)* the majority of *in vivo* AD studies are conducted in rodent models, due to their advantageous balance between genetic similarity to humans, behavioural complexity and experimental ease (Sosa et al., 2011). Often constructed by engineering genetic mutations in the *APP, PSEN1 or PSEN2* genes, these mice present with faulty amyloid processing, Aβ deposition, and some AD-like phenotypes (e.g. abnormalities in cognitive function and memory) (Gotz et al., 2018).

Mice deficient in, or overexpressing the human *APP* gene were initially used to understand the role of this protein in neurophysiology (Buxbaum et al., 1993, Takei et al., 2000, Zheng et al., 1996). Mice expressing AD-relevant mutations in human *APP* and *PSEN1/2* were then developed, such as the Swedish (*APP*, K670N/M671L), London (*APP*, V717F) and Finnish (*PSEN1*, M146L) mutations (Echeverria et al., 2004). These rodents show cognitive decline before neuron loss, as well as calcium dysregulation, excitotoxicity and progressive increase in $A\beta_{42}$-load (Schaeffer et al., 2011, Morrissette et al., 2009, Mattson et al., 2001, Sawamura et al., 2000, Oyama et al., 1998). Unfortunately, these models do not exhibit appropriate Aβ plaque or tau pathology, limiting their legitimacy (Gotz et al., 2018). However, the face validity of transgenic rodent models sharply improved upon conferring mice with multiple pathological mutations. For example, APP-overexpressing mice also exhibiting the *PSEN1* R278I mutation showed Aβ-depositions significantly earlier than *APP* single-mutants (Saito et al., 2011). The 3xTgAD model (including an *APP*, a *PSEN1* and a MAPT mutation) and 5xFAD model (including the Swedish, Florida and London *APP* mutations and two *PSEN1* mutations) both show earlier, more aggressive neuron loss, and greater, more recapitulative Aβ deposition (Oakley et al., 2006, Kimura and Ohno, 2009, Maarouf et al., 2013). While hyperphosphorylation of tau is observed in some of these rodent models, the presence of tangles is noticeably absent. The exception is the 3xTgAD model, which solved this problem, by incorporating a P301L mutation in the *MAPT* gene, along with *APP* and *PSEN1* mutations, conferring mice with neurofibrillary tangle pathology (Oddo et al., 2003). But the disease-relevance of this model to AD is tangential, as fAD mutations alone are rare in humans (let alone multiple concurrent mutations), and the P301L mutation is associated with frontotemporal dementia, not AD (Alberici et al., 2004).

While these models have allowed the interrogation of some pathomechanisms, they address the familial form of the disease rather than the sporadic form borne by over 99% of patients. Pathogenic phenotypes from fAD mutant rodents are only detected due to excessive mutation-loads not observed in the human population, and it is unclear to what degree we can extrapolate these results to the sporadic form. While research into rodents with genetic risk factors such as APOE4 or TREM2 is plentiful, the results are only somewhat related to AD, as the risk factors are not fully penetrant (Zhong et al., 2024).

While the expression of behavioural phenotypes is a stark advantage over *in vitro* models, rodent models cannot reproduce characteristic tau pathology without the introduction of disease-irrelevant mutations, let alone replicate the temporal cascade of Aβ deposition, tau hyperphosphorylation, tangle formation, neuroinflammation and neuronal loss (Gotz et al., 2018). A further disadvantage of animal studies is the inherent difference in genetic background between the model animal and human, conferring significant differences in the protein and tissue environments. Novel advances in *in vitro* culturing techniques, especially of the neurovascular unit which is traditionally not incorporated into *in vitro* drug screening for AD, offer exciting progress in addressing widespread validity issues that have hampered therapeutic development and disease modelling.

Table 1.1: Summary of experimental systems for CNS modelling.

	2D *In Vitro* Models 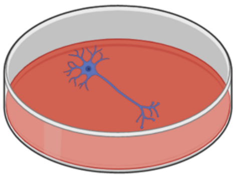	***In Vivo* Models** 	**Human 3D *In Vitro* Models** 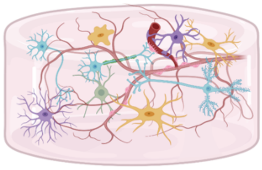
Experimental Ease/Speed	High	Low	High
***In Vivo* Cell Morphology**	Medium	High	High
Multi Cell-Cell Interactions	Low	High	High
Disease-Relevant Phenotypes	Low	Low	High

1.3.2 In vitro models of the neurovascular unit

1.3.2.1 Standard models

Compared to *in vivo* research, *in vitro* studies allow tight temporal control of experimental perturbations, and swift sample generation due to the relative ease of maintaining 2D cultured cells. They also provide the opportunity for larger sample sizes with higher throughput availability, and more complex molecular analyses prohibited by ethical considerations in animals. Additionally, usage of human-derived cell types is possible, giving experimenters confidence that any cell-intrinsic interactions are more species- and disease-relevant (Table 1.1).

There are two main types of cell lines used in classical *in vitro* modelling: immortalised and primary cell lines. Immortalised cell lines such as the human cerebral microvascular endothelial cell/D3 line (hCMEC/D3; CMEC) is a commonly used immortalised brain microvascular endothelial cell line that offers a convenient and reproducible model for BBB studies, though it may not fully replicate the complexity of *in vivo* endothelial cells (Weksler et al., 2013). Immortalised astrocytes and pericytes do exist (such as those immortalised using SV40 Large T antigen), but the human primary versions of these cells tolerate lab culturing and extended passage numbers well, so are preferable due to their lack of genetic modification (Brown et al., 2023, Zhang et al., 2016).

Primary cell lines possess a variety of advantages over immortalised cell lines. While ongoing culture of human neurons is impractical due to their post-mitotic nature and the invasive procedures required to harvest them, neurons from rodents are commonly harvested and cultured, however cannot be passaged, and are often used in mixtures with other cell types due to incomplete purification. There are commercial sources of human astrocytes (Lonza), pericytes (HBVP, ScienCell), and brain microvascular endothelial cells (HBMEC, ScienCell), although HBMECs are particularly sensitive to extended culturing. For these reasons, experimentation on endothelial cells often use immortalised cells (CMECs) or primary cells extracted from the fetal umbilical vein (HUVECs). Immortalised and primary lines provided a useful basic platform to probe cellular behaviours with relative ease and high throughput. However, even primary cell lines have problems, such as a lack of tissue-specific properties, non-representative responses to microenvironmental cues, and inappropriate cell age for aged-disease modelling (e.g. the aforementioned primary astrocytes and pericytes are extracted at a fetal stage) (Brown et al., 2013).

1.3.2.2 iPSCs

In 2006, four transcription factors (OCT3/4, SOX2, KLF4 and c-MYC) were delivered into mouse fibroblasts to produce the first induced pluripotent stem cells (Takahashi and Yamanaka, 2006). These cells mimic the self-renewal and differentiation capacity of embryonic stem cells, but replace the invasive retrieval of embryonic material with less-invasively retrieved adult somatic cells (e.g. skin fibroblasts or peripheral blood mononuclear cells). Next, this process was reproduced in human fibroblasts (Takahashi et al., 2007a) and other human cell types (Staerk et al., 2010, Aasen et al., 2008, Zhou et al., 2012). These advances were quickly followed by successful directed differentiating towards a wide variety of terminal cell types (Burridge and Zambidis, 2013, Huang et al., 2014, Kadzik and Morrisey, 2012, Spence et al., 2011). These novel methods provided scalable generation of large numbers of cells, access to hitherto inaccessible human cell types (e.g. neurons and other brain cells) and the potential observation of patient- and genome-specific phenotypes.

For the purpose of neurovascular research, efficient derivation of endothelial cells, pericytes and astrocytes is imperative. iPSC-derived brain microvascular endothelial cells (iBMECs) were first derived by initial differentiation into a mixed neural/endothelial culture, before subsequent selective purification onto a fibronectin and collagen IV-coated surface (Lippmann et al., 2012b). Since then, the protocol has been improved by the addition of retinoic acid to differentiation media enhancing barrier properties (Lippmann et al., 2014b), while replacing serum with B27 (a defined mixture of vitamins, antioxidants, lipids, and growth factors) increased derivation consistency and provided full definition of media components (Neal et al., 2019). Efficient, fully-defined pericyte differentiation from iPSCs was first performed by Orlova et al. (2014) using mesoderm-inducing factors (such as CHIR99021) to enhance lineage commitment before vascular specification. Current methods employ a similar structure, with successful derivation along both mesodermal and neural crest lineages being achieved (Faal et al., 2019). Astrocytes originate from radial glia which are progenitor cells from the developing brain that guide neuronal migration (Cheslow and Alvarez, 2016). The derivation of astrocytes involves first deriving neural precursor cells (NPCs) by the initial generation of aggregated embryoid bodies, subsequent neuronal patterning into neural rosettes, before selection of NPCs (Chambers et al., 2009). Subsequently, extended culture in proprietary astrocyte medium, was shown to effectively differentiate NPCs towards functional astrocytes (Tcw et al., 2017).

1.3.3 2D neurovascular models in Alzheimer's disease research

A consideration when developing *in vitro* cultures for AD modelling is to recognise the contribution of all cell types in the pathobiology of the disease. While the neuronal pathology of AD is most widely documented, astrocytes, microglia, oligodendrocytes, endothelial cells and pericytes are all involved in the degenerative pathway. Experimental models of AD designed around non-vascular cells have been reviewed extensively elsewhere (Mungenast et al., 2016, Karmirian et al., 2023, Pinals and Tsai, 2022). Of the cell types, neurovascular components have received significantly less attention, yet have been shown to contribute heavily to disease processes (Nortley et al., 2019, Li, 2023, Liddelow et al., 2017).

Simple 2D neurovascular models involving immortalised or primary endothelial monolayers have been widely used to assess BBB integrity. Transwell systems, featuring semipermeable membranes, facilitate these studies by enabling luminal and abluminal cell seeding, allowing assays such as transendothelial electrical resistance (TEER), dye permeability, and immunofluorescent localization (Adil and Somanath, 2021). These models are easy to use, cost-effective, and scalable to high-throughput formats. For example, Ni et al. (2017) used CMECs to show that exposure to TNF-α increased barrier permeability to dextran, while also decreasing TEER. In another study, transwell-cultured CMECs were used to demonstrate that Aβ can induce BBB permeability, and that somatostatin can abrogate this effect by regulating LRP1, suggesting potential therapeutic effect (Paik et al., 2019). The transwell model is also amenable to co-culture configurations, with Zhang et al. (2011) showing primary rat astrocytes modulate the behaviour of primary mouse endothelial cells, reporting more representative TEER, permeability and tight junction expression than 2D monocultured endothelial cells. Conditioned media from non-iPSC-derived 2D vascular cultures have also been interrogated for relevant secreted molecules (Smyth et al., 2018). 2D cultured HUVECs and CMECs have shown similar but distinct protein secretion profiles, identifying a number of chemoattractants relevant for angiogenesis, cell motility and inflammation (Schmidt et al., 2009). Primary human pericytes have similarly been investigated, showing that some transcriptionally upregulated cytokines were downregulated at the protein level, and that co-culture with CMECs triggered the upregulation of proteins such as angiopoietin-1, bFGF, thrombospondin-1, osteopontin, PDGF-AB/-BB and IGFBP-3 (Kurmann et al., 2021).

When these 2D methods are used with human iPSC-derived cells, physiologically-relevant functional properties are better demonstrated, and relevant genetic contributions can be delineated. iBMECs derived from controls, and familial AD patients with mutations in *PSEN1* or *PSEN2* showed differences in barrier function, that correlated with dysfunctional tight junctions and lower efflux pump activity (Raut et al., 2021b). These pathological iBMECs also showed elevated $A\beta_{40}$ secretion compared to control iBMECs. Rieker et al. (2019) characterized the secretory profiles of iPSC-derived endothelial cells, demonstrating significantly elevated levels of inflammatory cytokines, including IL-1α, IFNγ, ENA-78, and Kallikrein 3, in isogenic cell lines harbouring the APOE4 allele compared to those with APOE3. While the secretory profiles of *in vitro* astrocytes have been characterised more widely (Sullivan et al., 2024, López-Teros et al., 2024), further studies investigating the basal cytokine secretion of human iPSC-derived endothelial cells and pericytes need to be performed due to derivation method differences and genetic variability of iPSC lines. Other recent investigations into various pathogenic implications of APOE in 2D, isogenic iBMECs have been performed (Ding et al., 2024, Blanchard et al., 2020). Ding et al. (2024) demonstrated that iBMECs with different *APOE* genotypes have similar barrier permeability and transport properties, but transwell barrier models generated with APOE4 iBMECs exhibit heightened amyloid clearance and deposition. The extent to which *APOE* genotype interacts with inflammatory stressors and altered Aβ isoform dynamics, remains largely unexplored. Given the multifactorial nature of AD pathogenesis, further investigations incorporating multicellular, physiologically-relevant models are necessary to fully elucidate the mechanisms linking *APOE* genotype, neurovascular inflammation, and Aβ pathology.

Unfortunately, the 2D substrates used for *in vitro* experimentation provide a significantly different environment to the 3D, soft, highly functionalised, multicellular milieu that a living brain cell exists in. Adherence to a stiff, solid surface creates experimental artefacts such as inappropriate release of inflammatory markers, improper morphology, alterations in proliferation and viability and other structural and functional changes (Costa et al., 2016, Langhans, 2018). To combat this, recent studies have involved cell culture within various 3D matrices to provide *in vivo*-like physicochemical stimuli and a larger range of motility (Chaudhuri, 2017, Watson et al., 2017).

1.3.4 Current 3D, iPSC-based neurovascular models

In comparison to classical 2D culturing, 3D culturing better mimics the biochemical and biomechanical properties of *in vivo* tissues (Table 1.1). The field of 3D culturing encompasses a diversity of methods including: free floating spheroids and organoids, manually encapsulated ECM-based cultures, bioprinted ECM-based cultures and chip systems (Table 1.2). The best models of the neurovascular unit aim to combine iPSCs, 3D culturing and bioprinting, to provide more relevant *in vitro* environments that better recapitulate complex neurovascular disorders like AD.

1.3.4.1 Floating organoid and spheroid models

Spheroids are conglomerates of terminal cells (Nzou et al., 2020a) or actively differentiating cells with limited potency, like the multipotent neural progenitor cells in the neurospheres cultured by Jorfi et al. (2018). This lack of control of cellular composition also presents as underrepresentation of glia and vasculature, creating potentially unrepresentative constructs (Pașca et al., 2015, Shoemaker et al., 2021). In a self-assembling floating culture model, spheroids consisting of primary human astrocytes, pericytes and endothelial cells have displayed high levels of tight junction

Table 1.2: 3D neurovascular modelling techniques. Abbreviations: BBB: Blood Brain Barrier; ECM: Extracellular Matrix.

Model Type	Description	Advantages	Limitations	Example Studies
Spheroids	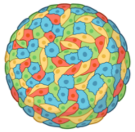 Aggregates of terminally differentiated or progenitor cells	Supports natural cell-cell interactions, multicellular, and some BBB functionality	Lack of controlled cellular composition, limited vascularization, diffusion-limited oxygen and nutrient supply	Nzou et al., 2020; Jorfi et al., 2018; Shoemaker et al., 2021
Organoids	 Self-organizing, stem cell-derived aggregates	Captures complex differentiation, long-term culture potential, forms discrete brain regions	High variability, lack of functional vasculature, expensive, diffusion-limited oxygen and nutrient supply, labour-intensive	Lancaster et al., 2013; Pellegrini et al., 2020; Sun et al., 2024
Manual Hydrogels	 Cells encapsulated within natural or synthetic ECM-like hydrogels using non-automated processes	Tunable properties, better structural support than free-floating models	Batch-to-batch variability, manual seeding reduces reproducibility and scalability	Blanchard et al., 2020; Majumder et al., 2024
Bioprinted Hydrogels	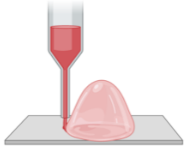 Automated deposition of bioinks containing cells and hydrogel components in defined architectures	Tunable properties, reproducible, precise spatial control, scalable for drug discovery	Requires optimization for fragile cell types, some bioinks lack functional complexity	Yee et al., 2024; Utama et al., 2021; Jung et al., 2022
Microfluidic Chips	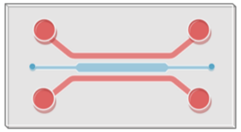 Perfusable microchannels often incorporating other neurovascular components	Mimics vascular flow, enables co-culture with precise control over microenvironment	Low scalability, specialized equipment, can oversimplify neurovascular complexity	Fengler et al., 2022; Gijzen et al., 2020; Kurosawa et al., 2022

expression, efflux pump activity, receptor-mediated transcytosis, and demonstrated VEGF-dependant, *in vivo*-like permeability to drugs (Cho et al., 2017). Diffusion limitations in spheroids, as shown in Nzou et al. (2018), create hypoxic cores due to inadequate oxygen and nutrient penetration into the spheroid's interior. Another from this group, incorporates 6 cell types (endothelial cells, pericytes, astrocytes, oligodendrocytes, microglia and neurons) in a "staged-assembly" model that generated a highly impermeable barrier. Upon hypoxic insult, the barrier's permeability was significantly increased, including the release of pro-inflammatory cytokines and oxidative stress mediators (Nzou et al., 2020a, Nzou et al., 2018).

Cerebral organoids, on the other hand, are grown from pluripotent cells resulting in complex self-organisation less impeded by experimenter-intervention (Lancaster et al., 2013, Lancaster and Knoblich, 2014). Discrete brain features such as cortical layers, hippocampal structures, and choroid plexus-like areas have been shown to emerge in cerebral organoids (Pellegrini et al., 2020, Quadrato et al., 2017). Since their introduction, cerebral organoids been generated with varied arrays of cell types, striking culture longevity and human brain-like electrochemical properties (Velasco et al., 2019, Trujillo et al., 2019, Hendriks et al., 2024). The lack of functional vascularization is a major weakness of this method, limiting nutrient and drug diffusion, but recent advances like co-culturing with endothelial cells and synthetic vascular networks offer promising areas of research (Lee et al., 2016, Nwokoye and Abilez, 2024). Stankovic et al. (2024) reported that schizophrenia patient-derived organoids exhibited altered endothelial inflammation pathways measured by single cell RNA sequencing, and PECAM-1-positive vessels that were longer and more permeable, revealing distinct vascular and inflammatory defects compared to control organoids. Using mesenchymal stem cells to support fused neural and endothelial cell spheroids elicited neurovascular tissues with enhanced expression of genes and proteins related to matrix remodelling, BBB integrity and mature cortical patterning (Song et al., 2019). These authors also investigated different cell type ratios, finding that a 1:2:3 ratio of neural:endothelial:mesenchymal cells optimised neurovascular interactions, corroborating some measures of neuron-astrocyte ratios (Canfield et al., 2017). On the other hand, Sun et al. (2024) created vascularized brain assembloids by combining forebrain organoids with myeloid progenitors HUVECs, demonstrating enhanced maturation characteristics. When using human tauP301S-mutant iPSCs, these assembloids displayed elevated total and phosphorylated tau levels, altered microglia morphology, astrocytic activation, and an altered neuroinflammatory cytokine profiles, offering a robust model to investigate tauopathy. While certainly a significant disease modelling tool, structural differences, cell-type/size variability, scalability, high costs and technical imaging methods hinder the applicability of organoids to drug discovery efforts (Andrews and Kriegstein, 2022).

Despite their advancements, floating aggregate models have significant limitations. The lack of perfusion prevents replication of *in vivo* flow dynamics, leading to immature vasculature and weak barrier properties. Significant heterogeneity in size and composition harshly limits reproducibility, and prolonged cultures risk necrotic core formation due to poor nutrient and oxygen diffusion, reducing their utility for long-term studies.

1.3.4.2 Manual hydrogel-based models

Hydrogel-based 3D cultures are used to encompass cells within a substance that mimics the native ECM. While the chemical and mechanical properties of the model are determined by the interactions and secretions of cells in free-floating 3D cultures (like organoids and spheroids), hydrogel cultures can be tuned by dilution or modification of the hydrogel composition. These gels generally involve a hydrophilic, polymeric structure, allowing incorporation of water molecules that facilitate nutrient, waste and oxygen diffusion (Nguyen and West, 2002). The most commonly used hydrogel, Matrigel, is a complex, undefined mixture derived from the ECM of Engelbreth-Holm-Swarm mouse sarcoma cells. Matrigel is lauded for its ability to mimic the native ECM environment, providing biochemical signals for cell adhesion and growth, but its non-defined composition introduces batch-to-batch variability, affecting reproducibility and scalability (Aisenbrey and Murphy, 2020b). Contrastingly, synthetic hydrogels can remedy the variability of Matrigel, by incorporating important functional elements into a fully defined matrix, allowing *in vivo* architecture, replicability, full definition of gel composition, and tunable stiffness to resemble relevant tissue areas (Nguyen and West, 2002, Hynes et al.). This makes them a better fit for the reproducibility and scalability required for impactful disease modelling and drug discovery (Papadimitriou et al., 2018). These gels classically involve an inert polymer backbone, that can be chemically-modified and mixed with peptides and other molecules to promote cell function and growth (Papadimitriou et al., 2018). To promote *in vivo*-like adhesion properties in the *in vitro* construct, basement membrane components like collagen IV, fibronectin and laminin are incorporated with the synthetic hydrogel backbone. This can be achieved using full length proteins, or smaller, more specific integrin-binding domains from those proteins (Schwartz et al., 2015). Peptides sequences like RGD and YIGSR have commonly added in defined quantities, and have been shown to produce *in vivo*-like cell attachment in a wide array of central and peripheral tissue contexts (Flanagan et al., 2006, Cunha et al., 2011). To overcome scalability and reproducibility challenges, advanced techniques such as bioprinting are increasingly being employed to construct complex, *in vitro* analogues with precise spatial and compositional control.

The contribution of APOE genotype to amyloid pathology was recently described in an elegant model that encapsulated iPSC-derived endothelial cells, pericytes and astrocytes into Matrigel (Blanchard et al., 2020). This methodology showed robust *in vivo* like structural formation, and significantly increased expression of BBB transcripts in the triculture, compared to mono and co-cultures. Strikingly, the authors showed that pathogenic pericytes were necessary for robust Aβ accumulation in APOE4-carrying 3D tricultures. The use of isogenic, patient-derived iPSC lines in this example is significant, as they provide increased disease-relevance compared to the more general immortalised and primary lines that are often chosen for convenience or ease of culture, although many are still constrained by the non-defined nature of Matrigel (Aisenbrey and Murphy, 2020a, Zeng et al., 2014). In addition to Matrigel, human neural organoids have also been encapsulated using PEG hydrogels (Majumder et al., 2024). While this expectedly reduced variability compared to Matrigel-based organoids, PEG-cultured organoids also showed greater neuronal diversity, enhanced neurovascular and inflammatory gene expression, showcasing PEG's value for creating consistent and functionally enriched neurovascular cultures.

Manual seeding approaches are limited by batch-to-batch variability, labour-intensive preparation, and inconsistent spatial organization of cells within the hydrogel matrix. These factors can lead to reduced reproducibility and scalability, hindering their utility for high-throughput drug screening applications.

1.3.4.3 Bioprinted hydrogel-based models

Bioprinting is the process of using automated, additive manufacturing techniques to precisely layer bioinks into three-dimensional structures that mimic biological tissues. This offers precise spatial control over deposition of cells, biomaterials, and growth factors, however advantages vary between the three main bioprinting methods microextrusion, stereolithography and inkjet bioprinting. Microextrusion uses continuous pressure to extrude bioink through a nozzle, creating stable, scaffold-like structures that are suitable for tissue engineering but with lower spatial resolution due to the larger nozzle size (Davoodi et al., 2020). Stereolithography (also known as laser-assisted printing), uses a focused laser to cross-link bioinks layer-by-layer, providing high-resolution constructs with fine structural detail, but is inapt for some sensitive cell culture applications because of laser exposure and bioink viscosity (Štěpanovská et al., 2021, Xiong et al., 2017). Inkjet bioprinting (also known as drop-on-demand bioprinting) ejects precise droplets of bioink to build up structures. This offers gentler handling and higher viability of cells, making it suitable for printing fragile or single-cell suspensions (Davoodi et al., 2020). However, the structural stability of inkjet bioprinted constructs is lower than microextrusion methods, lacking the strength needed for larger, load-bearing constructs, limiting its application in some complex tissue engineering contexts (Weygant et al., 2022). The Rastrum from Inventia Life Science is one inkjet platform that has enabled the efficient, scalable culture of hepatocytes and cancer cells (Yee et al., 2024, Utama et al., 2021, Jung et al., 2022).

Some bioprinting approaches facilitate endothelial-organoid co-culture by creating soft, gelatin methacryloyl (GelMA)-based channel scaffolds that surround a mature organoid. These HUVEC-lined channels can sprout and infiltrate cortical organoids, supporting long-term culture (Cadena et al., 2024). This system, however, could only bioprint approximately 12 constructs per hour, which creates issues with scalability for drug discovery applications. Other systems, such as drop-on-demand bioprinting systems such as the Rastrum, are better targeted to generation of reproducible and scalable solutions for drug discovery (Utama et al., 2021). Using the drop-on-demand approach of the Rastrum bioprinter, numerous disease- and tissue-relevant cultures have been achieved, however neurovascular constructs have not been generated (Yee et al., 2024, Jung et al., 2022).

Despite their promise in drug discovery, bioprinted models also face challenges that need to be circumvented before their potential can be realised. While platforms like the Rastrum enable high reproducibility and physiological relevance, bioprinting fragile stem-cell-derived cells requires careful optimization. Additionally, the choice of bioink and printing resolution can impact the accuracy of cellular arrangements and the long-term functionality of tissues.

1.3.4.4 Model-on-a-chips

Organ-on-a-chip systems, simulate tissue functionality in miniaturized, controlled environments, using microfluidic channels for fluid flow, and modular compartments to mimic physical features of the native environment (Piergiovanni et al., 2021). Adriani et al. (2017, 2015) used a microfluidic device that allowed the development of a perfusable channel surrounded by an endothelial monolayer, with primary rat neurons and astrocytes seeded on the abluminal side in a collagen I gel. Endothelial cells formed a barrier that showed low permeability and tight junction expression, and neurons showed functional Ca^{2+} activity and complex neurite branching morphology. A 3D microvessel model from Jamieson and colleagues showed that co-cultured pericytes directly contacted iBMECs, with stabilisation of abluminal pericyte localisation, and physiologically-relevant permeability to Lucifer yellow (Jamieson et al., 2019). Aspects of AD-induced BBB dysfunction such as increased permeability, increased reactive oxygen species, decreased junctional protein expression and Aβ deposition was observed in a similar microfluidic model, using a CMEC lined perfusable microchannel, with Matrigel encapsulated fAD/control neural progenitor cells (NPCs) in the abluminal compartment (Shin et al., 2019, Choi et al., 2014). This model was also employed to support the co-culture of iPSC-derived endothelial cells, pericytes, and astrocytes, yielding perfusable microvascular networks that recapitulate critical BBB features such as low permeability and dynamic cell-cell interactions (Campisi et al., 2018).

While these systems provide a richly integrated disease modelling environment, they are generally ill-equipped to handle experiments where increased throughput are required, like those inherent in the drug discovery process. Novel formats such as the Mimetas Organoplate combine high-throughput capability with physiological relevance, using perfusable microfluidic channels within a standard well-plate format to replicate neurovascular dynamics and enable precise investigation of barrier transport mechanisms (Fengler et al., 2022, Gijzen et al., 2020, Kurosawa et al., 2022). Fengler et al. (2022) utilized human iBMECs in an Organoplate system to create microvessels capable of performing higher throughput permeability screens, with primary pericyte conditioned media used to improve iBMEC maturation and barrier integrity, highlighting the consideration of cell-cell communication in representative disease modelling. Other comparable cultures have shown a similarly tight barriers, in addition to significant upregulation of relevant endothelial transporters, and functionality of active transporters to native substrates (Kurosawa et al., 2022). A new version of the Organoplate system, the Organoplate Graft, allows the creation of a perfusable HUVEC vascular bed which can subsequently vascularise pre-cultured spheroids/organoids, allowing investigation of chemically-induced and cell-induced angiogenesis (Russell et al., 2023).

While microfluidic chip systems enable precise control over cellular microenvironments and facilitate co-culture setups, they often rely on synthetic plastics like polydimethylsiloxane which can absorb small hydrophobic molecules, involve human-engineered channel architectures (rather than cell-defined) and may oversimplify the complexity of native neurovascular architecture.

1.3.4.5 Overview of the current state

Whilst these advancements in 3D neurovascular culture systems are promising, their translation into replicable, high-throughput drug screening platforms remains a significant challenge. Floating models are limited by batch-to-batch variability and the absence of vascular-like flow, both of which reduces their predictive value. Manual 3D systems, while often incorporating defined hydrogel matrices, suffer from labour-intensive preparation and scalability issues. Organ-on-chip devices offer enhanced control of microenvironmental conditions but require specialized expertise and equipment, limiting widespread adoption. Current bioprinting approaches, though capable of precise architectural replication, often lack functional maturity and consistency. To facilitate translatable high throughput drug discovery and target identification, a critical next step lies in integrating these advances into a platform that combines *in vivo* relevance with reduced experimental variability and automation of time-consuming manual processes. Furthermore, the application of these models to study Alzheimer's disease-related neurovascular pathology remains underexplored, emphasizing the need for targeted investigations to bridge this gap.

1.4 Overview & Aims

Given the limited availability of scalable, replicable, and high-throughput models that mimic the neurovascular environment in Alzheimer's disease, this project will develop, validate, and interrogate neurovascular pathology with a novel 3D culture system. Using the Rastrum, a novel 3D bioprinter developed by Inventia Life Sciences, cells can be accurately and replicably seeded in standard plate formats. The fully-defined hydrogel encapsulating the cells uses a polyethylene glycol backbone structure, incorporating matrix metalloprotease-degradable sequences that allow cellular remodelling of the extracellular environment. The gel also contains adhesion peptide sequences and free proteins, that further mimic the *in vivo* ECM. This methodology provides a scalable and replicable platform, amenable to higher-throughput drug-discovery and disease modelling efforts.

Chapter 3 aims to validate the cell identity and functional characteristics of the endothelial cell and pericyte lines that will be used for this project. 2D immunocytochemistry is used to ensure that all primary, secondary and iPSC-derived lines express typical cell-specific markers, while endothelial cells are also tested for monolayer permeability and trans-endothelial electrical resistance to verify functionality. Once validated, these models are applied to study the effects of Aβ, pgLPS and ecLPS, in order to determine how neurodegenerative proteinopathy and bacterial endotoxins influence endothelial and pericyte function. While bacterial contributions to neuroinflammation in AD have been proposed, the specific interactions between LPS subtypes and the neurovascular unit remain underexplored. This work aims to fill that gap by investigating how different LPS sources modulate barrier integrity and cytokine secretion.

In Chapter 4, optimisation of bioprinting parameters and culture conditions is explored in order to generate a novel, high-quality disease modelling and drug discovery tool. Alterations in hydrogel stiffness, adhesion peptide composition, media composition, and Rho-associated protein kinase (ROCK) inhibition are examined in endothelial cells, pericytes and astrocytes under monoculture and co-culture. Viability assays and immunofluorescent techniques are used to measure cell health, marker expression and structural organisation of bioprinted constructs. The resultant bioprinting platform and is then ready to be used in a context that examines the disease modelling capability of this model.

Chapter 5 applies this model to investigate AD pathological hallmarks in a novel *in vitro* system with high *in vivo* relevance. By treating CMECs and iBMECs with combinations of $A\beta_{40}$, $A\beta_{42}$, pgLPS and ecLPS, we examine the physiological-relevance of this novel 3D environment and investigate mechanistic questions surrounding the synergy of neuroinflammatory and Aβ-induced endothelial pathology. Measured $A\beta_{40}$ and $A\beta_{42}$ deposition patterns echo key isoform-specific differences observed in human AD proteinopathy, supporting the face validity of this model. Whereas basal cytokine secretion profiles and junctional expression highlight key differences between bioprinted iBMECs and CMECs, informing their suitability for specific modelling cases, and offering future avenues for iPSC-derived model optimisation. Ultimately, this thesis bridges critical gaps in neurovascular disease modelling, providing a much-needed framework for studying neuroinflammation, Aβ deposition, and endothelial dysfunction in a scalable physiologically-relevant context.

Chapter 2: Methods

All equipment and reagents were supplied by Sigma Aldrich or Thermo Fisher Scientific unless otherwise specified. All cells were incubated at 37 °C and 5 % CO_2. All data are presented as mean ± standard deviation (SD) unless otherwise specified, and all statistical analysis was performed in Prism 10 (Graphpad, version 10.4.0).

2.1. *Maintenance and identity of iPSCs*

Table 2.1: iPSC line characteristics. Abbreviations: iPSC: induced Pluripotent Stem Cell, *APOE*: Apolipoprotein E, fAD: familial Alzheimer's disease, mRNA: messenger ribonucleic acid, *PSEN2*: presenilin 2. (a) Cedars-Sinai Cell Repository, (b) New York Stem Cell Foundation Research Institute, (c) Alzheimer's Disease Research Center, University of California, Irvine.

Code	**Catalogue name**	**Sex**	**Age (years)**	**Disease Status**	**Known disease genetics**	**Origin Tissue**	**Reprogramming Method**
CTR06	CS06iCTR -n2(a)	F	82	Healthy Control	-	Fibroblast	Episomal Plasmid
CTR71	CS71iCTR-20nxx(a)	F	61	Healthy Control	-	Fibroblast	Episomal Plasmid
CTR88	CS88iCTR -nxx(a)	M	57	Healthy Control	-	Fibroblast	Episomal Plasmid
fAD08	CS08iFAD -n4(a)	F	81	Alzheimer's Disease	*PSEN2 (*N141I)	Fibroblast	Episomal Plasmid
fAD948	050948- 01-MR- 028(b)	F	40	Alzheimer's Disease	*PSEN2 (*N141I)	Fibroblast	mRNA
fAD950	050950- 01-MR- 079(b)	F	37	Alzheimer's Disease	*PSEN2 (*N141I)	Fibroblast	mRNA
AD33	ADRC iPS 22 Clone 9(c)	F	81	Alzheimer's Disease	*APOE* (ε3/ε3)	Fibroblast	Sendai virus
AD44	ADRC iPS 20 Clone 6(c)	F	72	Alzheimer's Disease	*APOE* (ε4/ε4)	Fibroblast	Sendai virus
CTR33	ADRC iPS 53 Clone 3(c)	F	76	Healthy Control	*APOE* (ε3/ε3)	Fibroblast	Sendai virus

iPSC lines (Table 2.1) were obtained through the Cedars-Sinai iPSC Core, New York Stem Cell Foundation Research Institute or the Alzheimer's Disease Research Center, University of California, Irvine with approval from the University of Sydney's Institutional Biosafety Committee (#17E020). iPSCs were maintained on 8.3 μg/cm^2 Matrigel (354230, Corning) with mTeSR1 (85850, Stem Cell Technologies), and were passaged using either StemPro Passaging Tool (23181010, Life Technologies) or using 0.5 mM ethylenediaminetetraacetic acid (EDTA; E6758) in phosphate-buffered saline (PBS; P3813). For the latter method, iPSCs were incubated with 0.5 mM EDTA for 5 minutes until cells begin to separate from each other. Then colonies were detached by gently, but firmly, expelling media over the surface of the plate before replating.

2.2. *Maintenance of primary and immortalised cell lines*

HEK293 cells were cultured in medium consisting of Dulbecco's Modified Eagle Medium (DMEM; 11995-065) supplemented with 5% fetal bovine serum (FBS; 16000044) and 100 U/mL penicillin/streptomycin (P4333).

CMECs were cultured on flasks and plates coated with 10 µg/mL rat tail collagen type 1 (collagen I, C3867) (or 100 µg/mL for glass substrates and transwell membranes). CMEC medium consisted of Endothelial Basal Medium 2 (EBM2; CC-3156, Lonza) supplemented with 5% FBS, 1.4 µM hydrocortisone (H0135), 5 µg/mL ascorbic acid (A8960), 1% chemically defined lipid concentrate (L0288), 10 mM 4-(2-hydroxyethyl)-1-piperazineethanesulfonic acid (HEPES; H4034), 1 ng/mL basal fibroblast growth factor (bFGF; PHG6015). For passaging, cells were detached with 0.25% trypsin/0.53 mM EDTA and spun at 500 *g* for 5 min.

Human umbilical vein endothelial cells (HUVECs; C2517AS, Lonza) were cultured in Endothelial Growth Medium 2 (EGM-2; CC-3162, Lonza). Cells were passaged with 0.25% trypsin/EDTA and spun at 200 *g* for 5 min.

Normal Human Astrocytes (Lonza) were cultured on 8.3 µg/cm^2 Matrigel (354230, In Vitro) in Astrocyte Growth Medium (AGM; CC-3186, Lonza). For passaging, human astrocytes were detached with accutase (A6964) and centrifuged at 180 *g* for 5 min.

Human Brain Vascular Pericytes (HBVPs; 1200, ScienCell) were cultured on poly-L-lysine-coated vessels (2 µg/cm^2, P1274) in Pericyte Medium (1201, ScienCell). For passaging, HBVPs were detached with accutase and centrifuged at 200 *g* for 5 min.

2.3. *iBMEC differentiation*

The protocol for derivation of iPSC-derived brain microvascular endothelial cells (iBMECs) from iPSCs follows that outlined in Neal et al. (2019) (Figure 2.1). This involves the initial differentiation into a mixed neural/endothelial culture, and subsequent selective purification onto a fibronectin and collagen IV-coated surface (Lippmann et al., 2012a). Briefly, iPSCs were singularised with accutase, resuspended in mTeSR1 with 10 µM Y-27632 (In Vitro, RDS12541) and seeded at 15,800 cells/cm² on 16.6 µg/cm² Matrigel-coated plates. 24 h later, medium was changed to E6 medium (A1516401), and changed daily for 4 days. Medium was then changed to human endothelial serum-free media (hESFM; 11111044) with 0.5% B27 (17504044), 20 ng/mL bFGF and 10 µM all-trans retinoic acid (RA; R2625), and left for 48 h. Cells were then singularised and plated onto substrates coated with 400 µg/mL collagen IV (C5533) and 100 µg/mL fibronectin (F1141). 24 h later, RA and bFGF were removed from the media. Assays were performed 24 h after the removal of bFGF and RA.

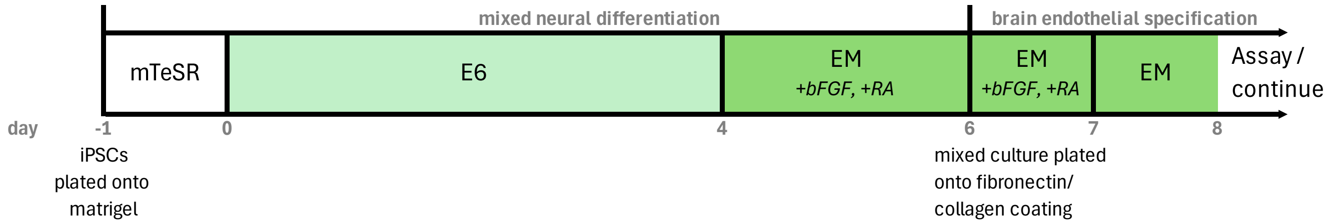

Figure 2.1: iBMEC differentiation scheme. bFGF: basic fibroblast growth factor, RA: Retinoic acid, EM: Endothelial medium.

2.4. *iPericyte differentiation*

Derivation of iPericytes follows the protocol outlined in Faal et al. (2019) with minor modifications (Figure 2.2). iPericytes derived from this method proliferate in response to PDGF-BB-PDGFRβ interactions, contract in response to endothelin-1 and promote barrier properties of endothelial cells (King et al., 2024, Faal et al., 2019). Briefly, iPSCs were singularised with accutase, resuspended in mTeSR1 with 10 µM Y-27632 and seeded at 20,000 cells/cm² on 8.3 µg/cm² Matrigel-coated plates. 24 h later, medium was changed to neural crest induction medium consisting of DMEM/F12 (11320033), 1x B27 supplement (17504044), 0.5% bovine serum albumin (A9647), 3 µM CHIR99021 (SML1046) and 1x Glutamax (35050061), and changed daily. On day 5, cells were switched to Pericyte Medium without passaging (Lonza, 1201), and cultured for at least 5 days for differentiation into pericytes.

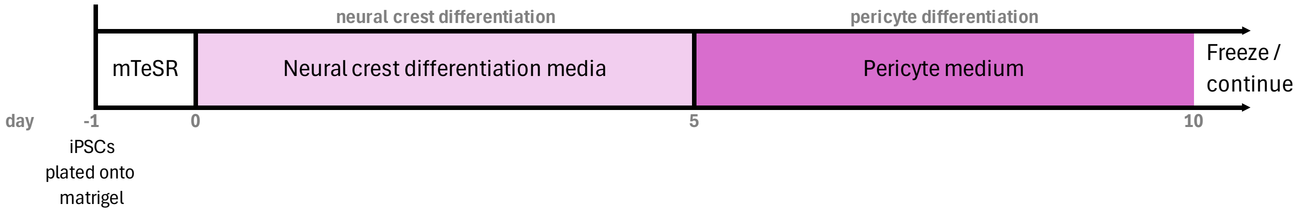

Figure 2.2: iPericyte Differentiation scheme.

2.5. *iAstrocyte differentiation*

The protocol for NPC derivation follows that outlined in the STEMdiff Neural System Kit (Stem Cell Technologies), then for derivation to astrocytes, the protocol from Tcw et al. (2017) was used (Figure 2.3). iAstrocytes derived via this method secrete cytokines in response to inflammatory stimuli, undergo phagocytosis and promote microglial phagocytosis (Tcw et al., 2017, Sullivan et al., 2024). They also display a similar RNA landscape to human fetal astrocytes (Sullivan et al., 2024). iPSCs were cultured in mTeSR1 supplemented with 10 ng/mL FGF2 Stembeads (StemCultures, SB500). On day 0, cells were dissociated with Gentle Cell Dissociation Reagent (Stem Cell Technologies, 07179), centrifuged at 300 *g* for 5 min, resuspended in STEMdiff Neural Induction Medium (Stem Cell Technologies, 05835), and plated in an ultra-low attachment U-well plate (CLS7007) at 9000 cells/well for embryoid body formation. On day 5, 10-12 embryoid bodies were transferred onto a 8.3 μg/cm^2 Matrigel-coated 6-well plate, using sterile, wide-bore pipette tips. On day 14, after the formation of neural rosettes, 1 mL of STEMdiff Neural Rosette Selection Reagent (Stem Cell Technologies, 05832) was incubated with cells at 37 °C for 70 min. Rosettes were then dislodged using DMEM/F12 (10565) and centrifuged at 350 *g* for 5 min. Rosettes were plated on 8.3 μg/cm^2 Matrigel-coated plates in STEMdiff Neural Induction Medium and 24 h later this was changed to NPC medium (DMEM/F12, 1x N2 (Life Tech, 17502-048), 1x B27 -RA (Life Tech, 12587-010) and 20 ng/mL bFGF) for differentiation into NPCs. After 4 days, NPCs were passaged with accutase, centrifuged at 500 *g* for 5 min, then seeded at 15,000 cells/cm^2 onto 8.3 μg/cm^2 Matrigel coated plates. 24 h after, medium was changed to Astrocyte Medium (ScienCell, 1801) and cells were cultured for 4 weeks to obtain full differentiation.

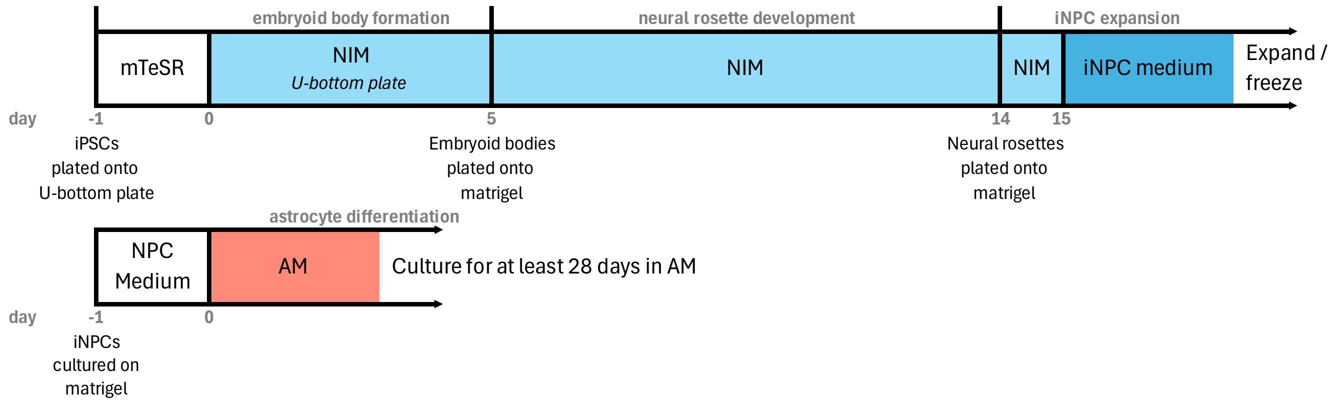

Figure 2.3: iAstrocyte differentiation scheme. Abbreviations: NIM: Neural induction medium, iNPC: iPSC-derived neural progenitor cell, AM: Astrocyte medium.

2.6. *3D bioprinting*

3D bioprinting was performed using the Rastrum bioprinter (Inventia Life Sciences (ILS)) as per the manufacturer's instructions. After successful greenlighting of the bioprinter, inert base activator (F3, ILS), inert base bioink (F32, ILS) and cell bioink (1.1 kPa: F226; 1.5 kPa: F203; ILS) were added to the printer cartridge. During priming and printing of the inert base layer, cells were dissociated, centrifuged and resuspended in a 50:50 mix of activator solution (F205, ILS) and 6 mg/mL collagen IV in PBS (C5533, final plate concentration = 1.5 mg/mL) and added to the cartridge. Cell-laden gels were printed using the "Imaging plate model" or "Large plug" protocol in 96-well Phenoplates (Revvity, 6055300). This process prints one drop of bioink onto the well followed by an equivalent drop of activator-cell mixture to initiate gelation. Cell-type-specific parameters are described below.

2.6.1. *Bioprinted human astrocyte monocultures*

After singularisation and centrifugation using standard protocols, human astrocytes were resuspended at 5 x 10^6 cells/mL, for a final density of 2.5 x 10^6 cells/mL. Bioprinted human astrocyte cultures were analysed on day three after media changes every day.

2.6.2. *Bioprinted CMEC monocultures*

After singularisation and centrifugation using standard protocols, CMECs were resuspended at 10 x 106 cells/mL, for a final density of 5 x 106 cells/mL. Media was changed at least every two days.

2.6.3. *Bioprinted iBMEC monocultures*

iBMECs frozen at day 6 were thawed swiftly, centrifuged at 1100 x *g* for 1 min, resuspended in EM and plated into T25 flasks coated with 400 µg/mL collagen IV (C5533) and 100 µg/mL fibronectin (F1141). Media was changed 3-6 h later to remove non-adherent cells. The next day bFGF, RA and ROCKi were removed to induce a barrier phenotype. 24 h later 10 µM ROCKi was added unless otherwise specified. Fully confluent iBMECs were then detached using Accutase, until mostly singularised (30-60 minutes), then centrifuged at 1100 x *g* for 1 min. iBMECs were resuspended at 10 x 10^6 cells/mL, for a final density of 5 x 10^6 cells/mL. On day 1, 24 h post-printing, ROCKi was either removed, replaced, or reduced depending on the treatment condition. In the ROCKi reduction condition, ROCKi concentration was reduced by 2 µM daily, i.e. 8 µM on day 1, 6 µM on day 2, 4 µM on day 3, 2 µM on day 4, and no ROCKi from day 5. Media was changed daily for 14 days, then 1-2 days thereafter.

For bioprinted 2D controls, wells were coated as normal, then cells were bioprinted without activator directly into media-laden wells. For manual 2D controls, wells were coated as normal, iBMECs were passaged as in 2.3, then manually pipetted into wells.

For treated iBMEC monocultures in Chapter 5, iBMECs were printed and cultured using the ROCKi reduction scheme. On day 27, cultures were treated with an inflammatory stimulus (10 µg/mL ecLPS, 10 µg/mL pgLPS, or media) combined with an Aβ stimulus (1 µM $A\beta_{42}$, 1 µM $A\beta_{40}$, 1 µM $A\beta_{42:40}$, or vehicle (0.5% ammonium hydroxide) – see Section 2.14 for more details). At day 28, supernatants were removed from “large plug” cultures for cytokine array analyses, and “imaging model” cultures were tested for viability or fixed for immunofluorescence.

2.6.4. Bioprinted CMEC:HBVP co-culture

After simultaneous singularisation and centrifugation using standard protocols, CMECs and HBVPs were resuspended at 10 x 10^6 cells/mL, for a final cell density of 5 x 10^6 cells/mL, with an endothelial:pericyte ratio of 1:1. CMEC:HBVP co-cultures were fixed after 12 days. Media was changed at least every two days.

2.6.5. Bioprinted primary/immortalized neurovascular triculture

After simultaneous singularisation and centrifugation using standard protocols, CMECs, HBVPs and human astrocytes were resuspended at 10 x 10^6 cells/mL, for a final cell density of 5 x 10^6 cells/mL, with an endothelial:pericyte:astrocyte ratios of 2:1:1 (Nzou et al., 2020b). Media was changed daily.

2.6.6. *Bioprinted primary/iPSC-derived neurovascular triculture*

Before printing, iBMECs were cultured as described in (2.1.3), while HBVPs and iAstrocytes were cultured and passaged using standard protocols (2.2 , 2.5). After simultaneous singularisation and centrifugation, iBMECs, HBVPs and iAstrocytes were resuspended at 7 x 10^6 cells/mL, for a final cell density of 3.5 x 10^6 cells/mL, with an endothelial:pericyte:astrocyte ratio of 5:1:1 (Blanchard et al., 2020), and 2:1:1 (Nzou et al., 2020b). Gels were cultured in AM with 10 ng/mL VEGF and 10 ng/mL PDGF-BB for 7 days, and AM thereafter. Media was changed daily.

2.7. *2D Immunofluorescence*

All solutions were made in PBS unless otherwise stated. Cells were fixed with either 100% ice-cold MeOH (AH2304) or 4% paraformaldehyde (47608) for 10 min. For the MeOH fixation (used for 2D endothelial cells), samples were then rehydrated for 20 mins in PBS. For the paraformaldehyde fixation (all other cell lines), samples were permeabilized with 0.1% Triton-X-100 (X100) for 10 min. All samples were then blocked with 5% FBS (blocking solution) for 60 min and primary antibody added in blocking solution and left overnight at 4°C. Samples were then incubated with secondary antibodies in blocking solution for 1 h at room temperature. Cells were washed 3 times in PBS. Samples in plates were incubated with DAPI (10236276001, 1:800) for 10 min, washed once and then stored at 4°C in 200 µL PBS. Samples maintained on glass slides (94.6170.802; Sarstedt) were mounted using Fluoroshield (F6182), sealed with a #1 glass coverslip then stored at 4 °C in the dark.

All samples were imaged with a Cytation 3 (BioTek, Gen5 v2 software) or Leica SP8 (Leica, LAS X software) microscope. The details of all primary and secondary antibodies are outlined in Tables 2.2 and 2.3.

2.8. *3D Immunofluorescence*

All solutions were made in PBS unless stated otherwise. All incubations were performed at room temperature (RT) unless stated otherwise. 3D samples in Section 4.2.1.1 were prepared for immunofluorescence using the following protocol adapted from the manufacturers protocol. 3D samples were washed with PBS, fixed with 4% paraformaldehyde for 20 min, washed 3 times with PBS, then permeabilized with 0.1%

Triton-X-100 for 30 min. Samples were washed 3 x 10 min in PBS, then blocked with blocking solution for 30 min. Primary antibodies were added in blocking solution and left overnight at 4 °C. Samples were washed 3 x 10 min in PBS, then incubated with secondary antibodies in blocking solution for 1 h at RT. Samples were then washed 3 x 10 min in PBS, and incubated for 10 min with 20 µM Hoechst (62249) or DAPI (1:800), washed once more with PBS. Samples were then stored in 200 µL PBS before imaging.

Table 2.2: Primary antibody information for immunocytochemistry experiments

Target	Antibody Species	Vendor	Product number	Dilution	[Stock] (mg/mL)
AQP4	rabbit	ThermoFisher	PA5-53234	1:300	0.3
CD13	rabbit	ThermoFisher	PA582156	1:100	0.05
EpCAM	rabbit	Abcam	ab71916	1:400	1
GFAP	rabbit	Abcam	ab7260	1:500	Not specified
Nanog	rabbit	Stemgent	09-0020	1:100	0.5
Nestin	mouse	Stem Cell	60091	1:2000	0.5
NG2	mouse	ThermoFisher	372700	1:100	0.5
Occludin	mouse	Thermofisher	OC-3F10	1:100	0.5
OCT3/4	mouse	Stem Cell	60093.1	1:1000	0.5
PAX6	rabbit	Stem Cell	60094	1:500	2
PDGFRβ	rabbit	ThermoFisher	MA515143	1:100	0.004
PECAM-1	rabbit	ThermoFisher	RB-10333-P	1:50	0.02
PECAM-1	mouse	Abcam	ab9498	1:1000	1
S100β	mouse	Sigma Aldrich	S2532	1:1000	8
VE cadherin	rabbit	Abcam	ab33168	1:400	1

Table 2.3: Secondary antibody information for immunocytochemistry experiments

Species Reactivity	Host	Conjugate	Vendor	Product Number	Dilution	[Stock] (mg/mL)
Mouse	Donkey	Alexa Fluor 488	ThermoFisher	A-21202	1:200	2
Rabbit	Goat	Alexa Fluor 568	ThermoFisher	A-11011	1:200	2
Rabbit	Donkey	Alexa Fluor 594	ThermoFisher	A-21207	1:200	2
Rat	Goat	Alexa Fluor 647	ThermoFisher	A-21247	1:200	2

2.9. *Optimised 3D Immunofluorescence*

All solutions were made in PBS unless stated otherwise. All incubations were performed at RT unless stated otherwise. Due to the presence of high-intensity non-specific signals in these 3D immunofluorescent samples seen when using the method in Section 2.8, an optimised immunofluorescence preparation protocol was developed, incorporating longer incubation, longer washes and gel clearing (used from Section 4.2.2 onwards). This method combined elements from the manufacturer's protocol with techniques found in the literature to lower non-specific binding in a reasonable time frame (Blanchard et al., 2020, Nürnberg et al., 2020). This protocol is used from Section 4.2.2 onwards.

In the optimised protocol 3D samples were washed with PBS, fixed with 4% paraformaldehyde in PBS for 20 min, washed 3 x 10 min in PBS, then permeabilized with 0.1% Triton-X-100 for 30 min. Samples were washed 3 x 10 min on a rocker in PBS, then blocked with blocking solution for 60 min. Primary antibodies were added in blocking solution and left for 24 h at 4°C. Samples were then washed 3 times (1 min, 5 min, 60 min) in PBS + 0.1% v/v Tween-20 (PBST; P1379), then washed for 24 h at 4°C on a rocker and incubated with secondary antibodies in blocking solution for 24 h at 4°C. Samples were then washed 3 times (1 min, 5 min, 60 min) in PBST, then washed for 24 h at 4°C, on a rocker. Samples were washed once in PBST incubated for 10 min with 20 µM Hoechst, and washed twice more with PBST (1 min). Samples were then stored for at least 24 h in 150 µL 88% Glycerol (Chem-Supply, GA010-2.5L-P) before imaging. All samples in Chapter 3, 4 were imaged with a Leica SP8 (Leica, LAS X software).

For quantification of 3D Aβ fluorescence, images were taken and analysed with the Opera Phenix Plus (Revvity, Harmony version 5.1 software). A 10x dry objective was used to capture Z-stacks over 206.4 µm height (6.45 µm step distance) over nine 1217.61 µm x 1217.61 µm tiles, with global images generated using 10% overlap stitching. Hoechst, HiLyte™ Fluor 488 and AlexaFluor 594 channels were captured by solid state excitation lasers at 405 nm, 488 nm and 561 nm. Details of the analysis sequence are provided in Table 2.4. Briefly, and an absolute threshold was applied to the 594 channel to remove high intensity artefacts. A local threshold was then applied to each channel to segment the volume of stained area, then intensity and volume values were calculated. Two-way ANOVA with Tukey's multiple comparisons test was used to test statistically significant differences between the means of all conditions.

Table 2.4: Harmony image analysis sequence.

Input Image	Input		
	Flatfield Correction: None **Stack Processing**: 3D **Min. Global Binning**: 3		
Find Image Region	Input	Method	Output
Aβ	**Channel**: Alexa 488 **ROI**: None	**Method**: Local Threshold **Threshold**: 0.6 **Scale**: 15 μm^2 **Output Region**: Amyloid Region	**Output Population**: Amyloid Population
Find Image Region	Input	Method	Output
VECadherin Correction	**Channel**: Alexa 594 **ROI**: None	Method: Absolute Threshold Low: 200 High: 5000 Output Region: CorrectedVECad	Output Population: CorrectedVECad
Find Image Region	Input	Method	Output
VECadherin	**Channel**: Alexa 594 **ROI**: None	**Method**: Local Threshold **Threshold**: 0.4 **Scale**: 40 μm^2 **Output Region**: VECadRegion	**Output Population**: VECadPopulation
Find Image Region	Input	Method	Output
Hoechst	**Channel**: HOECHST33342 **ROI**: None	**Method**: Local Threshold **Threshold**: 0.5 **Scale**: 15 μm^2 **Output Region**: NucleiRegion	**Output Population**: NucleiPopulation
Calculate Intensity Properties	Input	Method	Output
Aβ	**Channel**: Alexa 488 **Population**: AmyloidPopulation **Region**: AmyloidRegion	**Method**: Standard	
Calculate Morphology Properties	Input	Method	Output
Aβ	**Channel**: Alexa 488 **Population**: AmyloidPopulation **Region**: AmyloidRegion	**Method**: Standard	Sum of Volumes
Calculate Properties	Input	Method	Output
Aβ	**Channel**: Alexa 488 **Population**: AmyloidPopulation **Region**: AmyloidRegion	**Formula**: A*B **A**: AmyloidRegion Intensity **B**: AmyloidRegion Volume	Sum of Objects Mean*Volume
Calculate Intensity Properties	Input	Method	Output
VECadherin	**Channel**: Alexa 594 **Population**: VECadPopulation **Region**: VECadRegion	**Method**: Standard	
Calculate Morphology Properties	Input	Method	Output
VECadherin	**Channel**: Alexa 594 **Population**: VECadPopulation **Region**: VECadRegion	**Method**: Standard	Sum of Volumes
Calculate Properties	Input	Method	Output
VECadherin	**Channel**: Alexa 594 **Population**: VECadPopulation **Region**: VECadRegion	**Formula**: A*B **A**: VECadRegion Intensity **B**: VECadRegion Volume	Sum of Objects Mean*Volume
Calculate Intensity Properties	Input	Method	Output
Hoechst	**Channel**: HOECHST33342 **Population**: HoechstPopulation **Region**: HoechstRegion	**Method**: Standard	
Calculate Morphology Properties	Input	Method	Output
Hoechst	**Channel**: HOECHST33342 **Population**: HoechstPopulation **Region**: HoechstRegion	**Method**: Standard	Sum of Volumes
Calculate Properties	Input	Method	Output
Hoechst	**Channel**: HOECHST33342 **Population**: HoechstPopulation **Region**: HoechstRegion	**Formula**: A*B **A**: HoechstRegion Intensity **B**: HoechstRegion Volume	Sum of Objects Mean*Volume
Calculate Position Properties	Input	Method	Output
Aβ and VECadherin	**Population**: AmyloidPopulation **Region**: AmyloidRegion	**Method**: Cross Population **Population**: VECadPopulation **Region**: VECadRegion	ROI Border Distance

2.10. *Calcein AM/Ethidium Homodimer-1 viability and morphology*

A LIVE/DEAD viability kit (L3224) was used to assess viability and morphology in 3D cultures. For bioprinted human astrocytes, viability and morphology was analysed at day three to allow for morphological development. For 3D CMECs and iBMECs, constructs were analysed at day 1, 7, 14, or 28 post-bioprinting to index viability over the longitudinal life of the culture. Bioprinted cells were washed with PBS, incubated in 2 µM calcein AM, 4 µM ethidium homodimer-1 (EthD), and 20 µM Hoechst in cell-specific media (37°C, 30 min). Wells were washed with PBS and fluorescent images taken using the Axio Observer Z1 (Zeiss, ZEN 3.4) (for day 1 experiments performed at the ILS laboratory) or the Cytation 3 Cell Imaging Multi-Mode Reader (BioTek, Gen5 v2 software) using 375 nm, 480 nm, and 560 nm excitation filters.

For astrocytes, one 30 µm Z-stack containing at least 80 cells was taken per well, with each gel condition performed in duplicate. Images were analysed in FIJI, and blinded using the File Name Encrypter tool. Maximum intensity projections of the Z-stacks were pre-processed by removing background from the DAPI channel (Process > Subtract Background > Rolling ball radius = 10.0), and sharpening the calcein AM channel (Process > Sharpen). Viability was calculated by manually counting calcein AM-positive cells and EthD-positive dead cells. Longest process lengths were measured by using the line tool to draw a line from the edge of the tip of the longest process to the nearest point of the nucleus. Cell area was measured using the freeform tool to manually trace the perimeter of cells, were the cell perimeter did not ambiguously overlap with other cells. Live cell percentage was calculated by dividing the number of calcein AM-positive nuclei with the number of EthD-positive nuclei. One-way ANOVA with Dunnett's multiple comparisons test was used to test for differences between conditions and the control. For iBMECs, one 30 µm Z-stack containing at least 80 cells was taken per well, with each gel condition performed in duplicate. Live cell percentage was calculated by divding the number of calcein AM-positive nuclei with the number of EthD-positive nuclei. An unpaired t-test was used to test for differences between conditions and the control.

2.11. *CellTiter-Blue viability assay*

For viability measurements, 20 µL of CellTiter-Blue Reagent (G8080; Promega) was added to cells in a 96-well plate containing 100 µL media per well. Viable cells metabolize resazurin to the fluorescent molecule, resorufin. After 4 h at 37 °C, 100 µL of supernatant was harvested into a black-walled 96-well plate (Greiner, 655079), and fluorescence recorded using a PolarStar Omega plate reader (BMG Labtech; Omega version 1.3) at 560/590nm. Background fluorescence from media was subtracted, and data presented as raw fluorescence units. One-way ANOVA with Šídák's multiple comparisons test was used to test for differences between treatment means and their vehicle.

2.12. *Fluorescein permeability assay*

Cells were seeded on 1.12 cm^2, 0.4 µm pore transwell filters in 12-well plates (CLS3401). For iBMECs, filters were coated with 400 µg/mL collagen IV and 100 µg/mL fibronectin, for CMECs filters were coated with 100 µg/mL Collagen I. A full media change was performed 1 h before the start of the assay. Medium in the apical chamber was replaced with 10 µM sodium fluorescein (46960) diluted in fresh medium. 150 µL of medium was immediately removed from the basolateral chambers, transferred to a clear-bottom, black-walled, 96-well plate, and replaced with 150 µL of fresh medium. This was repeated every 15 min for a total of 75 min. Fluorescence of the samples was measured by a PolarStar Omega microplate reader using an excitation wavelength of 485 nm and an emission wavelength of 520 nm. The effective permeability (P_e) value was calculated as described in Stebbins et al. (2016). Each condition was performed in duplicate, with at least 3 biological replicates performed. Transport across a coated transwell filter lacking cells was also measured to correct permeability values for mass transfer resistance due to the filter and coatings. One-way ANOVA with was used to test for differences, with experiment-specific multiple comparisons tests.

2.13. *Transendothelial electrical resistance assay*

xCelligence E-Plate VIEW 96 plates (EliTech Group, 300601020) were coated with cell-specific coatings (see Chapter 3.2.1 and 3.2.2), then background measurements acquired. Cells were seeded in 200 µL of media. Endothelial cells were seeded at 100,000 cells/well. The E-plate was connected to the real-time cell analysis (RTCA) station within an incubator and impedance measurements were taken at 2 h intervals. Media was changed at 24 h, and measurements taken for at least 5 days to ensure monolayer formation and stabilisation. Maximum changes in Cell Index (CI) were analysed using the RTCA software (version 1.2), then converted to ohms x cm^2 by the following equation (Srinivasan et al., 2015):

$$TEER = (CI \times 15 + ohms(t(0))) \times 0.32$$

One-way ANOVA with Tukey's multiple comparisons test was used to test statistically significant differences between the means of all conditions.

2.14. Aβ preparation, application and deposition

Lyophilised $A\beta_{42}$ and $A\beta_{40}$ monomers, conjugated to the HiLyte™ Fluor 488 fluorophore (Anaspec, AS-60479-01, $A\beta_{42}$; AS-60491-01, $A\beta_{40}$), were dissolved in 100 µL of 0.5 % NH_4OH at 4 °C. These solutions were centrifuged (16,000 *g*, 10 min, 4 °C) to remove any aggregates. The supernatant was then aliquoted into working volumes, immediately snap frozen in liquid N_2 and stored at -80 °C. Protein concentration was measured using the Pierce™ bicinchoninic acid assay (23225) using a BMG POLARstar Omega plate reader. The enhanced protocol of this assay was used for a lower working range, 5 – 250 µg/mL.

Frozen aliquots were quickly defrosted by submerging in room temperature water to prevent icicle formation. For application, 20 nM $A\beta_{42:40}$ refers to solution containing 10 nM $A\beta_{42}$ and 10 nM $A\beta_{40}$. To measure deposition, cells were treated with Aβ-laden media for 24 h, before fixing and preparing for immunofluorescence (as in Section 2.6).

For quantification of 2D Aβ fluorescence, 16-bit images taken with a Leica SP8 were analysed using FIJI (Schindelin et al., 2012). 488 nm signal was transformed by a specified threshold (minimum = 125, maximum = maximum), before measuring the area of thresholded fluorescent Aβ signal as a percentage of total area. One-way ANOVA with Dunnett's multiple comparisons test was used to test for differences between conditions and the control (No cells + 100 nM $A\beta_{42:40}$) (* $p < 0.05$).

2.15. Enzyme-linked immunosorbent assays (ELISAs)

iBMECs or iPericytes were plated in 24-well plates at a density of 1.25×10^5 / cm^2 or $5 \times 10^4/cm^2$, respectively in 600 µL media. 48 h after plating, cells were treated with 10 µg/mL LPS from *E. coli* (ecLPS; L4391), 10 µg/mL LPS from *P. gingivalis* (pgLPS; SMB00610) or 100 nM $A\beta_{42:40}$. Supernatants were harvested after 24 h, centrifuged (10,000 *g,* 1 min) and the supernatant stored at -80 °C. IL-6 ELISA (DY206; R&D

Systems) was performed according to manufacturer's protocol, except for a modified standard range, from 0.586-600 pg/mL. 450 nm / 570 nm absorbance was measured with the POLARstar Omega plate reader, and concentrations were interpolated from a standard curve fitted with a sigmoidal dose-response (variable slope) model. One-way ANOVA with Dunn's multiple comparisons test was used to test for differences between treatment means and their vehicle.

2.16. Proteome profiler arrays

In 2D, cells and treatments were prepared as in Section 2.15. In 3D, cells and treatments were prepared as in Section 2.6.3. Protein levels of 105 cytokines were measured using the Proteome Profiler Human XL Cytokine Array Kit (ARY022B; R&D Systems), as per the manufacturer's instructions, using 1 mL of 2D cell supernatant, or 800 µL of pooled supernatant from 10 wells of 3D cultures. A ChemiDoc MP (Bio-Rad) was used to image membranes at multiple exposure times. Two exposure times were chosen to analyse both lowly (10 s) and highly expressed (1 s) cytokines (Kurmann et al., 2021, Kim et al., 2023). Signal intensity for each cytokine was measured in duplicate and determined using total pixel intensity in FIJI. In accordance with recent literature, cytokines with average pixel densities < 10 % of the maximum were considered background and discarded from analysis (Goshi et al., 2020). Multiple two-way ANOVAs were performed between experimental treatments and their vehicle, with a two-stage linear step-up procedure of Benjamini, Krieger and Yekutielie used to control the false-discovery rate, with Q < 0.05. This method of multiple comparisons correction balances sensitivity and specificity in large-scale hypothesis testing, unlike overly conservative family-wise error rate methods (Benjamini et al., 2006). By considering the distribution of all p-values, it enhances power and adaptability, making it especially suitable for high-dimensional data like proteomics studies (Diz et al., 2011). Trends were defined as proteins with individual p values < 0.05, but q values > 0.05.

Hierarchical clustering was performed on array data, and heatmaps generated to observe clustering patterns. Mean cytokine intensities were collated and expressed as a percentage of the highest value for each cytokine. Relative percentage values were hierarchically clustered using an agglomerative approach with average linkage and Euclidean distance as the similarity metric. The clustering process was visualized using a dendrogram to highlight natural clustering patterns. The analysis was conducted using scipy, seaborn and matplotlib libraries in Python (Version 3.12.1; Python). Code is available in Figure 2.4.

2.17. Polymerase chain reaction & Sanger sequencing

iPSCs were grown to 80% confluency on 8.3 μg/cm^2 Matrigel-coated 6-well plates. Genomic DNA was extracted using the Purelink Genomic DNA Mini Kit (K182001), and concentration and purity was determined using the Qubit dsDNA HS Assay Kit (Q32851) as per the manufacturer's instructions. The *APOE* region was amplified using polymerase chain reaction (PCR), where 500 ng DNA was mixed with 25 μL NEBNext High-Fidelity 2X PCR Master Mix (New England Biolabs, 50-591-079), 500 nM forward primer (TCTTGGGTCTCTCTGGCTCA; Integrated DNA Technologies), and 500 nM reverse primer (GCTGCCCATCTCCTCCATC; Integrated DNA Technologies). The reaction was amplified using a T100 thermal cycler (Bio-Rad), with the following program: Initial denaturation at 98 °C for 30 s, followed by 40 cycles of denaturation for 10 s at 98 °C, annealing for 15 s at 69 °C and extension for 30 s at 72 °C; then a final extension at 72 °C for 2 min. Electrophoresis was performed on an E-gel Powerbase V4 (Invitrogen) at 100 V for 30 min, using a 1.2% agarose E-Gel with SYBR Safe (A42100), then visualised using an E-Gel Safe Imager Real Time Transilluminator (Invitrogen) to ensure specific amplification. The product band was excised from the gel and purified using the QIAquick Gel Extraction Kit (Qiagen, 28704). The purified PCR product was then submitted to the Australian Genome Research Facility for Sanger sequencing, and sequences at SNP locations rs429358 and rs7412 were analysed using SnapGene version 6.1.1.

2.18. CRISPR/Cas9 gene correction

Gene editing was performed as an exempt dealing, with approval from the University of Sydney's Institutional Biosafety Committee (#22E002). Guide RNA (gRNA) sequences were cloned into the LentiCRISPRV2 vector (Addgene, 52961, (Sanjana et al., 2014)) to direct gene editing to the rs429358 location, on exon 4 of *APOE*. Single-stranded oligonucleotides (ssODNs) provide effective templates for the CRISPR/Cas9 correction (Rivera-Torres et al., 2017). The template ssODN and gRNA sequences were designed (by Dr. Cesar Moreno, University of Sydney) to include asymmetric homology arms and silent mutations to increase the efficiency of homology-directed repair.

Table 2.5: Gene editing gRNA and ssODN sequences. Abbreviations: e3: Apolipoprotein E3, e4: Apolipoprotein E4, gRNA: guide RNA, ssODN: single-stranded oligodeoxynucleotide.

Name	**Sequence**
e3 > e4 gRNA	CACCGCGGACATGGAGGACGTGTG
e3 > e4 ssODN	GGAACAACTGACCCCGGTGGCGGAGGAGACGCGGGCACGGCTGTCCAAGGAGCTGCAGGCGGCGCAGGCCCGGCTGGGCGCAGACATGGAAGACGTCCGCGGACGCCTGGTCCAGTACCGCGGAGAGGTGCAGGCCATGCTCGGCCAGAGCACCGAGGAGCTGCGGGTGCGCCTCGCCTCCCACCTGCGCAAG
e4 > e3 gRNA	CACCGCGGACATGGAGGACGTGCG
e4 > e3 ssODN	GGAACAACTGACCCCGGTGGCGGAGGAGACGCGGGCACGGCTGTCCAAGGAGCTGCAGGCGGCGCAGGCCCGGCTGGGCGCAGACATGGAAGACGTCTGCGGACGCCTGGTCCAGTACCGCGGAGAGGTGCAGGCCATGCTCGGCCAGAGCACCGAGGAGCTGCGGGTGCGCCTCGCCTCCCACCTGCGCAAG

The Cas9-gRNA plasmid and ssODN were delivered via electroporation, using the Neon Transfection System (MPK1025). iPSCs were cultured as described until 60 - 80% confluent in a 6-well, then treated with 10 µM Y-27632 for 2 hours. iPSCs were washed once with PBS, then singularised with accutase and centrifuged at 200 *g* for 5 min. The pellet was resuspended in mTeSR Plus (Stem Cell Technologies, 100-0276) with 10 µM Y-27632 for counting, then 8 x 10^4 iPSCs per transfection were centrifuged at 200 *g* for 5 min. The pellet was then washed with PBS without resuspending, then resuspended in Resuspension Buffer R (Neon Transfection System) and added to 1 µg guide plasmid and 16.7 nM ssODN. 10 µL of this mix (containing 96,000 cells) was aspirated with a 10 µL Neon tip and electroporated using 2 x 20 ms pulses at 1200 V. The cells were immediately added to a 24-well plate coated with 8.3 µg/cm^2 Matrigel, in mTeSR Plus supplemented with CloneR2 (Stem Cell Technologies, 100-0691) at the manufacturers recommended concentration. After 24 h, media was changed to mTeSR Plus with 2 ug/mL puromycin (P7255) but without CloneR2, to select cells expressing the plasmid (in the case of poor attachment, CloneR2 concentration was halved here, before fully removing 24 h later). iPSCs were then inspected with a brightfield microscope to assess cell health before continuing.

Supplementary Figure 2.4: Hierarchical clustering algorithm and heatmap generation code. Mean cytokine intensities were collated and expressed as a percentage of the highest value for each cytokine. Relative percentage values were hierarchically clustered and visualised using the Seaborn library in Python (Version 3.12.1; Python).

```
import numpy as np                      # to handle numeric data
import matplotlib.pyplot as plt         # for visualization
import pandas as pd                     # for handling dataframe
import scipy.cluster.hierarchy as sch   # importing scipy.cluster.hierarchy
for dendrogram
import seaborn as sbn

ourData = pd.read_csv('CytoHeatMap-NORMALISED.csv')      # read the data
newData = ourData.iloc[:, [1, 2, 3, 4, 5, 6]].values     # extract the
groups from the dataset
labelList = ourData.iloc[:, 0].values                    # extract the
cytokine labels from the dataset

df = pd.DataFrame(data=newData, index=labelList, columns=["No
Cells","Basal","LPS","pgLPS","Vehicle","AB"]);
print(df);
print(df.columns);
print(df.index);

sbn.clustermap(df, cmap="YlOrRd");
plt.savefig("HeatMap.png")
plt.show();
```

Chapter 3: Characterisation and stimulus-response of 2D iPSC-derived vascular cell cultures

3.1. *Introduction*

Neurodegenerative diseases such as AD are associated with complex pathologies involving multiple cell types in the brain. Recent research has increasingly emphasized the role of the neurovascular unit, including brain microvascular endothelial cells and pericytes, in the progression of neurodegenerative disorders. Disruption of the BBB, a critical component of the neurovascular unit, is known to contribute to the onset and progression of AD by altering the brain's ability to regulate the passage of molecules and cells between the bloodstream and neural tissue.

In addition to hyperphosphorylated tangles of tau protein, amyloid β (Aβ) oligomers and plaques are the main pathological hallmark of AD. These peptides, particularly the longer $A\beta_{42}$ isoform, exhibit a higher propensity for aggregation and are implicated in the formation of toxic oligomers and plaques (Ahmed et al., 2010, Vadukul et al., 2017). $A\beta_{42}$ has been shown to disrupt endothelial tight junctions, impair pericyte function, and induce astrocytic reactivity, thereby contributing to BBB breakdown and exacerbating neuroinflammation (Miners et al., 2017, Park et al., 2016). Contrastingly, the shorter $A\beta_{40}$ isoform interacts uniquely with vascular cells, and is more prominently deposited in the vasculature compared to $A\beta_{42}$ (Robert et al., 2017). Investigating the distinct effects of Aβ peptides of varying lengths on neurovascular unit components is essential to understand how these interactions influence BBB integrity and contribute to AD pathology.

Aside from Aβ and tau, neuroinflammation is widely considered the third hallmark of AD and is characterized by the chronic activation of immune cells, leading to the release of pro-inflammatory cytokines, chemokines, and reactive oxygen species (Thakur et al., 2023). While classical proteinopathy can trigger neuroinflammation, peripheral inflammatory signals also play a significant role. Lipopolysaccharides (LPS) are bacteria-specific glycolipids found in gram-negative bacteria such as *Escherichia coli* and *Porphyromonas gingivalis*, and have been implicated in exacerbating neuroinflammatory responses in AD (Zhao et al., 2022). LPS can cross the compromised BBB, activating microglia and astrocytes to secrete pro-inflammatory mediators, amplifying Aβ deposition and tau hyperphosphorylation (Poole et al., 2013, Dominy et al., 2019). Importantly, LPS from *P. gingivalis* (pgLPS), a key pathogen in periodontitis, has been detected in the brains of AD patients, suggesting a link between peripheral *P. gingivalis* infection and neurodegenerative progression (Liu et al., 2024).

In contrast to the rarer, familial forms of AD, the more common sporadic disease is provoked by complex interactions between environmental risk factors and genetic risk factors, such as the ε4 allele of apolipoprotein E (APOE4). APOE4 is associated with increased Aβ aggregation, potentiated tau pathology and heightened neuroinflammatory responses, compared to the protective ε2 and neutral ε3 isoforms (Riedel et al., 2016a, Liu et al., 2023). APOE4-carriers exhibit heightened BBB permeability, reduced pericyte coverage, and impaired endothelial function, which collectively exacerbate cerebrovascular dysfunction in AD (Howe et al., 2020, Ferrari-Souza et al., 2023, Eisenbaum et al., 2024). To understand how *APOE* and the neurovascular unit contribute to AD cell pathology, it is vital to use isogenic cell lines to accurately delineate the impact of *APOE* mutations. Due to the limited availability of isogenic iPSC lines, clustered regularly interspaced short palindromic repeat (CRISPR)-Cas9 gene editing is a key technology that will enable development of these cellular tools.

The advent of induced pluripotent stem cell (iPSC) technology has revolutionized disease modelling by providing the ability to generate patient-specific lines that can be differentiated into various cell types. In contrast to analogous primary and immortalised cell lines, these cells offer the ability to look at human-specific mechanisms, with access to the high proliferation potential of iPSCs without deleterious impacts of genetic immortalisation methods. For this reason, iPSC-derived brain microvascular endothelial-like cells (iBMECs) and pericyte-like cells (iPericytes) offer promising tools for modelling the human BBB with greater accuracy. While iPSC-derived vascular cells have been successfully differentiated, there are wide knowledge gaps relating to functional maturity, stimulus responsiveness, and secretion profiles of iPSC-derived vascular cells, particularly in their interactions with amyloid pathology, inflammatory signals, and neurovascular integrity in Alzheimer's disease This is particularly important for modelling the BBB in AD, where response to proteinopathy, neuroinflammation and cytokine signalling are key pathological drivers.

This chapter presents the immunofluorescent and functional validation of iBMECs and iPericytes grown in 2D for BBB modelling. By applying Aβ, pgLPS, and LPS from *E. coli* (ecLPS) to iPSC-derived neurovascular cells, we investigate how Aβ and peripheral inflammatory stimuli might exacerbate AD pathology through vascular mechanisms. This includes indexing basal cytokine secretions, showing the secretion of vascular and neuroinflammatory mediators suggesting the potential that these cells exist in a primed inflammatory state. To address the importance of APOE genotype in AD modelling, the genotypes of a number of commercially available iPSC lines are sequenced, along with preliminary CRISPR-Cas9 experimentation aiming to generate iPSC lines with isogenically-switched *APOE* genotypes. This research paves the way for more accurate, multicellular, iPSC-derived disease models, and offers novel insights into the molecular underpinnings of AD-related vascular dysfunction.

3.2. *Results*

3.2.1. iBMEC differentiation and characterisation

The CS06iCTR-n2 iPSC line (CTR06), episomally reprogrammed from the skin fibroblasts of an 82-year old healthy female, was obtained from Cedars Sinai iPSC core. These cells were shown to express a normal karyotype, lack exogenous reprogramming vectors, express pluripotency markers and undergo successful trilineage differentiation (manufacturer's documentation). The expression of pluripotency markers OCT3/4 and Nanog were confirmed by immunocytochemistry, corroborating the manufacturer's results (Figure 3.1). iPSCs expressed low levels of nestin, and undetectable Pax6 (two markers indicative of the neural lineage), while also expressing EpCAM (an epithelial marker also involved in pluripotency) (Figure 3.1A). These iPSCs were used for all derivations described herein.

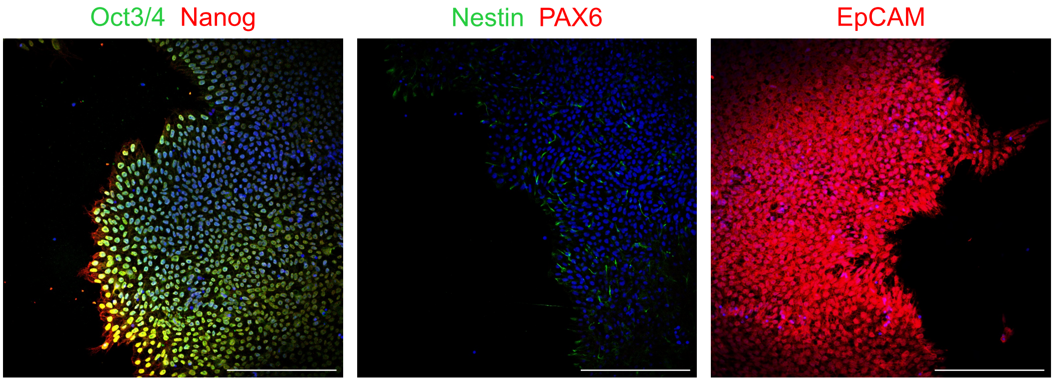

Figure 3.1: Immunofluorescence validation of iPSCs~~.~~ Representative images showing the expression of pluripotency cell markers OCT3/4 and

Nanog, NPC markers nestin and PAX6, and epithelial cell adhesion molecule (EpCAM). Scale bar represents 200 µm.

iBMECs were derived by initially differentiating iPSCs into a mixed neural/endothelial culture, and subsequent selective purification onto a fibronectin and collagen IV-coated surface (Neal et al., 2019). The resultant iBMECs were interrogated for endothelial markers alongside two commonly used endothelial cell lines (Figure 3.2A). The CMEC line is an immortalised cell line, originally taken from human brain capillary endothelial cells (Weksler et al., 2005) and HUVECs are a commonly used primary human endothelial cell line, taken from the umbilical vein (Park et al., 2006). Platelet endothelial cell adhesion molecule-1 (PECAM-1), an endothelial adhesion molecule involved in junctional cell-cell adhesion and leukocyte migration, was expressed in all three endothelial lines (Figure 3.2A). Similarly, vascular endothelial cadherin (VE cadherin), an endothelium specific adherens junction protein, was also expressed by all three cell lines (Figure 3.2A). Occludin, an enzyme that regulates the formation and maintenance of tight junctions, was expressed only by iBMECs, and localised to the cell edges, shown by the cobblestone pattern (Figure 3.2A). In comparison, CMEC and HUVEC samples did not express occludin to an appreciable degree. In addition, all three cell lines expressed some level of EpCAM, an adhesion glycoprotein found in epithelial cell adhesions, which has been recently purported to indicate non-endothelial cell identity (Lu et al., 2021) (Figure 3.2A). iBMECs also expressed laminin α4, a key basement membrane protein involved in blood-brain barrier integrity, and GLUT-1, a crucial glucose transporter responsible for facilitating energy supply (Figure 3.2B). Although EpCAM expression raises some concerns, expression of adherens junctions, tight junctions, BBB transporters and basement membrane component laminin α4 supports the endothelial phenotype of these cells.

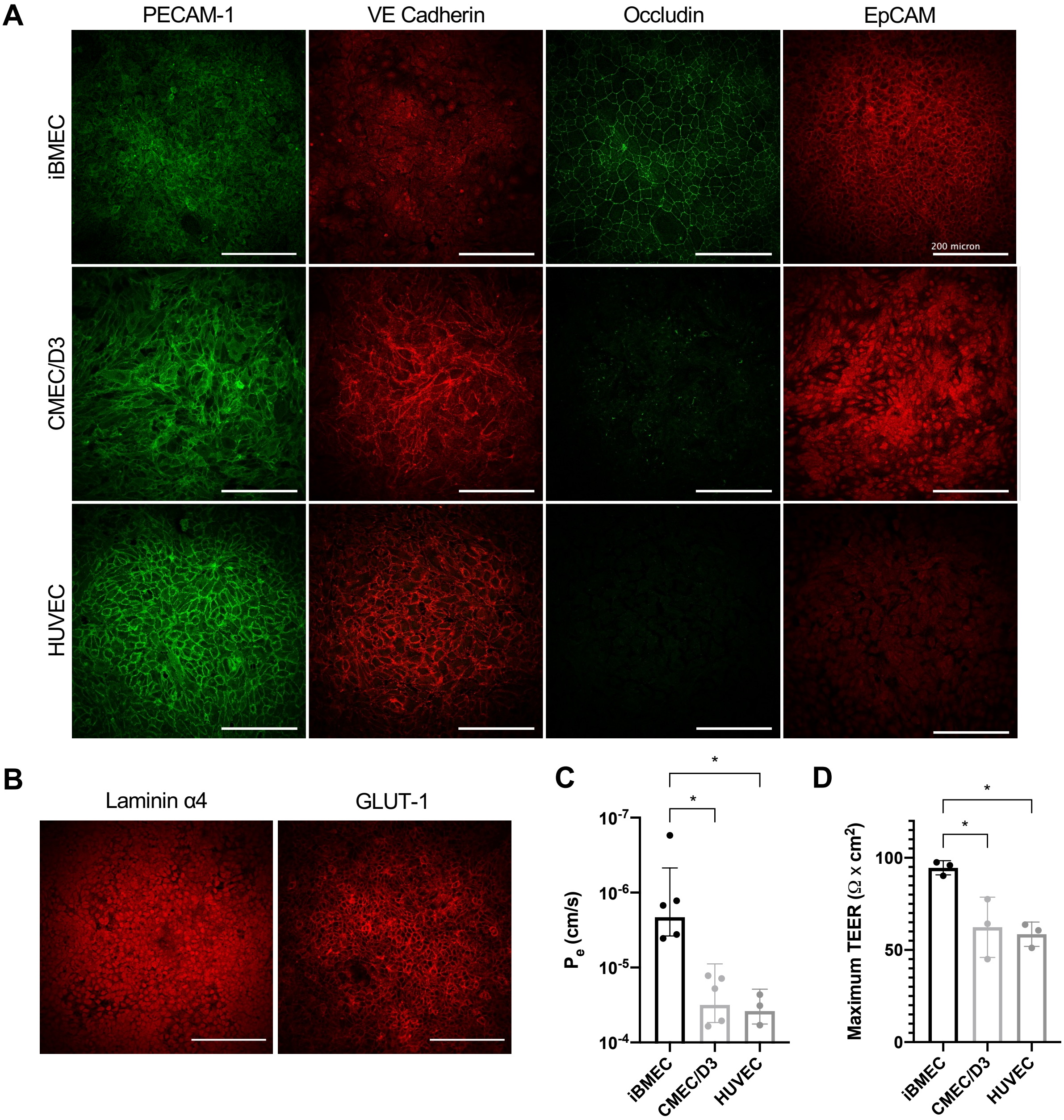

Figure 3.2: Immunofluorescence and functional validation of immortalised, primary and iPSC-derived endothelial cell lines. (A) Representative images showing the expression of endothelial cell markers platelet endothelial cell adhesion molecule-1 (PECAM-1), Vascular endothelial (VE) Cadherin, occludin and EpCAM in iBMEC, CMEC and HUVEC lines. Scale bar represents 200 µm. **(B)** Fluorescein effective permeability (P_e) values for CMEC, HUVEC and iBMEC monolayers. **(C)** Maximum transendothelial electrical resistance (TEER) values for iBMECs, CMEC and HUVEC monolayers measured by the xCelligence SP system. All data are reported as mean ± SD from $n \geq 3$, performed in duplicate. One-way ANOVA with Tukey's multiple comparisons test was used to test statistically significant differences between the means of all three conditions (* $p < 0.05$). **(D)** Representative images showing the expression of laminin α4 and glutamate transporter 1 (GLUT-1) in

iBMECs. Scale bar represents 200 μm. Abbreviations: CMEC: Cerebral Microvascular Endothelial Cell, HUVEC: Human Umbilical Vein Endothelial Cell, iBMEC: induced Brain Microvascular Endothelial Cell.

When compared to CMEC and HUVECs, iBMECs displayed enhanced barrier properties in functional assays. Permeability of iBMEC monolayers to sodium fluorescein was measured using a transwell system showing a P_e value of $2.1 \times 10^{-6} \pm 1.6$ cm/s. P_e values for CMEC ($3.1 \times 10^{-5} \pm 2.2$ cm/s) and HUVEC monolayers ($3.8 \times 10^{-5} \pm 1.9$ cm/s) were an order of magnitude higher, representing a significantly enhanced barrier phenotype in the iPSC derived cells (Figure 3.2C; $p = 0.045$ and $p=0.035$, respectively). In addition to this low permeability, *in vivo* iBMECs also display transendothelial electrical resistance (TEER), a property that can also be measured *in vitro*. Using the xCelligence real-time cell analysis system, endothelial monolayers were assessed for their maximum TEER via gold electrodes arrays embedded in the plates. iBMECs displayed a high TEER ($94.6 \pm 3.8\ \Omega \cdot \text{cm}^2$), that significantly exceeded both the CMEC ($62.3 \pm 16.4\ \Omega \cdot \text{cm}^2$) and the HUVEC ($58.5 \pm 6.6\ \Omega \cdot \text{cm}^2$) cell lines (Figure 3.2D; $p=0.018$ and $p=0.016$, respectively).

3.2.2. iPericyte differentiation and characterisation

iPericyte differentiation was performed according to the protocol published in Faal et al. (2019), where iPSCs were first differentiated into a neural crest lineage as described in Leung et al. (2016). These cells were then progressed to a neural crest-lineage pericyte by culturing in ScienCell pericyte medium. The resultant cells were then assessed by immunocytochemistry for the expression of platelet derived growth factor receptor β (PDGFRβ), neuron-glial antigen 2 (NG2) and membrane alanyl aminopeptidase (CD13). While none of these markers are pericyte-specific, when expressed together, these markers are considered to be indicative of pericyte identity (Armulik et al., 2011a). PDGFRβ is a surface receptor for platelet derived growth factors that regulates pericyte involvement in the neurovascular unit (Winkler et al., 2010). NG2 is a proteoglycan involved in pericyte-endothelial interactions, while CD13 is a membrane metalloprotease present in myeloid cells, some epithelial cells, and pericytes (Ozerdem et al., 2001, Kunz et al., 1994). All three of these markers were observed to be expressed in both iPSC-derived pericytes and the primary human brain vascular pericyte (HBVP) cell line (Figure 3.3A).

In corroboration with findings from Brown et al. (2023), iPSC-derived pericytes were observed in a variety of morphological states, including standard (polarised with 2 or more distinct projections), circular (smaller that standard, no distinct projections), balling (smaller than circular, appear "balled-up"), sheet (larger than standard, flattened membrane and nucleus) and spindle (long, thin, elongated cells with small nuclei) morphologies (Figure 3.3B). This morphological diversity mimics the plethora of states observed in human pericytes, and further attests to the *in vivo*-like identity of iPericytes derived using this method (Brown et al., 2023).

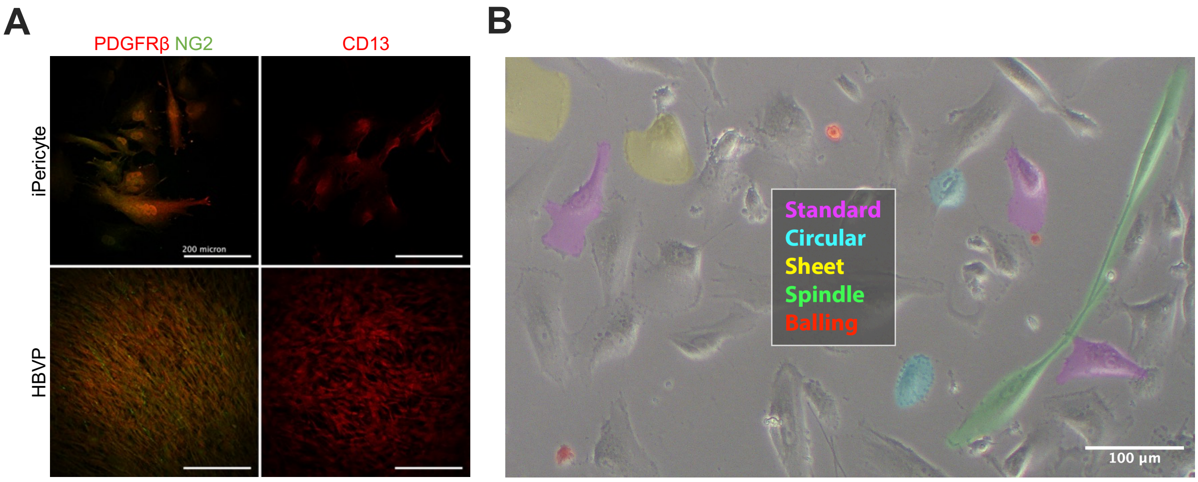

Figure 3.3: Microscopic validation of primary and iPSC-derived pericytes. (A) Representative images showing the expression of pericyte cell markers PDGFRβ, CD13 and NG2 in HBVP and iPericyte cell lines. Scale bar represents 200 µm. **(B)** Representative brightfield image showing the heterogeneous morphological categories of iPericytes highlighted by colours. Magenta = standard, cyan = circular, yellow = sheet, green = spindle, red = balling (Brown et al., 2023). Scale bar represents 100 µm. Abbreviations: CD13: Cluster of Differentiation 13, HBVP: Human Brain Vascular Pericyte, NG2: Neural/Glial Antigen 2, PDGFRB: Platelet-Derived Growth Factor Receptor β.

3.2.3. iBMECs and iPericytes display limited inflammatory reactivity

We next aimed to characterise the treatment responsiveness of the iPSC-derived endothelial cells and pericytes by measuring IL-6 secretion and endothelium permeability after treatment with Aβ monomer preparations, ecLPS or pgLPS. While treatment with ecLPS has been shown to affect permeability and cytokine secretion in primary endothelial cells, the effects of ecLPS, pgLPS and Aβ in iBMECs have not been examined (Smyth et al., 2018). iPericytes are known to secrete inflammatory mediators, including IL-6, in response to ecLPS, so we expected our iPericytes to replicate this phenotype (Smyth et al., 2018). Post-treatment viability was also measured to ensure that treatment-induced cell death was not a factor in any observed differences.

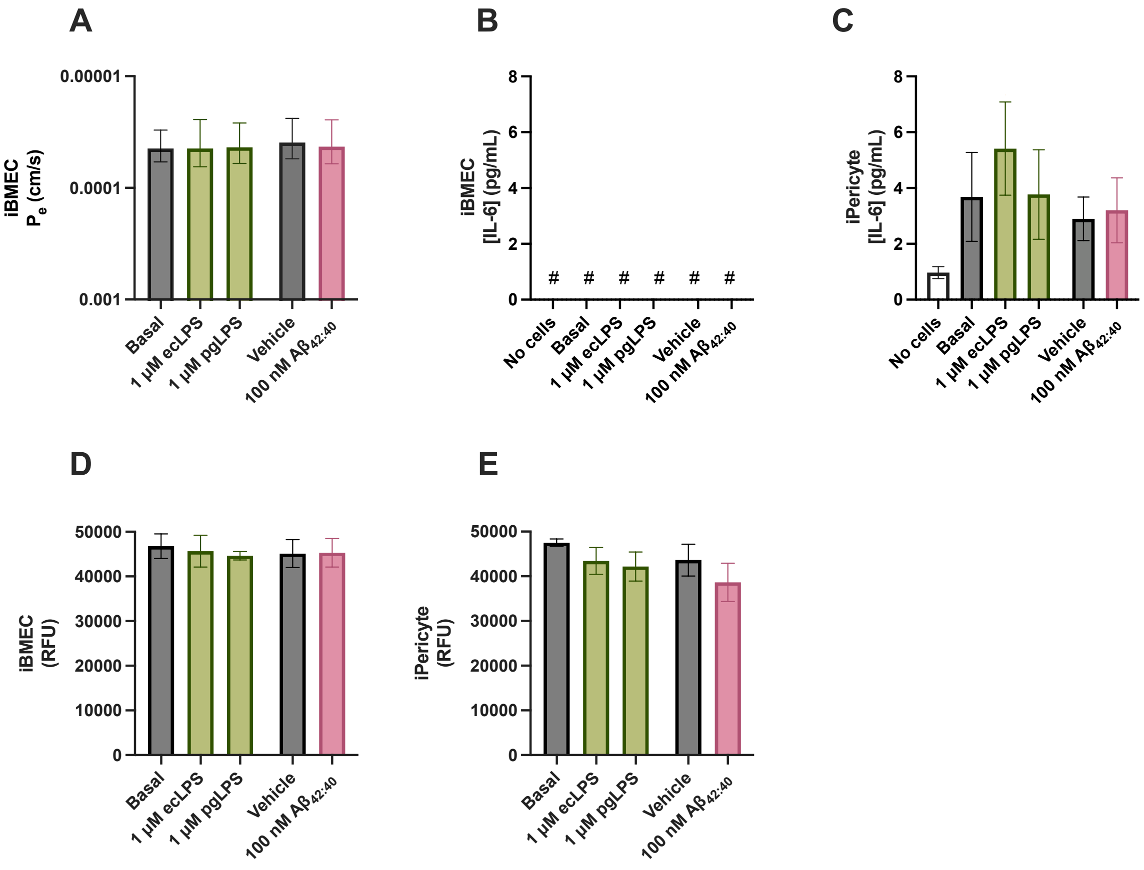

Figure 3.4: iBMEC and iPericyte functional signatures in 2D. (A) Effective permeability of iBMEC monolayers to sodium fluorescein after 24 h treatment (Vehicle denotes 0.5% ammonium hydroxide in PBS, used to dissolve Aβ preparations only). One-way ANOVA with Šídák's multiple comparisons test was used to test for differences between treatments means and their vehicle. **(B)** iBMEC and **(C)** iPericyte IL-6 release measured by ELISA after 24 h treatment (# denotes IL-6 concentration below detection limit). One-way ANOVA with Dunn's multiple comparisons test was used to test for differences between treatment means and their vehicle. **(D)** iBMEC and **(E)** iPericyte metabolic viability as measured by a CellTiter-Blue assay after 24 h treatment. Data shown as raw fluorescence units (RFU) corrected by subtracting fluorescence elicited by media. One-way ANOVA with Šídák's multiple comparisons test was used to test for differences between treatment means and their vehicle. All data are reported as mean ± SD from n ≥ 3, performed in duplicate. Aβ: Amyloid β, ecLPS: *Escherichia coli* Lipopolysaccharide, iBMEC: induced Brain Microvascular Endothelial Cell, P_e: Effective Permeability, pgLPS: *Porphyromonas gingivalis* Lipopolysaccharide, RFU: Relative Fluorescence Units.

Firstly, we tested the ability of endothelial cells to respond to inflammatory triggers in the transwell-format fluorescein permeability assay. In our hands, neither A$\beta_{42:40}$, ecLPS or pgLPS significantly affected permeability in these iBMECs (Figure 3.4A).

Basal iBMECs, and iBMECs treated with A$\beta_{42:40}$, ecLPS and pgLPS all produced negligible IL-6, with mean values falling below the detection range of the assay (Figure 3.4B). In iPericytes, basal secretion of IL-6 was detected (3.68 ± 1.59 pg/mL), however treatment with A$\beta_{42:40}$, ecLPS and pgLPS did not significantly change the IL-6 levels measured in conditioned media (Figure 3.4C).

A$\beta_{42:40}$, ecLPS and pgLPS did not reduce iBMEC viability when measured by a CellTiter-Blue assay (Figure 3.4D & 3.4E).

3.2.4. Aβ monomer application results in deposition on 2D iBMECs

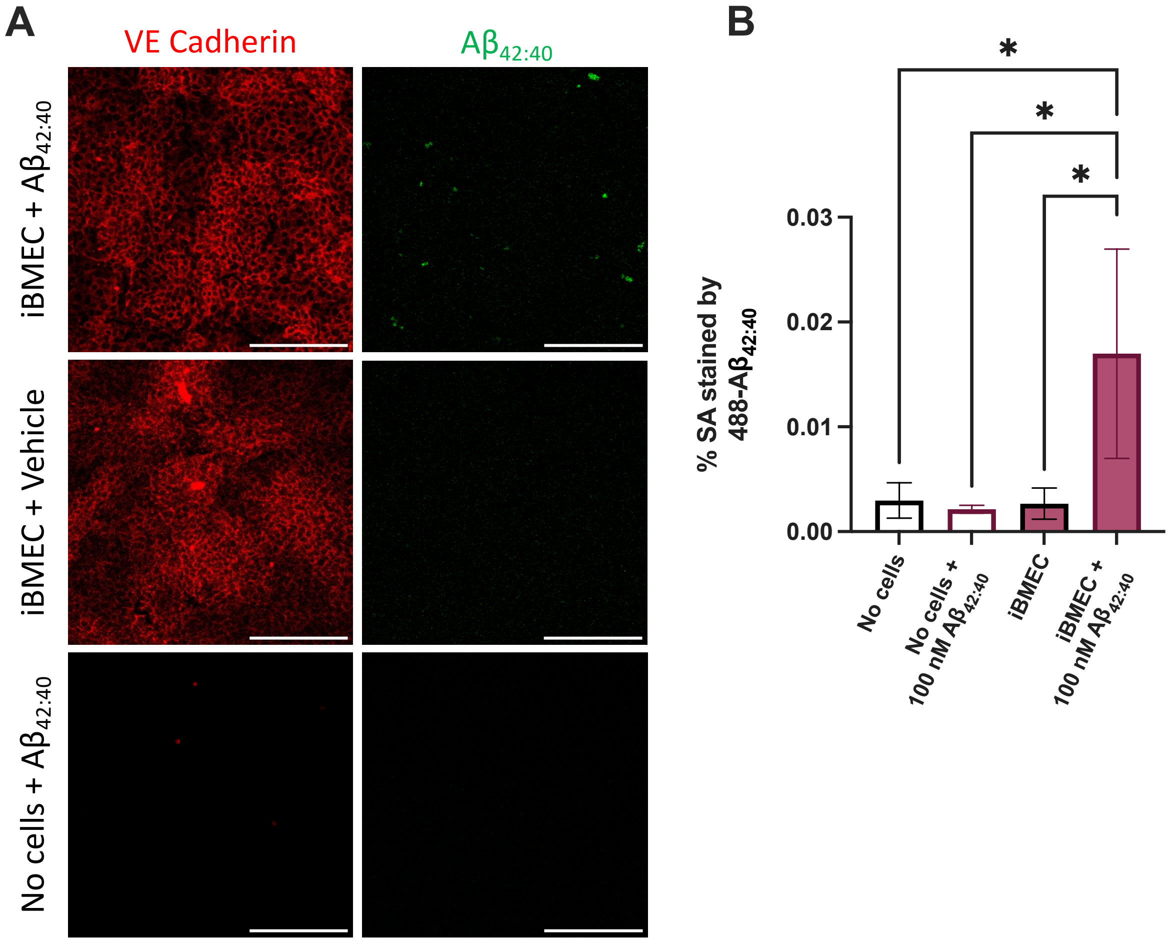

Figure 3.5: Aβ deposition in iBMEC monolayers. (A) Representative immunofluorescent images showing A$\beta_{42:40}$ deposits on 2D cultured iBMECs.

Scale bar represents 200 µm. $A\beta_{42:40}$-HiLyte™ Fluor 488 preparations were dissolved in 0.5% ammonium hydroxide in PBS (Vehicle) **(B)** Quantification of surface area (SA) of fluorescent $A\beta_{42:40}$ signal in 2D iBMEC cultures after 24 h treatment. Data are reported as mean percentage of thresholded area ± SD from n = 3, performed in duplicate. One-way ANOVA with Dunnett's multiple comparisons test was used to test for differences between conditions and the control (No cells + 100 nM $A\beta_{42:40}$) (* $p < 0.05$). Abbreviations: Aβ: Amyloid β, iBMEC: induced Brain Microvascular Endothelial Cell, VE cadherin: Vascular Endothelial Cadherin.

Aβ preparations of varying lengths and aggregation states cause disruption of *in vitro* endothelial monolayers, providing insight into the mechanisms underlying cerebral amyloid angiopathy in AD pathology (Li et al., 2015, Liu et al., 2018). However, their effects on iPSC-derived iBMECs and iPericytes remain unexplored. Here, we investigated whether 24 h application of initially monomeric $A\beta_{42:40}$ would result in deposition of aggregates in 2D cultured iPSC-derived vascular cells. To measure this, we treated iBMECs with 100 nM fluorescent $A\beta_{42:40}$ which became deposited on iBMEC cultures (Figure 3.5A). We also treated wells without cells to check whether any of the retained $A\beta_{42:40}$ signal could be due to Aβ species sticking to the plastic wells or the well coatings. iBMECs treated with the Aβ preparation exhibited a significantly higher percentage of area covered by fluorescent signal than when $A\beta_{42:40}$ was applied to the fibronectin/collagen surface coating (Figure 3.5B). The retained $A\beta_{42:40}$ signal in the fibronectin/collagen-coated wells did not differ significantly compared to that of empty, uncoated wells or of cells without $A\beta_{42:40}$ treatment.

When repeating this process in iPericytes, significant loss of cells was observed during washing phases of immunofluorescence preparation (data not shown). Further investigations into higher cell densities, increased Matrigel concentrations and alternative washing techniques may be possible solutions to this issue.

3.2.5. iBMECs and iPericytes exhibit distinct basal inflammatory secretomes

While there have been some more comprehensive cytokine secretion data released for primary/immortalised endothelial cells and pericytes (Kurmann et al., 2021), inflammatory secretomes from iBMECs and iPericytes are poorly characterised. Given that our iBMECs and iPericytes displayed divergent IL-6 response phenotypes, a broader inflammatory profile of these cell lines was warranted to determine their functional state. Thus, the Proteome Profiler Human XL Cytokine Array was used to index basal protein release in iBMECs and iPericytes, and investigate whether ecLPS, pgLPS and A$\beta_{42:40}$ treatment significantly affect these levels of those compounds in conditioned media. As in Kurmann et. al. (2021) and Kim et. al. (2023), array membranes were analysed at two exposure time points, increasing the dynamic range to observe markers at low and high expression levels.

3.2.5.1. iBMEC secretome

Basal cytokine secretion was measured by comparing the mean total density between iBMEC-conditioned media, and media without cells. Proteins that were significantly different ($q < 0.05$) from media at the short 1 sec array development exposure time point were: extracellular matrix metalloproteinase inducer (EMMPRIN; 4516 a.u ± 250, $q = 0.0033$, mean difference = 4125), Growth/differentiation factor 15 (GDF-15; 6954 a.u ± 1778, $q < 0.0001$, , mean difference = 6746), insulin-like growth factor-binding protein-2 (IGFBP-2 ;10614 a.u ± 1783, $q < 0.0001$, mean difference = 10507), IGFBP- 3 (9994 a.u ± 2950, $q < 0.0001$, mean difference = 9807), Macrophage migration inhibitory factor (MIF; 3624 a.u ± 620, $q = 0.0131$, mean difference = 3426), Matrix metalloproteinase-9 (MMP-9; 7661 a.u ± 2736, $q < 0.0001$, mean difference = 7423) and osteopontin (16392 a.u ± 3017, $q < 0.0001$, mean difference = 16000) (Figure 3.6A).

At the longer 10 sec array development exposure timepoint, the density of proteins significantly different from media were: cystatin C (8783 a.u ± 1785, $q < 0.0001$, mean difference = 6472), basic fibroblast growth factor (bFGF; 6570 a.u ± 809, $q < 0.0001$, mean difference = 4454), fibroblast growth factor-19 (FGF-19; 9479 a.u ± 1241, $q < 0.0001$, mean difference = 5167), IL-17A (9670 a.u ± 3032, $q < 0.0001$, mean difference = 4819), monocyte chemoattractant protein-1 (MCP-1; 0072 a.u ± 3983, $q < 0.0001$, mean difference = 7616), platelet-derived growth factor-AA (PDGF-AA; 9940 a.u ± 3000, $q < 0.0001$, mean difference = 7901), pentraxin 3 (9355 a.u ± 3649, $q < 0.0001$, mean difference = 5512), resistin (9273 a.u ± 2196, $q = 0.0078$, mean difference = 3118) and thrombospondin-1 (10371 a.u ± 4736, $q < 0.0001$, mean difference = 8069) (Figure 3.6B).

Cytokine arrays were also performed in iBMECs treated with 10 μg/mL ecLPS, 10 μg/mL nM pgLPS or 100 nM A$\beta_{42:40}$ (dissolved 0.5% NH_4OH in PBS). Only one significantly different cytokine was observed, with a decrease in Lipocalin-2 after ecLPS administration ($q = 0.0272$, mean difference = -4407) (Supplementary Table

3.2). A weak trend towards increased RBP4 concentration was also see after vehicle administration (q = 0.2404, mean difference = 4793). Proteins with non-significant pixel density differences are listed in Supplementary Table 3.2.

To better understand the overall distribution of protein secretion between treatment conditions, hierarchical clustering of cytokine secretion profiles was performed and visualised using a heatmap (Figure 3.8A). Notable features include Aβ and its vehicle condition grouping separately from basal, and, ecLPS and pgLPS forming a separate cluster, indicating potential shared mechanisms .

3.2.5.2. iPericyte secretome

When comparing iPericyte-conditioned media to media without cells, basally-secreted cytokines identified at the short exposure time point were: IGFBP-2 (4965 a.u ± 1199, q = 0.0071, mean difference = 4906) and serpin E1 (11291 a.u ± 1739, q < 0.0001, mean difference = 10229) (Figure 3.7A).

At the long exposure timepoint, cytokines observed included: EMMPRIN (14447 a.u ± 3916, q < 0.0001, mean difference = 9835), FGF-19 (8229 a.u ± 2706, q < 0.0001, mean difference = 5072), MIF (6766 a.u ± 1202, q < 0.0001, mean difference = 5738), osteopontin (12440 a.u ± 9329, q < 0.0001, mean difference = 9797) and PDGF-AA (10440 a.u ± 3856, q < 0.0001, mean difference = 8566) (Figure 3.7B).

iPericyte-secreted cytokines were also measured after treatment with 10 µg/mL ecLPS, 10 µg/mL nM pgLPS or 100 nM A$\beta_{42:40}$. None of the measured cytokines were differentially expressed when compared to cells treated with vehicle (Supplementary Table 3.3). However, there was some notable trends, with both ecLPS- and pgLPS-treated iPericytes trending towards decreases in epidermal growth factor (EGF) (ecLPS: q = 0.2131, mean difference = -3954; pgLPS q = 0.5204, mean difference = -2884). ecLPS and Aβ-vehicle application also elicited a slight trend towards decreases in Serpin E1 (ecLPS: q = 0.2718, mean difference = -3301; Aβ-vehicle: q = 0.1747, mean difference = -3821). Proteins with non-significant pixel density differences are listed in Supplementary Table 3.3.

To better understand the overall distribution of protein secretion across treatment conditions, hierarchical clustering of cytokine secretion profiles was conducted and visualized using a heatmap for iPericytes (Figure 3.8A). Notable features include a broadly elevated cytokine profile in the condition treated with 0.5% ammonium hydroxide (the vehicle used to dissolve Aβ), and ecLPS-induced conditioned media clustering further away from the basal iPericytes compared to pgLPS, suggesting that ecLPS may induce a more pronounced alteration in the pericyte secretome.

3.2.6. APOE sequencing

The genetic diversity of iPSC lines from unrelated humans can hinder the ability to make accurate conclusions following differential assay results. For this reason, isogenic control lines are the gold standard for investigating the effect of specific gene mutations on cell outcomes. We set out to use CRISPR/Cas9 machinery to create isogenic, homozygous ε4 cell lines from homozygous ε3 iPSC lines, and vice versa. Interrogating these cell lines in 2D and 3D culture formats would provide a clearer understanding about how *APOE* genotype affects vascular AD pathology.

Firstly, the *APOE* genotype of iPSC lines in our lab were sequenced, which is additionally useful due to the well-documented effects on APOE experimental outcomes (Lin et al., 2018a). Genomic DNA was extracted from six iPSC lines, and these were Sanger sequenced by the Australian Genome Research Facility. Representative electropherograms are shown in Figure 3.9. Of the six iPSC lines, three were confirmed as homozygous for the ε3 allele (CTR06, CTR71 and fAD08), while the other three were heterozygous ε3/ε4 (CTR88, fAD948, fAD950). These findings were used in work from our lab which has now been published. This showed differences in other experimental systems based on these cell lines were explained by differences in *APOE* genotype rather than the presence of *PSEN2* fAD mutations (Sullivan et al., 2024).

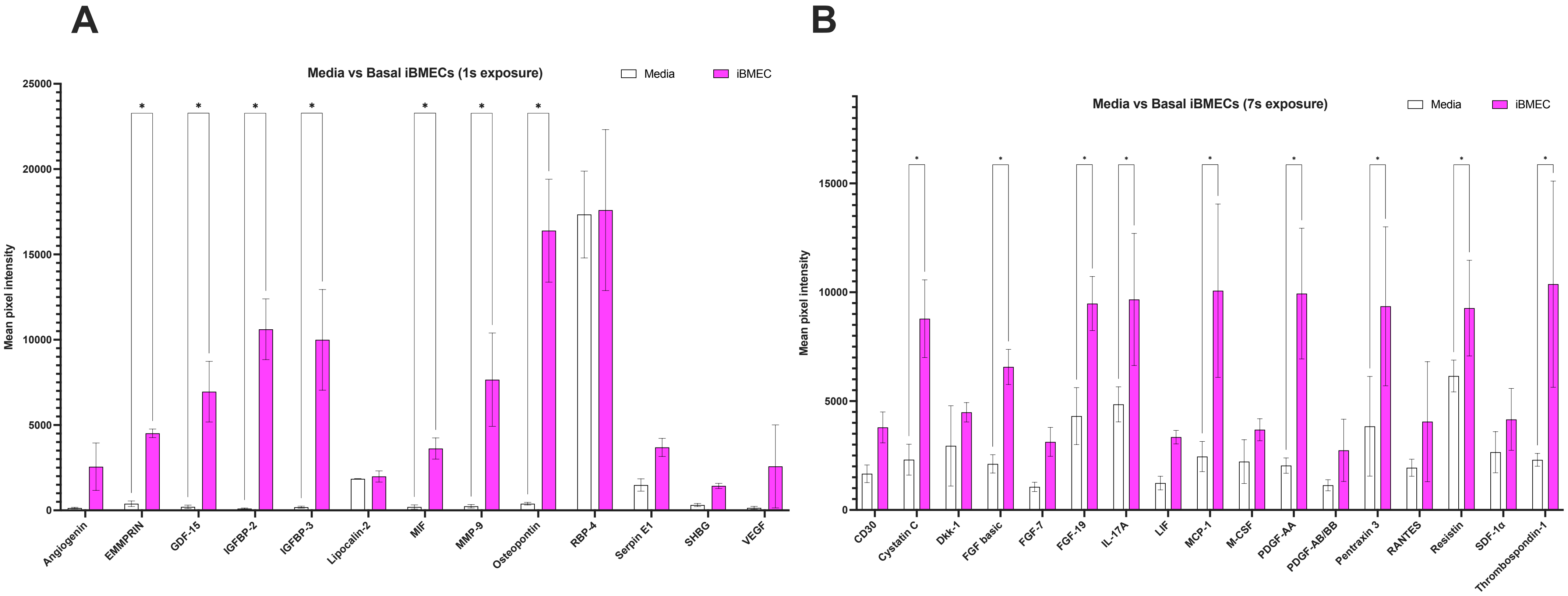

Figure 3.6: Basal cytokine secretion in iBMECs. Cytokines with a mean q value < 0.5 when compared to the basal media without cells are included. Two exposure times **(A)** 1 s and **(B)** 7 s, were analysed to determine relative expression of proteins with high and low abundance. Data are reported as mean signal intensity ± SD from n = 3. For statistical testing, a two-way ANOVA with a two-stage linear step-up procedure of Benjamini, Krieger and Yekutielie was used to control the false-discovery rate, with Q < 0.05. Cytokines with mean pixel density under 10 % of the maximum were not included in the statistical analysis. See Abbreviations (page viii) for full list of cytokine names

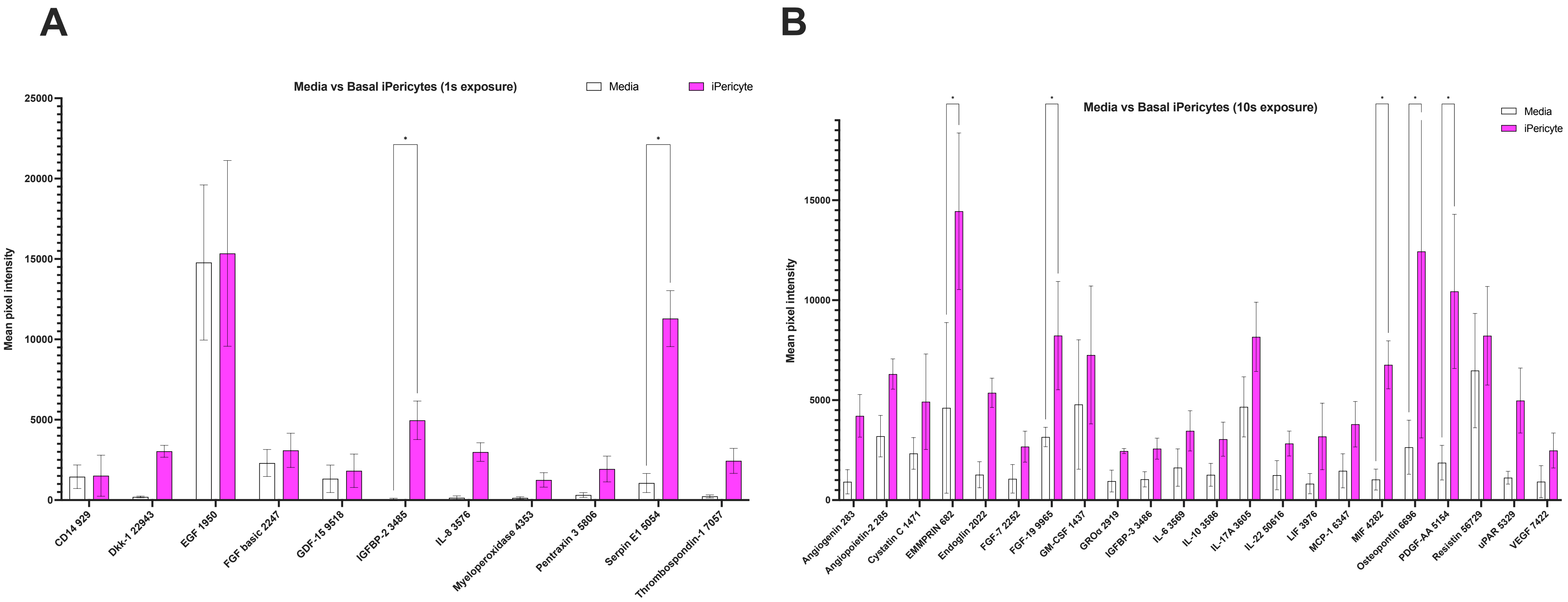

Figure 3.7: Basal cytokine secretion in iPericytes. Cytokines with a mean q value < 0.5 when compared to the basal media without cells are included. Two exposure times **(A)** 1 s and **(B)** 10 s, were analysed to determine relative expression of proteins with high and low abundance. Data are reported as mean signal intensity ± SD from n = 3. For statistical testing, a two-way ANOVA with a two-stage linear step-up procedure of Benjamini, Krieger and Yekutielie was used to control the false-discovery rate, with Q < 0.05. Cytokines with mean pixel density under 10 % of the maximum were not included in the statistical analysis. See Abbreviations (page viii) for full list of cytokine names.

Figure 3.8: Hierarchical clustering of secreted cytokine signatures in treated (A) iBMECs and (B) iPericytes.

Y-axis consists of markers of interest (right) and their clustering profile (left), while x-axis contains treatment condition (bottom) and clustering (top). See Abbreviations (page viii) for full list of cytokine names. Cytokines and treatment conditions are hierarchically clustered according to similarity. Source code is available in Figure 2.4.

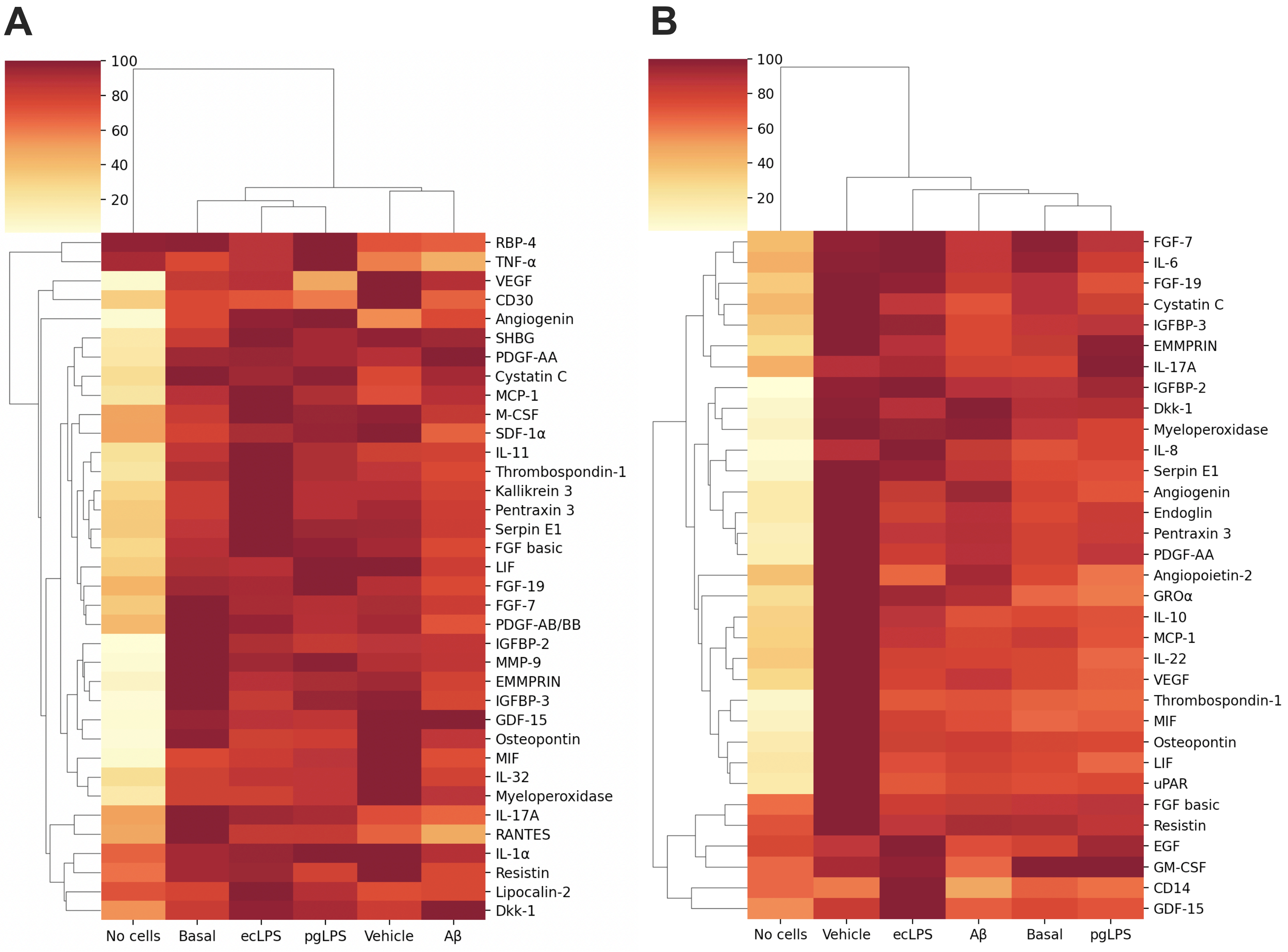

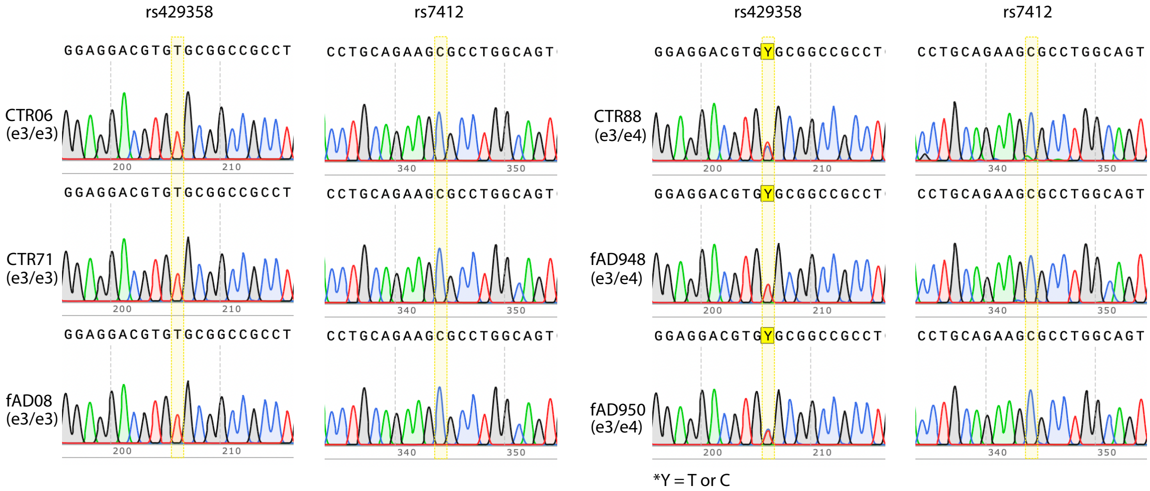

Figure 3.9: *APOE* genotyping of iPSC lines. Sanger sequencing chromatograms showing *APOE* genotype at codon 112 (rs429358) and codon 158 (rs7412) for 6 iPSC lines. Yellow highlight indicates the position of the single nucleotide polymorphism that determines APOE genotype. Y indicates T or C nucleotide. Reproduced from Sullivan et al. (2024)

3.2.7. CRISPR/Cas9 gene editing of iPSCs

As no homozygous ε4 iPSCs were detected, new homozygous ε3 (CTR33 and AD33), and homozygous ε4 iPSC lines (AD44) were procured. These cell lines, sourced from the Alzheimer's Disease Research Centre at the University of California, Irvine, had already been genotyped at *APOE*, and had associated AD-relevant patient characteristics available (Table 3.1). For these reasons, these cells were chosen to CRISPR-edit.

The CRISPR/Cas9 machinery found in the adaptive immune system of bacteria and archea, has been repackaged as a gene-editing tool, acting as a set of “molecular scissors” to edit mammalian genomes (Doudna and Charpentier, 2014). Cas9 is a nuclease that uses a guide RNA to target a specific sequence location, before inducing a double-stranded break. Three-nucleotide protospacer-adjacent motifs (PAMs) in the cell’s genome bind with paired nucleotides in the gRNA, directing Cas9 to induce a DSB three base pairs upstream. Repair mechanisms are then triggered by the cell, with non-homologous end joining (NHEJ) being more prevalent than homology-directed repair (HDR). While NHEJ generates insertions and deletions that can cause gene truncation or inactivation, HDR uses a template (e.g. homologous chromosomes, or sister chromatids in the native context) to accurately fix the DSB. This mechanism can be exploited in a research-context by providing synthetic DNA (e.g. a single-stranded oligodeoxynucleotides or ssODN) to induce desired genetic changes with accuracy.

Table 3.1: Clinical & genetic characteristics of iPSC lines sourced from ADRC. iPSCs sourced from the Alzheimer's Disease Research Centre, University of California, Irvine. Abbreviations: AD: Alzheimer's Disease, APOE: Apolipoprotein E, CDR: Clinical Dementia Rating, MMSE: Mini-Mental State Examination.

Code	Sex	Age (years)	*APOE* genotype	Biopsy			Current		
				MMSE	CDR	Diagnosis	MMSE	CDR	Diagnosis
AD33	F	81	e3/e3	22	0.5	Probable AD	-	3	AD
AD44	F	72	e4/e4	24	1	AD	16	2	AD
CTR33	F	76	e3/e3	30	0	None	30	0	None

The workflow of this experiment is explained diagrammatically in Figure 3.10 and 3.11A. Briefly, CRISPR/Cas9 machinery and guide RNA was delivered via the LentiCRISPRV2 plasmid (Figure 3.11B). Delivery via electroporation occurs via a pulse-mediated opening of temporary pores in cell membranes, allowing entry of the vector and template. Electroporation is preferable to lipofectamine when transfecting iPSCs (Xu et al., 2018). After transfection, puromycin can be added to selectively grow only cells expressing the construct. Once enough cells are produced, single cells can be isolated by limited dilution, before the expansion of monoclonal colonies and sequencing to confirm colonies with successful knock-in. Once desirable clones are confirmed, they are further interrogated using G-band karyotyping to rule out karyotypic abnormalities, and trilineage differentiation potential is assessed to substantiate the maintenance of pluripotency.

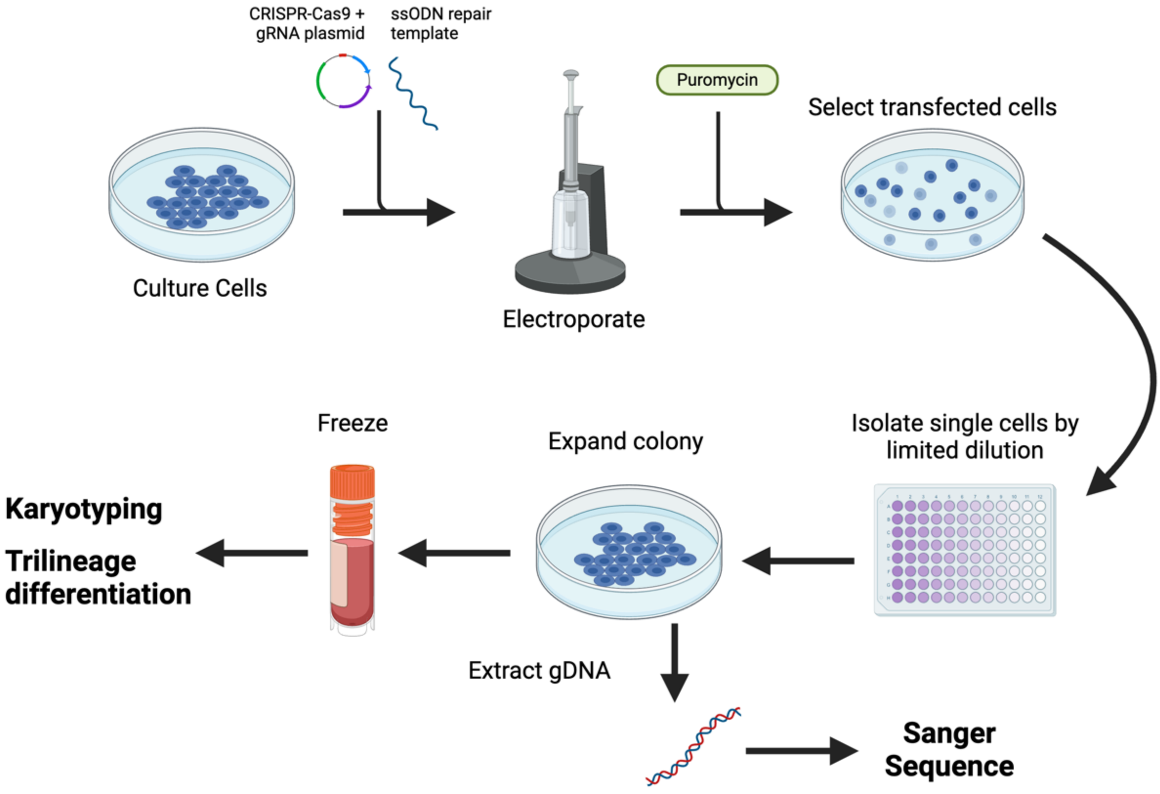

Figure 3.10: Workflow of CRISPR/Cas9-mediated editing of iPSCs for the creation of isogenic control lines. Abbreviations: CRISPR-Cas9: Clustered Regularly Interspaced Short Palindromic Repeats-Associated Protein 9, gRNA: guide RNA, ssODN: single-stranded Oligodeoxynucleotide.

The plasmid used here contains the gRNA sequences (Table 2.5) under the U6 promotor, while expressing the Cas9 nuclease and puromycin-resistance cassette under the EF-1a core promotor (Figure 3.11B). The ssODN repair templates (Table 2.5) for HDR contain asymmetrical homology arms for improved HDR efficiency and introduce six predicted silent mutations to deter subsequent Cas9-binding to successfully HDR-edited sequences (Designed by Cesar Moreno, The University of Sydney).

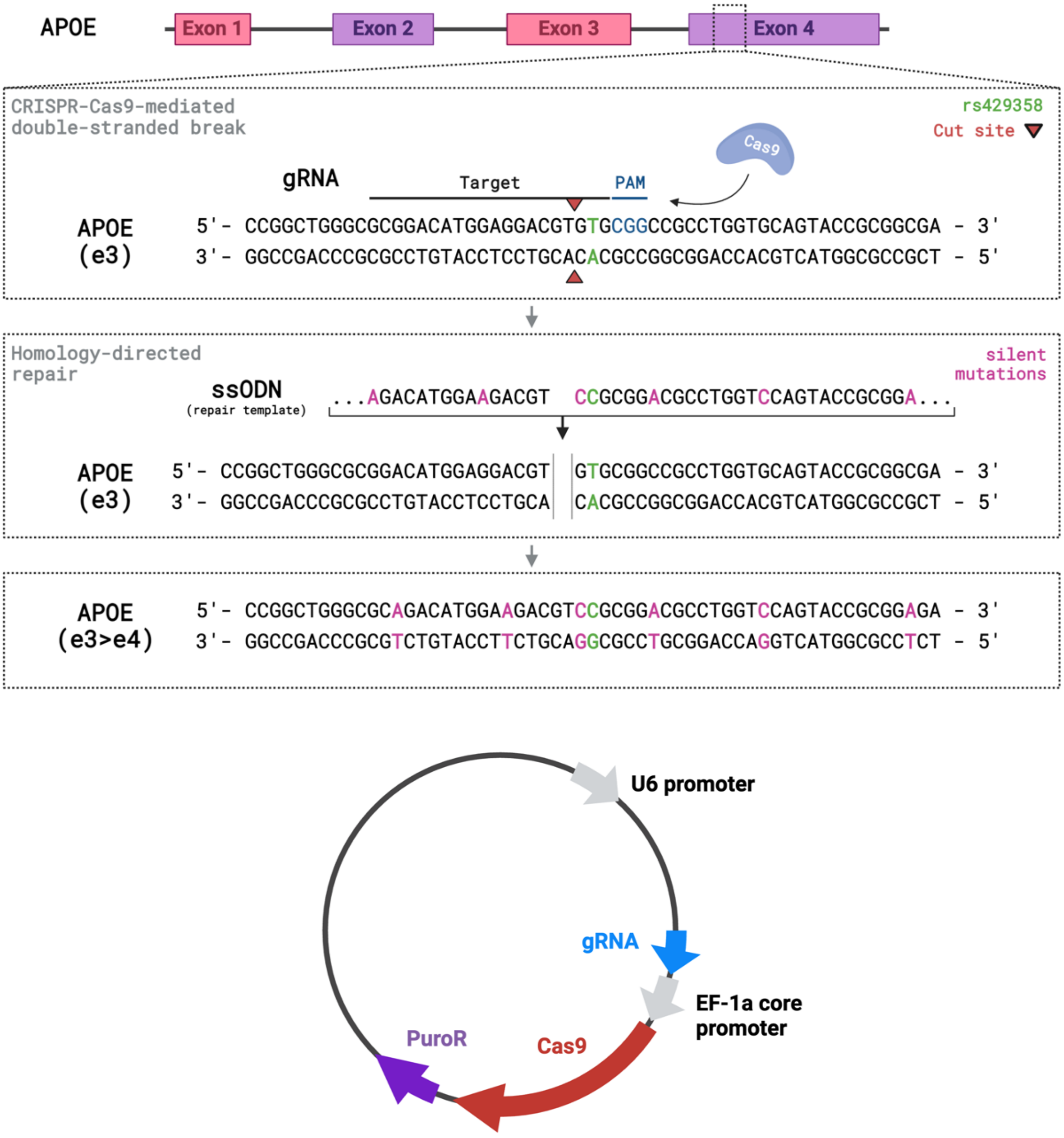

Figure 3.11: Genetic machinery for *APOE* targeting and transfection. **(A)** Genetic targeting of the *APOE* gene. The guide RNA targets exon 4 of the *APOE* gene, inducing a double stranded break (red triangle) 1 bp upstream of rs429358 SNP (green) and 3 bp upstream of the PAM sequence (blue). The repair template for HDR is an ssODN, containing predicted-silent mutations (purple) to deter targeting of already-edited DNA. **(B)** Simplified vector map of the LentiCRISPRV2 plasmid, containing Cas9 machinery and puromycin resistance cassette expressed under the EF-1α promoter, and gRNA expressed under the U6 promoter. Abbreviations: APOE: Apolipoprotein E, Cas9: CRISPR-associated Protein 9, EF-1a: Elongation Factor 1 Alpha, gRNA: guide

RNA, PuroR: Puromycin Resistance, ssODN: single-stranded Oligodeoxynucleotide, U6: RNA Polymerase III Promoter.

An initial experiment was performed to ensure that the plasmid was expressed effectively in HEK293 cells. After lipofectamine-induced transfection of the Cas9-gRNA plasmid and ssODN into HEK293 cells, puromycin treatment induced widespread cell death in conditions that were not treated with the plasmid, but did not induce this same effect in cells treated with the plasmid, suggesting successful expression of the vector (data not shown).

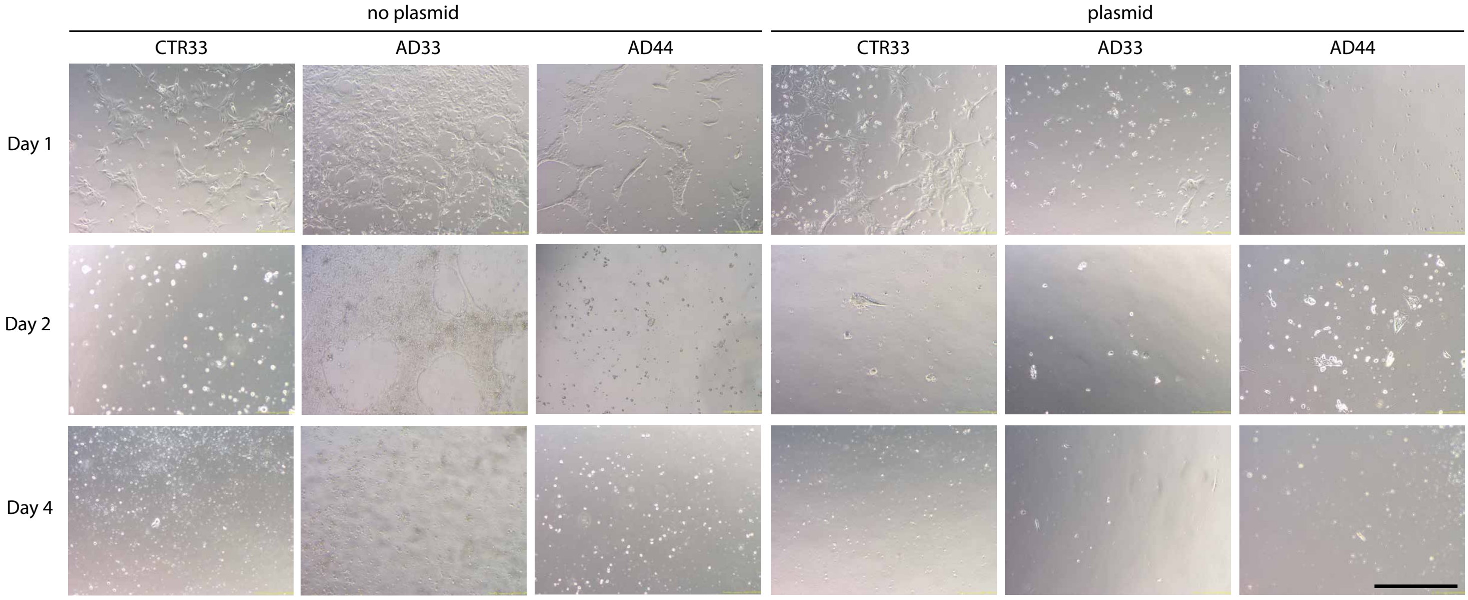

Figure 3.12: Electroporation of iPSCs induces detachment suggestive of cell death. Representative brightfield images showing cell detachment and poor growth in CTR33, AD33 and AD44 iPSC lines at 1, 2, and 4 days post-electroporation. Scale bar represents 500 µm.

24 h after electroporated iPSC were replated, CTR33-iPSC had successfully sat down, whereas AD33 and AD44 iPSCs weakly attached as sparse single cells. At 48 h post-electroporation (24 h after puromycin addition) significant cell detachment was observed in all three cell conditions (Figure 3.12), indicative of puromycin-induced cell death and inadequate expression of the plasmid. Due to time constraints, these experiments were abandoned at this point.

3.3. *Discussion*

3.3.1. Neurovascular iPSC derivation and validation

In the current study, endothelial cells and pericytes were derived from a healthy patient-derived iPSC line and compared to commonly used primary and immortalised lines of the same cell type. While all three endothelial cell lines expressed PECAM-1 and VE cadherin, iBMECs displayed an enhanced barrier phenotype compared to the CMEC and HUVEC lines, showing expression of the tight junction protein occludin, decreased permeability to sodium fluorescein, and increased maximum TEER. The iBMEC fluorescein permeability data reported here align with literature values, which suggest an effective *in vitro* permeability in the order of 1 x 10^{-6} cm/s (Wilson et al., 2015, Hollmann et al., 2017, Neal et al., 2019). It must be noted, however, that the TEER values observed for the present iBMECs differ from the values reported in the original iBMEC derivation protocol paper (Neal et al., 2019) and those reported in another paper using iBMECs derived from the same iPSC line as that derivation paper (Raut et al., 2021a), which report TEER values an order of magnitude higher. This is likely explained by the differences in measurements between the Agilent xCelligence system used in this study, and EVOM Voltohmmeter used in the other studies. Specifically, the lack of basolateral fluid compartment in the xCelligence system, as opposed to the transwell systems used in voltohmmeter experiments, may impact the development of *in vivo*-like cell polarity, resulting in lower resistance (Benson et al., 2013). The xCelligence system also uses a higher frequency stimulation (10,000-50,000 Hz as opposed to 12.5 Hz in the EVOM system), which may more accurately capture transcellular resistance as opposed to paracellular resistance – with transcellular resistance being more relevant for TEER readings (Benson et al., 2013). While *in vivo* TEER and effective permeability measurements cannot be easily measured, the human BBB is estimated to have a TEER in excess of 8000 Ω x cm^2 and low permeability values that differ substantially depending on method and molecule (Smith and Rapoport, 1986). Nevertheless, the iBMECs reported in the present study display a higher TEER and lower permeability than the CMEC and HUVEC lines, suggesting that electrical and permeability properties of iBMECs better recapitulate the *in vivo* vasculature. While only one iPSC line was interrogated in these experiments, Neal et. al. (2019) reports the differentiation of four different iPSC lines, with similar results, supporting the methods' reproducibility (further discussion of iPSC line variability is included in Chapter 6).

Adherens junction proteins PECAM-1 and VE cadherin were expressed by all three cell lines, while the tight junction protein occludin, was expressed only by iBMECs, supporting an enhanced endothelial phenotype compared to HUVECs and CMECs. iBMEC's expression of PECAM-1, VE cadherin, occludin, laminin α4 and GLUT-1, plus the lower permeability and enhanced TEER, demonstrates an endothelial phenotype that is more similar to *in vivo* than HUVECs and CMECs.

In addition to endothelial markers, the expression of EpCAM, and epithelial adhesion protein, was revealed in iBMECs. A recent study investigating various iBMEC derivation methods posited that EpCAM expression was indicative of incorrect cell identity (Lu et al., 2021). This work suggested that current methods produced cells that lacked appropriate endothelial lineage genes and expressed inappropriate gene clusters from the epithelial lineage, highlighting the need for protocols that produce pure and consistent endothelial populations. In contrast, CMECs do not exhibit this ambiguity and demonstrate more stable transcriptional alignment with classical endothelial markers, positioning them as a barrier with potentially more canonically endothelial characteristics (Weksler et al., 2013). The iPSC line investigated in the current study was shown to express EpCAM, aligning with the protein's role in pluripotency (Lu et al., 2010). As such, it is possible that the EpCAM expression observed in iBMECs represents residual expression from this previous cell-identity, and that EpCAM protein is in the process of being downregulated. Delayed downregulation of EpCAM has been described in human embryonic stem cell-derived embryoid bodies, where OCT3/4 expression was significantly reduced after 1 week, while EpCAM protein was still present after 3 weeks of culturing (Ng et al., 2010). These results highlight the importance of taking into consideration cell maturity and culture timing when using immunofluorescence to determine cell identity. Given that protocols based on the initial iBMEC derivation method from Lippmann et al. (2012b), suggest assaying the cells only 48 hours after barrier induction, the functional impact of observing cells in identity flux may be underappreciated (Lippmann et al., 2014a, Stebbins et al., 2016, Neal et al., 2019). Although monocultured iBMECs at this stage do have *in vivo*-like characteristics, co-culture with pericytes/astrocytes, and inter-donor differences has been shown to modulate native expression profiles and functional barrier properties, suggesting that further investigation into iBMEC maturation under co-culture conditions may be warranted (Patel et al., 2017).

In the case of the iPSC-derived pericytes, immunocytochemistry confirmed that the expression of cell type markers was comparable between the iPSC-derived and immortalised cells, however iPericytes were noticeably larger then HBVPs. This discrepancy in size between these two cell types is not observable in recent literature (King et al., 2024), however differences in confluency at the time of imaging may explain part of the difference. iPericytes did, however, display the wide range of morphological categories that have been reported (Brown et al., 2023).

3.3.2. 2D iPSC-derived neurovascular cell function

Neither iBMECs nor iPericytes displayed significant viability changes following treatment with $A\beta_{42:40}$, ecLPS or pgLPS, indicating the robustness of these cell types *in vitro*, and that subsequent treatment results are not confounded by cell death.

While IL-6 release was undetectable in iBMECs under all conditions, iPericytes secreted low levels of IL-6 irrespective of treatment. The lack of treatment-induced IL-6 response in these cells is intriguing, as there is considerable literature reporting IL-6 release after ecLPS treatment in primary human pericytes, primary human endothelial cells and immortalised human endothelial cells (Johnson et al., 2018, Smyth et al., 2018, Gaceb et al., 2017), although data on iPSC-derived pericytes is lacking. Because our results do not replicate the IL-6 secretion of other ecLPS-treated endothelia and pericytes, it may be possible that pgLPS and Aβ can also elicit pro-inflammatory cytokine release, when applied in a different context. For example, alternative inflammatory mediators, such as IFNγ or IL-1β, may be necessary to observe the IL-6 upregulations seen in other studies. Indeed Smyth et al. (2018) reported that IL-1β elicited considerably larger cytokine responses in both pericytes and endothelia. Regardless, basal IL-6 secretion by iPericytes highlights their active role in vascular inflammation, consistent with other literature (Szepes et al., 2020, Peltonen et al., 2024). Nevertheless, the nature and degree of LPS-induced neurovascular inflammatory responses in the human *in vivo* context is unclear, so the results of the previous and current studies are best interpreted in tandem.

Treatment with $A\beta_{42:40}$ or LPS did not significantly alter iBMEC monolayer permeability to sodium fluorescein. This contrasts with *in vivo* findings where chronic inflammation and Aβ burden contribute to barrier disruption (Lai et al., 2021, Banks et al., 2015), and *in vitro* findings in CMEC monolayers where nanomolar Aβ application increased permeability and decreased Aβ transport (Qosa et al., 2014). Aβ-laden conditioned media from Swedish mutant iPSC-derived neurons induces

HBMEC activation and increased permeability, an effect that is blocked by genetically inhibiting Aβ production in the neurons (Shin et al., 2023). In tandem with our results, this suggests there may be other elements that work alongside Aβ to modulate endothelial permeability. The lack of permeability changes in this model could reflect the limitations of static, 2D transwell systems, which lack the dynamic flow conditions that cause shear stress and elicit other physicochemical properties *in vivo*. Additionally, the acute treatment timeframe may have been insufficient to induce structural damage to the endothelial layer, emphasizing the need for prolonged or repeated exposures to better mimic chronic disease processes.

In our 2D iBMECs, we observed a measurable $A\beta_{42:40}$ deposition after 24 h application, that was significantly higher compared to control wells with fibronectin/collagen-coated surfaces. This finding underscoring the selective retention of Aβ by endothelial cells is particularly relevant to cerebral amyloid angiopathy, where vascular Aβ accumulation contributes to endothelial dysfunction and local inflammation. The mechanistic involvement of surface receptors such as RAGE and LRP1, which facilitate *in vivo* Aβ uptake and transcytosis, could be investigated in the future to probe this phenotype and its relevance to human AD (Zhou et al., 2021).

These outcomes reinforce the importance of studying neurovascular interactions in a cell-type-specific context. However, the inability of 2D systems to fully recapitulate dynamic neurovascular interactions necessitate the incorporation of 3D co-cultures and extended treatment paradigms that are explored future chapters. These refinements will provide a more comprehensive understanding of neurovascular contributions to AD and offer a foundation for therapeutic targeting of the BBB.

3.3.3. 2D iPSC-derived neurovascular secretomes

While primary/immortalised endothelial cells and pericytes (like CMECs and HBVPs) have been well-studied using broad-spectrum protein arrays, iBMECs have only been investigated under significantly different conditions (i.e. different derivation method, culture media, iPSC properties and lack of comparison to basal media), and iPericytes have not been tested (Kurmann et al., 2021, Smyth et al., 2018, Rieker et al., 2019), so we measured the basal secretomes of these cells to understand their function in unstimulated conditions.

3.3.3.1. *Basal iBMEC secretions*

Under basal conditions, iBMECs secreted 14 cytokines that were significantly different from the signal produced by media: EMMPRIN, GDF-15, IGFBP-2, IGFBP-3, MIF, MMP-9, osteopontin, cystatin C, FGF-b, FGF-19, IL-17A, MCP-1, PDGF-AA, and thrombospondin-1. These cytokines are implicated in a wide array of functions including inflammation, angiogenesis, BBB maintenance and neurodegeneration. The activation of IGFBP-2 and IGFBP-3 in iBMECs suggests involvement of the insulin-like growth factor signalling pathway critical for endothelial cell survival and function, angiogenesis, and neurovascular integrity (Bonham et al., 2018, Das et al., 2013, Jan et al., 2006, Kim et al., 2016). This pathway can modulate vascular permeability and inflammation, both of which are crucial for BBB regulation and AD progression. Similarly, the secretion of MMP-9, osteopontin, and IL-17A and MIF, suggests the activation of MMP and pro-inflammatory pathways, which are essential for tissue remodelling, angiogenesis, and inflammation (Ringland et al., 2020, Nasiri et al., 2020, Ladwig et al., 2017). Elevated basal levels of MMP-9, osteopontin, cystatin C and IL-17A suggest that iBMECs may have a pro-inflammatory phenotype, possibly due to epigenetic or inflammatory priming that could produce heightened responses to pathogenic stimuli as seen in neurodegenerative diseases (Lauridsen et al., 2017, Li et al., 2023b). Further investigation into these basal cytokine levels could clarify whether iBMECs represent an early model of neurovascular dysfunction, reflecting disease-associated changes in endothelial cell behaviour before overt pathology.

Using the same array, Rieker et al. (2019) found 18 cytokines in the iBMEC-conditioned media Angiopoietin-2, bFGF, DKK-1, EGF, ENA-78, GDF-15, GRO-α, IFN-γ, IGFBP-2, IL-1α, IL-8, Kallikrein 3, MCP-1, Osteopontin, PDGF-AA, Pentraxin-3, Serpin E1 and Thrombospondin-1. Our iBMECs displayed an overlapping but distinct secretion profile, with six similarly expressed proteins (GDF-15, IGFBP-2, Osteopontin, MCP-1, PDGF-AA, and Thrombospondin-1) suggesting that iBMECs were comparable. This study utilised a different iteration of the iBMEC derivation protocol, and also used altered culturing conditions (VascuLife medium, low oxygen incubation and no collagen IV in well coatings). These experimental differences could explain the disparate secretion profiles, along with the genetic variation involved in using separate iPSC donor sources.

In another study, secretions from primary human endothelial cells were indexed (Smyth et al., 2018). This study did not look at the difference between cell conditioned media and unconditioned media, but if we look at the raw data and apply our 10% max cut off we see that their endothelial cells also produced six similar proteins: IGFBP-3, IGFBP-2, PDGF-AA, MCP-1, Osteopontin, MMP-9, suggesting that our iBMECs have a secretion signature similar to both primary BMECs, and other iBMECs published in the literature, providing converging evidence of their basal role in inflammation, angiogenesis, and extracellular matrix regulation (Smyth et al., 2018).

3.3.3.2. Treated iBMEC secretions

In contrast to the basal state, treatment with inflammatory stimuli (ecLPS and pgLPS) or $A\beta_{42:40}$ did not significantly alter cytokine secretion in iBMECs except for in the case of Lipocalin-2 reduction in ecLPS treated media. This lack of response is curious, considering the expansive secretion profiles of primary BMECs after inflammatory insult with LPS or IL-1β (Smyth et al., 2018).

Given that iBMECs are typically assessed immediately after derivation, within 48 hours of retinoic acid removal, their developmental maturity may limit their functional responsiveness. Insufficient TLR4 expression at this early stage could hinder their sensitivity to inflammatory stimuli, as suggested by Tsioti et al. (2023). It is possible that iBMECs require more complex cues or a prolonged exposure to inflammatory stimuli to mount a robust cytokine response. This finding may also suggest that while iBMECs exhibit baseline inflammatory and angiogenic signalling, their response to acute inflammatory triggers could be muted or delayed. One other potential limitation is that array sensitivity or cell number might not allow for the levels of secreted proteins to breach detection limit. Given the importance of iBMECs in neurovascular modelling of inflammatory disorders, future studies could explore modifying the timing of treatments, increased stimulus concentrations, co-administration with other inflammatory cues (such as IFN-γ) and co-culture with multiple neurovascular unit cell types.

Given the complexity of understanding vascular responses to various pathogenic stimuli, heat map like the one generated can provide a useful way to look at broad expression profiles. The treated iBMEC secretomes reveal distinct clustering patterns: Aβ and Aβ's vehicle condition group closely and are distinctly separated from basal, indicating that treatment with Aβ's weak ammonium hydroxide vehicle solution may exert vascular-specific effects. Moreover, ecLPS and pgLPS form a separate cluster, suggesting that their similar structural features elicit comparable mechanisms of relative protein release.

3.3.3.3. *Basal iPericyte secretions*

In iPericytes cultured under basal conditions, IGFBP-2, serpin E1, EMMPRIN, FGF-19, MIF, osteopontin, and PDGF-AA were significantly elevated when compared to Sciencell Pericyte Medium. These proteins are associated with numerous functions including cellular growth, differentiation, inflammation, extracellular matrix remodelling, tissue repair, and pericyte recruitment, all of which are critical for neurovascular unit stability and BBB maintenance (Allard and Duan, 2018, Bacher et al., 1998, Hasaneen et al., 2016, Karimi-Abdolrezaee et al., 2012, Li et al., 2016, Morita et al., 2019, Wang et al., 1998). Notably, IGFBP-2, EMMPRIN, FGF-19, MIF, osteopontin, and PDGF-AA are all expressed in both iPericytes and iBMECs, highlighting the critical role of crosstalk between these two cell types within defined signalling streams.

In Smyth et al. (2018), conditioned media from basal HBVPs were observed to similarly express both IGFBP-2 and MCP-1, while also secreting CD40 Ligand, IL-11, MMP-9, Kallikrein 3, TFF3, IL-12 p70, Angiogenin, Complement Factor D, IL-19, and SDF-1α. Our iPericytes have an overlapping expression of IGFBP-2 and MCP-1 that provides evidence of stable, pericyte-relevant functional cascades relating to angiogenic regulation, extracellular matrix remodelling, and inflammatory signalling (Rensink et al., 2004, Jansson et al., 2014). Contrastingly, the diversity of differences in protein secretion highlight the importance of cellular context in determining the *in vitro* expression of *in vivo* physiology, with differences in differentiation protocols, culture conditions, and cell sources contributing to variations in pericyte behaviour. Human *in vivo* pericyte secretomes are influenced by microenvironmental factors such as regional specialization, vascular niche, and disease state, and it is too early to determine which of these models more accurately reflects human pericyte physiology in neurovascular contexts.

3.3.3.4. *Treated iPericyte secretions*

iPericytes treated with ecLPS, pgLPS or Aβ$_{42:40}$ did not significantly alter cytokine secretion. This is interesting given their well-documented role as immune mediators at the neurovascular interface, and the reported cytokine secretions in response to ecLPS (Smyth et al., 2018, Torok et al., 2021). LPS-treated HBVPs in Smyth (2018) showed increases in ICAM-1, VCAM-1, CX3CL1, IL-6, IL-8, IP-10, MCP-1, and RANTES measured by a cytometric bead array. The absence of similar inflammatory response may represent an intrinsic difference in the iPSC-derived pericytes compared to their primary counterparts. There were, however, trends toward EGF decreases in both ecLPS- and pgLPS-treated iPericytes. EGF is a crucial anti-inflammatory mediator with roles in cellular proliferation, migration, and wound healing in the neurovascular unit (Schreier et al., 2014). EGF can supress heightened inflammatory and vasculogenic signals in neurovascular models, so it's downregulation in our iPericytes could suggest diminished capacity to counteract inflammatory cascades triggered by LPS exposure (Lee et al., 2024).

Similarly to iBMECs, iPericytes may require different or more prolonged exposure to inflammatory stimuli to elicit a significant cytokine response in our system. Previous research has indicated that pericytes might exhibit greater resistance to acute inflammatory changes compared to endothelial cells (Smyth et al., 2018). This suggests that, while iPericytes display baseline levels of inflammatory and angiogenic activity, their response to insult may require the presence of other environmental factors, necessitating experimental adjustments to observe these phenotypes *in vitro*.

Heatmap analysis of the secretions from treated iPericyte media revealed an unexpected broad cytokine elevation from the condition treated with 0.5% ammonium hydroxide (the vehicle used to dissolve Aβ). This anomaly warrants further investigation into potential underlying factors influencing baseline secretion levels with weak ammonium hydroxide vehicles. Additionally, ecLPS-induced conditioned media clustered further from the basal iPericyte secretion profile compared to pgLPS, suggesting that ecLPS may induce a more pronounced alteration in the pericyte secretome, potentially reflecting a stronger inflammatory response or a distinct activation pathway, emphasising the complexity of pericyte-mediated responses to inflammatory stimuli.

3.3.4. CRISPR/Cas9 gene editing

In the final part of this chapter, we aimed to generate isogenic iPSC lines with homozygous *APOE* ε3 to ε4, or ε4 to ε3 switched genotypes. While some attempts to create such isogenic lines have been published (Muñoz et al., 2021, Blanchard et al., 2020, Budny et al., 2024, Lin et al., 2018b), isogenic *APOE* cell lines are of limited commercial availability. It is critical to develop larger libraries of genetically diverse iPSC lines in order to improve understanding of *APOE* mutation effects due to the large variability inherent with iPSC lines due to differences in donor genetics, reprogramming methods, culturing techniques. Little is known about the influence of *APOE* status on endothelial and pericyte phenotypes and generation of these cells would have provided tools to explore this.

We aimed to use lentivirally-introduced CRISPR, with gRNA and ssODN templates carefully optimized for targeted integration and high HDR efficiency. Electroporation is the preferred transfection methodology in iPSCs, however a phenomenon called arcing (where high sample conductivity disrupts the voltage separation) can decrease cell viability (Xu et al., 2018). Although experiments were designed to avoid this by managing salt concentration and conductivity of solutions, arcing was observed in some instances. This may have affected cell viability or the opening of membrane pores during the electroporation process, causing poor uptake of the vector.

Successfully creating CRISPR knock-in iPSC lines is made challenging due to the poor transduction efficiency of iPSCs, intrinsically low efficiency of HDR, and sensitive growth conditions of low-confluency iPSCs (Navarro-Guerrero et al., 2021, Xu et al., 2019). In addition to the aforementioned considerations there are a number of novel methods being developed to improve HDR efficiency in iPSCs (Shahryari et al., 2021, Patel et al., 2022, Zhang et al., 2021, Fu et al., 2022). Tethering the repair-template to the Cas9 nuclease has been shown to increase efficiency by increasing spatial availability of the template (Aird et al., 2018). Cold shocking cells after transfection (Guo et al., 2018), and exogenously inhibiting NHEJ are other methods to optimise HDR efficiency (Maruyama et al., 2015).

3.3.5. Chapter Summary

In this chapter we validated iPSC-derived vascular cells, showing that iBMECs expressed common endothelial markers PECAM-1, VE cadherin and occludin, and displayed enhanced barrier properties when compared to HUVEC and CMEC lines, with higher TEER values and lower permeability. iPericytes expressed markers, PDGFRβ, NG2, CD13, indicative of pericyte identity. iBMECs were also shown to harbour measurable Aβ deposits when treated with monomer preparations of $A\beta_{42}$ and $A\beta_{40}$.

Cytokine arrays revealed that iBMECs and iPericytes exhibit distinct basal cytokine secretion profiles that align with those reported in the literature. iBMECs produced protein secretion profiles underscoring their role in barrier integrity, matrix remodelling, inflammation and angiogenesis. iPericytes also exhibited a cytokine profile consistent with their role in stabilizing endothelial cells and regulating BBB integrity. Notably, neither iBMECs nor iPericytes demonstrated significant cytokine alterations in response to acute stimulation with Aβ or inflammatory lipopolysaccharides, suggesting that these cells may require chronic or multi-faceted stimuli to mimic the complex inflammatory environment seen in AD. However, the diverse basal secretion of functional cytokines suggests constitutive activity of vascular pathways.

The chapter's findings suggest noteworthy cell-autonomous features in iPSC-derived vascular cells, but the extent to which these *in vitro* functional and secretory phenotypes relate to human neurodegenerative symptoms and mechanisms requires further validation in more complex models. Generating more biomimetic *in vitro* culture systems to replicate and further develop these findings is a critical next step toward improving their physiological relevance and translational potential.

Supplementary Figure 3.13: Blot membranes from iBMECs and iPericytes at low exposure (1 s) and high exposure (10 s). Two exposure times were performed to determine relative expression of proteins with high and low abundance. Magenta crosses denote data points that were not analysed due to overexposure in at least one membrane). Cytokine intensities were measured in duplicate, from n = 3 experiments.

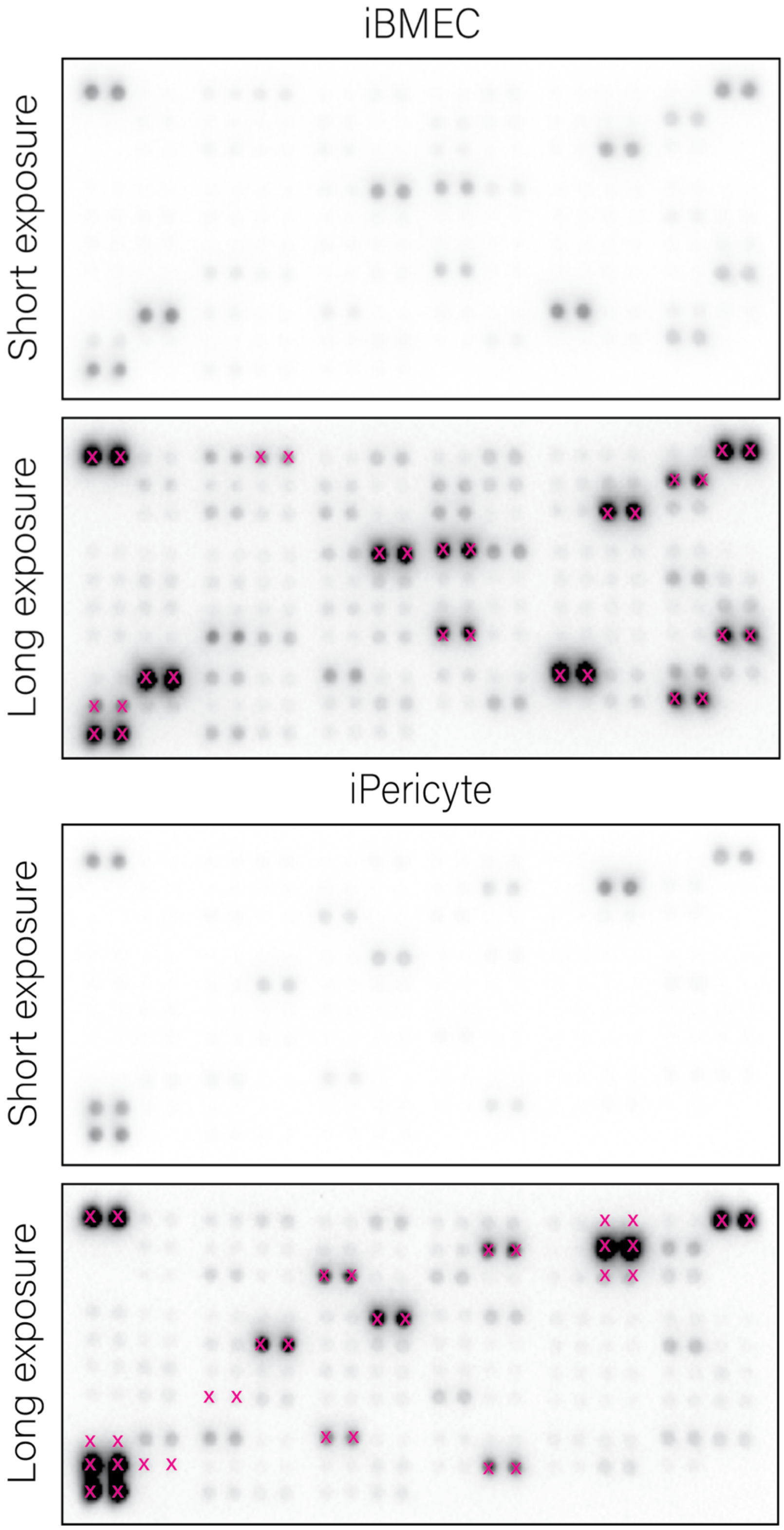

Supplementary Table 3.2: iBMEC-secreted cytokine data measured using the proteome profiler array. For statistical testing, a two-way ANOVA with a two-stage linear step-up procedure of Benjamini, Krieger and Yekutielie was used to control the false-discovery rate, with Q < 0.05. Cytokines with mean pixel density under 10 % of the maximum were not included in the statistical analysis. See Abbreviations (page viii) for full list of cytokine names.

iBMEC Differences (sorted by p value)

Short Exposure

MEDIA - BASAL				
Cytokine	Mean Diff.	Discovery?	q value	Individual P Value
GDF-15 9518	-6746	Yes	<0.0001	<0.0001
IGFBP-2 3485	-10507	Yes	<0.0001	<0.0001
IGFBP-3 3486	-9807	Yes	<0.0001	<0.0001
MMP-9 4318	-7423	Yes	<0.0001	<0.0001
Osteopontin 6696	-16000	Yes	<0.0001	<0.0001
EMMPRIN 682	-4125	Yes	0.0033	0.0032
MIF 4282	-3426	Yes	0.0118	0.0131
VEGF 7422	-2430	No	0.0525	0.0739
Angiogenin 283	-2421	No	0.0525	0.0751
Serpin E1 5054	-2206	No	0.0655	0.1039
SHBG 6462	-1122	No	0.2312	0.4037
RBP-4 5950	-256.7	No	0.4452	0.848
Lipocalin-2 3934	-136.7	No	0.4452	0.9187

BASAL - LPS				
Cytokine	Mean Diff.	Discovery?	q value	Individual P Value
Osteopontin 6696	3016	No	0.9944	0.1161
RBP-4 5950	1963	No	0.9944	0.303
IGFBP-3 3486	1628	No	0.9944	0.3922
IGFBP-2 3485	999	No	0.9944	0.5988
Angiogenin 283	-727.7	No	0.9944	0.7013
GDF-15 9518	618.3	No	0.9944	0.7445
Serpin E1 5054	-609.3	No	0.9944	0.7481
Lipocalin-2 3934	-582	No	0.9944	0.759
EMMPRIN 682	538	No	0.9944	0.7767
MMP-9 4318	434	No	0.9944	0.819
SHBG 6462	-295.7	No	0.9944	0.8761
MIF 4282	-262.7	No	0.9944	0.8898
VEGF 7422	-125.9	No	0.9944	0.947

BASAL - pgLPS				
Cytokine	Mean Diff.	Discovery?	q value	Individual P Value
Osteopontin 6696	2799	No	>0.9999	0.1431
IGFBP-2 3485	1674	No	>0.9999	0.3779
VEGF 7422	1107	No	>0.9999	0.5591
Angiogenin 283	-832	No	>0.9999	0.6604
GDF-15 9518	781	No	>0.9999	0.68
MIF 4282	-533.3	No	>0.9999	0.7781
IGFBP-3 3486	424.7	No	>0.9999	0.8224
Serpin E1 5054	-418.3	No	>0.9999	0.825
EMMPRIN 682	375.3	No	>0.9999	0.8428
Lipocalin-2 3934	-306	No	>0.9999	0.8715
RBP-4 5950	-281	No	>0.9999	0.8819
SHBG 6462	-175.3	No	>0.9999	0.9262
MMP-9 4318	87.67	No	>0.9999	0.963

BASAL - VEHICLE (AB)				
Cytokine	Mean Diff.	Discovery?	q value	Individual P Value
RBP-4 5950	4793	No	0.2404	0.0176
IGFBP-2 3485	1392	No	>0.9999	0.4797
MIF 4282	-1131	No	>0.9999	0.5653
MMP-9 4318	794	No	>0.9999	0.6863
Angiogenin 283	659.9	No	>0.9999	0.7371
VEGF 7422	-494.2	No	>0.9999	0.8014
Serpin E1 5054	-392.7	No	>0.9999	0.8416
Osteopontin 6696	-318.7	No	>0.9999	0.8711
EMMPRIN 682	268.3	No	>0.9999	0.8914
SHBG 6462	-260.3	No	>0.9999	0.8946
GDF-15 9518	-243	No	>0.9999	0.9016
IGFBP-3 3486	161.3	No	>0.9999	0.9345
Lipocalin-2 3934	78.33	No	>0.9999	0.9682

VEHICLE (AB) - AB				
Cytokine	Mean Diff.	Discovery?	q value	Individual P Value
Osteopontin 6696	2378	No	>0.9999	0.2853
IGFBP-3 3486	2124	No	>0.9999	0.3394
MIF 4282	1248	No	>0.9999	0.5736
RBP-4 5950	691	No	>0.9999	0.755
EMMPRIN 682	644.7	No	>0.9999	0.771
Angiogenin 283	-634.2	No	>0.9999	0.7746
Serpin E1 5054	580	No	>0.9999	0.7934
VEGF 7422	326.5	No	>0.9999	0.8828
MMP-9 4318	306	No	>0.9999	0.8901
IGFBP-2 3485	174.3	No	>0.9999	0.9372
Lipocalin-2 3934	-63	No	>0.9999	0.9773
SHBG 6462	57	No	>0.9999	0.9795
GDF-15 9518	-20	No	>0.9999	0.9928

Long Exposure

MEDIA - BASAL				
Cytokine	Mean Diff.	Discovery?	q value	Individual P Value
Cystatin C 1471	-6472	Yes	<0.0001	<0.0001
FGF basic 2247	-4454	Yes	<0.0001	<0.0001
FGF-19 9965	-5167	Yes	<0.0001	<0.0001
IL-17A 3605	-4819	Yes	<0.0001	<0.0001
MCP-1 6347	-7617	Yes	<0.0001	<0.0001
PDGF-AA 5154	-7901	Yes	<0.0001	<0.0001
Pentraxin 3 5806	-5512	Yes	<0.0001	<0.0001
Thrombospondin-1 7057	-8069	Yes	<0.0001	<0.0001
Resistin 56729	-3118	Yes	0.0078	0.0011
CD30 943	-2131	No	0.145	0.0244
RANTES 6352	-2116	No	0.145	0.0255
LIF 3976	-2110	No	0.145	0.0259
FGF-7 2252	-2068	No	0.1498	0.029
PDGF-AB/BB 5154/5155	-1606	No	0.4292	0.0894
Dkk-1 22943	-1542	No	0.4603	0.1028
SDF-1α 6387	-1507	No	0.4655	0.1108
M-CSF 1435	-1464	No	0.4794	0.1213
GM-CSF 1437	-1381	No	0.5363	0.1437
BDNF 627	-1338	No	0.5542	0.1567
C-Reactive Protein 1401	-1267	No	0.6038	0.1797
Vitamin D BP 2638	-1161	No	0.7006	0.2189
IL-2 3558	-1109	No	0.706	0.2401
BAFF 10673	-1086	No	0.706	0.25
Apolipoprotein A-I 335	-1081	No	0.706	0.2521
ST2 9173	-1020	No	0.7116	0.28
IL-31 386653	-964.7	No	0.7116	0.3067
RAGE 177	-963	No	0.7116	0.3075
IL-18 Bpa 10068	-960.3	No	0.7116	0.3089
IL-22 50616	-945	No	0.7116	0.3166
Angiopoietin-2 285	-943	No	0.7116	0.3177
DPPIV 1803	-897.2	No	0.7407	0.3417
Cripto-1 6997	-820.5	No	0.8074	0.3845
IL-6 3569	-753	No	0.8231	0.4248
I-TAC 6373	-749.2	No	0.8231	0.4271
IFN-γ 3458	-746.7	No	0.8231	0.4287
Lipocalin-2 3934	-699	No	0.8327	0.4587
VCAM-1 7412	680	No	0.8327	0.471
uPAR 5329	-666.7	No	0.8327	0.4797
IL-24 11009	-661.3	No	0.8327	0.4832
Complement Factor D 1675	-612.3	No	0.8515	0.5162
Flt-3 Ligand 2323	-607.6	No	0.8515	0.5195
MIP-3α 6364	572.3	No	0.8571	0.544
IL-1α 3552	-561.3	No	0.8571	0.5517
TFF3 7033	-509.7	No	0.8571	0.5889
IL-34 146433	447.3	No	0.8571	0.6353
G-CSF 1440	-446.7	No	0.8571	0.6357
IL-10 3586	-435.7	No	0.8571	0.6441
MIG 4283	-431	No	0.8571	0.6477
IL-19 29949	-429.3	No	0.8571	0.6489
MIP-3β 6363	-388.8	No	0.8571	0.6802
TfR 7037	-358.3	No	0.8571	0.704
CD14 929	-351.9	No	0.8571	0.709
Endoglin 2022	346	No	0.8571	0.7137
Relaxin-2 6019	-327	No	0.8571	0.7288
MCP-3 6354	-326.3	No	0.8571	0.7293
CD31 5175	-313	No	0.8571	0.7399
IL-5 3567	-310.1	No	0.8571	0.7422
HGF 3082	-309	No	0.8571	0.7432
IL-4 3565	-262	No	0.8571	0.7811
IL-27 246778	-256	No	0.8571	0.786
IL-1ra 3557	-247.7	No	0.8571	0.7928
Fas Ligand 356	-228.3	No	0.8571	0.8087
IL-15 3600	203.7	No	0.8571	0.829
ICAM-1 3383	-195.3	No	0.8571	0.8359
IL-23 51561	-191.3	No	0.8571	0.8392
IL-16 3603	177	No	0.8571	0.8511
IP-10 3627	171	No	0.8571	0.8561
TGF-α 7039	-157.6	No	0.8571	0.8673
IL-1β 3553	113.3	No	0.88	0.9043
CD40 ligand 959	98.67	No	0.88	0.9167
IL-8 3576	-70.67	No	0.8894	0.9403
Chitinase 3-like 1 1116	55.67	No	0.8894	0.9529
Adiponectin 9370	-12	No	0.9112	0.9898

BASAL - LPS				
Cytokine	Mean Diff.	Discovery?	q value	Individual P Value
Lipocalin-2 3934	-4407	Yes	0.0272	0.0003
Pentraxin 3 5806	-2059	No	>0.9999	0.0918
BDNF 627	-1633	No	>0.9999	0.1809
Angiopoietin-2 285	-1366	No	>0.9999	0.2626
MCP-1 6347	-1353	No	>0.9999	0.2672
Apolipoprotein A-I 335	-1262	No	>0.9999	0.3006
Thrombospondin-1 7057	-1068	No	>0.9999	0.3809
IL-23 51561	-943	No	>0.9999	0.4392
TfR 7037	-891.7	No	>0.9999	0.4645
MIP-3α 6364	-887.3	No	>0.9999	0.4666
Angiopoietin-1 284	-833.7	No	>0.9999	0.494
M-CSF 1435	-811.7	No	>0.9999	0.5054
IFN-γ 3458	-807.3	No	>0.9999	0.5077
FGF basic 2247	-803.3	No	>0.9999	0.5098
Dkk-1 22943	-771.3	No	>0.9999	0.5268
SDF-1α 6387	-705	No	>0.9999	0.5629
TFF3 7033	-703	No	>0.9999	0.564
IL-1ra 3557	-699.7	No	>0.9999	0.5659
IL-31 386653	-698	No	>0.9999	0.5668
MIG 4283	-697.3	No	>0.9999	0.5672
IL-34 146433	-677.7	No	>0.9999	0.5782
RAGE 177	-654	No	>0.9999	0.5915
uPAR 5329	-653	No	>0.9999	0.5921
RANTES 6352	643	No	>0.9999	0.5978
IL-22 50616	-632.3	No	>0.9999	0.6038
IL-27 246778	-587.3	No	>0.9999	0.6298
VCAM-1 7412	-521.7	No	>0.9999	0.6686
IL-17A 3605	513.3	No	>0.9999	0.6736
I-TAC 6373	-503.3	No	>0.9999	0.6796
Cystatin C 1471	502.7	No	>0.9999	0.68
DPPIV 1803	490.7	No	>0.9999	0.6872
IL-24 11009	-485	No	>0.9999	0.6906
Complement Factor D 1675	-482.3	No	>0.9999	0.6922
PF4 5196	-480.3	No	>0.9999	0.6934
IL-5 3567	-475.3	No	>0.9999	0.6965
IL-10 3586	-470.7	No	>0.9999	0.6993
IL-16 3603	-460.7	No	>0.9999	0.7054
IL-33 90865	-453	No	>0.9999	0.7101
IL-1α 3552	-451.7	No	>0.9999	0.7109
ST2 9173	-437.3	No	>0.9999	0.7197
IL-18 Bpa 10068	-423	No	>0.9999	0.7285
MCP-3 6354	-406.3	No	>0.9999	0.7388
IL-1β 3553	-398	No	>0.9999	0.7439
C-Reactive Protein 1401	-381.3	No	>0.9999	0.7543
BAFF 10673	-362.3	No	>0.9999	0.7662
Vitamin D BP 2638	-361.3	No	>0.9999	0.7668
IL-6 3569	-350.3	No	>0.9999	0.7737
IL-15 3600	-347	No	>0.9999	0.7758
IP-10 3627	-345.3	No	>0.9999	0.7769
CD40 ligand 959	-341	No	>0.9999	0.7796
Fas Ligand 356	-306.3	No	>0.9999	0.8015
G-CSF 1440	302.3	No	>0.9999	0.804
GM-CSF 1437	-287.3	No	>0.9999	0.8136
IL-8 3576	-259.3	No	>0.9999	0.8314
FGF-19 9965	248.7	No	>0.9999	0.8383
FGF-7 2252	245.3	No	>0.9999	0.8404
CD30 943	244	No	>0.9999	0.8413
HGF 3082	-235.3	No	>0.9999	0.8468
IL-4 3565	-193.3	No	>0.9999	0.8739
TGF-α 7039	-186	No	>0.9999	0.8787
Resistin 56729	-164	No	>0.9999	0.8929
Chitinase 3-like 1 1116	-147.7	No	>0.9999	0.9035
CD14 929	-144	No	>0.9999	0.9059
Relaxin-2 6019	-140	No	>0.9999	0.9085
IL-2 3558	-125	No	>0.9999	0.9183
Flt-3 Ligand 2323	-93.33	No	>0.9999	0.9389
PDGF-AA 5154	-92	No	>0.9999	0.9398
IL-19 29949	-89.33	No	>0.9999	0.9416
PDGF-AB/BB 5154/5155	89.33	No	>0.9999	0.9416
ICAM-1 3383	-62.33	No	>0.9999	0.9592
CD31 5175	-59.33	No	>0.9999	0.9612
LIF 3976	56	No	>0.9999	0.9633
Endoglin 2022	43.67	No	>0.9999	0.9714
MIP-3β 6363	-24	No	>0.9999	0.9843
Adiponectin 9370	21	No	>0.9999	0.9862
Cripto-1 6997	-5.667	No	>0.9999	0.9963

BASAL - pgLPS				
Cytokine	Mean Diff.	Discovery?	q value	Individual P Value
Lipocalin-2 3934	-2249	No	>0.9999	0.0452
Apolipoprotein A-I 335	-1628	No	>0.9999	0.1466
Resistin 56729	1377	No	>0.9999	0.2191
SDF-1α 6387	-951	No	>0.9999	0.3958
IL-23 51561	-902	No	>0.9999	0.4206
Pentraxin 3 5806	-810	No	>0.9999	0.4695
IL-22 50616	-794	No	>0.9999	0.4783
CD30 943	776	No	>0.9999	0.4883
MIG 4283	-769.7	No	>0.9999	0.4919
IL-17A 3605	759.7	No	>0.9999	0.4975
Endoglin 2022	-756.3	No	>0.9999	0.4994
IL-34 146433	-724	No	>0.9999	0.5179
IL-1ra 3557	-683	No	>0.9999	0.5418
MIP-3α 6364	-673.7	No	>0.9999	0.5474
DPPIV 1803	653	No	>0.9999	0.5597
FGF basic 2247	-648.3	No	>0.9999	0.5625
RANTES 6352	639.7	No	>0.9999	0.5678
M-CSF 1435	-629	No	>0.9999	0.5742
Angiopoietin-2 285	-624.7	No	>0.9999	0.5769
Adiponectin 9370	-573.3	No	>0.9999	0.6086
IL-33 90865	-558.7	No	>0.9999	0.6178
IL-27 246778	-555.3	No	>0.9999	0.6199
Dkk-1 22943	-520.3	No	>0.9999	0.6421
CD40 ligand 959	-519.7	No	>0.9999	0.6425
FGF-19 9965	-510.3	No	>0.9999	0.6485
IL-31 386653	-508	No	>0.9999	0.65
IL-1β 3553	-504.7	No	>0.9999	0.6521
HGF 3082	-469	No	>0.9999	0.6753
IL-16 3603	-464.3	No	>0.9999	0.6783
Angiopoietin-1 284	-456	No	>0.9999	0.6838
GM-CSF 1437	-445.7	No	>0.9999	0.6905
TFF3 7033	-442.7	No	>0.9999	0.6925
IL-10 3586	-439.7	No	>0.9999	0.6945
Complement Factor D 1675	-436.7	No	>0.9999	0.6965
IL-24 11009	-406	No	>0.9999	0.7168
TfR 7037	-386.7	No	>0.9999	0.7298
IP-10 3627	-371.3	No	>0.9999	0.7401
IL-15 3600	-368.7	No	>0.9999	0.7419
Chitinase 3-like 1 1116	-361.7	No	>0.9999	0.7466
Fas Ligand 356	-361.3	No	>0.9999	0.7469
VCAM-1 7412	-354.3	No	>0.9999	0.7516
G-CSF 1440	338.7	No	>0.9999	0.7622
IFN-γ 3458	-336	No	>0.9999	0.7641
LIF 3976	-330.7	No	>0.9999	0.7677
FGF-7 2252	328	No	>0.9999	0.7695
PF4 5196	-320.7	No	>0.9999	0.7745
MCP-1 6347	-306.7	No	>0.9999	0.7841
PDGF-AB/BB 5154/5155	304.3	No	>0.9999	0.7857
IL-6 3569	-300.3	No	>0.9999	0.7885
IL-19 29949	-296.7	No	>0.9999	0.791
IL-1α 3552	-285	No	>0.9999	0.799
Flt-3 Ligand 2323	-284.3	No	>0.9999	0.7995
IL-4 3565	-281.7	No	>0.9999	0.8013
uPAR 5329	-280	No	>0.9999	0.8025
MCP-3 6354	-255	No	>0.9999	0.8198
IL-18 Bpa 10068	-245	No	>0.9999	0.8267
ST2 9173	-201	No	>0.9999	0.8575
C-Reactive Protein 1401	-181.7	No	>0.9999	0.8711
IL-5 3567	-181.3	No	>0.9999	0.8713
PDGF-AA 5154	179	No	>0.9999	0.8729
BAFF 10673	177	No	>0.9999	0.8744
MIP-3β 6363	167.3	No	>0.9999	0.8812
BDNF 627	156	No	>0.9999	0.8892
Cripto-1 6997	149.3	No	>0.9999	0.8939
TGF-α 7039	137.3	No	>0.9999	0.9023
CD31 5175	137.3	No	>0.9999	0.9023
ICAM-1 3383	-108.3	No	>0.9999	0.9229
Cystatin C 1471	100.3	No	>0.9999	0.9286
I-TAC 6373	-99.67	No	>0.9999	0.929
RAGE 177	-95.33	No	>0.9999	0.9321
Thrombospondin-1 7057	-94.33	No	>0.9999	0.9328
Relaxin-2 6019	51.33	No	>0.9999	0.9634
Vitamin D BP 2638	30	No	>0.9999	0.9786
IL-2 3558	16.67	No	>0.9999	0.9881
IL-8 3576	13.33	No	>0.9999	0.9905
CD14 929	8.533	No	>0.9999	0.9939

BASAL - VEHICLE (AB)				
Cytokine	Mean Diff.	Discovery?	q value	Individual P Value
IL-17A 3605	2558	No	>0.9999	0.0451
Cystatin C 1471	2116	No	>0.9999	0.0972
MCP-1 6347	1766	No	>0.9999	0.166
TfR 7037	-1371	No	>0.9999	0.2819
Pentraxin 3 5806	-1347	No	>0.9999	0.2902
RANTES 6352	1325	No	>0.9999	0.2982
BDNF 627	-1295	No	>0.9999	0.3093
CD30 943	-1231	No	>0.9999	0.3338
SDF-1α 6387	-1154	No	>0.9999	0.3649
IL-1α 3552	-985.3	No	>0.9999	0.439
TFF3 7033	-830	No	>0.9999	0.5144
Endoglin 2022	-821.7	No	>0.9999	0.5187
Apolipoprotein A-I 335	-782.7	No	>0.9999	0.5387
Angiopoietin-2 285	-772	No	>0.9999	0.5443
VCAM-1 7412	-759.7	No	>0.9999	0.5507
M-CSF 1435	-688	No	>0.9999	0.5889
PDGF-AA 5154	670	No	>0.9999	0.5987
Resistin 56729	-624	No	>0.9999	0.624
IL-1ra 3557	-622	No	>0.9999	0.6251
FGF-19 9965	554	No	>0.9999	0.6634
IFN-γ 3458	-549.3	No	>0.9999	0.6661
IL-5 3567	-529.3	No	>0.9999	0.6775
Thrombospondin-1 7057	508.7	No	>0.9999	0.6894
Vitamin D BP 2638	-491	No	>0.9999	0.6997
IL-2 3558	476.3	No	>0.9999	0.7082
Fas Ligand 356	-467	No	>0.9999	0.7137
IL-33 90865	-447.7	No	>0.9999	0.7251
MIG 4283	-431.3	No	>0.9999	0.7347
PF4 5196	-412.3	No	>0.9999	0.746
MIP-3α 6364	-405.4	No	>0.9999	0.7501
Lipocalin-2 3934	394.3	No	>0.9999	0.7567
IL-16 3603	-388.3	No	>0.9999	0.7603
IL-13 3596	-382	No	>0.9999	0.7641
Adiponectin 9370	-363.7	No	>0.9999	0.7751
LIF 3976	-358	No	>0.9999	0.7785
Cripto-1 6997	341.5	No	>0.9999	0.7884
IL-31 386653	-315	No	>0.9999	0.8045
IL-22 50616	-291	No	>0.9999	0.8192
ST2 9173	-290.7	No	>0.9999	0.8194
IL-4 3565	-280.7	No	>0.9999	0.8255
Chitinase 3-like 1 1116	-275	No	>0.9999	0.8289
DPPIV 1803	274.3	No	>0.9999	0.8293
FGF basic 2247	-267.7	No	>0.9999	0.8334
uPAR 5329	-256.3	No	>0.9999	0.8404
TARC 6361	-255.7	No	>0.9999	0.8408
FGF-7 2252	255	No	>0.9999	0.8412
RAGE 177	-254.3	No	>0.9999	0.8416
ICAM-1 3383	246.5	No	>0.9999	0.8465
CD14 929	-243.3	No	>0.9999	0.8484
IL-19 29949	-241	No	>0.9999	0.8498
IL-1β 3553	-201.1	No	>0.9999	0.8745
IP-10 3627	-200.9	No	>0.9999	0.8746
PDGF-AB/BB 5154/5155	200	No	>0.9999	0.8751
IL-27 246778	-199.3	No	>0.9999	0.8755
TIM-3 84868	-190	No	>0.9999	0.8813
CD40 ligand 959	-177.3	No	>0.9999	0.8892
Angiopoietin-1 284	-168.3	No	>0.9999	0.8948
IL-23 51561	-163.3	No	>0.9999	0.8979
IL-34 146433	-156.1	No	>0.9999	0.9024
IL-18 Bpa 10068	-150	No	>0.9999	0.9062
IL-8 3576	137.7	No	>0.9999	0.9139
GM-CSF 1437	-133.7	No	>0.9999	0.9164
IL-10 3586	128	No	>0.9999	0.9199
G-CSF 1440	123.7	No	>0.9999	0.9226
MCP-3 6354	-122.7	No	>0.9999	0.9232
TGF-α 7039	-119.7	No	>0.9999	0.9251
HGF 3082	117.4	No	>0.9999	0.9265
IL-15 3600	-117.2	No	>0.9999	0.9267
Flt-3 Ligand 2323	-80.47	No	>0.9999	0.9496
Row 7	-79	No	>0.9999	0.9505
BAFF 10673	-75.33	No	>0.9999	0.9528
C-Reactive Protein 1401	72.33	No	>0.9999	0.9547
CD31 5175	67.67	No	>0.9999	0.9576
Relaxin-2 6019	-65.67	No	>0.9999	0.9589
Dkk-1 22943	64	No	>0.9999	0.9599
MIP-3β 6363	50.33	No	>0.9999	0.9685
IL-24 11009	46	No	>0.9999	0.9712
IL-6 3569	-42	No	>0.9999	0.9737
I-TAC 6373	-33.33	No	>0.9999	0.9791
Complement Factor D 1675	-9.333	No	>0.9999	0.9941
ENA-78 6374	3.267	No	>0.9999	0.998

VEHICLE (AB) - AB				
Cytokine	Mean Diff.	Discovery?	q value	Individual P Value
Resistin 56729	2308	No	>0.9999	0.0661
MCP-1 6347	-1846	No	>0.9999	0.1411
Vitamin D BP 2638	1779	No	>0.9999	0.1562
SDF-1α 6387	1727	No	>0.9999	0.1685
CD30 943	1635	No	>0.9999	0.1924
Cystatin C 1471	-1541	No	>0.9999	0.2191
Pentraxin 3 5806	1449	No	>0.9999	0.2479
FGF-19 9965	1333	No	>0.9999	0.2876
Apolipoprotein A-I 335	1267	No	>0.9999	0.3121
GM-CSF 1437	1262	No	>0.9999	0.3139
FGF basic 2247	1224	No	>0.9999	0.3287
PDGF-AA 5154	-1201	No	>0.9999	0.338
Thrombospondin-1 7057	1136	No	>0.9999	0.3646
Dkk-1 22943	-998.7	No	>0.9999	0.4255
BDNF 627	969.3	No	>0.9999	0.4392
uPAR 5329	874.7	No	>0.9999	0.4851
TfR 7037	837.3	No	>0.9999	0.504
RANTES 6352	820	No	>0.9999	0.5128
Endoglin 2022	805.3	No	>0.9999	0.5204
MIG 4283	783.7	No	>0.9999	0.5317
IL-22 50616	766	No	>0.9999	0.5409
IL-17A 3605	729	No	>0.9999	0.5607
LIF 3976	699	No	>0.9999	0.5769
CD40 ligand 959	684.7	No	>0.9999	0.5847
IL-1α 3552	663.7	No	>0.9999	0.5963
IL-18 Bpa 10068	634.7	No	>0.9999	0.6124
PDGF-AB/BB 5154/5155	577	No	>0.9999	0.6451
M-CSF 1435	576.3	No	>0.9999	0.6455
MIP-3α 6364	552	No	>0.9999	0.6595
CD31 5175	528.7	No	>0.9999	0.673
IL-19 29949	508.3	No	>0.9999	0.6849
IL-33 90865	500.7	No	>0.9999	0.6894
IP-10 3627	491.3	No	>0.9999	0.6949
Adiponectin 9370	485	No	>0.9999	0.6986
PF4 5196	434.7	No	>0.9999	0.7286
IL-27 246778	422.7	No	>0.9999	0.7358
IL-6 3569	405.3	No	>0.9999	0.7463
IL-16 3603	401	No	>0.9999	0.7489
Relaxin-2 6019	379	No	>0.9999	0.7622
MCP-3 6354	371.7	No	>0.9999	0.7667
IL-1ra 3557	370.3	No	>0.9999	0.7675
IL-15 3600	367.8	No	>0.9999	0.769
I-TAC 6373	366.7	No	>0.9999	0.7697
C-Reactive Protein 1401	365.7	No	>0.9999	0.7703
ST2 9173	343	No	>0.9999	0.7842
IL-1β 3553	333.7	No	>0.9999	0.7899
FGF-7 2252	317.7	No	>0.9999	0.7998
IL-34 146433	308.1	No	>0.9999	0.8057
TARC 6361	306.7	No	>0.9999	0.8066
IL-31 386653	298.7	No	>0.9999	0.8115
IL-4 3565	294.7	No	>0.9999	0.814
TFF3 7033	289.7	No	>0.9999	0.8171
Lipocalin-2 3934	-281	No	>0.9999	0.8225
Fas Ligand 356	277.7	No	>0.9999	0.8246
IL-13 3596	276.6	No	>0.9999	0.8252
MIP-3β 6363	260.7	No	>0.9999	0.8351
IL-8 3576	227.1	No	>0.9999	0.8561
DPPIV 1803	-215.7	No	>0.9999	0.8633
IL-5 3567	213.7	No	>0.9999	0.8646
Row 7	-206.3	No	>0.9999	0.8692
ENA-78 6374	196.6	No	>0.9999	0.8753
Angiopoietin-2 285	-160.7	No	>0.9999	0.8979
G-CSF 1440	-143	No	>0.9999	0.9091
IL-2 3558	135.7	No	>0.9999	0.9137
Cripto-1 6997	-122.2	No	>0.9999	0.9223
CD14 929	-113	No	>0.9999	0.9281
BAFF 10673	110	No	>0.9999	0.93
RAGE 177	109.7	No	>0.9999	0.9302
IFN-γ 3458	109	No	>0.9999	0.9307
IL-24 11009	100.7	No	>0.9999	0.9359
ICAM-1 3383	94.87	No	>0.9999	0.9396
IL-23 51561	93.67	No	>0.9999	0.9404
VCAM-1 7412	92	No	>0.9999	0.9414
Angiopoietin-1 284	-91	No	>0.9999	0.9421
Flt-3 Ligand 2323	67.47	No	>0.9999	0.957
HGF 3082	60.63	No	>0.9999	0.9614
TIM-3 84868	57.33	No	>0.9999	0.9635
Chitinase 3-like 1 1116	33.33	No	>0.9999	0.9788
TGF-α 7039	31	No	>0.9999	0.9803
IL-10 3586	-26.33	No	>0.9999	0.9832
Complement Factor D 1675	-10.33	No	>0.9999	0.9934

Supplementary Table 3.3: iPericyte-secreted cytokine data measured using the proteome profiler array. For statistical testing, a two-way ANOVA with a two-stage linear step-up procedure of Benjamini, Krieger and Yekutielie was used to control the false-discovery rate, with Q < 0.05. Cytokines with mean pixel density under 10 % of the maximum were not included in the statistical analysis. See Abbreviations (page viii) for full list of cytokine names.

iPericyte Differences (sorted by p value)

Short Exposure

MEDIA - BASAL				
Cytokine	Mean Diff.	Discovery?	q value	Individual P Value
Serpin E1 5054	-10229	Yes	<0.0001	<0.0001
IGFBP-2 3485	-4906	Yes	0.0071	0.0015
IL-8 3576	-2841	No	0.134	0.0563
Dkk-1 22943	-2835	No	0.134	0.0567
Thrombospondin-1 7057	-2210	No	0.2537	0.1343
Pentraxin 3 5806	-1616	No	0.4262	0.2706
Myeloperoxidase 4353	-1120	No	0.5991	0.4438
FGF basic 2247	-787.3	No	0.6937	0.5896
EGF 1950	-567.7	No	0.6937	0.6971
GDF-15 9518	-495.2	No	0.6937	0.7341
CD14 929	-62.1	No	0.8299	0.966

BASAL - LPS				
Cytokine	Mean Diff.	Discovery?	q value	Individual P Value
EGF 1950	-3954	No	0.2131	0.0184
Serpin E1 5054	-3301	No	0.2718	0.0471
IL-8 3576	-1165	No	>0.9999	0.4746
IGFBP-2 3485	-720.3	No	>0.9999	0.6579
CD14 929	-719	No	>0.9999	0.6585
GDF-15 9518	-580.7	No	>0.9999	0.721
Pentraxin 3 5806	-164	No	>0.9999	0.9196
FGF basic 2247	149	No	>0.9999	0.9269
Myeloperoxidase 4353	-135.1	No	>0.9999	0.9337
Thrombospondin-1 7057	-110.3	No	>0.9999	0.9459
Dkk-1 22943	22	No	>0.9999	0.9892

BASAL - pgLPS				
Cytokine	Mean Diff.	Discovery?	q value	Individual P Value
EGF 1950	-2884	No	0.5204	0.0451
IGFBP-2 3485	-399.7	No	>0.9999	0.7763
IL-8 3576	-237.3	No	>0.9999	0.866
Serpin E1 5054	175.3	No	>0.9999	0.9008
Myeloperoxidase 4353	135	No	>0.9999	0.9235
CD14 929	106	No	>0.9999	0.9399
GDF-15 9518	97.67	No	>0.9999	0.9446
FGF basic 2247	-86.67	No	>0.9999	0.9509
Pentraxin 3 5806	-82.33	No	>0.9999	0.9533
Thrombospondin-1 7057	37.67	No	>0.9999	0.9786
Dkk-1 22943	-29	No	>0.9999	0.9835

BASAL - VEHICLE (AB)				
Cytokine	Mean Diff.	Discovery?	q value	Individual P Value
Serpin E1 5054	-3821	No	0.1747	0.0151
EGF 1950	-1299	No	0.9572	0.3949
Thrombospondin-1 7057	-1184	No	0.9572	0.4376
IL-8 3576	-704	No	0.9572	0.6437
IGFBP-2 3485	-587	No	0.9572	0.6996
FGF basic 2247	-537	No	0.9572	0.7241
Pentraxin 3 5806	-486.7	No	0.9572	0.749
Dkk-1 22943	-338	No	0.9572	0.8241
Myeloperoxidase 4353	-193.1	No	0.9572	0.8989
GDF-15 9518	-171.3	No	0.9572	0.9103
CD14 929	168.7	No	0.9572	0.9116

VEHICLE (AB) - AB				
Cytokine	Mean Diff.	Discovery?	q value	Individual P Value
EGF 1950	2556	No	0.8959	0.1026
Serpin E1 5054	2218	No	0.8959	0.1551
Thrombospondin-1 7057	1019	No	>0.9999	0.5098
FGF basic 2247	581.7	No	>0.9999	0.7062
IGFBP-2 3485	539.7	No	>0.9999	0.7265
GDF-15 9518	336.4	No	>0.9999	0.8274
CD14 929	264.4	No	>0.9999	0.8639
Pentraxin 3 5806	258.3	No	>0.9999	0.867
IL-8 3576	207.3	No	>0.9999	0.893
Myeloperoxidase 4353	27.83	No	>0.9999	0.9856
Dkk-1 22943	-27	No	>0.9999	0.986

Long Exposure

MEDIA - BASAL				
Cytokine	Mean Diff.	Discovery?	q value	Individual P Value
EMMPRIN 682	-9835	Yes	<0.0001	<0.0001
MIF 4282	-5738	Yes	<0.0001	<0.0001
Osteopontin 6696	-9797	Yes	<0.0001	<0.0001
PDGF-AA 5154	-8566	Yes	<0.0001	<0.0001
FGF-19 9965	-5072	Yes	0.0001	<0.0001
Endoglin 2022	-4095	Yes	0.003	0.0003
uPAR 5329	-3861	Yes	0.0056	0.0006
IL-17A 3605	-3502	Yes	0.0149	0.0019
Angiogenin 283	-3297	Yes	0.0239	0.0034
Angiopoietin-2 285	-3109	Yes	0.0361	0.0056
Cystatin C 1471	-2585	No	0.123	0.0211
GM-CSF 1437	-2478	No	0.144	0.027
LIF 3976	-2361	No	0.1711	0.035
MCP-1 6347	-2331	No	0.1711	0.0374
IL-6 3569	-1837	No	0.429	0.1005
IL-10 3586	-1783	No	0.4435	0.1108
Resistin 56729	-1743	No	0.4481	0.1189
SDF-1α 6387	-1705	No	0.453	0.1273
FGF-7 2252	-1610	No	0.4974	0.1496
IL-22 50616	-1584	No	0.4974	0.1564
VEGF 7422	-1558	No	0.4974	0.1634
IGFBP-3 3486	-1530	No	0.4974	0.1708
GROα 2919	-1501	No	0.4991	0.1792
VCAM-1 7412	-1377	No	0.5783	0.2176
BAFF 10673	-1353	No	0.5783	0.2257
Vitamin D BP 2638	-1316	No	0.5884	0.2389
Angiopoietin-1 284	-1203	No	0.6272	0.2815
ST2 9173	-1188	No	0.6272	0.2873
IFN-γ 3458	-1183	No	0.6272	0.2896
IL-4 3565	-1136	No	0.6272	0.3091
Leptin 3952	-1129	No	0.6272	0.3119
CD31 5175	-1069	No	0.6272	0.3385
HGF 3082	-1063	No	0.6272	0.341
MCP-3 6354	-1047	No	0.6272	0.3484
IL-27 246778	-1039	No	0.6272	0.3522
IL-31 386653	-1038	No	0.6272	0.3525
Row 8	-931.9	No	0.6414	0.4039
IL-19 29949	-918.3	No	0.6414	0.4107
TfR 7037	-918.3	No	0.6414	0.4107
IL-32 9235	-913.1	No	0.6414	0.4134
Cripto-1 6997	-902.7	No	0.6414	0.4187
PDGF-AB/BB 5154/5155	-867.6	No	0.6414	0.437
Chitinase 3-like 1 1116	-852.5	No	0.6414	0.445
Fas Ligand 356	-852.5	No	0.6414	0.445
Relaxin-2 6019	-803.7	No	0.6414	0.4715
IL-2 3558	-785.7	No	0.6414	0.4815
Complement Factor D 1675	-778.9	No	0.6414	0.4853
IL-12 p70 3593	-771.6	No	0.6414	0.4894
RBP-4 5950	-766	No	0.6414	0.4925
Apolipoprotein A-I 335	-735	No	0.6414	0.5102
M-CSF 1435	-734.1	No	0.6414	0.5107
IP-10 3627	-687.6	No	0.6432	0.5378
ENA-78 6374	-670.8	No	0.6432	0.5478
IL-15 3600	-668.1	No	0.6432	0.5494
I-TAC 6373	-663.2	No	0.6432	0.5524
RAGE 177	-610.7	No	0.6562	0.5842
CD40 ligand 959	-601	No	0.6562	0.5902
MIP-3β 6363	-579.3	No	0.6562	0.6037
IL-1α 3552	-578	No	0.6562	0.6045
MMP-9 4318	-557	No	0.6594	0.6177
TGF-α 7039	-508.5	No	0.6682	0.6486
IL-1β 3553	-471.7	No	0.6682	0.6725
IL-5 3567	-469.4	No	0.6682	0.674
G-CSF 1440	-466.9	No	0.6682	0.6756
Adiponectin 9370	-452.7	No	0.6682	0.685
DPPIV 1803	-447.2	No	0.6682	0.6886
TIM-3 84868	-357.9	No	0.7147	0.7484
IL-1ra 3557	-342.7	No	0.7147	0.7588
IL-18 Bpa 10068	-301.4	No	0.7248	0.7871
IL-16 3603	-294.1	No	0.7248	0.7921
Kallikrein 3 354	112.3	No	0.8298	0.9198

BASAL - LPS				
Cytokine	Mean Diff.	Discovery?	q value	Individual P Value
IL-17A 3605	-1554	No	>0.9999	0.2321
MIF 4282	-1466	No	>0.9999	0.2594
GROα 2919	-1059	No	>0.9999	0.4149
FGF-19 9965	-855	No	>0.9999	0.5104
IL-2 3558	-831.7	No	>0.9999	0.522
SDF-1α 6387	-824.7	No	>0.9999	0.5255
Angiopoietin-2 285	791.7	No	>0.9999	0.5422
EMMPRIN 682	-716.7	No	>0.9999	0.5811
IL-1α 3552	618.7	No	>0.9999	0.6338
MCP-3 6354	-617.3	No	>0.9999	0.6346
IL-5 3567	555.7	No	>0.9999	0.6687
IL-27 246778	-543.3	No	>0.9999	0.6757
IL-1β 3553	-532.3	No	>0.9999	0.6819
Osteopontin 6696	-502.3	No	>0.9999	0.6989
VCAM-1 7412	490.7	No	>0.9999	0.7056
IL-10 3586	-463	No	>0.9999	0.7215
Resistin 56729	450.7	No	>0.9999	0.7286
RAGE 177	-433	No	>0.9999	0.7388
MMP-9 4318	-429.7	No	>0.9999	0.7408
IFN-γ 3458	424.3	No	>0.9999	0.7439
PDGF-AA 5154	-420	No	>0.9999	0.7464
Relaxin-2 6019	405	No	>0.9999	0.7551
TfR 7037	393.3	No	>0.9999	0.762
CD31 5175	-387	No	>0.9999	0.7657
Angiogenin 283	-367	No	>0.9999	0.7775
RBP-4 5950	-361	No	>0.9999	0.781
IL-12 p70 3593	-354.7	No	>0.9999	0.7848
IL-32 9235	-354.3	No	>0.9999	0.785
Apolipoprotein A-I 335	-348.7	No	>0.9999	0.7883
Vitamin D BP 2638	347.7	No	>0.9999	0.7889
IL-1ra 3557	-331.3	No	>0.9999	0.7986
IGFBP-3 3486	-329.7	No	>0.9999	0.7996
uPAR 5329	315	No	>0.9999	0.8083
Endoglin 2022	-304.7	No	>0.9999	0.8145
IL-19 29949	284.3	No	>0.9999	0.8267
Chitinase 3-like 1 1116	-283.7	No	>0.9999	0.8271
IL-31 386653	-282.3	No	>0.9999	0.8279
G-CSF 1440	-271.3	No	>0.9999	0.8345
IL-18 Bpa 10068	-238	No	>0.9999	0.8546
ST2 9173	-216.7	No	>0.9999	0.8675
Fas Ligand 356	214	No	>0.9999	0.8691
BAFF 10673	205.7	No	>0.9999	0.8742
I-TAC 6373	-178.3	No	>0.9999	0.8908
GM-CSF 1437	160.7	No	>0.9999	0.9015
MIP-3β 6363	-159.7	No	>0.9999	0.9021
TIM-3 84868	-151.7	No	>0.9999	0.907
PF4 5196	-146	No	>0.9999	0.9105
LIF 3976	143.3	No	>0.9999	0.9121
Leptin 3952	140	No	>0.9999	0.9141
MCP-1 6347	-131.7	No	>0.9999	0.9192
M-CSF 1435	-127.3	No	>0.9999	0.9219
IL-6 3569	-122	No	>0.9999	0.9251
Angiopoietin-1 284	-113	No	>0.9999	0.9307
Kallikrein 3 354	113	No	>0.9999	0.9307
IP-10 3627	-96	No	>0.9999	0.9411
IL-4 3565	93	No	>0.9999	0.9429
Cystatin C 1471	87.67	No	>0.9999	0.9462
TGF-α 7039	-87.67	No	>0.9999	0.9462
ENA-78 6374	87.33	No	>0.9999	0.9464
IL-34 146433	87	No	>0.9999	0.9466
IL-33 90865	-86.57	No	>0.9999	0.9468
DPPIV 1803	85.33	No	>0.9999	0.9476
HGF 3082	60	No	>0.9999	0.9631
IL-22 50616	-58.67	No	>0.9999	0.964
Complement Factor D 1675	-57.33	No	>0.9999	0.9648
Cripto-1 6997	-47	No	>0.9999	0.9711
VEGF 7422	-32.33	No	>0.9999	0.9801
FGF-7 2252	-31.67	No	>0.9999	0.9805
CD40 ligand 959	-30	No	>0.9999	0.9816
Row 8	28.67	No	>0.9999	0.9824
PDGF-AB/BB 5154/5155	24.33	No	>0.9999	0.985
Adiponectin 9370	-11	No	>0.9999	0.9932
IL-15 3600	11	No	>0.9999	0.9932
IL-16 3603	-7.667	No	>0.9999	0.9953

BASAL - pgLPS				
Cytokine	Mean Diff.	Discovery?	q value	Individual P Value
EMMPRIN 682	-2462	No	>0.9999	0.0588
IL-17A 3605	-2409	No	>0.9999	0.0645
FGF-19 9965	1471	No	>0.9999	0.258
Angiopoietin-2 285	1167	No	>0.9999	0.3692
PDGF-AA 5154	-1039	No	>0.9999	0.4242
VCAM-1 7412	-809.7	No	>0.9999	0.5332
TIM-3 84868	-779	No	>0.9999	0.5488
CD40 ligand 959	735	No	>0.9999	0.5716
Leptin 3952	654.7	No	>0.9999	0.6143
MMP-9 4318	-645.7	No	>0.9999	0.6192
Row 8	610	No	>0.9999	0.6387
IL-2 3558	-597	No	>0.9999	0.6459
CD31 5175	-578.2	No	>0.9999	0.6563
SDF-1α 6387	-566	No	>0.9999	0.6631
IL-5 3567	552.9	No	>0.9999	0.6704
DPPIV 1803	-550.3	No	>0.9999	0.6719
IL-6 3569	537.3	No	>0.9999	0.6792
IFN-γ 3458	534.3	No	>0.9999	0.6809
MCP-1 6347	502.7	No	>0.9999	0.6988
Resistin 56729	496.7	No	>0.9999	0.7022
Kallikrein 3 354	-465.7	No	>0.9999	0.72
Adiponectin 9370	457	No	>0.9999	0.725
Cystatin C 1471	444	No	>0.9999	0.7325
Endoglin 2022	-441	No	>0.9999	0.7343
LIF 3976	437.7	No	>0.9999	0.7362
Vitamin D BP 2638	427.3	No	>0.9999	0.7422
IL-22 50616	425.3	No	>0.9999	0.7434
ENA-78 6374	412.9	No	>0.9999	0.7506
Apolipoprotein A-I 335	403.3	No	>0.9999	0.7562
M-CSF 1435	395	No	>0.9999	0.7611
IL-31 386653	379	No	>0.9999	0.7705
Angiogenin 283	368.3	No	>0.9999	0.7768
PDGF-AB/BB 5154/5155	353	No	>0.9999	0.7858
BAFF 10673	352.3	No	>0.9999	0.7862
IL-19 29949	331.7	No	>0.9999	0.7985
FGF-7 2252	311.3	No	>0.9999	0.8106
Osteopontin 6696	302	No	>0.9999	0.8162
Cripto-1 6997	294	No	>0.9999	0.8209
VEGF 7422	293.7	No	>0.9999	0.8211
IL-1ra 3557	282	No	>0.9999	0.8281
Relaxin-2 6019	258.3	No	>0.9999	0.8424
MIF 4282	-256.3	No	>0.9999	0.8436
IL-18 Bpa 10068	-249	No	>0.9999	0.848
I-TAC 6373	-238.3	No	>0.9999	0.8544
IL-4 3565	227	No	>0.9999	0.8613
IL-16 3603	223.7	No	>0.9999	0.8633
IL-1α 3552	219.3	No	>0.9999	0.8659
Fas Ligand 356	214	No	>0.9999	0.8691
GROα 2919	211.7	No	>0.9999	0.8706
HGF 3082	205.3	No	>0.9999	0.8744
TGF-α 7039	-200	No	>0.9999	0.8776
Complement Factor D 1675	167.3	No	>0.9999	0.8975
IL-27 246778	166	No	>0.9999	0.8983
IL-15 3600	155	No	>0.9999	0.905
RBP-4 5950	-142.7	No	>0.9999	0.9125
IP-10 3627	142.3	No	>0.9999	0.9127
IL-10 3586	126	No	>0.9999	0.9227
MIP-3β 6363	-117.7	No	>0.9999	0.9278
IL-1β 3553	104.3	No	>0.9999	0.936
ST2 9173	103	No	>0.9999	0.9368
TfR 7037	93	No	>0.9999	0.9429
TARC 6361	-75.87	No	>0.9999	0.9534
IGFBP-3 3486	-62.33	No	>0.9999	0.9617
uPAR 5329	-49	No	>0.9999	0.9699
RAGE 177	-39.67	No	>0.9999	0.9756
IL-12 p70 3593	-27.67	No	>0.9999	0.983
Angiopoietin-1 284	22.33	No	>0.9999	0.9863
IL-32 9235	21.67	No	>0.9999	0.9867
GM-CSF 1437	18.67	No	>0.9999	0.9885
Chitinase 3-like 1 1116	-5.667	No	>0.9999	0.9965
G-CSF 1440	3.667	No	>0.9999	0.9977
MCP-3 6354	-1.667	No	>0.9999	0.999

BASAL - VEHICLE (AB)				
Cytokine	Mean Diff.	Discovery?	q value	Individual P Value
Osteopontin 6696	-3727	No	0.9828	0.0346
MIF 4282	-3566	No	0.9828	0.0432
Kallikrein 3 354	-2888	No	0.9828	0.1012
PDGF-AA 5154	-2874	No	0.9828	0.1029
IFN-γ 3458	-2825	No	0.9828	0.1088
MMP-9 4318	-2727	No	0.9828	0.1216
EMMPRIN 682	-2711	No	0.9828	0.1239
IL-1α 3552	-2538	No	0.9828	0.1496
Angiopoietin-2 285	-2024	No	0.9828	0.2502
TfR 7037	-2024	No	0.9828	0.2502
VCAM-1 7412	-1961	No	0.9828	0.2651
RAGE 177	-1896	No	0.9828	0.2812
uPAR 5329	-1716	No	0.9828	0.3295
Endoglin 2022	-1698	No	0.9828	0.3345
Apolipoprotein A-I 335	-1659	No	0.9828	0.3457
IL-32 9235	-1518	No	0.9828	0.3882
IL-5 3567	-1508	No	0.9828	0.3914
IL-27 246778	-1389	No	0.9828	0.4299
M-CSF 1435	-1311	No	0.9828	0.4562
Vitamin D BP 2638	-1306	No	0.9828	0.4578
GROα 2919	-1266	No	0.9828	0.4718
IL-17A 3605	-1223	No	0.9828	0.487
IL-31 386653	-1221	No	0.9828	0.4877
Angiogenin 283	-1212	No	0.9828	0.4909
MIG 4283	-1167	No	0.9828	0.5069
FGF-19 9965	-1090	No	0.9828	0.5356
TGF-α 7039	-1037	No	0.9828	0.5553
MCP-3 6354	-1023	No	0.9828	0.5607
PF4 5196	-1015	No	0.9828	0.5637
LIF 3976	-1004	No	0.9828	0.5681
IL-10 3586	-985.7	No	0.9828	0.5752
Chitinase 3-like 1 1116	-977	No	0.9828	0.5785
CD40 ligand 959	-885.7	No	0.9828	0.6145
IL-22 50616	-856.7	No	0.9828	0.6262
MCP-1 6347	-824.7	No	0.9828	0.6391
ST2 9173	-822	No	0.9828	0.6402
Resistin 56729	-801.3	No	0.9828	0.6486
IL-12 p70 3593	-766.3	No	0.9828	0.663
VEGF 7422	-751.3	No	0.9828	0.6692
SDF-1α 6387	-749	No	0.9828	0.6702
TIM-3 84868	-709.7	No	0.9828	0.6865
DPPIV 1803	-703.7	No	0.9828	0.689
IL-1ra 3557	-686	No	0.9828	0.6965
G-CSF 1440	-685.3	No	0.9828	0.6967
CD31 5175	-683.7	No	0.9828	0.6974
IL-4 3565	-678	No	0.9828	0.6998
BAFF 10673	-655.3	No	0.9828	0.7094
Cystatin C 1471	-647	No	0.9828	0.7129
Angiopoietin-1 284	-626.3	No	0.9828	0.7217
RBP-4 5950	-596.7	No	0.9828	0.7344
IL-33 90865	-588.7	No	0.9828	0.7378
GM-CSF 1437	572	No	0.9828	0.745
Row 8	-550.3	No	0.9828	0.7543
Adiponectin 9370	-548.3	No	0.9828	0.7552
IL-13 3596	-533.8	No	0.9828	0.7615
Fas Ligand 356	-527.3	No	0.9828	0.7643
TARC 6361	-524.7	No	0.9828	0.7654
I-TAC 6373	-505.7	No	0.9828	0.7737
Relaxin-2 6019	-497	No	0.9828	0.7775
IL-16 3603	-492.3	No	0.9828	0.7795
Growth Hormone 2688	-470.6	No	0.9828	0.789
MIP-1α/MIP-1β 6348/6351	-470	No	0.9828	0.7892
Leptin 3952	-462.7	No	0.9828	0.7925
IGFBP-3 3486	-455.3	No	0.9828	0.7957
TNF-α 7124	-449.9	No	0.9828	0.7981
MIP-3β 6363	-442.3	No	0.9828	0.8014
IL-1β 3553	-419	No	0.9828	0.8117
Complement Factor D 1675	-390.3	No	0.9828	0.8243
IP-10 3627	-349.3	No	0.9828	0.8425
IL-18 Bpa 10068	-339.1	No	0.9828	0.8471
IL-15 3600	-336.7	No	0.9828	0.8482
ENA-78 6374	-288.9	No	0.9828	0.8695
Cripto-1 6997	-280.7	No	0.9828	0.8732
HGF 3082	-262.3	No	0.9828	0.8814
IL-19 29949	-258	No	0.9828	0.8833
IL-34 146433	-245	No	0.9828	0.8892
IL-2 3558	-194	No	0.9951	0.9121
PDGF-AB/BB 5154/5155	-137.3	No	>0.9999	0.9377
IL-6 3569	-80.33	No	>0.9999	0.9636
FGF-7 2252	28.33	No	>0.9999	0.9871

VEHICLE (AB) - AB				
Cytokine	Mean Diff.	Discovery?	q value	Individual P Value
EMMPRIN 682	4310	No	>0.9999	0.0668
Osteopontin 6696	3030	No	>0.9999	0.1969
MIF 4282	2713	No	>0.9999	0.2479
GM-CSF 1437	1919	No	>0.9999	0.4135
IFN-γ 3458	1726	No	>0.9999	0.4618
MMP-9 4318	1720	No	>0.9999	0.4634
FGF-19 9965	1606	No	>0.9999	0.4935
Cystatin C 1471	1572	No	>0.9999	0.5029
uPAR 5329	1567	No	>0.9999	0.5042
PDGF-AA 5154	1524	No	>0.9999	0.5159
VCAM-1 7412	1213	No	>0.9999	0.605
IL-32 9235	1176	No	>0.9999	0.6163
RAGE 177	1170	No	>0.9999	0.618
IL-10 3586	1125	No	>0.9999	0.6316
TGF-α 7039	1081	No	>0.9999	0.6448
MCP-1 6347	1071	No	>0.9999	0.648
MIG 4283	1054	No	>0.9999	0.6532
IL-27 246778	1031	No	>0.9999	0.6604
IL-17A 3605	952.7	No	>0.9999	0.6846
LIF 3976	865.3	No	>0.9999	0.7122
TfR 7037	853.7	No	>0.9999	0.7159
IL-12 p70 3593	841.8	No	>0.9999	0.7196
IL-22 50616	825	No	>0.9999	0.725
M-CSF 1435	780.7	No	>0.9999	0.7392
Endoglin 2022	778.3	No	>0.9999	0.74
TNF-α 7124	771.7	No	>0.9999	0.7421
IL-1ra 3557	-764.4	No	>0.9999	0.7445
Resistin 56729	763	No	>0.9999	0.7449
IP-10 3627	739.9	No	>0.9999	0.7524
IGFBP-3 3486	731.2	No	>0.9999	0.7552
MCP-3 6354	729.4	No	>0.9999	0.7558
IL-1β 3553	722.9	No	>0.9999	0.7579
Cripto-1 6997	692.3	No	>0.9999	0.7678
RBP-4 5950	687.5	No	>0.9999	0.7694
CD40 ligand 959	669	No	>0.9999	0.7754
IL-15 3600	663.5	No	>0.9999	0.7772
Kallikrein 3 354	660.3	No	>0.9999	0.7783
MIP-1α/MIP-1β 6348/6351	652.2	No	>0.9999	0.781
IL-31 386653	647.7	No	>0.9999	0.7824
ENA-78 6374	646.9	No	>0.9999	0.7827
IL-34 146433	640.7	No	>0.9999	0.7847
PF4 5196	627.4	No	>0.9999	0.7891
IL-33 90865	621.9	No	>0.9999	0.7909
Leptin 3952	618.6	No	>0.9999	0.792
HGF 3082	618.2	No	>0.9999	0.7921
SDF-1α 6387	-590.3	No	>0.9999	0.8013
ST2 9173	590.3	No	>0.9999	0.8013
G-CSF 1440	578.4	No	>0.9999	0.8052
DPPIV 1803	575	No	>0.9999	0.8063
IL-19 29949	561.3	No	>0.9999	0.8108
IL-4 3565	548.3	No	>0.9999	0.8151
IL-13 3596	526.4	No	>0.9999	0.8224
IL-5 3567	521.6	No	>0.9999	0.824
Angiopoietin-2 285	515.3	No	>0.9999	0.8261
VEGF 7422	498.3	No	>0.9999	0.8317
IL-6 3569	489.7	No	>0.9999	0.8346
IL-1α 3552	486.7	No	>0.9999	0.8356
Angiopoietin-1 284	479.3	No	>0.9999	0.838
IL-16 3603	450.8	No	>0.9999	0.8476
BAFF 10673	447	No	>0.9999	0.8488
Growth Hormone 2688	420.3	No	>0.9999	0.8578
IL-2 3558	417.8	No	>0.9999	0.8586
Complement Factor D 1675	417.3	No	>0.9999	0.8588
PDGF-AB/BB 5154/5155	416.3	No	>0.9999	0.8591
Fas Ligand 356	398.3	No	>0.9999	0.8651
Row 8	396	No	>0.9999	0.8659
GROα 2919	377	No	>0.9999	0.8723
I-TAC 6373	360.1	No	>0.9999	0.878
TIM-3 84868	357.3	No	>0.9999	0.8789
FGF-7 2252	351.7	No	>0.9999	0.8808
Relaxin-2 6019	322	No	>0.9999	0.8908
Apolipoprotein A-I 335	321.7	No	>0.9999	0.8909
Angiogenin 283	266	No	>0.9999	0.9097
MIP-3β 6363	256.4	No	>0.9999	0.9129
TARC 6361	253.9	No	>0.9999	0.9138
Adiponectin 9370	80.67	No	>0.9999	0.9726
CD31 5175	76.33	No	>0.9999	0.974
Chitinase 3-like 1 1116	68.33	No	>0.9999	0.9768
Vitamin D BP 2638	57.67	No	>0.9999	0.9804
IL-18 Bpa 10068	3.667	No	>0.9999	0.9988

Chapter 4: Development of 3D, Rastrum-bioprinted vascular cultures

4.1. *Introduction*

The disordered human neurovascular unit consists of complex pathomechanisms that are prohibitively invasive to observe *in vivo* (Drummond and Wisniewski, 2017). Understanding how different cell types operate and communicate within the neurovascular unit is critical to understanding the neurodegenerative conditions which are typified by neurovascular dysfunction. For this reason, the ability of our *in vivo* and *in vitro* models to adequately recapitulate cellular phenotypes in human pathologies is vital.

Rodent models are the most common *in vivo* disease model for investigating disorders of the neurovascular unit. This allows the investigation of cell behaviour in a natural multicellular, 3D environment (Dawson et al., 2018, McGonigle, 2014). However, differences in genetics and behavioural phenotypes in animal models reduce the generalizability of these models to human CNS diseases (McGraw et al., 2017). Compared to rodents, human endothelia possess significant transcriptomic differences affecting barrier and inflammatory functions (Song et al., 2020), and engage in more extensive interaction with pericytes and astrocytes (Hartmann et al., 2015, Canfield et al., 2017).

On the other hand, *in vitro* studies are generally performed in monocultures plated on 2D surfaces—a significantly different adhesion environment to the 3D, multicellular matrix in the CNS (Birgersdotter et al., 2005). This causes meaningful differences in cell morphology, function, differentiation, and gene expression compared to the *in vivo* environment, challenging the relevance of these purportedly *in vivo*-like systems (Edmondson et al., 2014, Pound and Ritskes-Hoitinga, 2018, Sun et al., 2006, Liu et al., 2019). Therefore, it is necessary to improve *in vitro* culture systems to better mimic the human neurovascular environment and enhance physiological relevance. As opposed to more commonly used primary and immortalised cell lines, iPSC-derived cells are a more scalable cell source, with distinct phenotypes (as shown in Chapter 2) that may be more disease-relevant for human-specific diseases (Heikkilä et al., 2009, Zhang et al., 2017a). iPSCs also allow the production of floating 3D cerebral organoids, which display more appropriate developmental and structural aspects of the CNS

(Lancaster and Knoblich, 2014), but are poorly replicable and not ideal for investigation of some cell-types, including vascular cells (Di Lullo and Kriegstein, 2017, Quadrato et al., 2017). In addition to organoids, hydrogel-encapsulated 3D culture systems offer an alternative *in vitro* platform with advantageous scalability and replicability. Hydrogels using natural mixtures (such as Matrigel, a basement membrane extract from a mouse tumour line) are highly biocompatible, although, they suffer from batch-to-batch variability and constrained rheological characteristics unsuitable for widescale bioprinting (Aisenbrey and Murphy, 2020b, Mancha Sánchez et al., 2020). Contrastingly, synthetic hydrogels such as those made from polyethylene glycol (PEG), confer tunable biochemical and biomechanical properties, allowing accurate imitation of the specific extracellular environment being studied. The polymer chain length and concentration of PEG hydrogels can be varied to modulate stiffness and porosity (Zhu, 2010). Incorporation of matrix metalloprotease-sensitive peptide sequences can allow for cell-mediated biodegradation and migration, and covalent coupling of adhesion sequences which assist with cell survival and attachment (Figure 4.1) (Utama et al., 2021). While peptide sequences from fibronectin (such as RGD) and laminin (such as YIGSR) are common, peptides from other ECM components like collagen IV may also assist in appropriate functionalisation of synthetic hydrogels (Floquet et al., 2004, Brösicke et al., 2015). Additionally, gelation mechanisms of PEG hydrogels are compatible with drop-on-demand printing, a methodology offering higher throughput and consistency than temperature-gelation and manual-pipette gelation techniques). But, using these scalable bioprinting technologies to generate biomimetic iPSC-derived neurovascular cultures is a strategy that has not been investigated.

The Rastrum 3D bioprinting platform offers a modular, high-throughput solution for developing complex tissue models (Yee et al., 2024, Utama et al., 2021, Jung et al., 2022). Its droplet-on-demand technology ensures precise placement of bioinks, enabling the scalable fabrication of multicellular structures with consistent architecture and functionality. The modularity of the Rastrum system allows for tailored combinations of cell types and matrices, making it particularly advantageous for modelling dynamic and heterogeneous environments like the neurovascular unit.

For the purposes of advancing 3D neurovascular unit cultures for disease modelling and drug discovery, novel 3D models involving self-vascularising monocultures of endothelial cells, and multi-cell type cultures involving endothelial cells, pericytes and

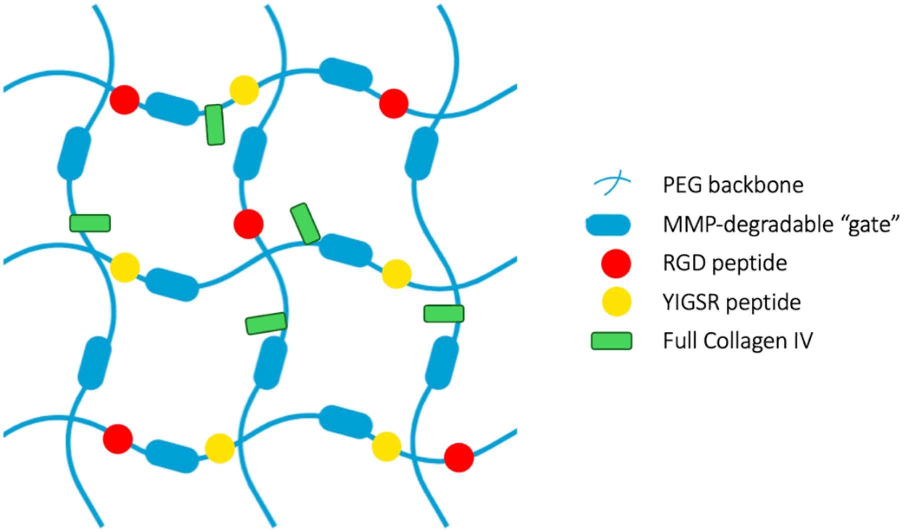

Figure 4.1: Hydrogel matrix composition diagram. 3D bioprintable matrix consists of a polyethylene glycol (PEG)-backbone with adjustable arm number and length that allows for tunable stiffness. Matrix metalloprotease (MMP)-cleavable sequences allow increased cell motility upon cell-mediated degradation. Full length collagen IV, Arg-Gly-Asp (RGD) peptide, and Tyr-Ile-Gly-Ser-Arg (YIGSR) peptide are incorporated for optimal cell adhesion.

astrocytes are needed. While innovative, 3D neurovascular cultures have been published (Blanchard et al., 2020), none have successfully demonstrated co-culturing, iPSC-derived cell types and scalable bioprinting in tandem. These models should be replicable, self-assemble into *in vivo*-like structures at the macro and micro scale, and display cell-specific morphology. This chapter aims to provide a tunable 3D bioprinting platform that supports the monoculture of both CMECs and iBMECs, and the triculture of endothelial cells, pericytes and astrocytes using a well-defined, bioprintable, *in vivo*-relevant matrix.

4.2. *Results*

4.2.1. *Vascular bioprinting development*

4.2.1.1. Initial monoculture and co-culture development

Using the Rastrum bioprinter, cells can be seeded within a proprietary PEG hydrogel, containing MMP-degradable sequences, crosslinked RGD and YIGSR peptides, and free collagen IV, to support the maintenance of cells in a synthetic, *in vivo*-like environment (Utama et al., 2020) (Figure 4.1). To test that endothelial cells and pericytes can survive this printing process and develop morphologically over time we began by printing immortalised endothelial cells (CMECs) and primary human brain vascular pericytes (HBVP) were seeded in monoculture and co-culture. Cells were seeded at a total of 5 x 10^6 cells/mL of gel, with the co-culture containing a 50:50 mixture of CMECs and HBVPs, adopted from *in vitro* co-cultures found in the literature (Nzou et al., 2018, Urich et al., 2013). 24 h after cell printing, cultures were imaged with calcein-AM and ethidium homodimer-1 (EthD) to verify that cells had survived the printing process, then stained for immunofluorescence imaging.

At day 1 and day 9, both monocultures and the co-culture supported viable cells, indicated by calcein-AM-positive staining, with some EthD-positive dead cells (Figure 4.2A). Given the presence of live cells, samples were fixed and stained for cell specific markers at day 12 (using 3D immunofluorescence protocol in Chapter 2.8), highlighting the formation of robust, micro-scale vascular-like networks. This is especially evident in the ring of PECAM-1-positive staining around the edge of the gel (Figure 4.2B). Endothelial markers PECAM-1 and occludin were also observed in close association with pericytic markers NG2 and PDGFRβ, respectively (Figure 4.2C).

Weaker signal-to-noise ratios were observed compared to standard 2D immunofluorescence assays using the same cell lines (Figure 4.2A). This may be attributed to the secretion of autofluorescent proteins by vascular cell types, as similar autofluorescence was not seen in empty gels (Supplementary Figure 4.11). Autofluorescence issues such as these are magnified in 3D opposed to 2D, due to increased metabolic states (Heaster et al., 2020, Cannon et al., 2017). Fluorescent signal is decreased towards the top portion of the gel due to increased light-scattering in the signal path (e.g. the central portion of Figure 4.2B), while DAPI-negative non-specific aggregates also hinder accurate visualisation (Figure 4.2B, white arrows). For this reason, an optimized immunofluorescence sample preparation protocol was developed incorporating increased incubation times, decreased temperature, and a clearing process to circumvent non-specific binding and light scattering. Full details of this protocol are outlined in the Chapter 2.9, and this protocol is used from 4.2.2 onwards.

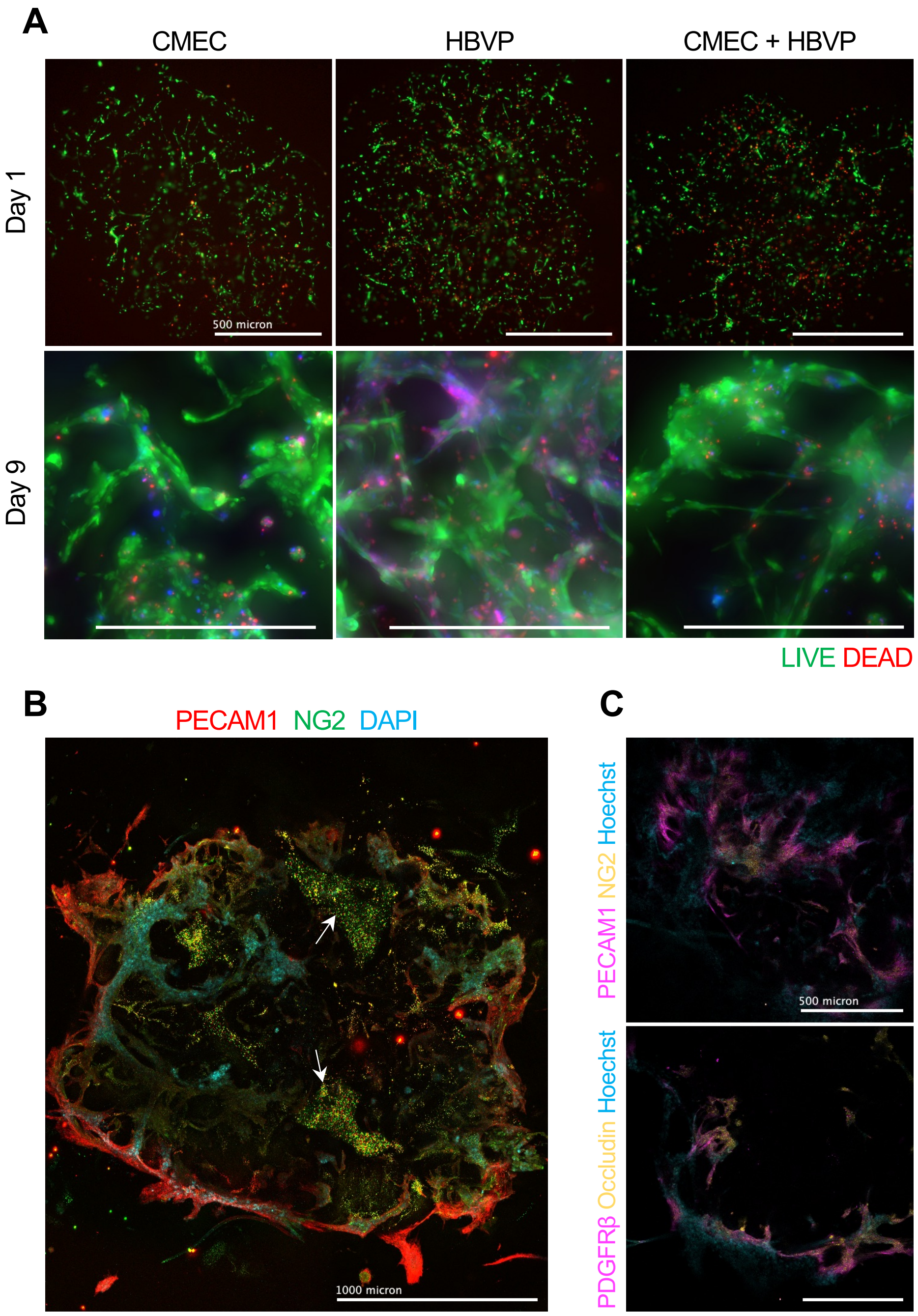

Figure 4.2: Maximum intensity projections of 3D co-cultures containing CMECs and HBVPs. (A) Representative maximum intensity projection of Cerebral Microvascular Endothelial Cell (CMEC) and Human Brain Vascular Pericyte (HBVP) co-cultures stained with calcein-AM (Live, green) and Ethidium Homodimer-1 (EthD; Dead, red). Scale bar represents 500 µm. (n = 1). **(B)** Representative maximum intensity projection of co-culture stained for endothelial cells (Platelet Endothelial Cell Adhesion Molecule-1; PECAM-1, red), pericytes (Neural/Glial Antigen 2; NG2, green) and nuclei (Hoechst, cyan). White arrows indicate areas containing non-specific artefacts. Scale bar represents 1000 µm. (n = 1) **(C)** Representative

maximum intensity projection of co-culture. Top: endothelial cells (PECAM-1, magenta), pericytes (NG2, yellow) and nuclei (Hoechst, cyan). Bottom: pericytes (Platelet-Derived Growth Factor Receptor β; PDGFRβ, red), endothelial cells (occludin, green) and nuclei (Hoechst, cyan). Scale bar represents 500 μm. (n = 1).

4.2.1.2. 2D iAstrocyte differentiation and characterisation

To enhance the physiological relevance of our endothelial-pericyte constructs, the incorporation of astrocytes is essential, as they represent the third key component of the neurovascular unit. iPSC-derived astrocytes (iAstrocytes) were differentiated by first deriving neural progenitor cells (NPCs) using the STEMDiff Neural System, then differentiating to astrocyte identity by culturing in proprietary astrocyte medium (Tcw et al., 2017). At the intermediate stage, NPCs were shown by immunocytochemistry to express the NPC markers nestin and PAX6 (Figure 4.3A).

Both iAstrocytes and primary human astrocytes were assessed by immunocytochemistry for expression of astrocyte markers in 2D. Glial Fibrillary Acidic Protein (GFAP), a structural intermediate filament protein and S100β, a calcium-binding protein expressed in mature astrocytes, are two common markers used to identify astrocytes. Aquaporin 4 (AQP4) is a membrane-bound water channel important for fluid dynamics of the glymphatic system and vasculature. All three markers were expressed in both the primary and iPSC-derived astrocytes (Figure 4.3B). Apart from this verification of cell identity marker expression, please note these iAstrocytes have undergone extensive functional characterisation by our lab elsewhere (Sullivan et al., 2023, Sullivan et al., 2024).

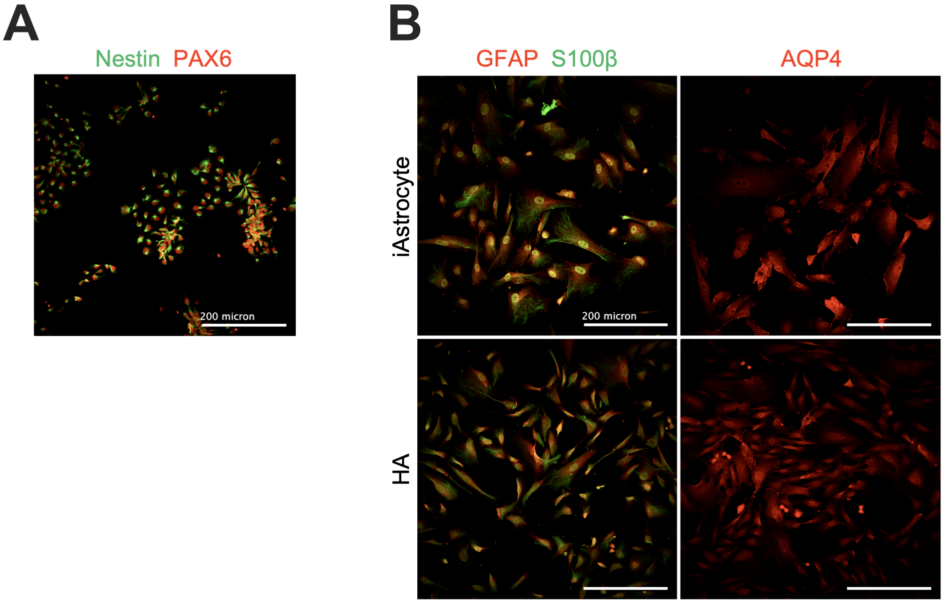

Figure 4.3: Immunofluorescence validation of 2D iPSC-derived neural progenitor cells, iPSC-derived astrocytes and primary astrocytes. (A) Representative image showing the expression of NPC markers nestin and PAX6 in iPSC-derived NPCs. Scale bar represents 200 μm. **(B)** Representative images showing the expression of astrocyte cell markers glial fibrillary acidic protein (GFAP), S100 Calcium-Binding Protein β (S100β) and aquaporin 4 (AQP4) in iAstrocyte and human fetal astrocyte lines. Scale bar represents 200 μm.

4.2.1.3. Hydrogel optimisation with human astrocytes

Our lab previously published some optimisation of PEG gel properties using human astrocytes (Sullivan et al., 2023). This work identified that gels containing both RGD and YIGSR peptides provided optimal biocompatibility, compared to less functionalised gels. That work also found that addition of free collagen IV was well tolerated, allowing the addition of this adhesion protein that performs important roles in CNS structural matrices (Gatseva et al., 2019). During this optimisation, 1.5 kPa gels were chosen over a 0.9 kPa gel, to ensure structural longevity, and stay within the boundaries of reported brain stiffnesses (Axpe et al., 2020, Weickenmeier et al., 2016). Since that research, 1.5 kPa bioinks were shown to possess poorer Rastrum ejection properties (personal communication with manufacturer). Additionally, altered concentrations of RGD and YIGSR peptides were instigated by the manufacturer (personal communication with manufacturer), so it was necessary to test whether these changes affected cell health. Given the importance of astrocytes to the neurovascular unit, we tested whether human astrocyte viability and morphology was affected by the new peptide concentrations, or by decreasing gel stiffness to 1.1 kPa (through modulation of PEG arm length) (Figure 4.4). Human astrocyte viability, measured as the percentage of calcein AM-positive cells to total DAPI-positive cells, was not significantly different between the 1.5 kPa gel (78.8% ± 5.35 SD), the 1.5 kPa new [peptides] gel (73.7% ± 8.53 SD), and the 1.1 kPa new [peptides] gel (78.9% ± 7.29 SD) (Figure 4.4A). Similarly, cell area remained stable across the three gel conditions (392 μm^2 ± 65.4 SD; 354 μm^2 ± 40.7 SD; 443 μm^2 ± 47.6 SD respectively; Figure 4.4B). Mean longest process length (30.5 μm^2 ± 4.34 SD; 28.5 μm^2 ± 4.21 SD; 29.6 μm^2 ± 4.86 SD respectively; Figure 4.4C) and the range of longest process lengths within a sample (115.0 ± 20.34 SD; 119.5 ± 19.63 SD; 107.8 ± 20.63 SD respectively; Figure 4.4D) were also not significantly different.

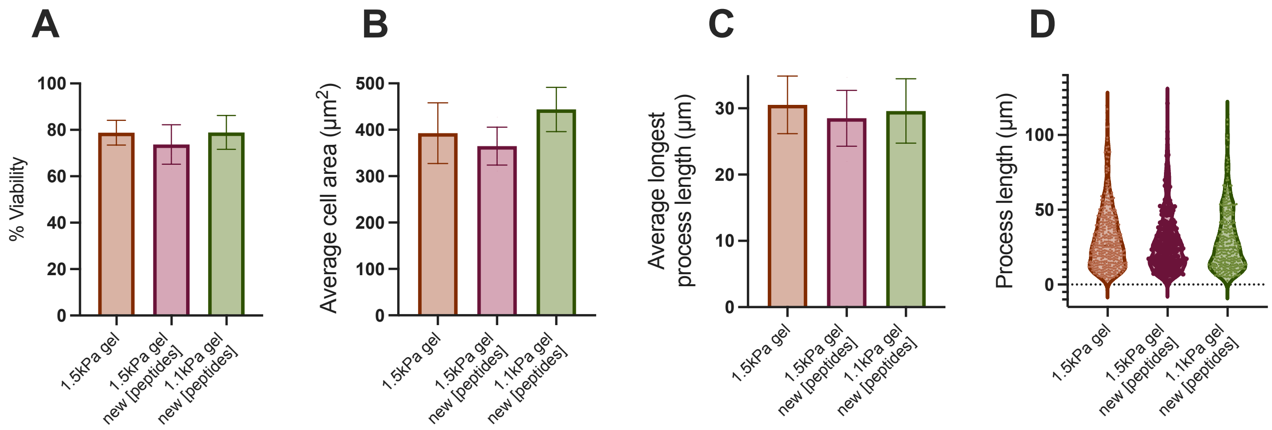

Figure 4.4: Viability and morphology of 3D human astrocytes in hydrogels of new peptide concentrations and stiffness. Primary human astrocytes were imaged 3 days after bioprinting, and interrogated by indexing **(A)** viability as percentage of live cells, **(B)** average cell area and **(C)** longest process length measured by manual tracing, and the **(D)** range of longest process lengths. Data shows the mean ± SD of n ≥ 3 independent experiments. A one-way ANOVA with Dunnett's multiple comparison test was used to identify statistically significant differences between gel conditions.

High concentrations of free collagen IV produced bubbles when ejecting into the waste cartridge, and left adherent deposits in the fluidic channels (personal communication with manufacturer). Because of this, we set out to test whether free collagen IV could be replaced by a shorter peptide sequence, reducing cost and batch-to-batch variability from externally-sourced protein. The five collagen IV-derived peptide sequences tested are displayed in Table 4.1. These were chosen by Inventia Life Sciences based on previous literature investigating the MNYYSNS motif found on the alpha 3 chain of collagen IV (Floquet et al., 2004, Brösicke et al., 2015). The bioinks each vary in the amino acids flanking the main adhesion sequence, affecting the conformation of the peptide and thus the availability for integrin binding.

Table 4.1: Collagen peptide sequences

Name	Sequence
Bioink A	C**MNYYSNS**KK
Bioink B	C**MNYYSNS**GGKK
Bioink C	CG**MNYYSNS**KK
Bioink D	CD**MNYYSNS**KK
Bioink E	C**NYYSNS**GGKK

After multiple bioprints were conducted with the novel bioinks, conspicuous variability issues were noted immediately after gelation. Bioinks A-E showed variability in the quality of gelation, evidenced by stark disparities in local cell density, compared to stably higher density in the hydrogels containing bioinks without the novel peptide sequences (Supplementary Figure 4.12). Contrary to this variability, viability percentage calculations suggested that removal of free collagen IV from the gel, or replacement of collagen IV with any of the five collagen peptide sequences does not affect viability (Figure 4.5). While these results indicate minimal disadvantage of the adhesion peptide substitutes to astrocyte viability, variability in structural integrity of the hydrogels may compromise future experiments that rely on replicability. Thus, the 1.1 kPa gel with new RGD and YIGSR concentrations and added collagen IV was chosen as the most appropriate gel for further experiments in Section 4.2.3 and Chapter 5. For these experiments, the advantage of reduced waste bubbling and fluidic deposits was preferable. However, to allow direct comparison alongside other data generated using the 1.5 kPa gel (published in Sullivan et al. (2023), other experiments presented in this chapter use the 1.5 kPa gel (except for the primary/iPSC-derived triculture in section 4.2.3).

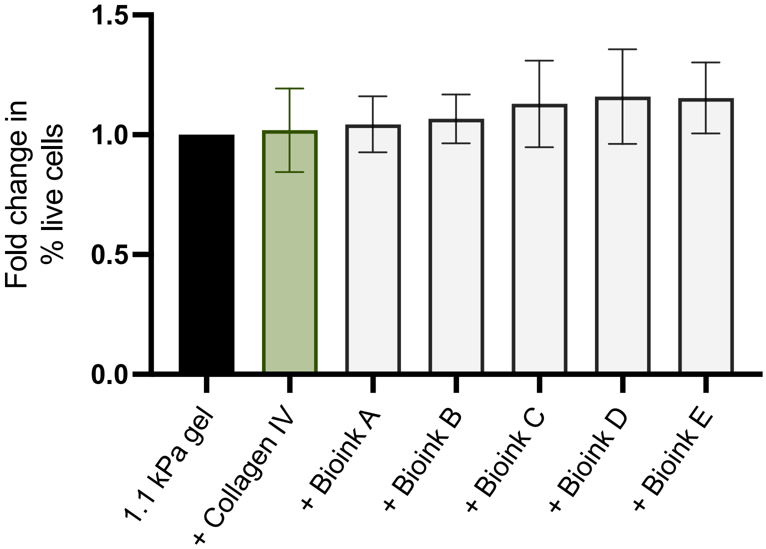

Figure 4.5: Viability of 3D human astrocytes in hydrogels with differing collagen integration. Primary human astrocytes were imaged 3 days after bioprinting, and interrogated by calculating the fold change in viability as percentage of live cells, compared to the 1.1 kPa gel without Collagen IV or novel peptides. All conditions in this experiment contained RGD and YIGSR at the new peptide concentrations determined in Fig 4.4. Data shows the mean ± SD of n ≥ 3 independent experiments. A one-way ANOVA with

Dunnett's multiple comparison test was used to identify statistically significant differences compared to the 1.1 kPa gel with collagen IV.

4.2.2. Characterising bioprinted endothelial monocultures

Once astrocytic bioprinting was optimised, we commenced optimisation of endothelial cell monoculture bioprinting. To optimise the monoculture of endothelial cells using the Rastrum bioprinting platform, we first needed to investigate the maintenance of viability and cell identity over time, and tested both CMECs and iBMECs to explore any cell source differences. As these monocultures will also form the basis for further development of multi-cell type cultures, we also assessed the suitability of ScienCell's astrocyte medium (AM), recently used to support astrocytes, endothelial cells, pericytes, and other CNS cell types in non-bioprinted, 3D, neurovascular co-culture systems (Nzou et al., 2020b, Blanchard et al., 2020).

CMECs were bioprinted in 2D into CMEC media (CM; see Chapter 2.2 for media composition) before measuring viability using a CellTiter-Blue assay. CMECs cultured in AM demonstrated higher viability compared to those cultured in CM at day 1 (Figure 4.6A). However, by day 7, this improvement was no longer statistically significant, though a trend toward enhanced viability in AM cultures persisted (CM vs. AM = -30%, $p = 0.0561$, Figure 4.6B).

After derivation in 2D, iBMECs were bioprinted or seeded in 2D onto fibronectin/collagen IV-coated wells. At day 1, when cultured in the suggested media from Neal et al. (Neal et al., 2019) (human endothelial serum-free medium with 0.5% B27 supplement, herein referred to as endothelial medium (EM)), 2D bioprinted iBMECs showed comparable viability to non-printed iBMECs plated manually in the gel with a pipette (Figure 4.6C). Culturing iBMECs in ScienCell AM increased the viability of 2D bioprinted iBMECs compared with EM at day 1.

Unlike in CMEC cultures, iBMECs are known to be more fragile, and exhibited poorer viability during passaging (Linville et al., 2022), a property our results echoed (Figure 4.7). Accordingly, we investigated the introduction of a rho-associated protein kinase inhibitor, Y-27632 (ROCKi) to support the survival and proliferation of iBMECs after the bioprinting process. By applying 10 μM ROCKi, cell viability of 2D bioprinted iBMECs was increased in both EM and AM conditions, with AM + ROCKi supporting the highest viability cultures (Figure 4.6C). After 7 days, good viability was evidenced in all AM-containing conditions, which reached 100% confluency, while EM conditions showed markedly lower viability (Figure 4.6D).

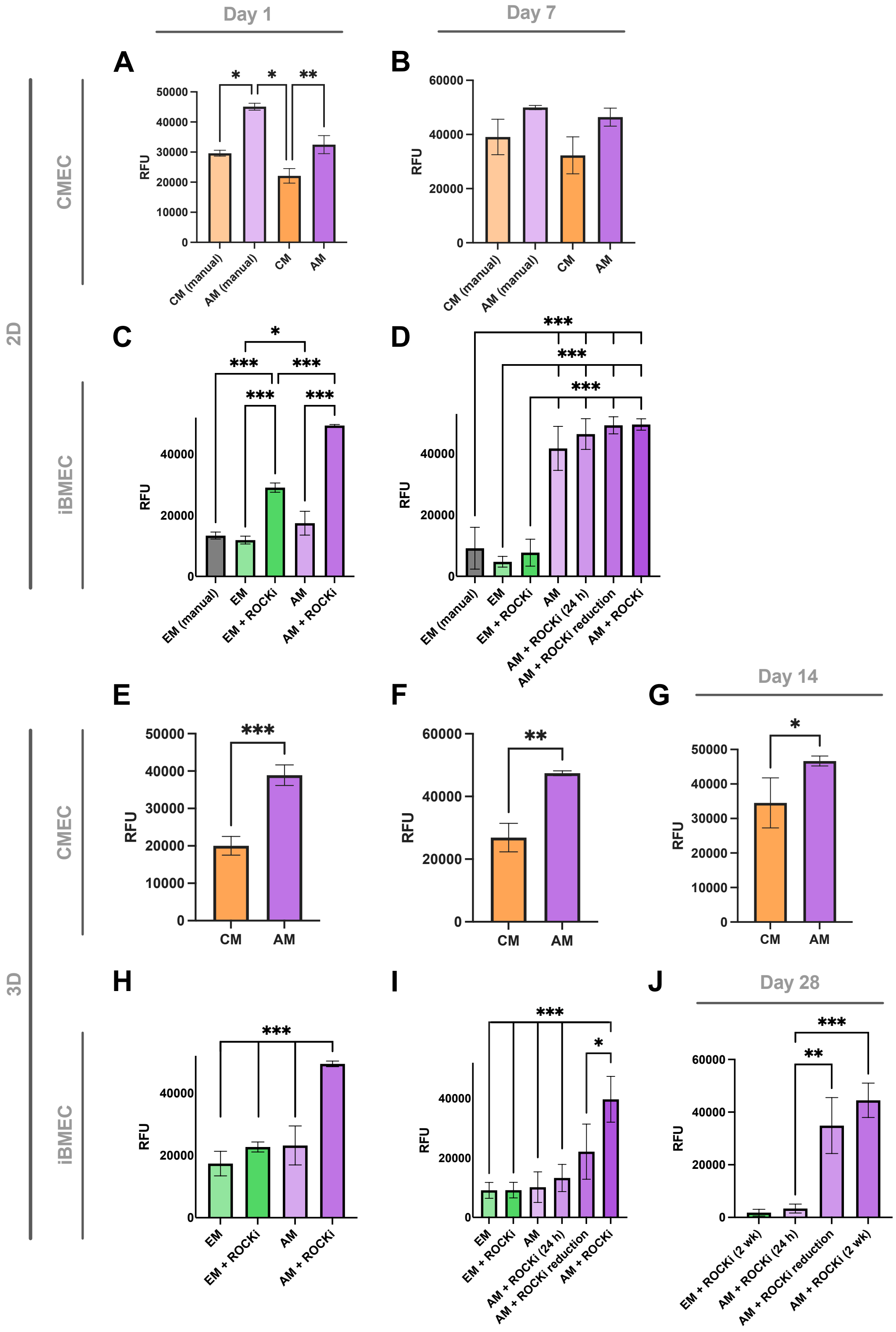

Figure 4.6: Viability of 2D and 3D bioprinted iBMEC and CMEC cultures. Comparison of raw fluorescence units (RFU) after 4 h incubation with CellTiter-Blue in 2D cultures at day 1 (**(A)**: CMEC, **(C)**: iBMEC) and day 7 (**(B)**: CMEC, **(D)**: iBMEC), and in 3D cultures at day 1 (**(E)**: CMEC, **(H)**: iBMEC), day 7 (**(F)**: CMEC, **(I)**: iBMEC), and **(G)** day 14 CMECs and **(J)** day 28 iBMECs. Graphs are presented as mean ± SD of $n \geq 3$ independent experiments. Means of all conditions are compared using a one-way ANOVA with Tukey's multiple comparisons test. $^{*}p < 0.05$, $^{**}p < 0.01$, and $^{***}p < 0.001$. AM, Astrocyte Medium; ANOVA, analysis of variance; EM, endothelial medium; iPSC, induced pluripotent stem cell; ROCKi: Rho-associated coiled-coil kinase inhibitor.

CMECs bioprinted in 3D PEG matrices displayed greater media dependency than in 2D cultures. At 24 hours post-bioprinting, cell viability was markedly higher in AM-containing media ($p = 0.0009$, Figure 4.6E), though this difference became less pronounced by day 7 ($p = 0.0015$, Figure 4.6F) and day 14 ($p = 0.0463$, Figure 4.6G). CMEC cultures were harvested for analysis at day 14 to prevent overconfluency, whereas iBMEC cultures were cultured until day 28 due to slower growth.

iBMECs bioprinted in 3D PEG matrices in comparison to 2D, displayed cell viability that was more media-dependent. At day 1, CellTiter-Blue results demonstrated that AM + ROCKi provided significantly higher cell viability than EM and AM without ROCKi (Figure 4.6H). iBMECs cultured in AM + ROCKi displayed a sufficient percentage of viable cells (67.71% ± 11.28 SD; Figure 4.7A). iBMECs in EM + ROCKi showed similar viability (56.75% ± 14.67 SD Figure 4.7A) but contained a high proportion of atypical nuclear staining that was delocalized from either calcein AM (live) or EthD (dead) staining, lowering the number of live cells per counting frame (Figure 4.7B, 4.7C). This mirrors CellTiter-Blue results that indicate EM provides suboptimal conditions for iBMEC survival in this system. In the two conditions that did not contain ROCKi, calcein AM staining was rarely associated with a typical live-cell morphology or appropriate nuclear staining (white arrows, Figure 4.7B). Because of this, live-cell counts were impractical, but this atypical live/dead finding corroborates CellTiter-Blue results suggesting poor viability in these conditions.

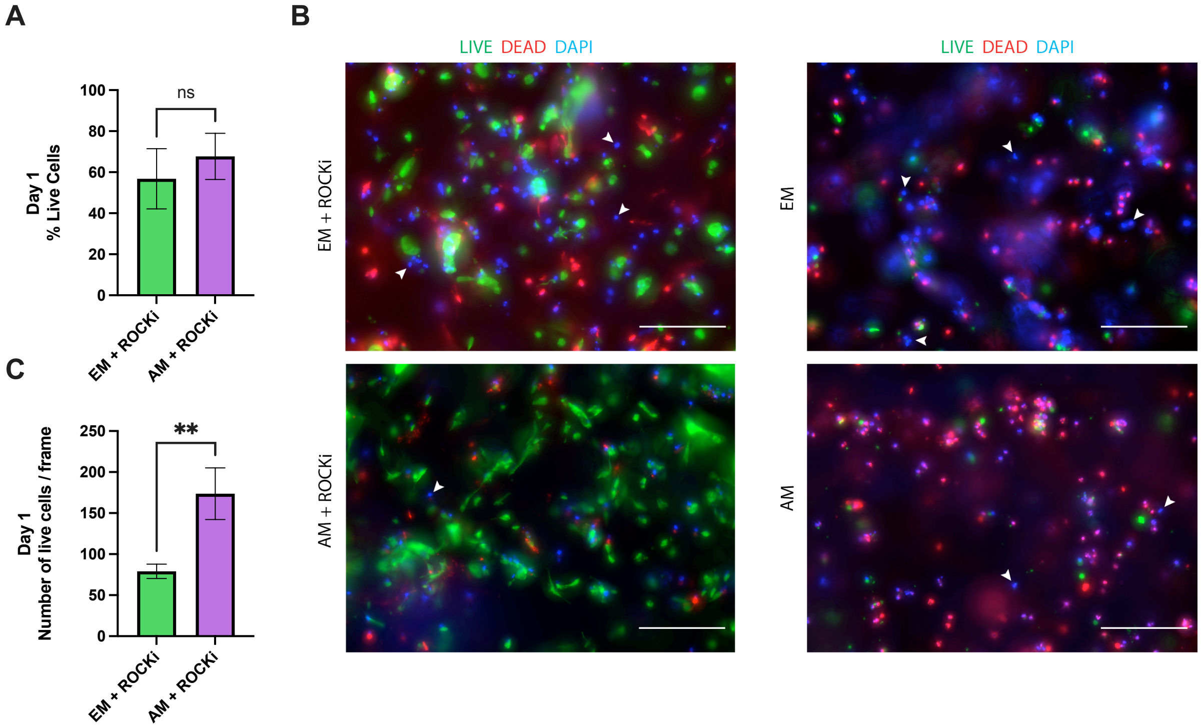

Figure 4.7: iBMECs exhibit media-dependent viability post-bioprinting. (A) Percentage of live iBMECs at day 1 post-bioprinting identified by Live/Dead staining were compared using an unpaired t-test. **(B)** Maximum intensity projections of iBMECs at day 1 cultured in endothelial medium (EM) or astrocyte medium (AM), with or without Rho-associated coiled-coil kinase inhibitor (ROCKi). LIVE: calcein AM, DEAD: EthD, DAPI (4′,6-diamidino-2-phenylindole): nucleus. White arrows indicate examples of atypical nuclear staining. Scale bar = 200 µm. **(C)** Number of countable live cells identified by Live/Dead staining were compared using an unpaired t-test (** $p < 0.01$).

At day 7, 3D bioprinted iBMECs cultured in AM+ROCKi retained high viability measured by CellTiter-Blue, while those cultured in EM (with or without ROCKi), and AM without ROCKi retained their comparably low viabilities (Figure 4.6I). Typically, ROCKi is removed after 24 h in culture (AM + 24 h ROCKi), however iBMEC viability significantly declined after the removal of ROCKi 24h post-bioprinting, compared with culturing in AM with daily ROCKi replacements, which had significantly higher viability than all other conditions. Unfortunately, ROCKi application may have deleterious effects on endothelial cell pathways (Cao et al., 2017). Therefore, a reduction scheme was devised to limit exposure, whereby ROCKi concentration was reduced by 2 µM per day starting on day 1 (AM + ROCKi reduction) (Figure 4.6D, I, J). At day 7, the viability of AM + ROCKi reduction was not significantly different from

AM + 24 h ROCKi (Figure 4.6I). By day 28, however, iBMECs cultured in AM with 2 weeks ROCKi, and the ROCKi reduction scheme show comparably high viability, compared with the significantly poorer viability in EM + ROCKi and AM + ROCKi (24h) conditions (Figure 4.6J). This is corroborated by live-cell counts, showing live-cell percentages for AM + ROCKi (66.58% ± 23.67 SD) and AM + ROCKi reduction (75.94% ± 3.68 SD) that are not significantly different (p = 0.54).

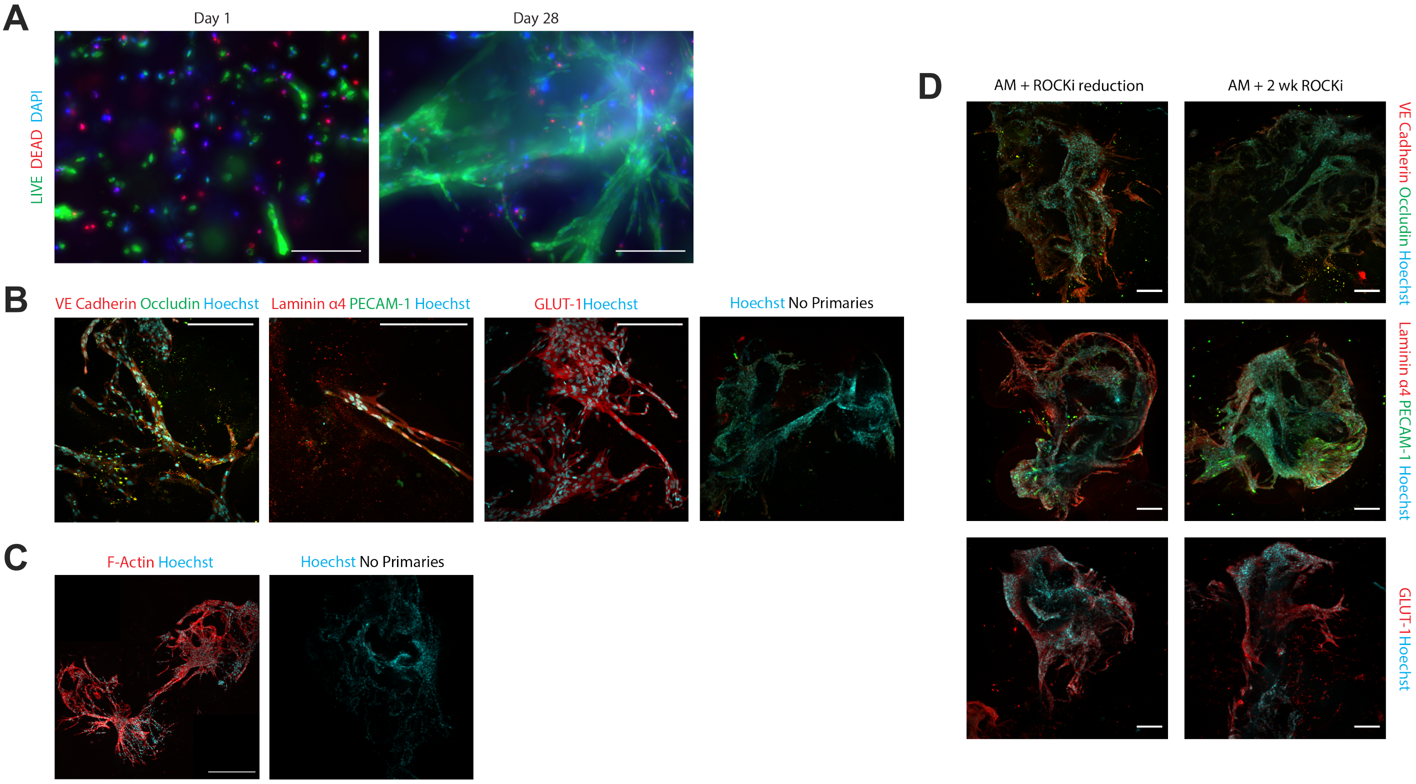

Figure 4.8: Immunofluorescent marker expression of 3D bioprinted iBMECs on day 28. (A) Maximum intensity projections of iBMECs at days 1 and 28, stained with calcein AM (LIVE) and Ethidium Homodimer-1 (DEAD). Scale bar = 200 µm. **(B)** Maximum intensity projections of the expression of vascular endothelial (VE) cadherin, occludin, laminin α4, platelet endothelial cell adhesion molecule-1 (PECAM-1), and glutamate transporter 1 (GLUT-1) by iBMECs. Scale bar = 200 µm. **(C)** Maximum intensity projection of F-actin staining of iBMECs shows the development of a complex network throughout the matrix. Scale bar = 500 µm. **(D)** Maximum intensity projections of 3D iBMECs at Day 28 under different media conditions showing expression of VE cadherin, occludin, laminin α4, PECAM-1 and GLUT-1. Scale bar = 200 µm.

At day 28 for iBMECs and day 14 for CMECs, cultures expressed markers and displayed cell morphology similar to *in vivo* vascular formations, progressing from small, rounded, singularized cells at day 1, to elongated multicellular structures that mimic *in vivo* vascular networks at day 28 (Figure 4.8A). The positive staining shown by these iBMEC networks included the adherens junctions protein VE cadherin, the adhesion protein, platelet endothelial cell adhesion molecule-1 (PECAM-1), the tight junction protein, occludin, the ECM protein, laminin α4, and the functional glucose transporter-1 (GLUT-1) (Figure 4.8B). The structural complexity of the vascular networks is highlighted by the staining of F-actin (Figure 4.8C). These markers were expressed when cultured under ROCKi for 2 weeks, or the ROCKi reduction scheme (Figure 4.8D).

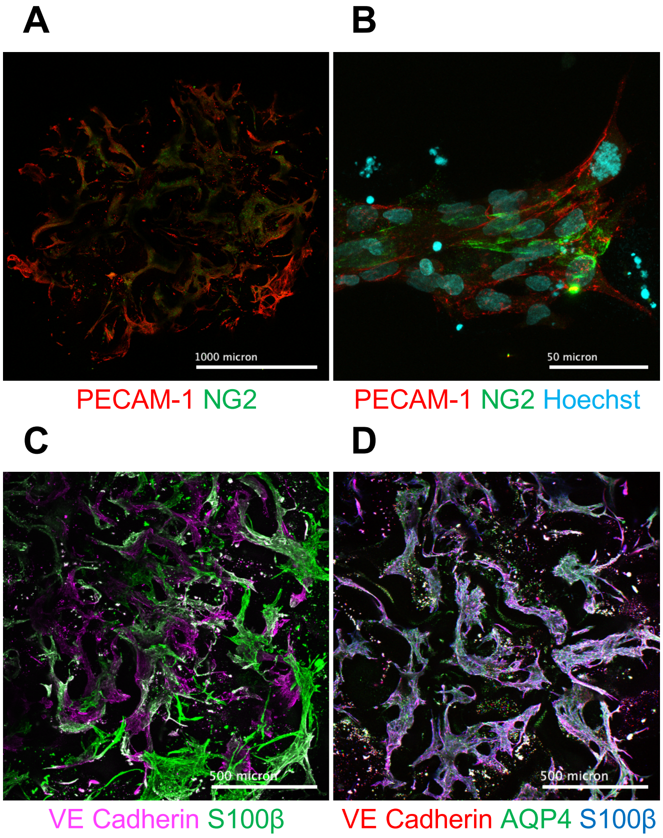

Figure 4.9: Immunofluorescent characterisation of 3D tricultures containing CMECs, HBVPs and human astrocytes. Images are displayed as maximum intensity projections. **(A)** Whole gel image of triculture labelled for platelet endothelial cell adhesion molecule-1 (PECAM-1; red) and neural/glial antigen 2 (NG2; green). Scale bar represents 1000 µm. **(B)** 93× magnification image of NG2-positive (green) cells flanking PECAM-1-positive (red) endothelial cells with Hoechst-positive (cyan) nuclei. Scale bar represents 50 µm. **(C)** Distinct expression of astrocytic and endothelial markers (VE cadherin = magenta, S100β = green). Scale bar represents 500 µm. **(D)** Close but distinct expression of astrocytic and endothelial markers (VE cadherin =

red, AQP4 = green, S100β = blue). Scale bar represents 500 μm. Abbreviations: AQP4: Aquaporin 4, NG2: Neural/Glial Antigen 2, S100β: S100 Calcium-Binding Protein β, VE cadherin: Vascular Endothelial Cadherin.

4.2.3. Characterising bioprinted vascular tricultures

Next, a triculture, using CMECs, HBVPs and human astrocytes was printed, and analysed using the optimised immunofluorescence staining protocol. This used the same 5 x 10^6 cells/mL seeding density as section 4.2.2, and a ratio of 50:25:25 endothelial cell:pericyte:astrocyte adopted from Nzou et. al. (2020b).

Immunocytochemistry was performed after 2 weeks upon formation of robust structural self-assembly. Whole gel imaging showed similar formation of a complex, PECAM-1-positive tubular network to the endothelial-pericyte co-culture condition (Figure 4.9A). Higher magnification imaging highlighted the close association of cell-specific markers. In figure 5B, NG2-positive pericytes are observed to flank PECAM-1-expressing endothelial cells. Endothelial VE cadherin and astrocytic AQP4 and S100β are seen to occupy the same structures, with distinct expression patterns, paralleling the *in vivo* environment where astrocytes envelop endothelial vascular tubes (Figure 4.9C,D). The AQP4 channel expressed on astrocytic endfeet also displays a closely related but distinct expression pattern (Figure 4.9D).

Upon replacing immortalized endothelial and primary astrocyte cell lines with iPSC-derived cell types, we observed that bioprinted iPSC-derived tricultures reached confluency faster. By day 14, this resulted in the formation of high-density cultures, which contracted in size. Significant cell death was observed at the core of the cultures, evidenced by central EthD staining. However this necrotic core was surrounded by calcein AM-positive, morphologically developed cells (Figure 4.10). This is an issue commonly encountered in floating organoids cultured past a critical size, where diffusion of nutrients and media to the central regions becomes insufficient, leading to a viable shell surrounding a necrotic core (Monzel et al., 2017). These findings suggest that this endothelial-pericyte-astrocyte triculture generated robust vascular-like structures with *in vivo*-reminiscent organization and marker expression, while revealing critical questions in cell type ratio, and bioprinting density when translating into iPSC-derived models.

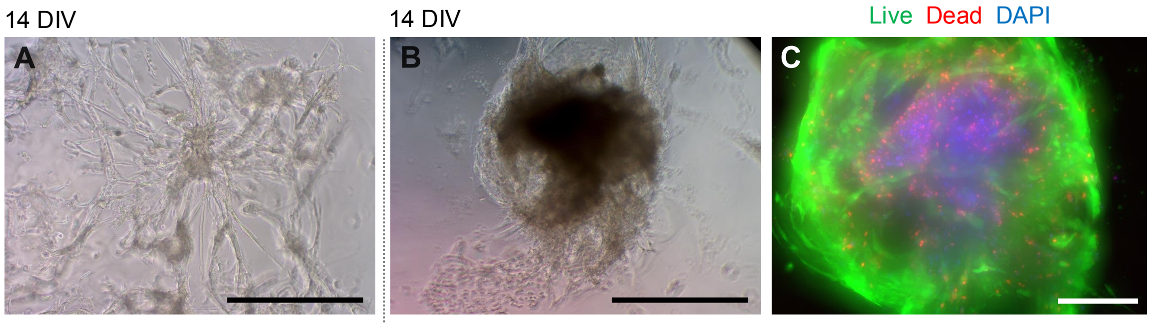

Endothelial Cell: Immortalised
Pericyte: Primary
Astrocyte: Primary

Endothelial Cell: iPSC-derived
Pericyte: Primary
Astrocyte: iPSC-derived

Figure 4.10: Observation of cell-type specific growth dynamics in neurovascular tricultures. At 14 days, neurovascular tricultures consisting of CMECs, HBVPs, and primary astrocytes show development of vascular-like morphology (left). In 14 day tricultures consisting of iBMECs, human brain vascular pericytes and iAstrocytes, cultures become overconfluent and form a necrotic core (centre, right). Live (green): Calcein AM-stained, Dead (red): Ethidium homodimer-1-stained, DAPI (blue; 4′,6-diamidino-2-phenylindole): nuclei. Scale bar represents 500 µm.

4.3. *Discussion*

The 3D monocultures and tricultures described here confirm that viable, multicellular vascular structures can be generated via Rastrum-mediated bioprinting in novel PEG-based hydrogels. This provides a foundation for the application of these nascent constructs to AD-modelling and drug discovery efforts.

4.3.1. Vascular bioprinting development

Initial bioprinting of CMEC and HBVP monocultures and co-cultures confirmed that the bioprinting process and hydrogel composition was suitable for producing viable endothelial and pericyte mono- and co-cultures. while also allowing for methodological development to ensure accurate immunofluorescent characterisation.

Building on prior optimization of PEG-based hydrogels for astrocyte biocompatibility, our investigation highlights the role of adhesion peptides and matrix stiffness on astrocyte viability and morphology in 3D cultures (Sullivan et al., 2023). Previous research in our lab indicated that hydrogels containing RGD and YIGSR peptides, and full-length collagen IV were well-suited for promoting cell viability and structural features. Here, we explored the viability of a softer 1.1 kPa gel, as recommended for better bioprinter ejection properties, alongside standardizing RGD and YIGSR peptide concentrations. This confirmed that human astrocytes tolerate variations in gel stiffness and adhesion peptide standardization without significant impact to viability or structural features. These findings underscore the flexibility of this PEG bioprinting system to support astrocyte cultures across a range of mechanical properties, aligning with reported brain stiffnesses (Axpe et al., 2020, Weickenmeier et al., 2016).

However, the transition from free collagen IV to shorter collagen-derived peptide sequences introduced unforeseen challenges. While replacement peptides did not affect astrocyte viability or bipolar morphology, the bioinks demonstrated notable variability in gelation characteristics. Observations of inconsistent gel appearance that were not observed in gels without the novel bioinks indicate potential consequences to hydrogel integrity, affecting experimental replicability. This variability in gelation likely arises from minor conformational differences in the adhesion peptide sequences tested. As the amino acid flanking regions modulate peptide binding availability, subtle changes in peptide conformation may affect gel formation and stability, although it is unclear why this would differentially affect replicate wells within the same plate (Floquet et al., 2004). Such variability underscores the importance of precise structural consistency in bioinks intended for 3D culture models and the need for ongoing evaluation to balance biofunctionality with reproducibility. In light of these observations, the 1.1 kPa hydrogel with collagen IV was chosen for use in Chapter 5, given its reliable gelation and support of astrocyte viability.

4.3.2. Bioprinted endothelial monocultures

To model the endothelial component of the neurovascular unit, iBMECs and CMECs were each bioprinted in monoculture using the 1.5 kPa hydrogel with collagen IV. The 1.5kPa gel was used over the 1.1kPa gel for experimental consistency within a published body of work (Sullivan et al., 2023). The monoculture approach enabled detailed analysis of changes in viability, and observation of self-assembled cellular morphology within the constructs, confirming the scaffold's value in supporting endothelial survival and identity.

Furthermore, we show that both iBMECs bioprinted in the 1.5 kPa hydrogel and cultured in AM with tapered ROCK inhibition remain viable for up to 4 weeks. ROCK inhibition is commonly employed *in vitro* to support the differentiation, expansion, and cytoprotection of brain endothelial cells (Joo et al., 2012, Niego et al., 2017), yet studies have indicated that prolonged exposure may disrupt VE cadherin junctions and modulate actin/myosin dynamics (Cao et al., 2017). Interestingly, iBMECs cultured with our novel, exposure-limiting ROCKi reduction scheme retained comparable viability, and morphology to those in the 2-week ROCKi culture protocol, suggesting that controlled ROCKi tapering could balance cytoprotection and barrier functionality. The effects on VE cadherin dynamics were not investigated here, but examined in Chapter 5. Additionally, the sustained expression of key junctional proteins (PECAM-1, VE cadherin, and occludin) and functional markers such as laminin α4 and the glucose transporter GLUT-1 throughout 28 days implies that both iBMECs and CMECs maintain their BBB-specific identity and function over extended culture periods, highlighting the suitability of this ROCKi strategy for long-term neurovascular unit models.

The iBMEC monocultures exhibited substantial vasculogenic-like self-assembly, a critical feature often overlooked in many current 3D endothelial models that rely on manual seeding or structural predefinition of the vascular channel (Brassard and Lutolf, 2019, Grebenyuk and Ranga, 2019). This dynamic structuring in iBMECs echoes similar behaviour in Matrigel, fibrin, and GelMA environments (Blanchard et al., 2020, Calderon et al., 2017), underscoring our system's potential for faithfully capturing endothelial morphologies and functions.

The iBMEC derivation protocol requires a 2D, selective attachment step, which necessitates 100% confluency of the cells before removal of retinoic acid and bFGF to complete the derivation. Unfortunately, this means iBMECs are only available for bioprinting 2-3 days after being held at 100% confluency. While this ensures complete differentiation, the metabolic and proliferative consequences of the cells enduring full confluency is unknown.

Finally, we observed bioprinted CMECs reaching high-confluency sooner than bioprinted iBMECs. Indeed, iBMECs may possess poorer growth characteristics because of the necessity of full confluency before bioprinting (Neal et al., 2019). This differential growth pattern between the two cell types suggests that, while iBMECs retain key BBB-like characteristics, CMECs may provide a quicker, more consistent cell line for drug development applications due to their robust growth and endothelial specificity. This observation has important implications for the design of neurovascular models tailored to specific research needs, from BBB integrity to drug transport studies, and reinforces the value of using CMECs alongside iBMECs in neurovascular research.

One limitation of our bioprinted iBMEC and CMEC models is their inability to support perfusion, limiting their utility for studies requiring fluid dynamics, such as barrier transport and mechanical stimulation. Models that incorporate fluid flow, such as perfusion-based systems (Kurosawa et al., 2022, Zhao et al., 2023), may therefore be better suited for applications in dynamic BBB functionality. However, our bioprinting method offers significant advantages in terms of automated fabrication, customizable gel compositions, high-throughput, and compatibility with standard plate formats, which enhance its applicability for mechanistic studies of vascular cell behaviour and model reproducibility. These attributes underscore the importance of developing a diverse toolkit of 3D modelling techniques to advance our understanding of *in vitro* vascular biology.

4.3.3. Bioprinting vascular tricultures

Building on this foundation of improved media composition for bioprinting of endothelial monocultures, vascular tricultures were bioprinted to integrate pericytes and astrocytes alongside endothelial cells, emulating a more comprehensive neurovascular environment. The results demonstrated robust cellular organization, in the primary/immortalized neurovascular triculture, validating the hydrogel matrix as conducive to multicellular structuring. Immunocytochemical staining revealed distinct, organized expression patterns of endothelial, pericytic and astrocytic markers.

In progressing these tricultures to iPSC-derived cell types, we observed that the resulting high-density cultures developed a necrotic core by day 14, a phenomenon well-documented in CNS organoids and other bioprinted models (Mihara et al., 2019, Monzel et al., 2017). This cell death likely results from limited nutrient and oxygen diffusion as the culture density increases, an issue that may be addressed by reducing cell seeding density. Another possible cause of this overgrowth is the addition of VEGF and PDGF-BB to the culture media, a technique used in the literature when seeding 3D neurovascular tricultures in Matrigel, presumably to promote survival and cell-cell communication (Blanchard et al., 2020). Removal of these known proliferative factors may dampen excessive proliferation to allow more recapitulative construct development, although it is curious that addition of these factors to tricultures using immortalised/primary cell lines did not elicit the same effect. An additional consideration here is the hydrogel stiffness used. These tricultures were bioprinted using the 1.1kPa gel, which has more MMP-degradable sequences compared to the 1.5kPa gel, increasing cell motility but potentially increasing susceptibility to gel degradation. One future avenue of investigation may focus on the differential expression of functional MMPs in primary vs. iPSC-derived vascular cell types.

Furthermore, selecting an optimal cell-type ratio for the triculture remains challenging, as certain ratios may mitigate or exacerbate the observed core necrosis due to varying metabolic demands or cell-independent proliferative capacity (Hribar et al., 2015). It is unclear whether one of the three cell types is more likely to induce overgrowth. Endothelial cells, pericytes and astrocytes can all respond proliferatively to either VEGF or PDGF-BB, while the impact of co-culturing (and subsequent release of proliferation mediators) could also induce this behaviour (Emerich et al., 2010, Krum et al., 2008, Guo et al., 2011, Gaceb et al., 2017, Bethel-Brown et al., 2011). Although modest attempts exist, there are no widely accepted consensus values for cell type ratios in the human brain. With research mainly focussed on neuron and general glia numbers, specific areas, such as the neurovascular unit are poorly understood (Miao et al., 2023, Keller et al., 2018). Stark methodological differences, the impact of post-mortem handling on tissue integrity, and unclear marker specificity hamper these efforts, but trends in multicellular *in vitro* models provide examples of effective approaches. In Chapter 4.2.3, four different endothelial:pericyte:astrocyte ratios were trialled with ratios from the literature: 2:1:1 (Nzou et al., 2020b, Urich et al., 2013), 2:1:2 (previous ratio with increased astrocyte number), 1:1:5 (Nzou et al., 2018), to examine if differing ratios had noticeable consequences upon inspection of brightfield images (data not shown). There were minimal noticeable differences apparent by qualitative visual inspection (although this was n = 1). Thus, immunofluorescent interrogation was performed on cultures in the 2:1:1 ratio, because this had been used successfully in multiple studies, and had proved amenable for further incorporation of other CNS cell types (Nzou et al., 2020b, Urich et al., 2013). Previous studies in neurovascular and parenchymal cultures, as well as peripheral organoid systems, highlight the necessity of precise ratio and methodological tuning to observe experimental outcomes (Nzou et al., 2018, Song et al., 2019). Although vascular cell-specific ratios weren't explored, Song et al. (2019) found that fusion of different ratios of MSCs, neural spheroids and endothelial spheroids significantly affected VEGF and FGF2 signalling, endothelial PECAM-1 expression, and differential regulation of

MMPs, P-gp and GLUT-1. Newer brain atlas efforts using novel sequencing techniques will undoubtedly make progress in this area in the near future, empowering the environment-appropriate construction of modular neurovascular cultures (Chen et al., 2024).

Once these models are further optimised, the translation of these techniques to more disease-relevant iPSC-derived cell types will further maximize the translational capacity of this model. Specifically, the incorporation of gene-edited, *APOE4* and control iPSC lines will allow novel access to poorly understood facets of AD pathobiology, in a platform that is highly relevant to the *in vivo* context, easily scalable for drug discovery efforts, and readily adaptable for investigating other diseases with complex multicellular milieus. Further development and analysis of bioprinted triculture systems such as these will enable their use as drug discovery tools by adding higher throughput and replicability to previously low-throughput disease modelling systems. Recent advancements in non-neurovascular bioprinted co- and tricultures highlight the potential of these systems to simulate complex *in vivo* environments with unprecedented fidelity (Yee et al., 2024, Russell et al., 2023, Sun et al., 2024). As this field progresses, expanding the applicability of such models to neurovascular diseases will yield valuable insights into disease mechanisms and therapeutic efficacy.

4.3.4. Chapter Summary

This chapter showcased the progressive development of bioprinting techniques to create vascular models of increasing complexity, from endothelial monocultures to integrated vascular tricultures. These findings underscore the significance of considered hydrogel and media composition to maintain appropriate viability and morphology within 3D bioprinted environments. A novel vascular triculture was established, achieving robust multicellular organization and cell-specific marker expression reminiscent of *in vivo* neurovascular structures.

Critically, this model's modular design and adaptability to iPSC-derived cell types underpin its potential as a replicable and scalable tool for drug discovery. The future optimised incorporation of iPSC-derived cells opens the possibility for disease-relevant adaptations, such as the integration of gene-edited APOE4 lines for Alzheimer's disease modelling. This flexibility positions this neurovascular unit model as a valuable platform for investigating neurovascular contributions to AD pathobiology, where the interplay between pathogenic proteins and vascular constituents is poorly understood. While challenges remain regarding cell-type-ratios and appropriate growth factor additions in iPSC-derived tricultures, the neurovascular model developed in this chapter offers a replicable, high-throughput approach to studying neurovascular interactions and disease mechanisms. In the next chapter these cultures will be manipulated to interrogate AD-related neurovascular dynamics, advancing our understanding and potentially informing therapeutic strategies.

Supplementary Figure 4.11: Lack of non-specific binding in immunofluorescent images from 3D bioprinted HBVPs and CMECs. Immunofluorescent images of 3D bioprinted HBVPs and CMECs. Abbreviations: CMEC: Cerebral Microvascular Endothelial Cell, HBVP: Human Brain Vascular Pericyte, NG2: Neural/Glial Antigen 2, PDGFRβ: Platelet-Derived Growth Factor Receptor β, PECAM: Platelet Endothelial Cell Adhesion Molecule-1. Scale bar represents 500 µm

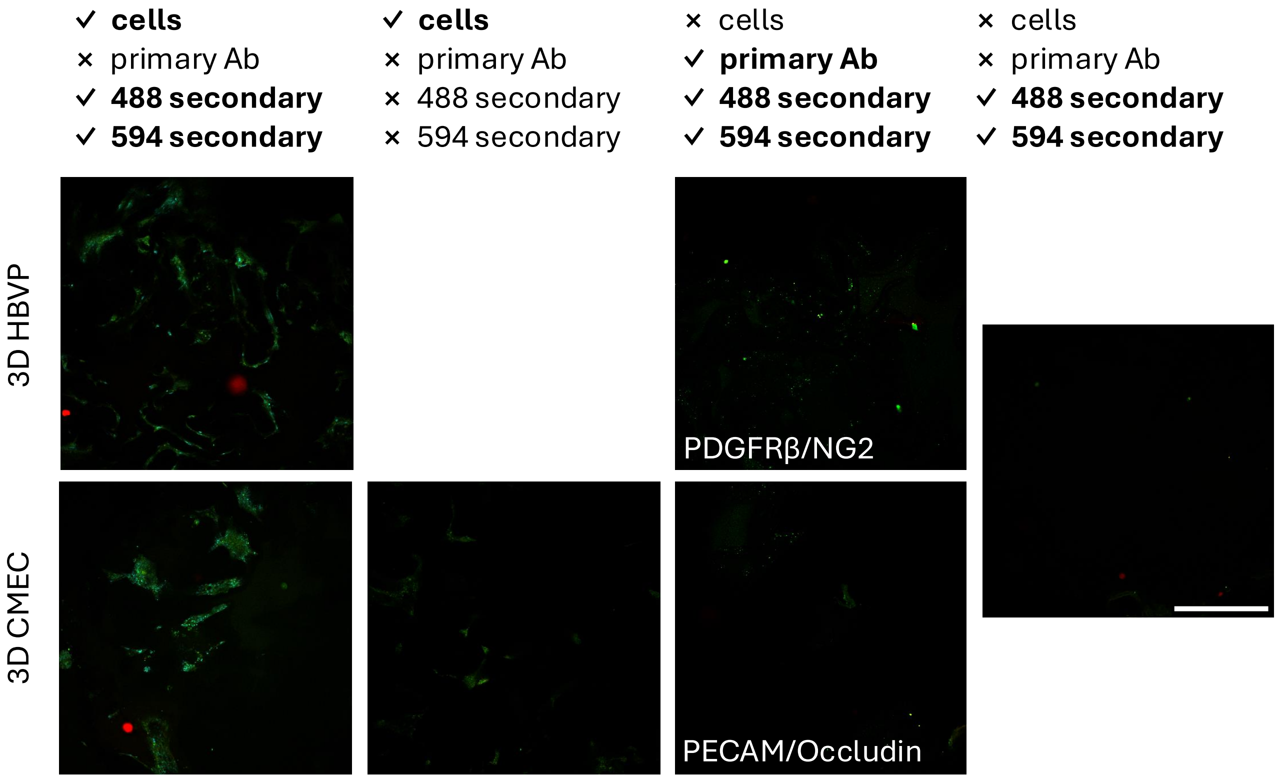

Supplementary Figure 4.12: Constructs bioprinted using novel collagen IV peptide-containing bioinks display poor visual replicability. Representative brightfield images . Bioink A (C**MNYYSNS**KK), Bioink B (C**MNYYSNS**GGKK), Bioink C (CG**MNYYSNS**KK), Bioink D (CD**MNYYSNS**KK), Bioink E (C**NYYSNS**GGKK). Scale bar represents 500 µm

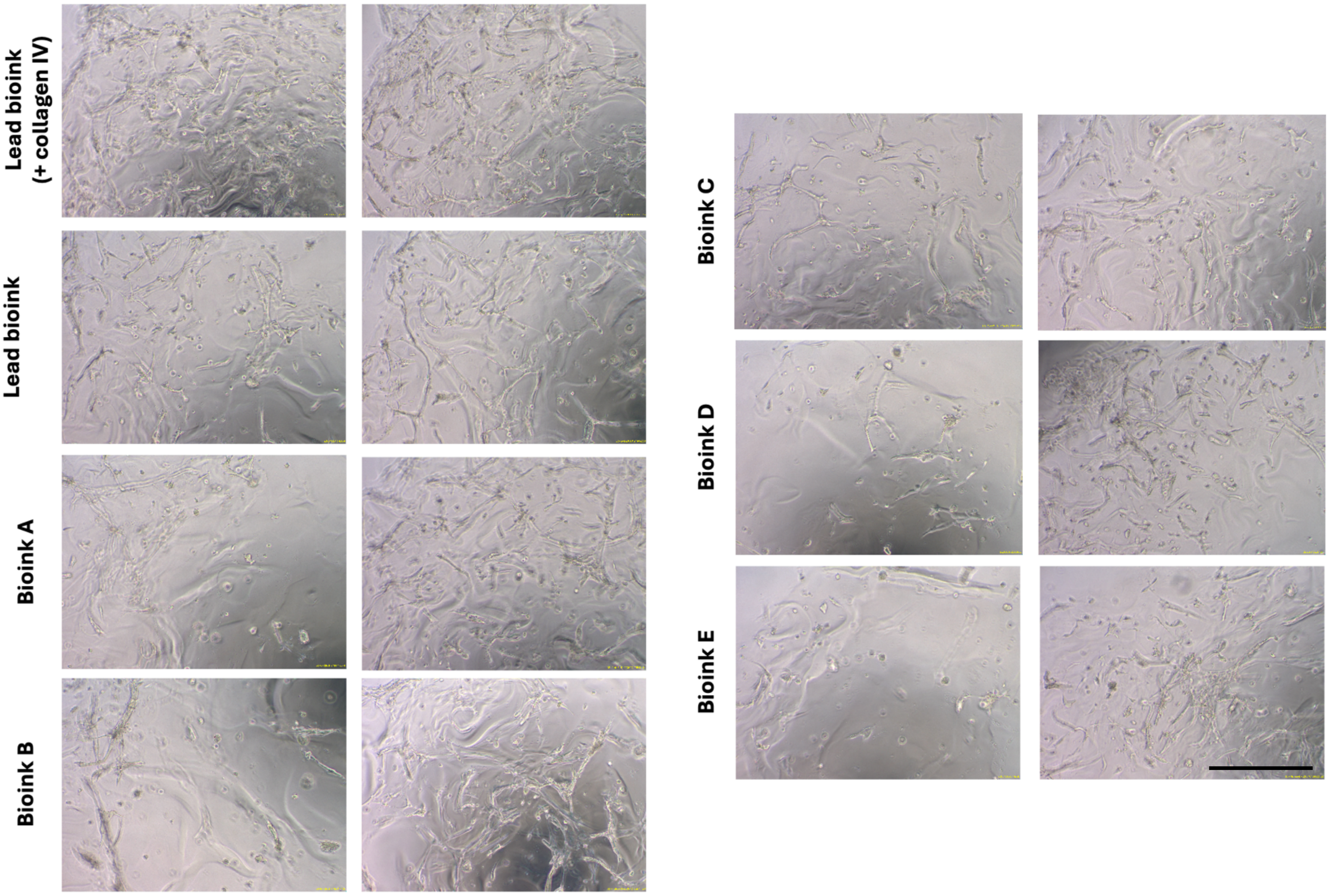

Chapter 5: Amyloid β and lipopolysaccharide treatment of 3D, bioprinted endothelial monocultures

5.1. Introduction

The neurovascular unit, composed of endothelial cells, pericytes, and astrocytes, is a complex interface that governs BBB integrity, cerebral blood flow and modulation of neuroinflammatory responses. This key nexus between the brain and periphery has also been implicated in the progression of AD pathology, and is a critical entity to replicate in the search for therapeutic strategies (Sweeney et al., 2018). The main pathological hallmark of AD, Aβ, exists in multiple isoforms, of which $A\beta_{40}$ and $A\beta_{42}$ are the most pathologically relevant (Kwak et al., 2020, Sengupta et al., 2016). These isoforms differ by only two amino acids but exhibit vastly different biophysical and pathological properties; $A\beta_{42}$ is more prone to aggregation, forming fibrils and plaques associated with AD, whereas $A\beta_{40}$ is the predominant form in cerebrospinal fluid and is implicated in vascular amyloid deposition and CAA (Jan et al., 2008, Herzig et al., 2006). The ratio of $A\beta_{42}$ to $A\beta_{40}$ has been proposed as a more informative way of measuring pathogenic Aβ as this ratio is higher in AD patients, and $A\beta_{42}$ is more susceptible to oligomerisation (Kwak et al., 2020, Sengupta et al., 2016). However, the presence of both $A\beta_{40}$ and $A\beta_{42}$ at the neurovascular unit can disrupt BBB integrity, trigger inflammation, and alter endothelial cell function, leading to neurovascular dysfunction that exacerbates AD pathology (Qosa et al., 2014, Li et al., 2022, Carrano et al., 2012).

The importance of studying Aβ at the neurovascular unit extends to its implications in CAA, a condition frequently co-occurring with AD and characterized by Aβ deposition in cerebral blood vessels. CAA contributes to cerebral microbleeds, increased risk of haemorrhage, and perivascular inflammation, all of which exacerbate cognitive decline (Janaway et al., 2014, Salvarani et al., 2016). Endothelial cells exposed to Aβ *in vitro* show altered tight junction protein expression, reduced TEER, and increased permeability, mirroring the vascular leakage and compromised BBB function observed in CAA and AD patients (Carrano et al., 2012, Kook et al., 2012, Marco and Skaper, 2006). The clearance of Aβ from the neurovascular unit is isoform-dependant, and differences in APOE genotype can further disrupt these clearance mechanisms

(Ding et al., 2024, Chang et al., 2013). *In vivo* studies reveal that while Aβ_{40} is more often deposited in the vasculature, Aβ_{42} is still critical for this deposition phenotype (McGowan et al., 2005). While the differential effects of Aβ_{40} and Aβ_{42} on endothelial cells have been studied, their deposition phenotype and effects on 3D endothelial cultures has not been investigated, particularly in the context of coexisting inflammatory stimuli.

Neuroinflammation significantly impacts endothelial cells in AD pathology by destabilizing the BBB and disrupting endothelial cell function. Exposure to LPS from bacteria such as *Escherichia coli* (ecLPS) and *Porphyromonas gingivalis* (pgLPS) induces a strong inflammatory response in endothelial cells, leading to the release of cytokines and chemokines that compromise BBB integrity (Lei et al., 2023). In particular, pgLPS, implicated in periodontal infection, is associated with AD progression due to its ability to elicit chronic inflammation, activate microglia, and exacerbate tau and Aβ pathology in preclinical models (Liu et al., 2024). When endothelial cells detect bacterial endotoxins via toll-like receptors, downstream signalling pathways are activated, increasing vascular permeability and extravasation of peripheral immune cells. This pro-inflammatory endothelial response not only disrupts BBB function but also fosters an environment conducive to Aβ aggregation, which in turn amplifies AD pathology (Nijhuis et al., 2003, Zullo et al., 2016). By weakening endothelial cell tight junctions and promoting oxidative stress, LPS-induced inflammation accelerates neurovascular damage, highlighting the importance of targeting endothelial inflammation in AD therapeutics and neurovascular models. Although LPS-induced neuroinflammation is implicated in BBB disruption and AD pathology, the effects of bacterial endotoxins on endothelial dysfunction and Aβ aggregation in a 3D bioprinted *in vitro* context has not been explored.

Recent advancements in *in vitro* models for studying the neurovascular unit aim to enhance human relevance and scalability for drug discovery purposes. Rodent models, which have traditionally dominated AD research, offer valuable insights into the mechanisms of Aβ accumulation and spread. However, interspecies differences in genetic, cellular, and neurovascular characteristics limit their translatability to human AD pathophysiology (McGraw et al., 2017). On the other hand, conventional 2D *in vitro* culture systems fall short of replicating the complex 3D microenvironment and multicellular interactions of the neurovasculature, resulting in altered cell morphology, gene expression, and functional properties that diminish the model's physiological relevance (Birgersdotter et al., 2005, Pound and Ritskes-Hoitinga, 2018). By leveraging technological advances such as iPSC-derived endothelial cells, and 3D bioprinting, it is now possible to create *in vitro* models that better replicate the structure and function of the human neurovascular unit.

Identifying drugs that can mitigate Aβ-induced neurovascular damage is central to the therapeutic development in AD. Traditional drug discovery approaches for AD have been limited by the lack of suitable models to predict human-specific neurovascular responses to Aβ and inflammatory stimuli. High-throughput 3D culture systems, like the PEG-based bioprinting system described in Chapter 4, allow for scalable testing of compounds and modulation of disease-relevant treatment, providing a unique platform to evaluate endothelial inflammation and Aβ deposition. By enabling systematic screening in a model that recapitulates key aspects of AD and CAA pathology, this approach has the potential to accelerate the discovery of novel therapeutics aimed at neurovascular targets in AD.

This chapter uses the 3D bioprinted endothelial cell monoculture model as a platform to develop scalable AD models using pathological treatments. By co-treating 3D bioprinted endothelial monocultures with two Aβ isoforms, plus ecLPS or pgLPS the cooperative interactions between these two critical pathological hallmarks are investigated. The viability, volume of deposited Aβ and relative expression of VE cadherin is measured to index endothelial integrity and understand how neuroinflammatory and amyloidogenic stressors synergize to disrupt the neurovasculature. Additionally, conditioned media from 3D bioprinted CMECs and iBMECs were investigated using a proteome array highlighting important differences in cell type functionality, and identifying key mediators that can serve as useful homeostatic and disease markers *in vitro*. These findings showcase a novel platform that can help elucidate the differential impacts of Aβ isoforms and inflammatory insults on endothelial function. The findings from these studies will inform the development of next-generation neurovascular models and therapeutic screening platforms, advancing our understanding of AD pathogenesis and the neurovascular contributions to disease progression.

5.2. Results

Endothelial cells were bioprinted in the 1.1 kPa PEG hydrogel with added collagen IV, and cultured for a total of 14 days (for CMECs which displayed faster growth) or 28 days (for iBMECs). 24 hours before analysis, cultures were treated with an inflammatory stimulus (10 µg/mL ecLPS, 10 µg/mL pgLPS) and a fluorescently-tagged Aβ stimulus (1 µM $A\beta_{42}$, 1 µM $A\beta_{40}$, 1 µM $A\beta_{42:40}$, or vehicle). Bioprinted CMEC cultures are observed to have comparable sizes and well positions, supporting the reproducibility of this bioprinting method (Figure 5.1). Cultures were then interrogated for viability, marker expression, Aβ deposition and structural features.

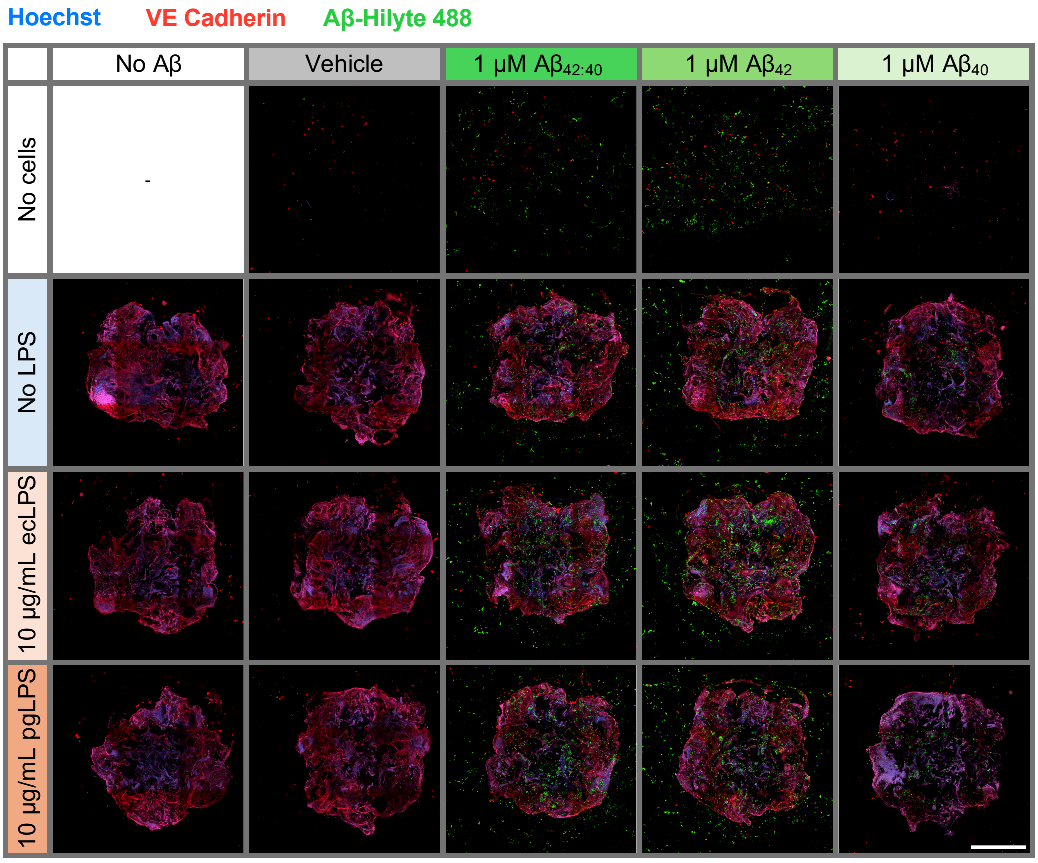

Figure 5.1: Representative immunofluorescent images of co-treated CMEC monocultures. Red: vascular endothelial cadherin, green: amyloid β (Aβ), blue, Hoechst. Abbreviations: ecLPS: Lipopolysaccharide from *Escherichia coli*, pgLPS: Lipopolysaccharide from *Porphyromonas gingivalis*, Vehicle: 0.5% ammonium hydroxide in phosphate buffered saline. Scale bar represents 1000 µm

5.2.1. *3D bioprinted endothelial monocultures remain viable after LPS and Aβ application*

Upon treatment of the endothelial constructs with inflammatory ecLPS or pgLPS, combined with Aβ treatments, CellTiter-Blue-measured cell viability did not significantly differ (Figure 5.2A,B). This includes comparisons within each inflammatory condition (between Aβ conditions) and within each Aβ condition (between inflammatory stimuli). Pooling the coefficient of variation for each cell line shows that iBMEC CellTiter-Blue fluorescence was significantly more variable than in CMECs (Figure 5.2C). This matched expectations, with a small number of iBMEC constructs appearing damaged or degraded in the second fortnight of culture, or during the immunofluorescence preparation thereafter.

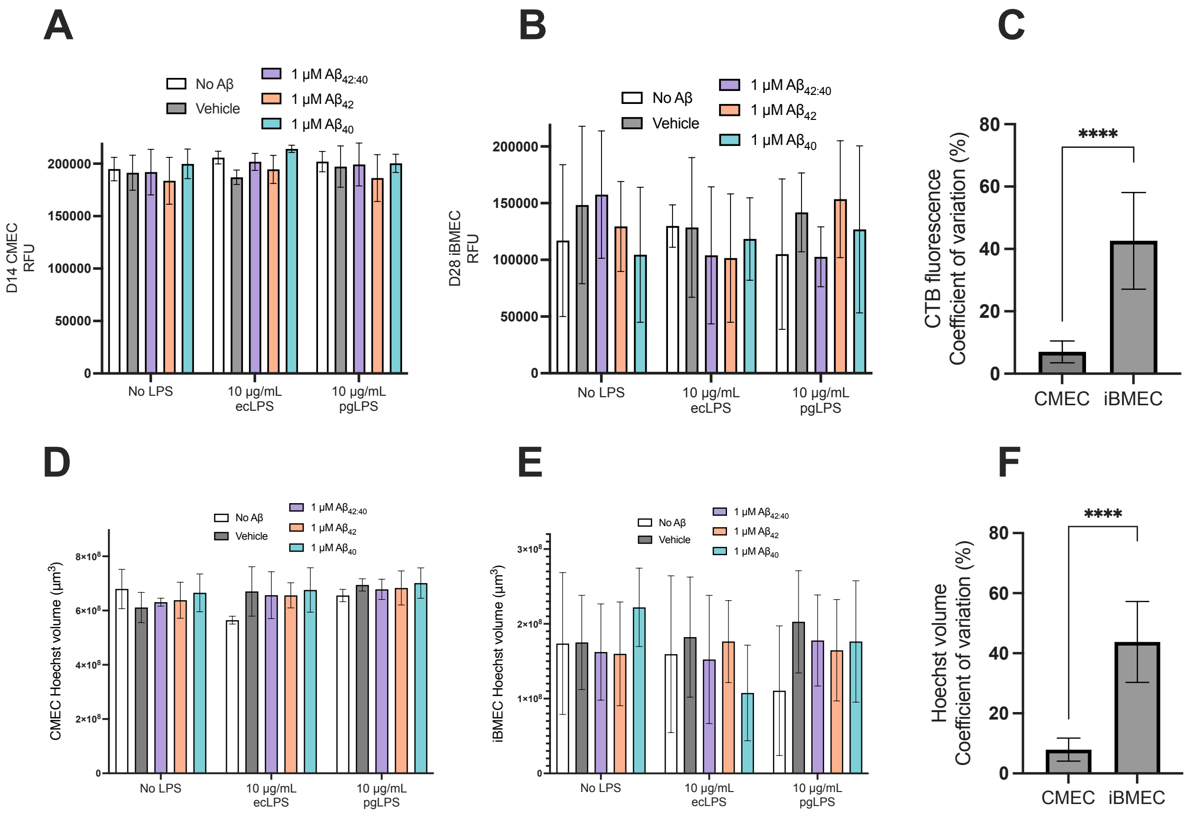

Figure 5.2: Viability and nuclei quantitation of 3D bioprinted CMEC and iBMEC monocultures. Metabolic viability as measured by raw fluorescence units (RFU) in a CellTiter-Blue (CTB) assay after **(A)** 14 days for bioprinted CMECs and **(B)** 28 days for bioprinted iBMECs. Data shown as raw fluorescence units (RFU) corrected by subtracting fluorescence elicited by media. One-way ANOVA with Šídák's multiple comparisons test was used to test for differences between treatment means and their vehicle. **(C)** Coefficient of variation for each CTB technical replicate, including all inflammatory- and Aβ-treatment conditions, were pooled to bioprinted CMEC and iBMEC groups (n = 15). An unpaired t-test with Welch's correction was used to test for difference in variation. Volume of measured Hoechst signal after **(D)** 14 days for bioprinted CMECs and **(E)** 28 days for bioprinted iBMECs. Data shown as cubic micrometers of measured signal. Two-way ANOVA with Tukey's multiple comparisons test was used to test for differences and interactions between inflammatory conditions and Aβ treatments. **(F)** Coefficient of variation for

each Hoechst volume technical replicate, including all inflammatory- and Aβ-treatment conditions, were pooled to bioprinted CMEC and iBMEC groups (n = 15). An unpaired t test with Welch's correction was used to test for difference in variation. All data are reported as mean ± SD from $n \geq 3$, performed in duplicate. Abbreviations: Aβ: amyloid β, ecLPS: Lipopolysaccharide from *Escherichia coli*, pgLPS: Lipopolysaccharide from *Porphyromonas gingivalis*, Vehicle: 0.5% ammonium hydroxide in phosphate buffered saline.

5.2.2. Aβ isoform and endothelial cell type affects Aβ deposition and VE cadherin expression in 3D bioprinted endothelial monocultures

After measuring viability, bioprinted constructs were imaged to index features of Hoechst expression, VE cadherin expression and deposition of fluorescent Aβ. Only the central tile of each 9-tile image was analysed to ensure the volume analysed contained comparable amounts of cell and hydrogel as this tile was reliably completely filled with 3D culture. Firstly, Hoechst-stained nuclear volume was compared across treatment conditions to provide a normalisation method relating to cell number at the time of analysis (although this measure does not perfectly index cell number, as nuclei size could differ between cell types). Hoechst-stained nuclear volume did not significantly differ based on Aβ or inflammatory insult, corroborating CellTiter-Blue viability (Figure 5.2D,E). By pooling the percent coefficient of variation from all cell containing conditions, higher variance in the volume of nuclear staining was observed between CMECs and iBMECs (Figure 5.2F), also echoing variance in viability measurements.

To evaluate amyloid deposition, the volume of fluorescent amyloid signal was normalized to Hoechst-stained nuclear volume. Across basal and inflammatory conditions in CMEC cultures, $A\beta_{40}$ signal was lower than both $A\beta_{42:40}$ and $A\beta_{42}$ (Figure 5.3A). Mean $A\beta_{42:40}$ signal measurements were between $A\beta_{40}$ or $A\beta_{42}$ in all conditions, suggesting that there was no synergistic effect of applying $A\beta_{42}$ and $A\beta_{40}$ together. In contrast, no differences were observed in retained Aβ signal between Aβ isoforms or inflammatory conditions in iBMEC cultures, although construct quality was variable (Figure 5.3B).

To evaluate VE cadherin expression, the volume of fluorescent amyloid signal was normalized to Hoechst-stained nuclear volume. Within endothelial cell types, Hoechst-normalised VE cadherin staining volume did not significantly differ between amyloid and inflammatory conditions (Figure 5.3C,D). However, CMECs expressed significantly more VE cadherin compared to iBMECs when compared within each treatment pair (Figure 5.3E,F)

Despite the lower total volume of $A\beta_{40}$ signal, this isoform colocalized with VE cadherin more frequently than $A\beta_{42}$ or $A\beta_{42:40}$ when applied to 3D bioprinted CMECs. This was quantitated by measuring the length of shared borders between Aβ and VE cadherin signals (Figure 5.3G) and by measuring the cumulative percentage of detected Aβ objects that colocalise with VE cadherin signals (Figure 5.3I). This colocalization pattern was not observed in iBMECs (Figure 5.3H,J), although it is likely that the lower replicability in iBMEC constructs affected statistical power (Figure 5.2C, 5.2F).

5.2.3. CMECs and iBMECs exhibit distinct basal inflammatory secretomes in 3D

To complement the 2D secretion profiles reported in Chapter 4, the basal secretion profiles of 3D bioprinted endothelial cells were investigated. Distinct secretion profiles have been reported in a number of 3D cultured vascular cell types, uncovering potential improvements in *in vivo*-relevant cell communication compared to 2D counterparts (Zhang et al., 2017b, Xie et al., 2017). The Proteome Profiler Human XL Cytokine Array was used to index basal protein secretion by comparing the mean total density between cell conditioned media, and media without cells.

Proteins significantly upregulated or downregulated in CMECs compared to basal media were: Dkk-1 ($q < 0.0001$, mean difference = -13728), RANTES ($q < 0.0001$, mean difference = -13220), PDGF-AB/BB ($q < 0.0001$, mean difference = -11583), CD31 / PECAM-1 ($q < 0.0001$, mean difference = -11096), IGFBP-3 ($q < 0.0001$, mean difference = -8949), angiogenin ($q < 0.0001$, mean difference = -8732), angiopoietin-2 ($q < 0.0001$, mean difference = -8229), IL-8 ($q < 0.0001$, mean difference = -7352), GROα ($q < 0.0001$, mean difference = -6652), MCP-1 ($q < 0.0001$, mean difference = -6396), EMMPRIN ($q < 0.0001$, mean difference = -5755), IGFBP-2 ($q < 0.0001$, mean difference = 7465), GDF-15 ($q < 0.0001$, mean difference = -5646), urokinase plasminogen activator receptor (uPAR; $q = 0.0002$, mean difference = -5480), stromal cell-derived factor-1α (SDF-1α; $q = 0.0009$, mean difference = -4807), PDGF-AA ($q = 0.0035$, mean difference = -4221), ST2 ($q = 0.0055$, mean difference = -3996), serpin E1 ($q = 0.0063$, mean difference = 3944), endoglin ($q = 0.0051$, mean difference = -3928), osteopontin ($q = 0.0089$, mean difference = 3780), pentraxin 3 ($q = 0.026$, mean difference = -3586), and thrombospondin-1 (q = 0.0328, mean difference = -3464) (Figure 5.4A, Table 5.1).

Proteins significantly upregulated or downregulated in iBMECs compared to basal media were: osteopontin (q < 0.0001, mean difference = -9189), chitinase 3-like 1 (q < 0.0001, mean difference = -8093), IL-8 (q < 0.0001, mean difference = -6693), GDF-15 (q < 0.0001, mean difference = -6485), vascular cell adhesion molecule-1 (VCAM-1; q < 0.0001, mean difference = -6404), bFGF (q < 0.0001, mean difference = 5675), angiogenin (q = 0.0001, mean difference = -5730), IGFBP-3 (q = 0.0005, mean difference = -5182), EMMPRIN (q = 0.0002, mean difference = -5137), urokinase plasminogen activator receptor (uPAR; q = 0.0005, mean difference = -4772), IGFBP-2 (q = 0.0017, mean difference = 4710), MCP-1 (q = 0.0011, mean difference = -4436), dickkopf-related protein 1 (Dkk-1; q = 0.0042, mean difference = -4140), stromal cell-derived factor-1α (SDF-1α; q = 0.0028, mean difference = -4004), serpin E1 (q = 0.0063, mean difference = 3598), and GROα (q = 0.0202, mean difference = -2708) (Figure 5.4B, Table 5.1).

Proteins that were significantly downregulated in iBMEC-conditioned media compared to CMEC-conditioned media include: RANTES (q < 0.0001, mean difference = 13521), PDGF-AB/BB (q < 0.0001, mean difference = 11675), CD31 / PECAM-1 (q < 0.0001, mean difference = 11119), dickkopf-related protein 1 (Dkk-1; q < 0.0001, mean difference = 9588), angiopoietin-2 (q < 0.0001, mean difference = 8713), GROα (q = 0.0012, mean difference = 3944), bFGF (q = 0.0026, mean difference = 3614), IGFBP-3 (q = 0.0036, mean difference = 3767), endoglin (q = 0.0051, mean difference = 3318), PDGF-AA (q = 0.0053, mean difference = 3302), ST2 (q = 0.0055, mean difference = 3282), and angiogenin (q = 0.02, mean difference = 3002) (Figure 5.5, Table 5.1).

In contrast, proteins significantly lower in CMEC-conditioned media compared to iBMEC-conditioned media include: VCAM-1 (q < 0.0001, mean difference = -6583), chitinase 3-like 1 (q < 0.0001, mean difference = -7582), osteopontin (q < 0.0001, mean difference = -12969), and IGFBP-2 (q = 0.0328, mean difference = -2755) (Figure 5.5, Table 5.1).

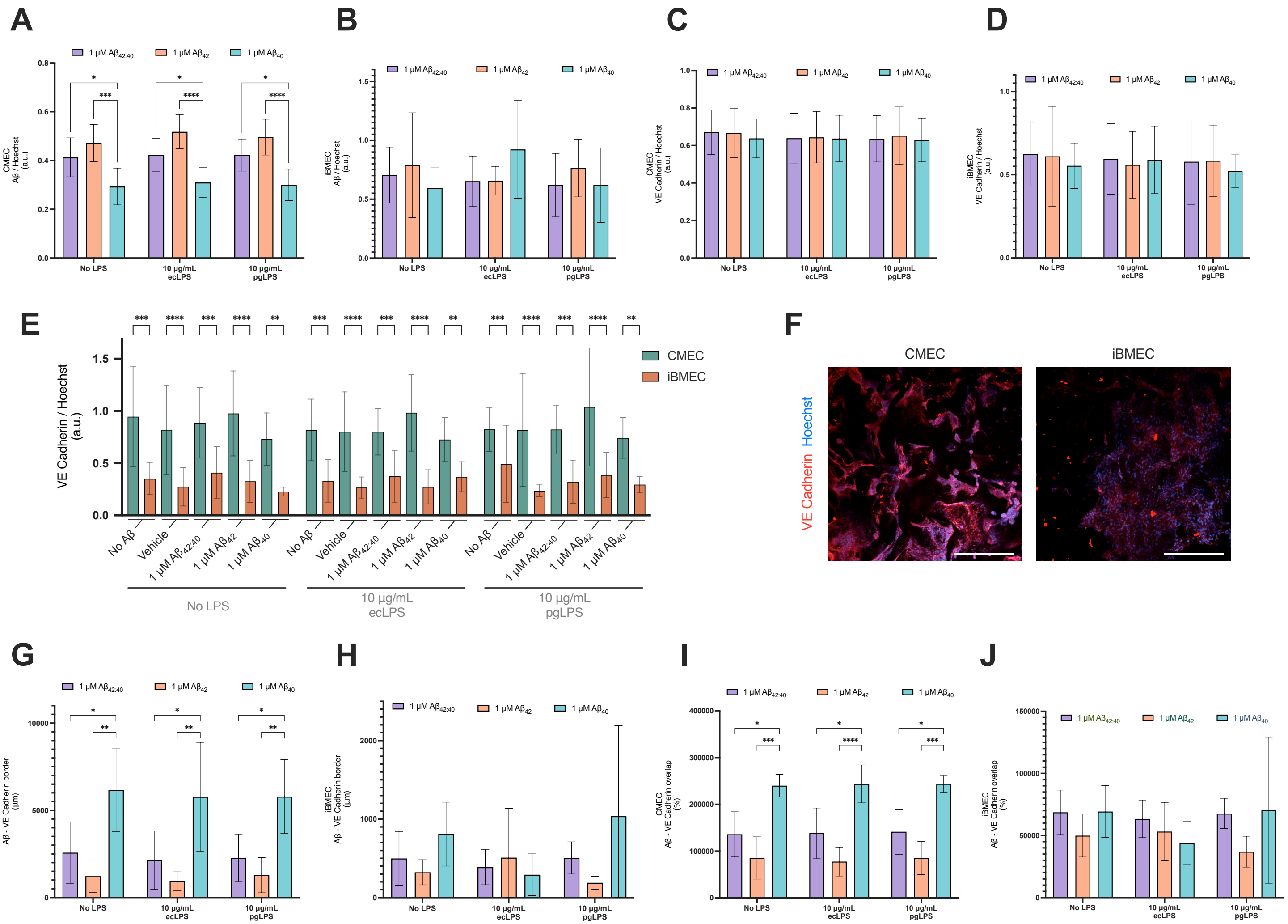

Figure 5.3: Aβ deposition and VE cadherin expression in 3D bioprinted CMEC and iBMEC monocultures. Hoechst-normalised Aβ fluorescence in **(A)** bioprinted CMECs after 14 days and **(B)** bioprinted iBMECs after 28 days. Means are compared using a two-way ANOVA with Tukey's multiple comparisons test. Hoechst-normalised VE cadherin fluorescence in **(C)** bioprinted CMECs after 14 days and **(D)** bioprinted iBMECs after 28 days. Means are compared using a two-way ANOVA with Tukey's multiple comparisons test. Hoechst-normalised VE cadherin expression in **(E)** bioprinted CMECs after 14 days and bioprinted iBMECs after 28 days. Means of each treatment pair are compared using a two-way ANOVA (main effects only) with Šídák's multiple comparisons test. **(F)** Representative immunofluorescence images of bioprinted day 14 CMECs and day 28 iBMECs showing VE cadherin expression (red) and Hoechst (blue). Border distance between Aβ fluorescence volume and VE cadherin fluorescence volume in **(G)** bioprinted CMECs after 14 days and **(H)** bioprinted iBMECs after 28 days. Means are compared using a two-way ANOVA with Tukey's multiple comparisons test. Cumulative percentage overlap of Aβ fluorescence objects with VE cadherin fluorescence volume in **(I)** bioprinted CMECs after 14 days and **(J)** bioprinted iBMECs after 28 days. Means are compared using a two-way ANOVA with Tukey's multiple comparisons test. Abbreviations: Aβ: amyloid β, ecLPS: Lipopolysaccharide from *Escherichia coli*, pgLPS: Lipopolysaccharide from *Porphyromonas gingivalis*, Vehicle: 0.5% ammonium hydroxide in phosphate buffered saline. *p < 0.05, **p < 0.01, and ***p < 0.001. Graphs are presented as mean ± SD of n ≥ 3 independent experiments.

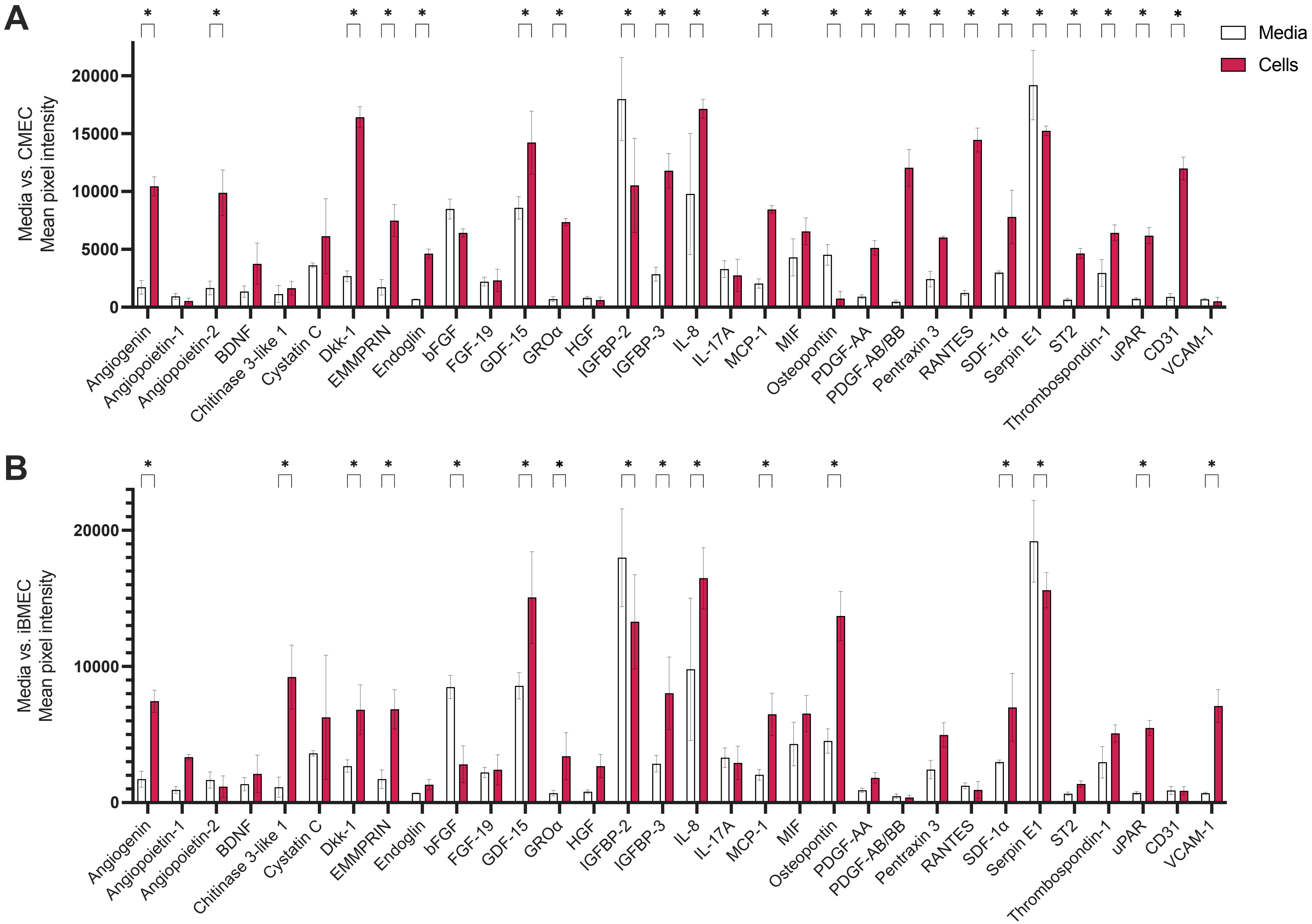

Figure 5.4: Basal cytokine secretion in 3D bioprinted endothelial monocultures. (A) CMECs and **(B)** iBMECs, were analysed to determine relative expression of proteins compared to media (Sciencell Astrocyte medium). Data are reported as mean signal intensity ± SD from n = 3 (n = 2 for media condition due to membrane issue). Cytokines with mean pixel density under 10 % of the maximum were not included in the statistical analysis or graph. For statistical testing, a two-way ANOVA with a two-stage linear step-up procedure of Benjamini, Krieger and Yekutielie was used to control the false-discovery rate, with Q < 0.05. Cytokines with a mean q value < 0.5 when compared to the basal media without cells were classified as a discovery and denoted with *. See Abbreviations (page viii) for full list of cytokine names.

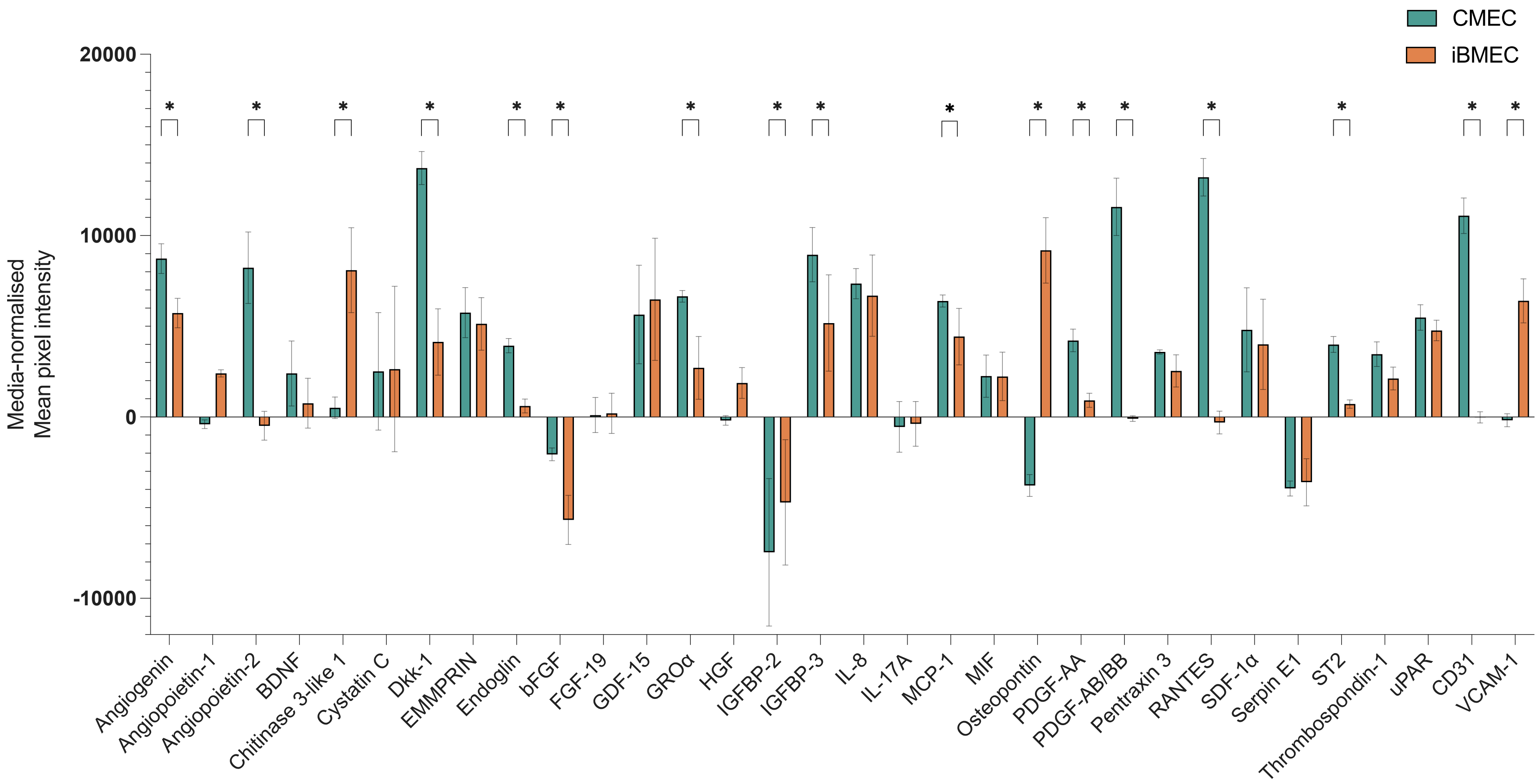

Figure 5.5: Relative cytokine secretion in 3D bioprinted CMECs vs. iBMECs. Cytokines with a mean q value < 0.5 when compared to the basal media without cells are included. Data are reported as mean signal intensity ± SD from n = 3. Cytokines with mean pixel density under 10 % of the maximum were not included in the statistical analysis or graph. For statistical testing, a two-way ANOVA with a two-stage linear step-up procedure of Benjamini, Krieger and Yekutielie was used to control the false-discovery rate, with Q < 0.05. Cytokines with a mean q value < 0.5 when compared to the basal media without cells were classified as a discovery and denoted with *. See Abbreviations (page viii) for full list of cytokine names.

Table 5.1: Relative proteome secretion measured using the proteome profiler array. Cytokines with mean pixel density under 10 % of the maximum were not included in the statistical analysis. For statistical testing, a two-way ANOVA with a two-stage linear step-up procedure of Benjamini, Krieger and Yekutielie was used to control the false-discovery rate, with Q < 0.05. Cytokines with a mean q value < 0.5 when compared to the basal media without cells were classified as a discovery (rows highlighted green). See Abbreviations (page viii) for full list of cytokine names.

Media vs. CMEC				
Cytokine	Mean Diff.	Discovery?	q value	Individual P Value
Dkk-1	-13728	Yes	<0.0001	<0.0001
RANTES	-13220	Yes	<0.0001	<0.0001
PDGF-AB/BB	-11583	Yes	<0.0001	<0.0001
CD31	-11096	Yes	<0.0001	<0.0001
IGFBP-3	-8949	Yes	<0.0001	<0.0001
Angiogenin	-8732	Yes	<0.0001	<0.0001
Angiopoietin-2	-8229	Yes	<0.0001	<0.0001
IL-8	-7352	Yes	<0.0001	<0.0001
GROα	-6652	Yes	<0.0001	<0.0001
MCP-1	-6396	Yes	<0.0001	<0.0001
EMMPRIN	-5755	Yes	<0.0001	<0.0001
IGFBP-2	7465	Yes	<0.0001	<0.0001
GDF-15	-5646	Yes	<0.0001	0.0001
uPAR	-5480	Yes	0.0002	0.0002
SDF-1α	-4807	Yes	0.0009	0.0009
PDGF-AA	-4221	Yes	0.0035	0.0034
ST2	-3996	Yes	0.0055	0.0054
Serpin E1	3944	Yes	0.0063	0.006
Endoglin	-3928	Yes	0.0051	0.0062
Osteopontin	3780	Yes	0.0089	0.0084
Pentraxin 3	-3586	Yes	0.026	0.0124
Thrombospondin-1	-3464	Yes	0.0328	0.0156
Cystatin C	-2515	No	0.1227	0.0779
BDNF	-2401	No	0.2902	0.0921
MIF	-2254	No	0.1835	0.1137
bFGF	2060	No	0.0518	0.148
IL-17A	545.5	No	0.9395	0.7008
Chitinase 3-like 1	-510.9	No	0.2516	0.719
Angiopoietin-1	399.2	No	0.8175	0.7786
HGF	189.8	No	0.9383	0.8936
VCAM-1	179.4	No	0.3148	0.8994
FGF-19	-105.9	No	0.9898	0.9405

Media vs. iBMEC				
Cytokine	Mean Diff.	Discovery?	q value	Individual P Value
Osteopontin	-9189	Yes	<0.0001	<0.0001
Chitinase 3-like 1	-8093	Yes	<0.0001	<0.0001
IL-8	-6693	Yes	<0.0001	<0.0001
GDF-15	-6485	Yes	<0.0001	<0.0001
VCAM-1	-6404	Yes	<0.0001	<0.0001
bFGF	5675	Yes	<0.0001	<0.0001
Angiogenin	-5730	Yes	0.0001	<0.0001
IGFBP-3	-5182	Yes	0.0005	0.0003
EMMPRIN	-5137	Yes	0.0002	0.0004
uPAR	-4772	Yes	0.0005	0.001
IGFBP-2	4710	Yes	0.0017	0.0011
MCP-1	-4436	Yes	0.0011	0.0021
Dkk-1	-4140	Yes	0.0042	0.004
SDF-1α	-4004	Yes	0.0028	0.0053
Serpin E1	3598	Yes	0.0063	0.0121
GROα	-2708	Yes	0.0202	0.0578
Cystatin C	-2645	No	0.1227	0.0638
Pentraxin 3	-2544	No	0.0783	0.0746
Angiopoietin-1	-2403	No	0.1447	0.0919
MIF	-2237	No	0.1835	0.1165
Thrombospondin-1	-2120	No	0.1435	0.1366
HGF	-1879	No	0.2942	0.1868
PDGF-AA	-918.7	No	0.1812	0.5178
BDNF	-756.5	No	0.6239	0.5942
ST2	-714.4	No	0.2152	0.6149
Endoglin	-610.4	No	0.2335	0.6672
Angiopoietin-2	483.6	No	0.2567	0.7334
IL-17A	377.6	No	0.9395	0.7902
RANTES	301.3	No	0.2912	0.8319
FGF-19	-197.3	No	0.9898	0.8895
PDGF-AB/BB	91.24	No	0.3321	0.9488
CD31	23.42	No	0.3454	0.9868

CMEC vs iBMEC				
Cytokine	Mean Diff.	Discovery?	q value	Individual P Value
RANTES	13521	Yes	<0.0001	<0.0001
PDGF-AB/BB	11675	Yes	<0.0001	<0.0001
CD31	11119	Yes	<0.0001	<0.0001
Dkk-1	9588	Yes	<0.0001	<0.0001
Angiopoietin-2	8713	Yes	<0.0001	<0.0001
VCAM-1	-6583	Yes	<0.0001	<0.0001
Chitinase 3-like 1	-7582	Yes	<0.0001	<0.0001
Osteopontin	-12969	Yes	<0.0001	<0.0001
GROα	3944	Yes	0.0012	0.0022
bFGF	3614	Yes	0.0026	0.0049
IGFBP-3	3767	Yes	0.0036	0.0034
Endoglin	3318	Yes	0.0051	0.0097
PDGF-AA	3302	Yes	0.0053	0.0101
ST2	3282	Yes	0.0055	0.0105
Angiogenin	3002	Yes	0.02	0.0191
IGFBP-2	-2755	Yes	0.0328	0.0312
MCP-1	1960	Yes	0.0434	0.1241
Angiopoietin-1	-2802	No	0.0897	0.0285
GDF-15	-838.9	No	0.1782	0.5091
SDF-1α	803.5	No	0.1845	0.5271
uPAR	708.4	No	0.202	0.577
Thrombospondin-1	1344	No	0.2034	0.2906
IL-8	658.7	No	0.2114	0.6041
EMMPRIN	618.5	No	0.2192	0.6262
Serpin E1	-346	No	0.2748	0.7852
Pentraxin 3	1042	No	0.2885	0.4122
HGF	-2069	No	0.2942	0.1046
BDNF	1645	No	0.3092	0.1963
IL-17A	-167.9	No	0.9395	0.8948
Cystatin C	-130.5	No	0.964	0.9181
FGF-19	-91.35	No	0.9898	0.9426
MIF	17.28	No	>0.9999	0.9891

5.3. Discussion

This study investigated our 3D bioprinted endothelial monoculture as a platform to develop scalable AD models using pathological treatments, while also exploring potential cooperative pathomechanisms of ecLPS/pgLPS and Aβ. While cell viability remained unaffected upon application of inflammatory LPS or Aβ, viability was significantly more variable in iBMEC compared to CMEC bioprinted cultures. Amyloid deposition patterns varied significantly between endothelial cell types. In CMECs $A\beta_{40}$ demonstrated lower deposition than $A\beta_{42}$ or $A\beta_{42:40}$, but colocalized more frequently with endothelial VE cadherin. Neither of these effects was observed in bioprinted iBMECs. Additionally, VE cadherin expression was higher in CMECs showed compared to iBMECs, but was unaffected by inflammatory or amyloidogenic stimuli. 3D bioprinted CMECs and iBMECs exhibited important differences in cell type secretome profiles, identifying key mediators that may serve as useful homeostatic and disease markers *in vitro*.

5.3.1. Differential Aβ deposition and marker expression in 3D bioprinted endothelial cultures

The high variability of bioprinted iBMECs observed in the viability and Hoechst parameters underscores important differences between iBMEC and CMEC cultures. iBMEC cultures displayed more variability, although it is unclear whether this is due to length of culture time (14 days for CMECs vs 28 days for iBMECs) or intrinsic cellular mechanisms. Increased time in culture may result in increased release of matrix degradation proteins (e.g. MMPs), that could progressively reduce the structural integrity of the hydrogel (Patterson and Hubbell, 2010). This aligns with some noted structural loss of iBMEC cultures during the washing steps of immunofluorescence preparation. Similarly, phenotypic differences of CMECs and iBMECs could be the cause, which would align with well-known fragility of many iPSC-derived cell-types (Linville et al., 2022). Regardless of the exact cause, this suggests that CMECs support a more robust and replicable neurovascular model in the bioprinting platform's current state. To better capitalise on the advantages of iPSC-derived vascular cells, further development examining additional determinants of stable iBMEC growth is warranted. Additional media optimisation, gentler bioprinting processes, or altered hydrogel stiffness and functionalisation may also offer improvements that improve the viability of this more *in vivo*-relevant cell source.

The higher deposition of $A\beta_{42}$ compared to $A\beta_{40}$ in 3D bioprinted CMEC monocultures highlights potential isoform-specific mechanisms in AD pathology. This difference in fluorescence could be due to altered fluorophore emission due to the structural difference between $A\beta_{40}$ and $A\beta_{42}$, although the difference is not seen in iBMECs, so this is unlikely. While the manufacturer reports equal emission wavelengths, comparing the relative emission strength of each conjugate would elucidate whether structural differences confound fluorescence readings. On the other hand, the higher overall deposition of $A\beta_{42}$ may align with its higher hydrophobicity and aggregation potential (Kwak et al., 2020, Sengupta et al., 2016). The absence of synergistic effects between $A\beta_{42}$ and $A\beta_{40}$ suggests that their pathogenic contributions may occur through independent pathways. Other studies have observed synergistic effects using *in silico* or 2D *in vitro* techniques (Li et al., 2023c, Chang et al., 2013, Chang and Chen, 2014). Increased colocalization of $A\beta_{40}$ with VE cadherin in CMECs corroborates the well-reported increased deposition of $A\beta_{40}$ in neurovasculature of AD patients, supporting the face validity of this model for examining neurovascular amyloid deposition (Herzig et al., 2004, Herzig et al., 2006). The enhanced colocalization of $A\beta_{40}$ with VE cadherin in CMECs suggests an isoform-specific interaction that may reflect differences in endothelial binding affinities or intracellular processing pathways for $A\beta_{40}$ compared to $A\beta_{42}$, potentially driven by distinct receptor-ligand dynamics or cellular uptake mechanisms. The overall higher $A\beta_{42}$ deposition without a corresponding rise in VE cadherin colocalization may suggest that accumulation results from increased adhesion to the hydrogel due to its higher aggregation and hydrophobicity, whereas increased VE cadherin colocalization of $A\beta_{42}$ may indicate a more cell-mediated process, involving uptake or metabolic processing. This challenges data showing that $A\beta_{40}$ deposition phenotypes are dependent on the presence of $A\beta_{42}$ (McGowan et al., 2005).While the absence of similar patterns in iBMECs could reflect cell-type-specific differences in Aβ interactions, it is more likely that the higher variability of iBMEC masks this effect in these cells.

VE cadherin expression was not altered by differences in inflammatory stimuli or Aβ isoform. This is counter to studies that demonstrate disrupted barrier and destabilised junctions after pgLPS exposure in rats and *in vitro* mouse BMECs (Lei et al., 2023), and ecLPS exposure in a wide variety of *in vivo* and human *in vitro* contexts (Lei et al., 2023, Chan et al., 2020). This difference could be attributed the short treatment duration, effect of 3D culturing, or lack of other LPS-sensitive cell types like pericytes or microglia (Banks et al., 2015, Kováč et al., 2011). While *P. gingivalis* has indeed been implicated in AD pathology, it's pathogenic constituents include other molecules, namely namely gingipains, that play key roles neuroinflammation and cognitive decline (Poole et al., 2013, Dominy et al., 2019). Future studies leveraging these bioprinted constructs could explore extended treatment durations and the effect of different pathogenic factors such as gingipains to better replicate chronic neuroinflammatory states.

Although there was no impact of inflammatory stimuli or Aβ on VE Cadherin levels, VE Cadherin levels were significantly higher in CMECs compared to iBMECs across all conditions. In addition, CMECs exhibited lower variability in viability and marker expression, indicating a more robust endothelial phenotype under these experimental conditions. While this may be an intrinsic difference between cell sources, this lower expression matches findings reporting disrupted VE cadherin dynamics upon ROCK inhibition (Cao et al., 2017). Although the tapered ROCKi protocol does limit exposure, VE cadherin disruption may be a lasting, unintended effect of this survival-enhancing technique.

5.3.2. Basal secretomes in 3D bioprinted endothelial cultures

Protein secretion profiles of monocultured endothelial cells in 3D environments remain underexplored, particularly in systems designed to emulate the neurovascular unit. This study addresses this gap by profiling cytokine and growth factor secretion in conditioned media from 3D bioprinted cultures of CMECs and iBMECs relative to media alone. The findings not only highlight key differences in the secretion profiles of these cell types but also provide insights into their vascular and neurovascular functionality within 3D bioprinted environments.

The basal media (Sciencell Astrocyte Medium) used in these cultures contained several cytokines, which were significantly modulated upon conditioning by endothelial cells. For instance, bFGF was present at high levels in the unconditioned media but showed marked reductions in conditioned media, suggesting substantial utilization by the endothelial cells, particularly iBMECs, for proliferation or maintenance of endothelial phenotype (Augustin-Voss et al., 1993). Similarly, serpin E1 and IGFBP-2, initially abundant in the media, were significantly reduced upon conditioning, hinting at its metabolic processing or sequestration by endothelial cells in both groups. Interestingly, osteopontin was cell type-specifically regulated; while it was reduced in

CMEC-conditioned media compared to basal, it was elevated in iBMEC cultures. While it is unclear why osteopontin would be present in the media to begin with, its differential expression may indicate divergent inflammatory states between the two cell types, with higher osteopontin in iBMEC-conditioned media reflecting pro-inflammatory activity (Lok and Lyle, 2019).

Several cytokines were upregulated in CMEC- compared to iBMEC-conditioned media including: angiogenin, Dkk-1, GRO-α, MCP-1, thrombospondin, and CD31/PECAM-1, all of which are associated with endothelial proliferation, vascular remodelling, and immune cell recruitment (Di et al., 2017, Hayashi et al., 2003, Kamińska et al., 2022, Koss et al., 2011, Sadagopan et al., 2012, Wimmer et al., 2019).

CMEC-specific cytokines, not detected at all iBMEC media, further highlight the increased relevance 3D CMECs over iBMECs. Angiopoietin-2, endoglin, PDGF-AA, PDGF-BB (angiogenic factors that regulate vascular development, stability, and endothelial-pericyte interactions), and RANTES and ST2 (inflammatory mediators involved in immune cell recruitment) reinforcing the superior vascular mimicry of CMECs in our 3D bioprinted system (Blecharz et al., 2016, Choi et al., 2009, Karimi-Abdolrezaee et al., 2012, Liang et al., 2017, Mancini et al., 2009, Suffee et al., 2017). In contrast to the comparable downregulation of IGFBP-2 in relation to media, IGFBP-3 was upregulated more prominently in CMEC than in iBMEC-conditioned media, suggesting its active secretion and potential role in modulating vascular integrity or cellular interactions in this cell type.

iBMECs displayed a narrower range of cell-specific cytokine upregulation, with chitinase 3-like 1 being upregulated compared to CMECs, and osteopontin and VCAM-1 being expressed in iBMECs but not CMECs. These iBMEC proteins highlight roles cell adhesion, inflammatory response modulation, and extracellular matrix interactions (Eidson et al., 2021, Wang et al., 1998, Wurm et al., 2019). This pattern of cytokine expression indicates that iBMECs may be inherently pro-inflammatory primed, reflecting a heightened basal state of activation that could influence their responses to inflammatory or amyloidogenic stimuli in disease-relevant contexts (Yan et al., 2016).

Several cytokines were similarly expressed across both endothelial cell types, including EMMPRIN, GDF-15, IL-8, SDF-1α, and uPAR, highlighting conserved roles in matrix remodelling, angiogenesis, and chemotactic signalling (Conroy et al., 2018, Hasaneen et al., 2016, Kim et al., 2015, Liu et al., 2010, Mori et al., 2015). Despite these shared profiles, the broader downregulation of functionally important endothelial proteins in iBMECs indicates a comparatively diminished endothelial identity. This finding, alongside lower VE cadherin expression levels, suggests that iBMECs may be less robust in maintaining vascular characteristics under prolonged 3D bioprinted culture conditions. However, these limitations could potentially be mitigated through further optimization of the 3D bioprinted matrix or media composition to better support iBMEC functionality.

In comparison to 2D proteome data reported in Chapter 3, several cytokines were consistently expressed in both 2D and 3D basal iBMEC cultures, including EMMPRIN, GDF-15, IGFBP-2, IGFBP-3, osteopontin, MCP-1, PDGF-AA, thrombospondin-1, and bFGF, indicating that roles in inflammation, angiogenesis, and endothelial function are conserved as dimensionality increases (Allard and Duan, 2018, Granata et al., 2004, Hasaneen et al., 2016, Hayashi et al., 2003, Karimi-Abdolrezaee et al., 2012, Kim et al., 2015, Koss et al., 2011, Seghezzi et al., 1998, Wang et al., 1998). In contrast, cytokines such as MMP-9, cystatin C, FGF-19, IL-17A, and MIF were detected only in 2D cultures, while endoglin, angiogenin, chitinase 3-like 1, VCAM-1 and RANTES were unique to 3D bioprinted iBMECs. While both 2D-specific molecules (MMP-9, cystatin C, FGF-19, IL-17A, MIF) and 3D-specific molecules (endoglin, angiogenin, chitinase 3-like 1, VCAM-1, RANTES) indicate pro-inflammatory primed endothelial phenotypes, this divergence suggests that the 3D environment shifts the nature of this inflammatory profile.

Downregulation of many functionally important endothelial proteins shows that 3D bioprinted iBMECs may not have as robust of a functional endothelial identity than CMECs, or that they aren’t as amenable to longitudinal culturing. This corroborates the lower VE cadherin expression observed in iBMECs, and reinforces the utility of CMECs as a robust, reliable 3D neurovascular model with a lower cultured time that allows for higher throughput.

5.4. Chapter Summary

This chapter explored the viability, protein secretion profiles, and amyloid interactions of 3D, monocultured CMECs and iBMECs at rest and on exposure to AD-related stimuli. While overall cell viability was unaffected by inflammatory or amyloidogenic stimuli, iBMECs exhibited greater variability and structural fragility and neurovasculature-related phenotype (eg VE Cadherin levels, neurovasculature-related cytokine secretion). Given this, CMECs may be a more advantageous 3D bioprinted model until further optimisation can support iPSC-derived vascular cells. Amyloid deposition patterns further underscored cell-type-specific differences, with CMECs replicating the lower total deposition and increased VE cadherin-association of $A\beta_{40}$, aligning with human AD-related vascular amyloid deposition. These effects were absent or masked in iBMECs, likely reflecting inherent variability.

Cytokine secretion profiles provided further insights into the distinct vascular characteristics of CMECs and iBMECs. While both cell types shared expression of several endothelial proteins, CMECs exhibited a broader range of vascular protein upregulation, including angiogenesis- and inflammation-associated factors, emphasizing their robust vascular identity. In contrast, iBMECs secreted fewer vascular-relevant factors (corroborating reduced VE cadherin expression) but displayed a distinctly primed inflammatory profile, suggesting limited vascular biomimicry in comparison to CMECs bioprinted using this system.re

These findings emphasize the need for further optimization of the bioprinting platform to support iBMEC functionality, including modifications to the hydrogel matrix, media composition, and culture conditions. By addressing these challenges, iPSC-derived iBMECs could be better leveraged for their potential as a scalable, patient-specific model for neurovascular research. Regardless, CMECs offer a robust and reliable model for neurovascular research, demonstrating consistent viability, stability, and functionality under the current bioprinting conditions. This chapter provides a foundation for future studies to refine 3D bioprinted constructs, enabling more accurate disease modelling and exploration of therapeutic strategies for neurovascular disorders, including Alzheimer’s disease.

Chapter 6: Discussion & Final Conclusions

6.1. Summary

AD remains a devastating neurodegenerative disorder with no disease-modifying treatments, driven in part by significant gaps in our ability to model its complex pathology *in vitro*. Traditional 2D models and animal studies, while invaluable, fail to recapitulate the multifaceted interactions within the neurovascular unit that underpin AD progression. This thesis sought to address these unmet needs by developing 3D, bioprinted neurovascular models, leveraging iPSC-derived cell types to create scalable and physiologically relevant systems. By integrating bioprinting techniques with stem cell differentiation and hydrogel optimization, this research uniquely contributes to bridging the translational gap between preclinical modelling and clinically effective treatments. This interdisciplinary methodology provides a foundation for more accurate representations of neurovascular AD pathology, offering novel insights into vascular dysfunction and laying the groundwork for improved therapeutic discovery.

Chapter 3 focused on the differentiation and characterization of iPSC-derived vascular cell types in 2D to validate their potential for modelling neurovascular interactions. Endothelial cells and pericytes were differentiated and assessed for functionality, revealing distinct secretory profiles and barrier properties that emulate *in vivo* counterparts. In 2D, iBMECs demonstrated enhanced barrier function when compared to CMECs and HUVECs. iBMECs and iPericytes were generally unresponsive to Aβ and LPS, although Aβ deposition was observed in 2D iBMECs, an important feature when modelling AD proteinopathy. This chapter established a robust foundation of validated vascular cell types, addressing critical barriers in the field and laying the groundwork for the development of more complex, multicellular systems.

Chapter 4 built on Chapter 3 by exploring the efficient bioprinting of monocultured endothelial cells, and the successful culture of a novel bioprinted triculture of endothelial cells, pericytes and astrocytes, to advance development of scalable neurovascular models. This chapter detailed media refinement that supported iBMEC viability and structural development by using astrocyte media and tapered inhibition of the ROCK pathway. Tricultures of endothelial cells, pericytes, and astrocytes were successfully developed, exhibiting close expression of cell-type specific markers reminiscent of neurovascular organisation. These findings present the capabilities of this bioprinting platform to generate physiologically-relevant neurovascular systems, while also highlighting challenges involving the optimization of culture conditions for iPSC-derived cells in complex 3D environments. This work marked a pivotal step in the evolution of neurovascular models by demonstrating the feasibility and potential of bioprinted systems to scalably recapitulate neurovascular complexity.

Chapter 5 then applied this platform's capabilities by investigating 3D bioprinted iBMEC responses to inflammatory and amyloidogenic stimuli, two key drivers of AD pathology. iBMEC monocultures were exposed to lipopolysaccharides (from *E. coli* and *P. gingivalis*, two neuroinflammation-relevant bacteria) and Aβ monomer preparations to evaluate their effects on cellular viability, Aβ deposition, and protein expression. Distinct responses between CMECs and iBMECs were observed, with differences in variability, amyloid deposition, vascular marker expression and secretomes. This chapter provided critical insights into the vulnerabilities of endothelial cells to inflammatory and Aβ insults, emphasizing the cell-type specific validity of such models for studying disease-relevant mechanisms. By simulating known aspects of amyloidogenic environments, this work highlighted the utility of these systems for unravelling the vascular mechanisms of isoform-specific Aβ pathology and evaluating potential therapeutic interventions in a modular, scalable setting.

By integrating multiple techniques, this body of work has generated a scalable and physiologically-relevant platform for investigating the complex cellular and molecular interactions that underpin neurovascular dysfunction. Traditional models have fallen short in capturing the intricate interplay of vascular and parenchymal components, limiting their translational relevance. This platform provides a versatile platform to simulate Aβ-related pathological environments and lays the groundwork for next-generation models that will more faithfully replicate human disease processes while allowing increased throughput. Moreover, the approach of blending cell biology, bioengineering, and disease modelling is highlighted as a critical nexus, where advances in the stagnating field of neurodegenerative disease might finally be found.

6.2. Future Directions

One critical step to capitalise on the translational value of this research platform is to integrate these models into the drug discovery pipeline. These models are a scalable and physiologically relevant platform for use in early-stage drug discovery, with a balanced throughput and human-relevance that bridges the gap between 2D *in vitro* and rodent *in vivo* models. A example application is a screening approach where 2D iBMECs (which demonstrated robust barrier-like properties compared to CMECs) could serve as an initial high-throughput screen for drugs targeting endothelial integrity. Promising compounds could then be tested in 3D bioprinted CMEC cultures (which exhibited more stable vascular organization) before progressing to more complex multicellular systems or *in vivo* models. This graded approach would maximize the efficiency of drug screening while maintaining physiological relevance, addressing a critical gap in neurovascular-targeted AD therapeutics.

Another key avenue for future exploration is the relative strengths of modular culture systems (like the one used here) as opposed to self-assembled organoid technology. Unlike modular culture systems, where terminal cell types are used, self-assembled organoids rely on intrinsic cellular cues to form tissue-like architectures from stem cell progenitors, potentially yielding more physiologically-accurate cell ratios, macrostructure and dynamic interactions (Lindhout et al., 2024). This self-organization may be better placed to capture some aspects of the neurovascular environment, especially developmentally-instructed elements like some signalling pathways. Despite this advantage, self-assembled organoids face significant challenges, particularly in replicability and imitating the static forces (e.g. construct stiffness) and dynamic forces (e.g. shear stress and nutrient flow) present *in vivo* (LaMontagne et al., 2022). Importantly, efforts to vascularise organoids are only in their infancy, with successful incorporation of vascular cell types still falling short of functional vasculature that can ameliorate necrosis and cell diversity issues. The decision of whether to use bioprinting processes (e.g. when scale and throughput are important), and whether to use self-assembled or modular multicellular cultures should be informed by the questions being posed by the researcher. Ultimately, this diversity of modalities is vital to broadening our understanding of complex homeostatic and disease processes.

Understanding the role of cytokine signalling in Alzheimer's disease remains a crucial area for future research. Neuroinflammatory pathways, mediated by complex cytokine networks, play a pivotal role in endothelial dysfunction, the progression of neurovascular pathology and AD. This study revealed an unexpectedly inert cytokine responses in 2D and 3D iBMECs and iPericytes upon inflammatory stimulation, raising important questions about the translatability of iPSC-derived neurovascular cells. Future research should explore whether single-cell RNA sequencing could uncover subtle transcriptional responses that are not evident at the protein level, or whether TLR4 expression is insufficient in these models to elicit a robust response to LPS. Additionally, incorporating prolonged or multi-factorial inflammatory stimuli, particularly in multicellular environments (containing classically inflammatory microglia and astrocyte), may provide a more physiologically relevant context to examine neurovascular dysfunction in AD.

Relatedly, the study of cell-cell communication within the neurovascular unit is critical for unravelling Alzheimer's disease mechanisms. Although this thesis demonstrated significant progress in developing multicellular constructs, measuring broad secretion profiles, and observing protein marker expression in this novel bioprinted platform, further investigation is needed to more granularly explore dynamic signalling processes. Emerging techniques, such as spatial transcriptomics and optogenetic tools, provide an opportunity to map signalling pathways with high spatial and temporal resolution (Mitroshina et al., 2023, Cao et al., 2024). These methods could elucidate how specific molecular interactions, such as astrocyte-pericyte crosstalk or endothelial-astrocyte signalling, influence disease progression. The current research rests upon assays using end point analyses that may miss important dynamic features; incorporating real-time imaging and live-cell tracking could allow researchers to observe novel time-sensitive cellular responses. As costs decrease for these emerging techniques, a multicellular approach could be used in early stage drug discovery, where more simplistic 2D culture systems are often used because of cost and data complexity. With improved automation of imaging and data analysis, the increased *in vivo*-relevance of multicellular assays could alleviate high error rates at this stage of the drug development pipeline.

Advancing hydrogel design is essential for improving the physiological relevance of neurovascular models. Current hydrogels, such as Matrigel, provide a supportive environment for cell growth but often include undefined growth factor profiles, limiting experimental reproducibility (Aisenbrey and Murphy, 2020b). Synthetic hydrogels, on the other hand, offer tunable properties but may initially lack the biological complexity required to support spontaneous cellular interactions. This study successfully established a synthetic PEG-based hydrogel system capable of supporting iPSC-derived neurovascular cells, although iBMEC quality and responsiveness was reduced, especially at longitudinal timepoints. Future efforts should focus on measuring the effects of additional ECM-mimetic components, or developing gentler bioprinting processes, to support longitudinal iPSC-derived cell health and function in synthetic hydrogels. Further, innovative developments in bioprinting techniques, such as higher resolution patterning, could refine spatial organization within hydrogel-based systems, enhancing cell-cell interactions and barrier formation. Future studies should investigate how hydrogel composition affects other key parameters like endothelial barrier integrity, astrocyte differentiation, and extracellular matrix deposition. These advancements will enable more accurate modelling of neurovascular dynamics and provide robust platforms for high-throughput drug discovery.

Achieving accurate vascular endothelial identities in iPSC-derived models remains a key challenge in neurovascular research. Given our iBMEC's expression of EpCAM, and reduced expression of VE cadherin in 3D, there is a clear need for more precise characterization techniques surrounding endothelial versus epithelial phenotypes (Lu et al., 2021). Recent advances, such as single-cell transcriptomics, have identified novel markers that may resolve this distinction in healthy and diseased humans, enabling a clearer identification of vascular identities and phenotypes (Garcia et al., 2022). Future efforts should focus on standardizing protocols in light of these advances to ensure consistent differentiation and phenotypic stability.

Another barrier to obtaining specific cell-identities in iPSC-derived systems is the variability inherent in usage of these patient-derived cells. While the difference in our iBMEC and iPericyte cytokine responses to other immortalised, primary, and iPSC-derived lines may be due to cell-intrinsic mechanisms, it is also possible that patient- and genetic-variability plays a role. To address this variability, the creation of deeply characterised reference lines (Pantazis et al., 2022) that have undergone extensive multi-omic profiling and functional validation could ensure consistent differentiation potential and minimize technical variability. These would provide a standardized resource for investigating disease-relevant phenotypes, and enable reliable cross-study comparisons and systematic exploration of genetic and environmental contributions to complex pathologies. While patient-derived cells can retain relevant pathological phenotypes, techniques to mimic aging in iPSC-derived models, such as using oxidative stressors or CRISPR-based methods, could better capture age-related phenotypes relevant to Alzheimer's disease (Mertens et al., 2021, Carr et al., 2024). Improved characterization of these models using transcriptomic and proteomic approaches will further enhance their utility, allowing researchers to benchmark them against *in vivo* data. Addressing variability in iPSC culture methods and minimizing phenotypic drift will be essential for improving the reliability and reproducibility of iPSC-based AD research.

Incorporating flow mechanics into neurovascular models offers an exciting avenue for replicating the dynamic forces of the *in vivo* environment. Although this thesis successfully demonstrated *in vivo*-like structural development in 3D neurovascular monocultures and tricultures, these structures don't involve blood flowing through lumens at high pressure, as in the human brain. The shear stress elicited by blood flow *in vivo*, influences endothelial barrier integrity and cellular signalling pathways (Warboys et al., 2010). Microfluidic platforms and organ-on-a-chip systems provide a promising way to introduce this flow into *in vitro* neurovascular models, simulating physiological conditions such as waste clearance and nutrient/blood-borne drug delivery (Fengler et al., 2022, Gijzen et al., 2020, Kurosawa et al., 2022). Recent advances, such as perfusable organ chips and microvessel-on-a-chip technologies, have demonstrated the potential to study complex processes like amyloid cycling and glymphatic clearance (Lee et al., 2020, Dessalles et al., 2021). However, these systems often prioritize physiological relevance over scalability, making them more suitable for late-stage drug discovery rather than high-throughput screening. Future research should aim to integrate flow mechanics into scalable platforms, bridging the gap between physiological fidelity and experimental efficiency.

6.3. Final Conclusions

This thesis set out to address the critical challenge of developing physiologically-relevant, human-derived neurovascular models to advance our understanding of Alzheimer's disease. By leveraging interdisciplinary methods—iPSC differentiation, 3D bioprinting, and innovative hydrogel technologies—key concerns in traditional *in vitro* and *in vivo* models have been addressed, including the lack of human-derived systems, limited scalability, poor biomimicry of 2D models and poor replicability of 3D models.

Firstly, the successful differentiation and functional characterization of vascular cell types was demonstrated, laying the groundwork for advanced neurovascular models. This 2D foundation was extended by optimising the longitudinal bioprinting of endothelial monocultures, and demonstrating successful culture of bioprinted neurovascular tricultures, highlighting the potential of these systems to recapitulate the structural and functional complexity of the neurovascular unit. 3D endothelial monocultures were then applied in a disease modelling context, by simulating amyloidogenic and inflammatory conditions, revealing face validity upon replication of Aβ deposition phenotypes.

Collectively, this research underscores the transformative potential of combining bioengineering with disease modelling to create systems that more faithfully mimic human pathology. By integrating these models into the drug discovery pipeline, we can improve understanding of neurovascular dysfunction, explore therapeutic targets, and ultimately contribute to the development of effective treatments for Alzheimer's disease. This thesis not only advances current methodologies but also lays the foundation for future innovation in the fields of neuroscientific disease modelling and drug discovery.

Chapter 7: References

Aasen, T., Raya, A., Barrero, M. J., Garreta, E., Consiglio, A., Gonzalez, F., Vassena, R., Bilić, J., Pekarik, V., Tiscornia, G., Edel, M., Boué, S. & Belmonte, J. C. I. 2008. Efficient and rapid generation of induced pluripotent stem cells from human keratinocytes. *Nature Biotechnology,* 26**,** 1276-1284.

Abisambra, J. F., Jinwal, U. K., Blair, L. J., O'leary, J. C., Li, Q., Brady, S., Wang, L., Guidi, C., Zhang, B., Nordhues, B. A., Cockman, M. E., Suntharalingham, A., Li, P., Jin, Y., Atkins, C. A. & Dickey, C. A. 2013. Tau Accumulation Activates the Unfolded Protein Response by Impairing Endoplasmic Reticulum-Associated Degradation. *Journal of Neuroscience,* 33**,** 9498-9507.

Adil, M. S. & Somanath, P. R. 2021. Endothelial Permeability Assays In Vitro. *Methods Mol Biol,* 2367**,** 177-191.

Adriani, G., Ma, D., Pavesi, A., Goh, E. L. & Kamm, R. D. 2015. Modeling the Blood-Brain Barrier in a 3D triple co-culture microfluidic system. *Annu Int Conf IEEE Eng Med Biol Soc,* 2015**,** 338-41.

Adriani, G., Ma, D., Pavesi, A., Kamm, R. D. & Goh, E. L. 2017. A 3D neurovascular microfluidic model consisting of neurons, astrocytes and cerebral endothelial cells as a blood-brain barrier. *Lab Chip,* 17**,** 448-459.

Ahmed, M., Davis, J. E., Aucoin, D., Sato, T., Ahuja, S., Aimoto, S., Elliott, J. I., Nostrand, W. E. V. & Smith, S. O. 2010. Structural Conversion of Neurotoxic Amyloid-B1–42 Oligomers to Fibrils. *Nature Structural & Molecular Biology,* 17**,** 561-567.

Aird, E. J., Lovendahl, K. N., St. Martin, A., Harris, R. S. & Gordon, W. R. 2018. Increasing Cas9-mediated homology-directed repair efficiency through covalent tethering of DNA repair template. *Communications Biology,* 1**,** 54.

Aisenbrey, E. A. & Murphy, W. L. 2020a. Synthetic alternatives to Matrigel. *Nature reviews. Materials,* 5**,** 539-551.

Aisenbrey, E. A. & Murphy, W. L. 2020b. Synthetic alternatives to Matrigel. *Nat Rev Mater,* 5**,** 539-551.

Alberici, A., Gobbo, C., Panzacchi, A., Nicosia, F., Ghidoni, R., Benussi, L., Hock, C., Papassotiropoulos, A., Liberini, P., Growdon, J. H., Frisoni, G. B., Villa, A., Zanetti, O., Cappa, S., Fazio, F. & Binetti, G. 2004. Frontotemporal dementia: impact of P301L tau mutation on a healthy carrier. *J Neurol Neurosurg Psychiatry,* 75**,** 1607-10.

Allard, J. B. & Duan, C. 2018. IGF-Binding Proteins: Why Do They Exist and Why Are There So Many? *Frontiers in Endocrinology,* 9.

Allt, G. & Lawrenson, J. G. 2001. Pericytes: cell biology and pathology. *Cells Tissues Organs,* 169**,** 1-11.

Alvarez, J. I., Cayrol, R. & Prat, A. 2011. Disruption of central nervous system barriers in multiple sclerosis. *Biochim Biophys Acta,* 1812**,** 252-64.

Alzheimer's Association 2023. 2023 Alzheimer's disease facts and figures. *Alzheimer's & Dementia,* 19**,** 1598-1695.

Amasheh, S., Meiri, N., Gitter, A. H., Schöneberg, T., Mankertz, J., Schulzke, J. D. & Fromm, M. 2002. Claudin-2 Expression Induces Cation-Selective Channels in Tight Junctions of Epithelial Cells. *Journal of Cell Science,* 115**,** 4969-4976.

Andreone, B. J., Chow, B. W., Tata, A., Lacoste, B., Ben-Zvi, A., Bullock, K., Deik, A., Ginty, D. D., Clish, C. B. & Gu, C. 2017. Blood-Brain Barrier Permeability Is Regulated by Lipid Transport-Dependent Suppression of Caveolae-Mediated Transcytosis. *Neuron,* 94**,** 581-594.e5.

Andrews, M. G. & Kriegstein, A. R. 2022. Challenges of Organoid Research. *Annu Rev Neurosci,* 45**,** 23-39.

Armulik, A., Genove, G. & Betsholtz, C. 2011a. Pericytes: developmental, physiological, and pathological perspectives, problems, and promises. *Dev Cell,* 21**,** 193-215.

Armulik, A., Genové, G. & Betsholtz, C. 2011b. Pericytes: Developmental, Physiological, and Pathological Perspectives, Problems, and Promises. *Developmental Cell,* 21**,** 193-215.

Armulik, A., Genove, G., Mae, M., Nisancioglu, M. H., Wallgard, E., Niaudet, C., He, L., Norlin, J., Lindblom, P., Strittmatter, K., Johansson, B. R. & Betsholtz, C. 2010. Pericytes regulate the blood-brain barrier. *Nature,* 468**,** 557-61.

Arnaud, L., Robakis, N. K. & Figueiredo-Pereira, M. E. 2007. It May Take Inflammation, Phosphorylation and Ubiquitination to 'Tangle' in Alzheimer's Disease. *Neurodegenerative Diseases,* 3**,** 313-319.

Arnaud, L. T., Myeku, N. & Figueiredo-Pereira, M. E. 2009. Proteasome–caspase–cathepsin sequence leading to tau pathology induced by prostaglandin J2 in neuronal cells. *Journal of Neurochemistry,* 110**,** 328-342.

Atri, A. 2019. Current and Future Treatments in Alzheimer's Disease. *Semin Neurol,* 39**,** 227-240.

Attrill, E., Ramsay, C., Ross, R. M., Richards, S. M., Sutherland, B. A., Keske, M. A., Eringa, E. C. & Premilovac, D. 2019. Metabolic-vascular Coupling in Skeletal Muscle: A Potential Role for Capillary Pericytes? *Clinical and Experimental Pharmacology and Physiology,* 47**,** 520-528.

Attwell, D., Buchan, A. M., Charpak, S., Lauritzen, M., Macvicar, B. A. & Newman, E. A. 2010. Glial and neuronal control of brain blood flow. *Nature,* 468**,** 232-43.

Attwell, D. & Laughlin, S. B. 2001. An energy budget for signaling in the grey matter of the brain. *J Cereb Blood Flow Metab,* 21**,** 1133-45.

Augustin-Voss, H. G., Voss, A. K. & Pauli, B. U. 1993. Senescence of aortic endothelial cells in culture: effects of basic fibroblast growth factor expression on cell phenotype, migration, and proliferation. *Journal of cellular physiology,* 157**,** 279-288.

Axpe, E., Orive, G., Franze, K. & Appel, E. A. 2020. Towards brain-tissue-like biomaterials. *Nature Communications,* 11**,** 3423.

Bacher, M., Meinhardt, A., Lan, H. Y., Dhabhar, F. S., Mu, W., Metz, C. N., Chesney, J., Gemsa, D., Donnelly, T. M., Atkins, R. C. & Bucala, R. 1998. MIF Expression in the Rat Brain: Implications for Neuronal Function. *Molecular Medicine,* 4**,** 217-230.

Baeten, K. M. & Akassoglou, K. 2011. Extracellular matrix and matrix receptors in blood-brain barrier formation and stroke. *Dev Neurobiol,* 71**,** 1018-39.

Baloyannis, S. J. & Baloyannis, I. S. 2012. The vascular factor in Alzheimer's disease: A study in Golgi technique and electron microscopy. *Journal of the Neurological Sciences,* 322**,** 117-121.

Banks, W. A., Gray, A. M., Erickson, M. A., Salameh, T. S., Damodarasamy, M., Sheibani, N., Meabon, J. S., Wing, E. E., Morofuji, Y., Cook, D. G. & Reed, M. J. 2015. Lipopolysaccharide-induced blood-brain barrier disruption: roles of cyclooxygenase, oxidative stress, neuroinflammation, and elements of the neurovascular unit. *Journal of Neuroinflammation,* 12**,** 223.

Baumann, N. & Pham-Dinh, D. 2001. Biology of Oligodendrocyte and Myelin in the Mammalian Central Nervous System. *Physiological Reviews,* 81**,** 871-927.

Beaufort, N., Corvazier, E., Mlanaoindrou, S., Bentzmann, S. D. & Pidard, D. 2013. Disruption of the Endothelial Barrier by Proteases From the Bacterial Pathogen Pseudomonas Aeruginosa: Implication of Matrilysis and Receptor Cleavage. *Plos One,* 8**,** e75708.

Bélanger, M., Desjardins, P., Chatauret, N. & Butterworth, R. F. 2005. Selectively Increased Expression of the Astrocytic/Endothelial Glucose Transporter Protein GLUT1 in Acute Liver Failure. *Glia,* 53**,** 557-562.

Bélarbi, K., Jopson, T., Tweedie, D., Arellano, C., Luo, W., Greig, N. H. & Rosi, S. 2012. TNF-α Protein Synthesis Inhibitor Restores Neuronal Function and Reverses Cognitive Deficits Induced by Chronic Neuroinflammation. *Journal of Neuroinflammation,* 9.

Bell, R. D., Winkler, E. A., Singh, I., Sagare, A. P., Deane, R., Wu, Z., Holtzman, D. M., Betsholtz, C., Armulik, A., Sallstrom, J., Berk, B. C. & Zlokovic, B. V. 2012. Apolipoprotein E controls cerebrovascular integrity via cyclophilin A. *Nature,* 485**,** 512-6.

Benjamini, Y., Krieger, A. M. & Yekutieli, D. 2006. Adaptive linear step-up procedures that control the false discovery rate. *Biometrika,* 93**,** 491-507.

Bennett, M. V. L., Contreras, J. E., Bukauskas, F. F. & Sáez, J. C. 2003. New Roles for Astrocytes: Gap Junction Hemichannels Have Something to Communicate. *Trends in Neurosciences,* 26**,** 610-617.

Benson, K., Cramer, S. & Galla, H.-J. 2013. Impedance-based cell monitoring: barrier properties and beyond. *Fluids and barriers of the CNS,* 10**,** 5-5.

Bertram, L. & Tanzi, R. E. 2009. Genome-wide association studies in Alzheimer's disease. *Hum Mol Genet,* 18**,** R137-45.

Bethel-Brown, C., Yao, H., Callen, S., Lee, Y. H., Dash, P. K., Kumar, A. & Buch, S. 2011. HIV-1 Tat-Mediated Induction of Platelet-Derived Growth Factor in Astrocytes: Role of Early Growth Response Gene 1. *The Journal of Immunology,* 186**,** 4119-4129.

Biffi, A. & Greenberg, S. M. 2011. Cerebral Amyloid Angiopathy: A Systematic Review. *J Clin Neurol,* 7**,** 1-9.

Binder, L. I., Frankfurter, A. & Rebhun, L. I. 1985. The distribution of tau in the mammalian central nervous system. *J Cell Biol,* 101**,** 1371-8.

Birgersdotter, A., Sandberg, R. & Ernberg, I. 2005. Gene expression perturbation in vitro--a growing case for three-dimensional (3D) culture systems. *Semin Cancer Biol,* 15**,** 405-12.

Bisht, K., Okojie, K. A., Sharma, K., Lentferink, D. H., Sun, Y. Y., Chen, H. R., Uweru, J. O., Amancherla, S., Calcuttawala, Z., Campos-Salazar, A. B., Corliss, B., Jabbour, L., Benderoth, J., Friestad, B., Mills, W. A., 3rd, Isakson, B. E., Tremblay, M., Kuan, C. Y. & Eyo, U. B. 2021. Capillary-associated microglia regulate vascular structure and function through PANX1-P2RY12 coupling in mice. *Nat Commun,* 12**,** 5289.

Biswas, P., Canosa, S., Schoenfeld, D., Schoenfeld, J., Li, P., Cheas, L. C., Zhang, J., Cordova, A., Sumpio, B. & Madri, J. A. 2006. PECAM-1 affects GSK-3beta-mediated beta-catenin phosphorylation and degradation. *Am J Pathol,* 169**,** 314-24.

Blanchard, J. W., Bula, M., Davila-Velderrain, J., Akay, L. A., Zhu, L., Frank, A., Victor, M. B., Bonner, J. M., Mathys, H., Lin, Y. T., Ko, T., Bennett, D. A., Cam, H. P., Kellis, M. & Tsai, L. H. 2020. Reconstruction of the human blood-brain barrier in vitro reveals a pathogenic mechanism of APOE4 in pericytes. *Nat Med,* 26**,** 952-963.

Blanchette, M. & Daneman, R. 2015. Formation and Maintenance of the BBB. *Mechanisms of Development,* 138**,** 8-16.

Blecharz, K., Frey, D., Schenkel, T., Prinz, V., Bedini, G., Krug, S. M., Czabanka, M., Wagner, J., Fromm, M., Bersano, A. & Vajkoczy, P. 2016. Autocrine Release of Angiopoietin-2 Mediates Cerebrovascular Disintegration in Moyamoya Disease. *Journal of Cerebral Blood Flow & Metabolism,* 37**,** 1527-1539.

Bobbie, M. W., Roy, S., Trudeau, K., Munger, S. J., Simon, A. M. & Roy, S. 2010. Reduced connexin 43 expression and its effect on the development of vascular lesions in retinas of diabetic mice. *Invest Ophthalmol Vis Sci,* 51**,** 3758-63.

Bonham, L. W., Geier, E. G., Steele, N. Z. R., Holland, D., Miller, B. L., Dale, A. M., Desikan, R. S., Yokoyama, J. S. & Initiative, A. S. D. N. 2018. Insulin-Like Growth Factor Binding Protein 2 Is Associated With Biomarkers of Alzheimer's Disease Pathology and Shows Differential Expression in Transgenic Mice. *Frontiers in Neuroscience,* 12.

Boudko, S. P., Danylevych, N., Hudson, B. G. & Pedchenko, V. 2018. Basement Membrane Collagen IV: Isolation of Functional Domains. 171-185.

Braet, F. & Wisse, E. 2002. Structural and Functional Aspects of Liver Sinusoidal Endothelial Cell Fenestrae: A Review. *Comparative Hepatology,* 1.

Brassard, J. A. & Lutolf, M. P. 2019. Engineering Stem Cell Self-organization to Build Better Organoids. *Cell Stem Cell,* 24**,** 860-876.

Brivio, V., Faivre-Sarrailh, C., Peles, E., Sherman, D. L. & Brophy, P. 2017. Assembly of CNS Nodes of Ranvier in Myelinated Nerves Is Promoted by the Axon Cytoskeleton. *Current Biology,* 27**,** 1068-1073.

Brösicke, N., Sallouh, M., Prior, L. M., Job, A., Weberskirch, R. & Faissner, A. 2015. Extracellular Matrix Glycoprotein-Derived Synthetic Peptides Differentially Modulate Glioma and Sarcoma Cell Migration. *Cell Mol Neurobiol,* 35**,** 741-53.

Brown, K. J., Seol, H., Pillai, D. K., Sankoorikal, B. J., Formolo, C. A., Mac, J. T., Edwards, N., Rose, M. C. & Hathout, Y. 2013. The Human Secretome Atlas Initiative: Implications in Health and Disease Conditions. *Biochimica Et Biophysica Acta (Bba) - Proteins and Proteomics,* 1834**,** 2454-2461.

Brown, L. S., King, N. E., Courtney, J. M., Gasperini, R. J., Foa, L., Howells, D. W. & Sutherland, B. A. 2023. Brain pericytes in culture display diverse morphological and functional phenotypes. *Cell Biol Toxicol,* 39**,** 2999-3014.

Budny, V., Knöpfli, Y., Meier, D., Zürcher, K., Bodenmann, C., Peter, S. L., Müller, T., Tardy, M., Cortijo, C. & Tackenberg, C. 2024. APOE4 Increases Energy Metabolism in APOE-Isogenic iPSC-Derived Neurons. *Cells,* 13.

Burridge, P. W. & Zambidis, E. T. 2013. Highly efficient directed differentiation of human induced pluripotent stem cells into cardiomyocytes. *Methods Mol Biol,* 997**,** 149-61.

Buxbaum, J. D., Christensen, J. L., Ruefli, A. A., Greengard, P. & Loring, J. F. 1993. Expression of APP in Brains of Transgenic Mice Containing the Entire Human APP Gene. *Biochemical and Biophysical Research Communications,* 197**,** 639-645.

Cadena, M. A., Sing, A., Taylor, K., Jin, L., Ning, L., Salar Amoli, M., Singh, Y., Lanjewar, S. N., Tomov, M. L., Serpooshan, V. & Sloan, S. A. 2024. A 3D Bioprinted Cortical Organoid Platform for Modeling Human Brain Development. *Adv Healthc Mater***,** e2401603.

Calderon, G. A., Thai, P., Hsu, C. W., Grigoryan, B., Gibson, S. M., Dickinson, M. E. & Miller, J. S. 2017. Tubulogenesis of co-cultured human iPS-derived endothelial cells and human mesenchymal stem cells in fibrin and gelatin methacrylate gels. *Biomater Sci,* 5**,** 1652-1660.

Campisi, M., Shin, Y., Osaki, T., Hajal, C., Chiono, V. & Kamm, R. D. 2018. 3D self-organized microvascular model of the human blood-brain barrier with endothelial cells, pericytes and astrocytes. *Biomaterials,* 180**,** 117-129.

Candelario-Jalil, E., Yang, Y. & Rosenberg, G. A. 2009. Diverse Roles of Matrix Metalloproteinases and Tissue Inhibitors of Metalloproteinases in Neuroinflammation and Cerebral Ischemia. *Neuroscience,* 158**,** 983-994.

Canfield, S. G., Stebbins, M. J., Morales, B. S., Asai, S. W., Vatine, G. D., Svendsen, C. N., Palecek, S. P. & Shusta, E. V. 2017. An isogenic blood-brain barrier model comprising brain endothelial cells, astrocytes, and neurons derived from human induced pluripotent stem cells. *J Neurochem,* 140**,** 874-888.

Cannon, T. M., Shah, A. T. & Skala, M. C. 2017. Autofluorescence Imaging Captures Heterogeneous Drug Response Differences Between 2D and 3D Breast Cancer Cultures. *Biomedical Optics Express,* 8**,** 1911.

Cao, J., Ehling, M., März, S., Seebach, J., Tarbashevich, K., Sixta, T., Pitulescu, M. E., Werner, A. C., Flach, B., Montanez, E., Raz, E., Adams, R. H. & Schnittler, H. 2017. Polarized actin and VE-cadherin dynamics regulate junctional remodelling and cell migration during sprouting angiogenesis. *Nat Commun,* 8**,** 2210.

Cao, J., Li, C., Cui, Z., Deng, S., Lei, T., Liu, W., Yang, H. & Chen, P. 2024. Spatial Transcriptomics: A Powerful Tool in Disease Understanding and Drug Discovery. *Theranostics,* 14**,** 2946-2968.

Carr, L. M., Mustafa, S., Care, A. & Collins-Praino, L. E. 2024. More than a number: Incorporating the aged phenotype to improve in vitro and in vivo modeling of neurodegenerative disease. *Brain, Behavior, and Immunity,* 119**,** 554-571.

Carrano, A., Hoozemans, J. J., Van Der Vies, S. M., Van Horssen, J., De Vries, H. E. & Rozemuller, A. J. 2012. Neuroinflammation and blood-brain barrier changes in capillary amyloid angiopathy. *Neurodegener Dis,* 10**,** 329-31.

Chabrier, M. A., Blurton-Jones, M., Agazaryan, A. A., Nerhus, J. L., Martínez-Coria, H. & Laferla, F. M. 2012. Soluble Aβ Promotes Wild-Type Tau Pathology<i>In Vivo</I>. *Journal of Neuroscience,* 32**,** 17345-17350.

Chambers, S. M., Fasano, C. A., Papapetrou, E. P., Tomishima, M., Sadelain, M. & Studer, L. 2009. Highly efficient neural conversion of human ES and iPS cells by dual inhibition of SMAD signaling. *Nat Biotechnol,* 27**,** 275-80.

Chan, Y. H., Harith, H. H., Israf, D. A. & Tham, C. L. 2020. Differential Regulation of LPS-Mediated VE-Cadherin Disruption in Human Endothelial Cells and the Underlying Signaling Pathways: A Mini Review. *Frontiers in Cell and Developmental Biology,* 7.

Chang, C. C., Althaus, J. C., Carruthers, C., Sutton, M. A., Steel, D. G. & Gafni, A. 2013. Synergistic Interactions Between Alzheimer's Aβ40 and Aβ42 on the Surface of Primary Neurons Revealed by Single Molecule Microscopy. *Plos One,* 8**,** e82139.

Chang, Y. J. & Chen, Y. R. 2014. The Coexistence of an Equal Amount of Alzheimer's Amyloid-β 40 and 42 Forms Structurally Stable and Toxic Oligomers Through a Distinct Pathway. *Febs Journal,* 281**,** 2674-2687.

Charoensaensuk, V., Chen, Y.-C., Lin, Y.-C., Ou, K.-L., Yang, L.-Y. & Lu, D. Y. 2021. Porphyromonas Gingivalis Induces Proinflammatory Cytokine Expression Leading to Apoptotic Death Through the Oxidative Stress/NF-κB Pathway in Brain Endothelial Cells. *Cells,* 10**,** 3033.

Chaudhuri, O. 2017. Viscoelastic hydrogels for 3D cell culture. *Biomater Sci,* 5**,** 1480-1490.

Chen, W., Sharma, R., Rizzo, A. N., Siegler, J., Garcia, J. G. N. & Jacobson, J. R. 2014. Role of Claudin-5 in the Attenuation of Murine Acute Lung Injury by Simvastatin. *American Journal of Respiratory Cell and Molecular Biology,* 50**,** 328-336.

Chen, X., Huang, Y., Huang, L., Huang, Z., Hao, Z. Z., Xu, L., Xu, N., Li, Z., Mou, Y., Ye, M., You, R., Zhang, X., Liu, S. & Miao, Z. 2024. A brain cell atlas integrating single-cell transcriptomes across human brain regions. *Nat Med,* 30**,** 2679-2691.

Cheslow, L. & Alvarez, J. I. 2016. Glial-endothelial crosstalk regulates blood–brain barrier function. *Current Opinion in Pharmacology,* 26**,** 39-46.

Cho, C. F., Wolfe, J. M., Fadzen, C. M., Calligaris, D., Hornburg, K., Chiocca, E. A., Agar, N. Y. R., Pentelute, B. L. & Lawler, S. E. 2017. Blood-brain-barrier spheroids as an in vitro screening platform for brain-penetrating agents. *Nat Commun,* 8**,** 15623.

Choi, S. H., Kim, Y. H., Hebisch, M., Sliwinski, C., Lee, S., D'avanzo, C., Chen, H., Hooli, B., Asselin, C., Muffat, J., Klee, J. B., Zhang, C., Wainger, B. J., Peitz, M., Kovacs, D. M., Woolf, C. J., Wagner, S. L., Tanzi, R. E. & Kim, D. Y. 2014. A three-dimensional human neural cell culture model of Alzheimer's disease. *Nature,* 515**,** 274-8.

Choi, Y.-S., Choi, H.-J., Min, J. K., Pyun, B.-J., Maeng, Y. S., Park, H., Kim, J., Kim, Y. M. & Kwon, Y. G. 2009. Interleukin-33 Induces Angiogenesis and Vascular Permeability Through ST2/TRAF6-mediated Endothelial Nitric Oxide Production. *Blood,* 114**,** 3117-3126.

Chow, B. W. & Gu, C. 2017. Gradual Suppression of Transcytosis Governs Functional Blood-Retinal Barrier Formation. *Neuron,* 93**,** 1325-1333 e3.

Cirrito, J. R., Deane, R., Fagan, A. M., Spinner, M. L., Parsadanian, M., Finn, M. B., Jiang, H., Prior, J. L., Sagare, A., Bales, K. R., Paul, S. M., Zlokovic, B. V., Piwnica-Worms, D. & Holtzman, D. M. 2005. P-glycoprotein deficiency at the blood-brain barrier increases amyloid-beta deposition in an Alzheimer disease mouse model. *J Clin Invest,* 115**,** 3285-90.

Cleveland, D. W., Hwo, S.-Y. & Kirschner, M. W. 1977. Purification of tau, a microtubule-associated protein that induces assembly of microtubules from purified tubulin. *Journal of Molecular Biology,* 116**,** 207-225.

Cline, E. N., Bicca, M. A., Viola, K. L. & Klein, W. L. 2018. The Amyloid-β Oligomer Hypothesis: Beginning of the Third Decade. *J Alzheimers Dis,* 64**,** S567-s610.

Conroy, S., Kruyt, F. a. E., Wagemakers, M., Bhat, K. & Dunnen, W. F. a. D. 2018. IL-8 Associates With a Pro-Angiogenic and Mesenchymal Subtype in Glioblastoma. *Oncotarget,* 9**,** 15721-15731.

Cordonnier, C. & Van Der Flier, W. M. 2011. Brain microbleeds and Alzheimer's disease: innocent observation or key player? *Brain,* 134**,** 335-44.

Cordonnier, C., Van Der Flier, W. M., Sluimer, J. D., Leys, D., Barkhof, F. & Scheltens, P. 2006. Prevalence and severity of microbleeds in a memory clinic setting. *Neurology,* 66**,** 1356-60.

Costa, E. C., Moreira, A. F., De Melo-Diogo, D., Gaspar, V. M., Carvalho, M. P. & Correia, I. J. 2016. 3D tumor spheroids: an overview on the tools and techniques used for their analysis. *Biotechnology Advances,* 34**,** 1427-1441.

Cummings, J., Zhou, Y., Lee, G., Zhong, K., Fonseca, J. & Cheng, F. 2024. Alzheimer's disease drug development pipeline: 2024. *Alzheimer's & Dementia: Translational Research & Clinical Interventions,* 10**,** e12465.

Cunha, C., Panseri, S., Villa, O., Silva, D. & Gelain, F. 2011. 3D culture of adult mouse neural stem cells within functionalized self-assembling peptide scaffolds. *Int J Nanomedicine,* 6**,** 943-55.

Das, S. K., Bhutia, S. K., Azab, B., Kegelman, T. P., Peachy, L., Santhekadur, P. K., Dasgupta, S., Dash, R., Dent, P., Grant, S., Emdad, L., Pellecchia, M., Sarkar, D. & Fisher, P. B. 2013. MDA-9/Syntenin and IGFBP-2 Promote Angiogenesis in Human Melanoma. *Cancer Research,* 73**,** 844-854.

Davies, L., Wolska, B., Hilbich, C., Multhaup, G., Martins, R., Simms, G., Beyreuther, K. & Masters, C. L. 1988. A4 amyloid protein deposition and the diagnosis of Alzheimer's disease: prevalence in aged brains determined by immunocytochemistry compared with conventional neuropathologic techniques. *Neurology,* 38**,** 1688-93.

Davoodi, E., Sarikhani, E., Montazerian, H., Ahadian, S., Costantini, M., Święszkowski, W., Willerth, S. M., Walus, K., Mofidfar, M., Toyserkani, E., Khademhosseini, A. & Ashammakhi, N. 2020. Extrusion and Microfluidic-Based Bioprinting to Fabricate Biomimetic Tissues and Organs. *Advanced Materials Technologies,* 5.

Dawson, T. M., Golde, T. E. & Lagier-Tourenne, C. 2018. Animal models of neurodegenerative diseases. *Nat Neurosci,* 21**,** 1370-1379.

De Kort, A. M., Kuiperij, H. B., Jäkel, L., Kersten, I., Rasing, I., Van Etten, E. S., Van Rooden, S., Van Osch, M. J. P., Wermer, M. J. H., Terwindt, G. M., Schreuder, F. H. B. M., Klijn, C. J. M. & Verbeek, M. M. 2023. Plasma amyloid beta 42 is a biomarker for patients with hereditary, but not sporadic, cerebral amyloid angiopathy. *Alzheimer's Research & Therapy,* 15**,** 102.

Deane, R., Wu, Z., Sagare, A., Davis, J., Du Yan, S., Hamm, K., Xu, F., Parisi, M., Larue, B., Hu, H. W., Spijkers, P., Guo, H., Song, X., Lenting, P. J., Van Nostrand, W. E. & Zlokovic, B. V. 2004. LRP/amyloid beta-peptide interaction mediates differential brain efflux of Abeta isoforms. *Neuron,* 43**,** 333-44.

Decker, J. M., Krüger, L., Sydow, A., Zhao, S., Frotscher, M., Mandelkow, E. & Mandelkow, E.-M. 2015. Pro-aggregant Tau impairs mossy fiber plasticity due to structural changes and Ca++ dysregulation. *Acta Neuropathologica Communications,* 3**,** 23.

Deczkowska, A., Keren-Shaul, H., Weiner, A., Colonna, M., Schwartz, M. & Amit, I. 2018. Disease-Associated Microglia: A Universal Immune Sensor of Neurodegeneration. *Cell,* 173**,** 1073-1081.

Dejana, E. & Orsenigo, F. 2013. Endothelial adherens junctions at a glance. *J Cell Sci,* 126**,** 2545-9.

Delrose, N. 2024. *Solute Transfer Across Blood-Brain Barrier* [Online]. [Accessed].

Dessalles, C. A., Ramón-Lozano, C., Babataheri, A. & Barakat, A. I. 2021. Luminal Flow Actuation Generates Coupled Shear and Strain in a Microvessel-on-Chip. *Biofabrication,* 14**,** 015003.

Deture, M. & Dickson, D. W. 2019. The Neuropathological Diagnosis of Alzheimer’s Disease. *Molecular Neurodegeneration,* 14.

Di Lullo, E. & Kriegstein, A. R. 2017. The use of brain organoids to investigate neural development and disease. *Nat Rev Neurosci,* 18**,** 573-584.

Di, M., Wang, L., Li, M., Zhang, Y., Liu, X., Zeng, R., Wang, H., Chen, Y., Chen, W., Zhang, Y. & Zhang, M. 2017. Dickkopf1 Destabilizes Atherosclerotic Plaques and Promotes Plaque Formation by Inducing Apoptosis of Endothelial Cells Through Activation of ER Stress. *Cell Death and Disease,* 8**,** e2917-e2917.

Ding, Y., Palecek, S. P. & Shusta, E. V. 2024. iPSC-derived blood-brain barrier modeling reveals APOE isoform-dependent interactions with amyloid beta. *Fluids Barriers CNS,* 21**,** 79.

Diz, A. P., Carvajal-Rodríguez, A. & Skibinski, D. O. 2011. Multiple hypothesis testing in proteomics: a strategy for experimental work. *Mol Cell Proteomics,* 10**,** M110.004374.

Dominy, S. S., Lynch, C., Ermini, F., Benedyk, M., Marczyk, A., Konradi, A., Nguyen, M., Haditsch, U., Raha, D., Griffin, C., Holsinger, L. J., Arastu-Kapur, S., Kaba, S., Lee, A., Ryder, M. I., Potempa, B., Mydel, P., Hellvard, A., Adamowicz, K., Hasturk, H., Walker, G. D., Reynolds, E. C., Faull, R. L. M., Curtis, M. A., Dragunow, M. & Potempa, J. 2019. Porphyromonas gingivalis in Alzheimer's disease brains: Evidence for disease causation and treatment with small-molecule inhibitors. *Sci Adv,* 5**,** eaau3333.

Dore-Duffy, P. & Cleary, K. 2011. Morphology and properties of pericytes. *Methods Mol Biol,* 686**,** 49-68.

Doudna, J. A. & Charpentier, E. 2014. The new frontier of genome engineering with CRISPR-Cas9. *Science,* 346**,** 1258096.

Drummond, E. & Wisniewski, T. 2017. Alzheimer's disease: experimental models and reality. *Acta Neuropathol,* 133**,** 155-175.

Dulmovits, B. M. & Herman, I. M. 2012. Microvascular Remodeling and Wound Healing: A Role for Pericytes. *The International Journal of Biochemistry & Cell Biology,* 44**,** 1800-1812.

Dyer, O. 2024. Aduhelm: Biogen abandons Alzheimer’s drug after controversial approval left it unfunded by Medicare. *BMJ,* 384**,** q281.

Echeverria, V., Ducatenzeiler, A., Alhonen, L., Janne, J., Grant, S. M., Wandosell, F., Muro, A., Baralle, F., Li, H., Duff, K., Szyf, M. & Cuello, A. C. 2004. Rat transgenic models with a phenotype of intracellular Abeta accumulation in hippocampus and cortex. *J Alzheimers Dis,* 6**,** 209-19.

Edmondson, R., Broglie, J. J., Adcock, A. F. & Yang, L. 2014. Three-dimensional cell culture systems and their applications in drug discovery and cell-based biosensors. *Assay Drug Dev Technol,* 12**,** 207-18.

Eidson, L. N., Gao, Q., Qu, H., Kikuchi, D. S., Campos, A. C. P., Faidley, E. A., Sun, Y., Kuan, C.-Y., Pagano, R. L., Lassègue, B., Tansey, M. G., Griendling, K. K. & Hernandes, M. S. 2021. Poldip2 Controls Leukocyte Infiltration Into the Ischemic Brain by Regulating Focal Adhesion Kinase-Mediated VCAM-1 Induction. *Scientific Reports,* 11.

Eisenbaum, M., Pearson, A., Ortiz, C., Koprivica, M., Cembran, A., Mullan, M., Crawford, F., Ojo, J. & Bachmeier, C. 2024. Repetitive head trauma and apoE4 induce chronic cerebrovascular alterations that impair tau elimination from the brain. *Exp Neurol,* 374**,** 114702.

Ellis, R. J., Olichney, J. M., Thal, L. J., Mirra, S. S., Morris, J. C., Beekly, D. & Heyman, A. 1996. Cerebral amyloid angiopathy in the brains of patients with Alzheimer's disease: the CERAD experience, Part XV. *Neurology,* 46**,** 1592-6.

Elwishahy, A., Antia, K., Bhusari, S., Ilechukwu, N. C., Horstick, O. & Winkler, V. 2021. Porphyromonas Gingivalis as a Risk Factor to Alzheimer’s Disease: A Systematic Review. *Journal of Alzheimer's Disease Reports,* 5**,** 721-732.

Emerich, D. F., Silva, E. A., Ali, O. A., Mooney, D. J., Bell, W. J., Yu, S. J., Kaneko, Y. & Borlongan, C. V. 2010. Injectable VEGF Hydrogels Produce Near Complete Neurological and Anatomical Protection Following Cerebral Ischemia in Rats. *Cell Transplantation,* 19**,** 1063-1071.

Eratne, D., Loi, S. M., Farrand, S., Kelso, W., Velakoulis, D. & Looi, J. C. 2018. Alzheimer's disease: clinical update on epidemiology, pathophysiology and diagnosis. *Australas Psychiatry,* 26**,** 347-357.

Faal, T., Phan, D. T. T., Davtyan, H., Scarfone, V. M., Varady, E., Blurton-Jones, M., Hughes, C. C. W. & Inlay, M. A. 2019. Induction of Mesoderm and Neural Crest-Derived Pericytes from Human Pluripotent Stem Cells to Study Blood-Brain Barrier Interactions. *Stem Cell Reports,* 12**,** 451-460.

Farkas, E. & Luiten, P. G. 2001. Cerebral microvascular pathology in aging and Alzheimer's disease. *Prog Neurobiol,* 64**,** 575-611.

Farrer, L. A., Cupples, L. A., Haines, J. L., Hyman, B., Kukull, W. A., Mayeux, R., Myers, R. H., Pericak-Vance, M. A., Risch, N. & Van Duijn, C. M. 1997. Effects of Age, Sex, and Ethnicity on the Association Between Apolipoprotein E Genotype and Alzheimer Disease: A Meta-analysis. *JAMA,* 278**,** 1349-1356.

Fengler, S., Kurkowsky, B., Kaushalya, S. K., Roth, W., Fava, E. & Denner, P. 2022. Human iPSC-derived brain endothelial microvessels in a multi-well format enable permeability screens of anti-inflammatory drugs. *Biomaterials,* 286**,** 121525.

Ferrari-Souza, J. P., Bellaver, B., Ferreira, P. C. L., Benedet, A. L., Povala, G., Lussier, F. Z., Leffa, D. T., Therriault, J., Tissot, C., Soares, C., Wang, Y. T., Chamoun, M., Servaes, S., Macedo, A. C., Vermeiren, M., Bezgin, G., Kang, M. S., Stevenson, J., Rahmouni, N., Pallen, V., Poltronetti, N. M., Cohen, A., Lopez, O. L., Klunk, W. E., Soucy, J. P., Gauthier, S., Souza, D. O., Triana-Baltzer, G., Saad, Z. S., Kolb, H. C., Karikari, T. K., Villemagne, V. L., Tudorascu, D. L., Ashton, N. J., Zetterberg, H., Blennow, K., Zimmer, E. R., Rosa-Neto, P. & Pascoal, T. A. 2023. APOEε4 potentiates amyloid β effects on longitudinal tau pathology. *Nat Aging,* 3**,** 1210-1218.

Flanagan, L. A., Rebaza, L. M., Derzic, S., Schwartz, P. H. & Monuki, E. S. 2006. Regulation of human neural precursor cells by laminin and integrins. *J Neurosci Res,* 83**,** 845-56.

Floquet, N., Pasco, S., Ramont, L., Derreumaux, P., Laronze, J. Y., Nuzillard, J. M., Maquart, F. X., Alix, A. J. & Monboisse, J. C. 2004. The antitumor properties of the alpha3(IV)-(185-203) peptide from the NC1 domain of type IV collagen (tumstatin) are conformation-dependent. *J Biol Chem,* 279**,** 2091-100.

Forner, S., Baglietto-Vargas, D., Martini, A. C., Trujillo-Estrada, L. & Laferla, F. M. 2017. Synaptic Impairment in Alzheimer's Disease: A Dysregulated Symphony. *Trends in Neurosciences,* 40**,** 347-357.

Fox, L. M., William, C., Adamowicz, D. H., Pitstick, R., Carlson, G. A., Spires-Jones, T. L. & Hyman, B. T. 2011. Soluble Tau Species, Not Neurofibrillary Aggregates, Disrupt Neural System Integration in a Tau Transgenic Model. *Journal of Neuropathology & Experimental Neurology,* 70**,** 588-595.

Fu, J., Fu, Y. W., Zhao, J. J., Yang, Z. X., Li, S. A., Li, G. H., Quan, Z. J., Zhang, F., Zhang, J. P., Zhang, X. B. & Sun, C. K. 2022. Improved and Flexible HDR Editing by Targeting Introns in iPSCs. *Stem Cell Rev Rep,* 18**,** 1822-1833.

Fukumoto, S., Hanazono, K., Komatsu, T., Iwano, H., Kadosawa, T. & Uchide, T. 2013. L-Type Amino Acid Transporter 1 (LAT1) Expression in Canine Mammary Gland Tumors. *Journal of Veterinary Medical Science,* 75**,** 431-437.

Furuse, M. 2010. Molecular basis of the core structure of tight junctions. *Cold Spring Harb Perspect Biol,* 2**,** a002907.

Furuse, M., Fujita, K., Hiiragi, T., Fujimoto, K. & Tsukita, S. 1998. Claudin-1 and -2: Novel Integral Membrane Proteins Localizing at Tight Junctions With No Sequence Similarity to Occludin. *The Journal of Cell Biology,* 141**,** 1539-1550.

Gaceb, A., Özen, I., Padel, T., Barbariga, M. & Paul, G. 2017. Pericytes Secrete Pro-Regenerative Molecules in Response to Platelet-Derived Growth Factor-Bb. *Journal of Cerebral Blood Flow & Metabolism,* 38**,** 45-57.

Garcia, F. J., Sun, N., Lee, H., Godlewski, B., Mathys, H., Galani, K., Zhou, B., Jiang, X., Ng, A. P., Mantero, J., Tsai, L. H., Bennett, D. A., Sahin, M., Kellis, M. & Heiman, M. 2022. Single-cell dissection of the human brain vasculature. *Nature,* 603**,** 893-899.

Gatseva, A., Sin, Y. Y., Brezzo, G. & Van Agtmael, T. 2019. Basement membrane collagens and disease mechanisms. *Essays Biochem,* 63**,** 297-312.

Gauthier, S., Albert, M., Fox, N., Goedert, M., Kivipelto, M., Mestre-Ferrandiz, J. & Middleton, L. T. 2016. Why has therapy development for dementia failed in the last two decades? *Alzheimers Dement,* 12**,** 60-4.

Gijzen, L., Marescotti, D., Raineri, E., Nicolas, A., Lanz, H. L., Guerrera, D., Van Vught, R., Joore, J., Vulto, P., Peitsch, M. C., Hoeng, J., Lo Sasso, G. & Kurek, D. 2020. An Intestine-on-a-Chip Model of Plug-and-Play Modularity to Study Inflammatory Processes. *SLAS Technology,* 25**,** 585-597.

Glenner, G. G. & Wong, C. W. 1984. Alzheimer's disease: initial report of the purification and characterization of a novel cerebrovascular amyloid protein. *Biochem Biophys Res Commun,* 120**,** 885-90.

Goshi, N., Morgan, R. K., Lein, P. J. & Seker, E. 2020. A primary neural cell culture model to study neuron, astrocyte, and microglia interactions in neuroinflammation. *Journal of Neuroinflammation,* 17**,** 155.

Gotz, J., Bodea, L. G. & Goedert, M. 2018. Rodent models for Alzheimer disease. *Nat Rev Neurosci,* 19**,** 583-598.

Granata, R., Trovato, L., Garbarino, G. M., Taliano, M., Ponti, R., Sala, G., Ghidoni, R. & Ghigo, E. 2004. Dual Effects of IGFBP-3 on Endothelial Cell Apoptosis and Survival: Involvement of the Sphingolipid Signaling Pathways. *The Faseb Journal,* 18**,** 1456-1458.

Grebenyuk, S. & Ranga, A. 2019. Engineering Organoid Vascularization. *Front Bioeng Biotechnol,* 7**,** 39.

Guo, Q., Mintier, G., Ma-Edmonds, M., Storton, D., Wang, X., Xiao, X., Kienzle, B., Zhao, D. & Feder, J. N. 2018. 'Cold shock' increases the frequency of homology directed repair gene editing in induced pluripotent stem cells. *Sci Rep,* 8**,** 2080.

Guo, S., Yang, X., Cheng, Y. & Qian, P. 2011. bFGF and PDGF-BB Have a Synergistic Effect on the Proliferation, Migration and VEGF Release of Endothelial Progenitor Cells. *Cell Biology International,* 35**,** 545-551.

Guo, T., Noble, W. & Hanger, D. P. 2017. Roles of tau protein in health and disease. *Acta Neuropathol,* 133**,** 665-704.

Haass, C., Schlossmacher, M. G., Hung, A. Y., Vigo-Pelfrey, C., Mellon, A., Ostaszewski, B. L., Lieberburg, I., Koo, E. H., Schenk, D., Teplow, D. B. & Et Al. 1992. Amyloid beta-peptide is produced by cultured cells during normal metabolism. *Nature,* 359**,** 322-5.

Halder, S. K., Delorme-Walker, V. & Milner, R. 2023. B1 Integrin Is Essential for Blood–brain Barrier Integrity Under Stable and Vascular Remodelling Conditions; Effects Differ With Age. *Fluids and Barriers of the CNS,* 20.

Hall, C. N., Reynell, C., Gesslein, B., Hamilton, N. B., Mishra, A., Sutherland, B. A., O'farrell, F. M., Buchan, A., Lauritzen, M. & Attwell, D. 2014a. Capillary Pericytes Regulate Cerebral Blood Flow in Health and Disease. *Nature,* 508**,** 55-60.

Hall, C. N., Reynell, C., Gesslein, B., Hamilton, N. B., Mishra, A., Sutherland, B. A., O'farrell, F. M., Buchan, A. M., Lauritzen, M. & Attwell, D. 2014b. Capillary pericytes regulate cerebral blood flow in health and disease. *Nature,* 508**,** 55-60.

Halliday, M. R., Rege, S. V., Ma, Q., Zhao, Z., Miller, C. A., Winkler, E. A. & Zlokovic, B. V. 2015. Accelerated pericyte degeneration and blood–brain barrier breakdown in apolipoprotein E4 carriers with Alzheimer's disease. *Journal of Cerebral Blood Flow & Metabolism,* 36**,** 216-227.

Hallmann, R., Horn, N., Selg, M., Wendler, O., Pausch, F. & Sorokin, L. M. 2005. Expression and function of laminins in the embryonic and mature vasculature. *Physiol Rev,* 85**,** 979-1000.

Harik, S. I. 1992. Changes in the glucose transporter of brain capillaries. *Can J Physiol Pharmacol,* 70 Suppl**,** S113-7.

Harold, D., Abraham, R., Hollingworth, P., Sims, R., Gerrish, A., Hamshere, M. L., Pahwa, J. S., Moskvina, V., Dowzell, K., Williams, A., Jones, N., Thomas, C., Stretton, A., Morgan, A. R., Lovestone, S., Powell, J., Proitsi, P., Lupton, M. K., Brayne, C., Rubinsztein, D. C., Gill, M., Lawlor, B., Lynch, A., Morgan, K., Brown, K. S., Passmore, P. A., Craig, D., Mcguinness, B., Todd, S., Holmes, C., Mann, D., Smith, A. D., Love, S., Kehoe, P. G., Hardy, J., Mead, S., Fox, N., Rossor, M., Collinge, J., Maier, W., Jessen, F., Schurmann, B., Heun, R., Van Den Bussche, H., Heuser, I., Kornhuber, J., Wiltfang, J., Dichgans, M., Frolich, L., Hampel, H., Hull, M., Rujescu, D., Goate, A. M., Kauwe, J. S., Cruchaga, C., Nowotny, P., Morris, J. C., Mayo, K., Sleegers, K., Bettens, K., Engelborghs, S., De Deyn, P. P., Van Broeckhoven, C., Livingston, G., Bass, N. J., Gurling, H., Mcquillin, A., Gwilliam, R., Deloukas, P., Al-Chalabi, A., Shaw, C. E., Tsolaki, M., Singleton, A. B., Guerreiro, R., Muhleisen, T. W., Nothen, M. M., Moebus, S., Jockel, K. H., Klopp, N., Wichmann, H. E., Carrasquillo, M. M., Pankratz, V. S., Younkin, S. G., Holmans, P. A., O'donovan, M., Owen, M. J. &

Williams, J. 2009. Genome-wide association study identifies variants at CLU and PICALM associated with Alzheimer's disease. *Nat Genet,* 41**,** 1088-93.

Hartmann, D. A., Underly, R. G., Watson, A. N. & Shih, A. Y. 2015. A Murine Toolbox for Imaging the Neurovascular Unit. *Microcirculation,* 22**,** 168-182.

Hartz, A. M., Zhong, Y., Wolf, A., Levine, H., 3rd, Miller, D. S. & Bauer, B. 2016. Aβ40 Reduces P-Glycoprotein at the Blood-Brain Barrier through the Ubiquitin-Proteasome Pathway. *J Neurosci,* 36**,** 1930-41.

Hasaneen, N. A., Cao, J., Pulkoski-Gross, A., Zucker, S. & Foda, H. D. 2016. Extracellular Matrix Metalloproteinase Inducer (EMMPRIN) Promotes Lung Fibroblast Proliferation, Survival and Differentiation to Myofibroblasts. *Respiratory Research,* 17.

Hayashi, T., Noshita, N., Sugawara, T. & Chan, P. H. 2003. Temporal Profile of Angiogenesis and Expression of Related Genes in the Brain After Ischemia. *Journal of Cerebral Blood Flow & Metabolism,* 23**,** 166-180.

Heaster, T. M., Humayun, M., Yu, J., Beebe, D. J. & Skala, M. C. 2020. Autofluorescence Imaging of 3D Tumor–Macrophage Microscale Cultures Resolves Spatial and Temporal Dynamics of Macrophage Metabolism. *Cancer Research,* 80**,** 5408-5423.

Heikkilä, T. J., Ylä-Outinen, L., Tanskanen, J. M., Lappalainen, R. S., Skottman, H., Suuronen, R., Mikkonen, J. E., Hyttinen, J. A. & Narkilahti, S. 2009. Human embryonic stem cell-derived neuronal cells form spontaneously active neuronal networks in vitro. *Exp Neurol,* 218**,** 109-16.

Hendriks, D., Pagliaro, A., Andreatta, F., Ma, Z., Van Giessen, J., Massalini, S., López-Iglesias, C., Van Son, G. J. F., Demartino, J., Damen, J. M. A., Zoutendijk, I., Staliarova, N., Bredenoord, A. L., Holstege, F. C. P., Peters, P. J., Margaritis, T., Chuva De Sousa Lopes, S., Wu, W., Clevers, H. & Artegiani, B. 2024. Human fetal brain self-organizes into long-term expanding organoids. *Cell,* 187**,** 712-732.e38.

Heneka, M. T., Carson, M. J., El Khoury, J., Landreth, G. E., Brosseron, F., Feinstein, D. L., Jacobs, A. H., Wyss-Coray, T., Vitorica, J., Ransohoff, R. M., Herrup, K., Frautschy, S. A., Finsen, B., Brown, G. C., Verkhratsky, A., Yamanaka, K., Koistinaho, J., Latz, E., Halle, A., Petzold, G. C., Town, T., Morgan, D., Shinohara, M. L., Perry, V. H., Holmes, C., Bazan, N. G., Brooks, D. J., Hunot, S., Joseph, B., Deigendesch, N., Garaschuk, O., Boddeke, E., Dinarello, C. A., Breitner, J. C., Cole, G. M., Golenbock, D. T. & Kummer, M. P. 2015. Neuroinflammation in Alzheimer's disease. *Lancet Neurol,* 14**,** 388-405.

Herzig, M. C., Van Nostrand, W. E. & Jucker, M. 2006. Mechanism of cerebral beta-amyloid angiopathy: murine and cellular models. *Brain Pathol,* 16**,** 40-54.

Herzig, M. C., Winkler, D. T., Burgermeister, P., Pfeifer, M., Kohler, E., Schmidt, S. D., Danner, S., Abramowski, D., Stürchler-Pierrat, C., Bürki, K., Van Duinen, S. G., Maat-Schieman, M. L., Staufenbiel, M., Mathews, P. M. & Jucker, M. 2004. Abeta is targeted to the vasculature in a mouse model of hereditary cerebral hemorrhage with amyloidosis. *Nat Neurosci,* 7**,** 954-60.

Hill, R. A., Тонг, Л., Yuan, P., Murikinati, S., Gupta, S. & Grutzendler, J. 2015. Regional Blood Flow in the Normal and Ischemic Brain Is Controlled by Arteriolar Smooth Muscle Cell Contractility and Not by Capillary Pericytes. *Neuron,* 87**,** 95-110.

Hohenester, E. 2019. Structural Biology of Laminins. *Essays in Biochemistry,* 63**,** 285-295.

Høilund-Carlsen, P. F., Alavi, A., Barrio, J. R., Castellani, R. J., Costa, T., Herrup, K., Kepp, K. P., Neve, R. L., Perry, G., Revheim, M.-E., Robakis, N. K., Sensi, S. L. & Vissel, B. 2024. Donanemab, another anti-Alzheimer's drug with risk and uncertain benefit. *Ageing Research Reviews,* 99**,** 102348.

Hollmann, E. K., Bailey, A. K., Potharazu, A. V., Neely, M. D., Bowman, A. B. & Lippmann, E. S. 2017. Accelerated differentiation of human induced pluripotent stem cells to blood-brain barrier endothelial cells. *Fluids Barriers CNS,* 14**,** 9.

Holmer, J., Eriksdotter, M., Schultzberg, M., Pussinen, P. J. & Buhlin, K. 2018. Association between periodontitis and risk of Alzheimer's disease, mild cognitive impairment and subjective cognitive decline: A case-control study. *J Clin Periodontol,* 45**,** 1287-1298.

Holmes, B. B. & Diamond, M. I. 2014. Prion-like Properties of Tau Protein: The Importance of Extracellular Tau as a Therapeutic Target*. *Journal of Biological Chemistry,* 289**,** 19855-19861.

Hooijmans, C. R., Graven, C., Dederen, P. J., Tanila, H., Van Groen, T. & Kiliaan, A. J. 2007. Amyloid beta deposition is related to decreased glucose transporter-1 levels and hippocampal atrophy in brains of aged APP/PS1 mice. *Brain Res,* 1181**,** 93-103.

Horwood, N. & Davies, D. C. 1994. Immunolabelling of hippocampal microvessel glucose transporter protein is reduced in Alzheimer's disease. *Virchows Arch,* 425**,** 69-72.

Howe, M. D., Mccullough, L. D. & Urayama, A. 2020. The Role of Basement Membranes in Cerebral Amyloid Angiopathy. *Frontiers in Physiology,* 11.

Hribar, K. C., Finlay, D., Ma, X., Qu, X., Ondeck, M. G., Chung, P., Zanella, F., Engler, A. J., Sheikh, F., Vuori, K. & Chen, S. C. 2015. Nonlinear 3D Projection Printing of Concave Hydrogel Microstructures for Long-Term Multicellular Spheroid and Embryoid Body Culture. *Lab on a Chip,* 15**,** 2412-2418.

Hsiao, H. Y., Chen, Y. C., Huang, C. H., Chen, C. C., Hsu, Y. H., Chen, H. M., Chiu, F. L., Kuo, H. C., Chang, C. & Chern, Y. 2015. Aberrant astrocytes impair vascular reactivity in Huntington disease. *Ann Neurol,* 78**,** 178-92.

Huang, S. X., Islam, M. N., O'neill, J., Hu, Z., Yang, Y. G., Chen, Y. W., Mumau, M., Green, M. D., Vunjak-Novakovic, G., Bhattacharya, J. & Snoeck, H. W. 2014. Efficient generation of lung and airway epithelial cells from human pluripotent stem cells. *Nat Biotechnol,* 32**,** 84-91.

Humphrey, J. D., Dufresne, E. R. & Schwartz, M. A. 2014. Mechanotransduction and Extracellular Matrix Homeostasis. *Nature Reviews Molecular Cell Biology,* 15**,** 802-812.

Hynes, W. F., Pepona, M., Robertson, C., Alvarado, J., Dubbin, K., Triplett, M., Adorno, J. J., Randles, A. & Moya, M. L. Examining metastatic behavior within 3D bioprinted vasculature for the validation of a 3D computational flow model. *Science Advances,* 6**,** eabb3308.

Ide, M., Harris, M., Stevens, A., Sussams, R., Hopkins, V., Culliford, D., Fuller, J., Ibbett, P., Raybould, R., Thomas, R., Puenter, U., Teeling, J., Perry, V. H. & Holmes, C. 2016. Periodontitis and Cognitive Decline in Alzheimer's Disease. *PLoS One,* 11**,** e0151081.

Igarashi, Y., Utsumi, H., Chiba, H., Yamada-Sasamori, Y., Tobioka, H., Kamimura, Y., Furuuchi, K., Kokai, Y., Nakagawa, T., Mori, M. & Sawada, N. 1999. Glial Cell Line-Derived Neurotrophic Factor Induces Barrier Function of Endothelial Cells Forming the Blood–Brain Barrier. *Biochemical and Biophysical Research Communications,* 261**,** 108-112.

Iliff, J. J., Wang, M., Liao, Y., Plogg, B. A., Peng, W., Gundersen, G. A., Benveniste, H., Vates, G. E., Deane, R., Goldman, S. A. & Nagelhus, E. A. 2012a. A Paravascular Pathway Facilitates CSF Flow Through the Brain Parenchyma and the Clearance of Interstitial Solutes, Including Amyloid Β. *Science Translational Medicine,* 4.

Iliff, J. J., Wang, M., Liao, Y., Plogg, B. A., Peng, W., Gundersen, G. A., Benveniste, H., Vates, G. E., Deane, R., Goldman, S. A., Nagelhus, E. A. & Nedergaard, M. 2012b. A paravascular pathway facilitates CSF flow through the brain parenchyma and the clearance of interstitial solutes, including amyloid β. *Sci Transl Med,* 4**,** 147ra111.

Itallie, C. M. V., Fanning, A. S., Holmes, J. H. & Anderson, J. M. 2010. Occludin Is Required for Cytokine-Induced Regulation of Tight Junction Barriers. *Journal of Cell Science,* 123**,** 2844-2852.

Izawa, Y., Gu, Y. H., Osada, T., Kanazawa, M., Hawkins, B. T., Koziol, J. A., Papayannopoulou, T., Spatz, M. & Zoppo, G. J. D. 2017. Β1-Integrin–matrix Interactions Modulate Cerebral Microvessel Endothelial Cell Tight Junction Expression and Permeability. *Journal of Cerebral Blood Flow & Metabolism,* 38**,** 641-658.

Jamieson, J. J., Linville, R. M., Ding, Y. Y., Gerecht, S. & Searson, P. C. 2019. Role of iPSC-derived pericytes on barrier function of iPSC-derived brain microvascular endothelial cells in 2D and 3D. *Fluids Barriers CNS,* 16**,** 15.

Jan, A., Gokce, O., Luthi-Carter, R. & Lashuel, H. A. 2008. The Ratio of Monomeric to Aggregated Forms of Aβ40 and Aβ42 Is an Important Determinant of Amyloid-β Aggregation, Fibrillogenesis, and Toxicity*. *Journal of Biological Chemistry,* 283**,** 28176-28189.

Jan, S. L., Meur, N. L., Cazes, A., Philippe, J. M., Cunff, M. L., Léger, J. J., Corvol, P. & Germain, S. 2006. Characterization of the Expression of the Hypoxia-induced Genes Neuritin, TXNIP and IGFBP3 in Cancer. *Febs Letters,* 580**,** 3395-3400.

Janaway, B. M., Simpson, J. E., Hoggard, N., Highley, J. R., Forster, G., Drew, D., Gebril, O. H., Matthews, F. E., Brayne, C., Wharton, S. B., Ince, P. G. & Study, A. 2014. Brain Haemosiderin in Older People: Pathological Evidence for an Ischaemic Origin of Magnetic Resonance Imaging (<scp>MRI</Scp>) Microbleeds. *Neuropathology and Applied Neurobiology,* 40**,** 258-269.

Jansson, D., Rustenhoven, J., Feng, S., Hurley, D., Oldfield, R. L., Bergin, P. S., Mee, E. W., Faull, R. L. & Dragunow, M. 2014. A role for human brain pericytes in neuroinflammation. *J Neuroinflammation,* 11**,** 104.

Jäntti, H., Sitnikova, V., Ishchenko, Y., Shakirzyanova, A., Giudice, L., Ugidos, I. F., Gómez-Budia, M., Korvenlaita, N., Ohtonen, S., Belaya, I., Fazaludeen, F., Mikhailov, N., Gotkiewicz, M., Ketola, K., Lehtonen, Š., Koistinaho, J., Kanninen, K. M., Hernández, D., Pébay, A., Giugno, R., Korhonen, P., Giniatullin, R. & Malm, T. 2022. Microglial amyloid beta clearance is driven by PIEZO1 channels. *J Neuroinflammation,* 19**,** 147.

Jellinger, K. A. 2002. Alzheimer disease and cerebrovascular pathology: an update. *J Neural Transm (Vienna),* 109**,** 813-36.

Jih, K.-Y., Hsu, T.-R., Fuh, J.-L., Lee, T.-H., Lin, Y.-S., Fang, S.-Y., Liao, Y.-C. & Lee, Y.-C. 2025. Early presentation of spastic paraparesis in individuals carrying PSEN1 mutations: a clinical and genetic analysis. *Alzheimer's Research & Therapy,* 17**,** 96.

Johnson, G. V. & Stoothoff, W. H. 2004. Tau phosphorylation in neuronal cell function and dysfunction. *J Cell Sci,* 117**,** 5721-9.

Johnson, R. H., Kho, D. T., O' Carroll, S. J., Angel, C. E. & Graham, E. S. 2018. The functional and inflammatory response of brain endothelial cells to Toll-Like Receptor agonists. *Scientific Reports,* 8**,** 10102.

Joo, H. J., Choi, D. K., Lim, J. S., Park, J. S., Lee, S. H., Song, S., Shin, J. H., Lim, D. S., Kim, I., Hwang, K. C. & Koh, G. Y. 2012. ROCK suppression promotes differentiation and expansion of endothelial cells from embryonic stem cell-derived Flk1(+) mesodermal precursor cells. *Blood,* 120**,** 2733-44.

Jorfi, M., D'avanzo, C., Tanzi, R. E., Kim, D. Y. & Irimia, D. 2018. Human Neurospheroid Arrays for In Vitro Studies of Alzheimer's Disease. *Scientific Reports,* 8**,** 2450.

Jouanne, M., Rault, S. & Voisin-Chiret, A. S. 2017. Tau protein aggregation in Alzheimer's disease: An attractive target for the development of novel therapeutic agents. *Eur J Med Chem,* 139**,** 153-167.

Jung, M., Skhinas, J. N., Du, E. Y., Tolentino, M. a. K., Utama, R. H., Engel, M., Volkerling, A., Sexton, A., O'mahony, A. P., Ribeiro, J. C. C., Gooding, J. J. & Kavallaris, M. 2022. A high-throughput 3D bioprinted cancer cell migration and invasion model with versatile and broad biological applicability. *Biomater Sci,* 10**,** 5876-5887.

Kadzik, Rachel s. & Morrisey, Edward e. 2012. Directing Lung Endoderm Differentiation in Pluripotent Stem Cells. *Cell Stem Cell,* 10**,** 355-361.

Kamińska, J., Tylicka, M., Dymicka-Piekarska, V., Mariak, Z., Matowicka-Karna, J. & Koper-Lenkiewicz, O. M. 2022. Canonical NF-κB Signaling Pathway and GRO-α/CXCR2 Axis Are Activated in Unruptured Intracranial Aneurysm Patients. *Scientific Reports,* 12.

Karimi-Abdolrezaee, S., Schut, D., Wang, J. & Fehlings, M. G. 2012. Chondroitinase and Growth Factors Enhance Activation and Oligodendrocyte Differentiation of Endogenous Neural Precursor Cells After Spinal Cord Injury. *Plos One,* 7**,** e37589.

Karmirian, K., Holubiec, M., Goto-Silva, L., Fernandez Bessone, I., Vitória, G., Mello, B., Alloatti, M., Vanderborght, B., Falzone, T. L. & Rehen, S. 2023. Modeling Alzheimer's Disease Using Human Brain Organoids. *Methods Mol Biol,* 2561**,** 135-158.

Karp, A., Kåreholt, I., Qiu, C., Bellander, T., Winblad, B. & Fratiglioni, L. 2004. Relation of education and occupation-based socioeconomic status to incident Alzheimer's disease. *Am J Epidemiol,* 159**,** 175-83.

Kastin, A. J., Fasold, M. B. & Zadina, J. E. 2002. Endomorphins, Met-Enkephalin, Tyr-Mif-1, and the P-Glycoprotein Efflux System. *Drug Metabolism and Disposition,* 30**,** 231-234.

Keller, D., Erö, C. & Markram, H. 2018. Cell Densities in the Mouse Brain: A Systematic Review. *Frontiers in Neuroanatomy,* 12.

Keren-Shaul, H., Spinrad, A., Weiner, A., Matcovitch-Natan, O., Dvir-Szternfeld, R., Ulland, T. K., David, E., Baruch, K., Lara-Astaiso, D., Toth, B., Itzkovitz, S., Colonna, M., Schwartz, M. & Amit, I. 2017. A Unique Microglia Type Associated with Restricting Development of Alzheimer's Disease. *Cell,* 169**,** 1276-1290.e17.

Kim, D. H., Lee, D., Chang, E. H., Kim, J. H., Hwang, J. W., Kim, J.-Y., Kyung, J. W., Kim, S. H., Oh, J. S., Shim, S. M., Na, D. L., Oh, W. & Chang, J. W. 2015. GDF-15 Secreted From Human Umbilical Cord Blood Mesenchymal Stem Cells Delivered Through the Cerebrospinal Fluid Promotes Hippocampal Neurogenesis and Synaptic Activity in an Alzheimer's Disease Model. *Stem Cells and Development,* 24**,** 2378-2390.

Kim, J., Lim, J., Yoo, I. D., Park, S. & Moon, J. S. 2023. TXNIP contributes to induction of pro-inflammatory phenotype and caspase-3 activation in astrocytes during Alzheimer's diseases. *Redox Biol,* 63**,** 102735.

Kim, J. H., Yoon, S. M., Song, S. U., Park, S. G., Kim, W. S., Park, I. G., Lee, J. & Sung, J. H. 2016. Hypoxia Suppresses Spontaneous Mineralization and Osteogenic Differentiation of Mesenchymal Stem Cells via IGFBP3 Up-Regulation. *International Journal of Molecular Sciences,* 17**,** 1389.

Kimura, R. & Ohno, M. 2009. Impairments in remote memory stabilization precede hippocampal synaptic and cognitive failures in 5XFAD Alzheimer mouse model. *Neurobiol Dis,* 33**,** 229-35.

King, N. E., Courtney, J. M., Brown, L. S., Fortune, A. J., Blackburn, N. B., Fletcher, J. L., Cashion, J. M., Talbot, J., Pébay, A., Hewitt, A. W., Morris, G. P., Young, K. M., Cook, A. L. & Sutherland, B. A. 2024. Induced pluripotent stem cell derived pericytes respond to mediators of proliferation and contractility. *Stem Cell Res Ther,* 15**,** 59.

King, P., Abraham, C. H., Zauner, K.-P. & Planque, M. R. R. D. 2015. Excitability Modulation of Oscillating Media in 3d-Printed Structures. *Artificial Life,* 21**,** 225-233.

Kisler, K., Nelson, A. R., Montagne, A. & Zlokovic, B. V. 2017. Cerebral blood flow regulation and neurovascular dysfunction in Alzheimer disease. *Nat Rev Neurosci,* 18, 419-434.

Kojro, E. & Fahrenholz, F. 2005. The non-amyloidogenic pathway: structure and function of alpha-secretases. *Subcell Biochem,* 38, 105-27.

Kook, S. Y., Hong, H. S., Moon, M., Ha, C. M., Chang, S. & Mook-Jung, I. 2012. $A\beta_{1-42}$-RAGE interaction disrupts tight junctions of the blood-brain barrier via Ca^{2+}-calcineurin signaling. *J Neurosci,* 32, 8845-54.

Koss, M. J., Pfister, M., Rothweiler, F., Michaelis, M., Činátl, J., Schubert, R. & Koch, F. 2011. Comparison of Cytokine Levels From Undiluted Vitreous of Untreated Patients With Retinal Vein Occlusion. *Acta Ophthalmologica,* 90.

Kováč, A., Erickson, M. A. & Banks, W. A. 2011. Brain Microvascular Pericytes Are Immunoactive in Culture: Cytokine, Chemokine, Nitric Oxide, and LRP-1 Expression in Response to Lipopolysaccharide. *Journal of Neuroinflammation,* 8.

Kress, B. T., Iliff, J. J., Xia, M., Wang, M., Wei, H., Zeppenfeld, D., Xie, L., Kang, H., Xu, Q., Liew, J., Plog, B. A., Ding, F. & Deane, R. 2014. Impairment of Paravascular Clearance Pathways in the Aging Brain. *Annals of Neurology,* 76, 845-861.

Krstic, D. & Knuesel, I. 2013. Deciphering the mechanism underlying late-onset Alzheimer disease. *Nat Rev Neurol,* 9, 25-34.

Krum, J. M., Mani, N. & Rosenstein, J. M. 2008. Roles of the Endogenous VEGF Receptors FLT-1 and FLK-1 in Astroglial and Vascular Remodeling After Brain Injury. *Experimental Neurology,* 212, 108-117.

Kumar, A., Singh, A. & Ekavali 2015. A review on Alzheimer's disease pathophysiology and its management: an update. *Pharmacol Rep,* 67, 195-203.

Kunz, J., Krause, D., Kremer, M. & Dermietzel, R. 1994. The 140-kDa protein of blood-brain barrier-associated pericytes is identical to aminopeptidase N. *Journal of neurochemistry,* 62, 2375-2386.

Kuring, J. K., Mathias, J. L. & Ward, L. 2020. Risk of Dementia in persons who have previously experienced clinically-significant Depression, Anxiety, or PTSD: A Systematic Review and Meta-Analysis. *J Affect Disord,* 274, 247-261.

Kurmann, L., Okoniewski, M. & Dubey, R. K. 2021. Transcriptomic Analysis of Human Brain -Microvascular Endothelial Cell Driven Changes in -Vascular Pericytes. *Cells* [Online], 10.

Kurosawa, T., Sako, D., Tega, Y., Debori, Y., Tomihara, Y., Aoyama, K., Kubo, Y., Amano, N. & Deguchi, Y. 2022. Construction and Functional Evaluation of a Three-Dimensional Blood-Brain Barrier Model Equipped With Human Induced Pluripotent Stem Cell-Derived Brain Microvascular Endothelial Cells. *Pharm Res,* 39, 1535-1547.

Kwak, S. S., Washicosky, K. J., Brand, E., Von Maydell, D., Aronson, J., Kim, S., Capen, D. E., Cetinbas, M., Sadreyev, R., Ning, S., Bylykbashi, E., Xia, W., Wagner, S. L., Choi, S. H., Tanzi, R. E. & Kim, D. Y. 2020. Amyloid-beta42/40 ratio drives tau pathology in 3D human neural cell culture models of Alzheimer's disease. *Nat Commun,* 11, 1377.

Ladwig, A., Walter, H. L., Hucklenbroich, J., Willuweit, A., Langen, K.-J., Fink, G. R., Rueger, M. A. & Schroeter, M. 2017. Osteopontin Augments M2 Microglia Response and Separates M1- and M2-Polarized Microglial Activation in Permanent Focal Cerebral Ischemia. *Mediators of Inflammation,* 2017, 7189421.

Lai, P.-H., Wang, T.-H., Zhang, N.-Y., Wu, K.-C., Yao, C.-C. J. & Lin, C.-J. 2021. Changes of Blood-Brain-Barrier Function and Transfer of Amyloid Beta in Rats With Collagen-Induced Arthritis. *Journal of Neuroinflammation,* 18.

Lambert, J. C., Heath, S., Even, G., Campion, D., Sleegers, K., Hiltunen, M., Combarros, O., Zelenika, D., Bullido, M. J., Tavernier, B., Letenneur, L., Bettens, K., Berr, C., Pasquier, F., Fievet, N., Barberger-Gateau, P., Engelborghs, S., De Deyn, P., Mateo, I., Franck, A., Helisalmi, S., Porcellini, E., Hanon, O., European Alzheimer's Disease Initiative, I., De Pancorbo, M. M., Lendon, C., Dufouil, C., Jaillard, C., Leveillard, T., Alvarez, V., Bosco, P., Mancuso, M., Panza, F., Nacmias, B., Bossu, P., Piccardi, P., Annoni, G., Seripa, D., Galimberti, D., Hannequin, D., Licastro, F., Soininen, H., Ritchie, K., Blanche, H., Dartigues, J. F., Tzourio, C., Gut, I., Van Broeckhoven, C., Alperovitch, A., Lathrop, M. & Amouyel, P. 2009. Genome-wide association study identifies variants at CLU and CR1 associated with Alzheimer's disease. *Nat Genet,* 41**,** 1094-9.

Lamontagne, E., Muotri, A. R. & Engler, A. J. 2022. Recent advancements and future requirements in vascularization of cortical organoids. *Frontiers in Bioengineering and Biotechnology,* 10**,** 1048731.

Lancaster, M. A. & Knoblich, J. A. 2014. Generation of cerebral organoids from human pluripotent stem cells. *Nat Protoc,* 9**,** 2329-40.

Lancaster, M. A., Renner, M., Martin, C. A., Wenzel, D., Bicknell, L. S., Hurles, M. E., Homfray, T., Penninger, J. M., Jackson, A. P. & Knoblich, J. A. 2013. Cerebral organoids model human brain development and microcephaly. *Nature,* 501**,** 373-9.

Landis, D. M. & Reese, T. S. 1974. Arrays of particles in freeze-fractured astrocytic membranes. *J Cell Biol,* 60**,** 316-20.

Langhans, S. A. 2018. Three-Dimensional in Vitro Cell Culture Models in Drug Discovery and Drug Repositioning. *Frontiers in Pharmacology,* 9.

Larson, M. & Lesné, S. 2011. Soluble Aβ Oligomer Production and Toxicity. *Journal of Neurochemistry,* 120**,** 125-139.

Lauridsen, H. M., Pellowe, A. S., Ramanathan, A., Liu, R., Miller-Jensen, K., Mcniff, J. M., Pober, J. S. & Gonzalez, A. L. 2017. Tumor Necrosis Factor-A and IL-17A Activation Induces Pericyte-Mediated Basement Membrane Remodeling in Human Neutrophilic Dermatoses. *American Journal of Pathology,* 187**,** 1893-1906.

Lee, H.-K., Velazquez Sanchez, C., Chen, M., Morin, P. J., Wells, J. M., Hanlon, E. B. & Xia, W. 2016. Three Dimensional Human Neuro-Spheroid Model of Alzheimer’s Disease Based on Differentiated Induced Pluripotent Stem Cells. *PLOS ONE,* 11**,** e0163072.

Lee, S. J., Koh, A., Lee, S. H. & Kim, K. W. 2024. Efficacy of epidermal growth factor in suppressing inflammation and proliferation in pterygial fibroblasts through interactions with microenvironmental M1 macrophages. *Scientific Reports,* 14**,** 22601.

Lee, Y. S., Choi, Y., Park, E. J., Kwon, S., Kim, H., Lee, J. Y. & Lee, D. H. 2020. Improvement of Glymphatic–lymphatic Drainage of Beta-Amyloid by Focused Ultrasound in Alzheimer’s Disease Model. *Scientific Reports,* 10.

Lei, S., Li, J., Yu, J., Li, F., Pan, Y., Chen, X., Ma, C., Zhao, W. & Tang, X. 2023. Porphyromonas gingivalis bacteremia increases the permeability of the blood-brain barrier via the Mfsd2a/Caveolin-1 mediated transcytosis pathway. *Int J Oral Sci,* 15**,** 3.

Lendvai, D., Morawski, M., Brückner, G., Négyessy, L., Glasz, T., Patonay, L., Matthews, R. T., Arendt, T. & Alpár, A. 2011. Perisynaptic Aggrecan-based Extracellular Matrix Coats in the Human Lateral Geniculate Body Devoid of Perineuronal Nets. *Journal of Neuroscience Research,* 90**,** 376-387.

Leng, F., Hinz, R., Gentleman, S., Hampshire, A., Dani, M., Brooks, D. J. & Edison, P. 2022. Neuroinflammation Is Independently Associated With Brain Network Dysfunction in Alzheimer’s Disease. *Molecular Psychiatry,* 28**,** 1303-1311.

Lepelletier, F. X., Mann, D. M., Robinson, A. C., Pinteaux, E. & Boutin, H. 2017. Early changes in extracellular matrix in Alzheimer's disease. *Neuropathol Appl Neurobiol,* 43**,** 167-182.

Leung, A. W., Murdoch, B., Salem, A. F., Prasad, M. S., Gomez, G. A. & García-Castro, M. I. 2016. WNT/β-catenin signaling mediates human neural crest induction via a pre-neural border intermediate. *Development,* 143**,** 398-410.

Li, J., Li, M., Ge, Y., Chen, J., Ma, J., Wang, C., Sun, M., Wang, L., Yao, S. & Yao, C. 2022. B-Amyloid Protein Induces Mitophagy-Dependent Ferroptosis Through the CD36/PINK/PARKIN Pathway Leading to Blood–brain Barrier Destruction in Alzheimer's Disease. *Cell & Bioscience,* 12.

Li, J., Wu, X., Tan, X., Wang, S., Qu, R., Wu, X., Chen, Z., Wang, Z. & Chen, G. 2023a. The Efficacy and Safety of Anti-Aβ Agents for Delaying Cognitive Decline in Alzheimer's Disease: A Meta-Analysis. *Frontiers in Aging Neuroscience,* 15.

Li, L., Song, J., Chuquisana, O., Hannocks, M.-J., Loismann, S., Vogl, T., Roth, J. & Sorokin, L. 2020. Endothelial Basement Membrane Laminins as an Environmental Cue in Monocyte Differentiation to Macrophages. *Frontiers in Immunology,* 11.

Li, N., Luo, R., Zhang, W., Wu, Y., Hu, C., Liu, M., Jiang, D., Jiang, Z., Zhao, X., Wang, Y. & Li, Q. 2023b. IL-17A promotes endothelial cell senescence by up-regulating the expression of FTO through activating JNK signal pathway. *Biogerontology,* 24**,** 99-110.

Li, P. 2023. Pericyte Loss in Diseases. *Cells,* 12**,** 1931.

Li, X., Yang, Z., Chen, Y., Zhang, S., Wei, G. & Zhang, L. 2023c. Dissecting the Molecular Mechanisms of the Co-Aggregation of Aβ40 and Aβ42 Peptides: A REMD Simulation Study. *The Journal of Physical Chemistry B,* 127**,** 4050-4060.

Li, Y., Zhang, W., Doughtie, A., Cui, G., Li, X., Pandit, H., Yang, Y., Li, S. & Martin, R. C. G. 2016. Up-Regulation of Fibroblast Growth Factor 19 and Its Receptor Associates With Progression From Fatty Liver to Hepatocellular Carcinoma. *Oncotarget,* 7**,** 52329-52339.

Li, Y., Zhou, S., Li, J., Sun, Y., Hasimu, H., Liu, R. & Zhang, T. 2015. Quercetin Protects Human Brain Microvascular Endothelial Cells From Fibrillar B-Amyloid1–40-Induced Toxicity. *Acta Pharmaceutica Sinica B,* 5**,** 47-54.

Liang, T., Zhu, L., Gao, W., Gong, M., Ren, J., Yao, H., Wang, K. & Shi, D. 2017. Coculture of Endothelial Progenitor Cells and Mesenchymal Stem Cells Enhanced Their Proliferation and Angiogenesis Through <scp>PDGF</Scp> and Notch Signaling. *Febs Open Bio,* 7**,** 1722-1736.

Liddelow, S. A., Guttenplan, K. A., Clarke, L., Bennett, F. C., Bohlen, C. J., Schirmer, L., Bennett, M. L., Münch, A. E., Chung, W. S., Peterson, T. C., Wilton, D. K., Frouin, A., Napier, B. A., Panicker, N., Kumar, M., Buckwalter, M. S., Rowitch, D. H., Dawson, V. L., Dawson, T. M., Stevens, B. & Barres, B. A. 2017. Neurotoxic Reactive Astrocytes Are Induced by Activated Microglia. *Nature,* 541**,** 481-487.

Lier, J., Streit, W. J. & Bechmann, I. 2021. Beyond Activation: Characterizing Microglial Functional Phenotypes. *Cells,* 10.

Lin, Y.-F., Smith, A. V., Aspelund, T., Betensky, R. A., Smoller, J. W., Gudnason, V., Launer, L. J. & Blacker, D. 2018a. Genetic Overlap Between Vascular Pathologies and Alzheimer's Dementia and Potential Causal Mechanisms. *Alzheimer S & Dementia,* 15**,** 65-75.

Lin, Y. T., Seo, J., Gao, F., Feldman, H. M., Wen, H. L., Penney, J., Cam, H. P., Gjoneska, E., Raja, W. K., Cheng, J., Rueda, R., Kritskiy, O., Abdurrob, F., Peng, Z., Milo, B., Yu, C. J., Elmsaouri, S., Dey, D., Ko, T., Yankner, B. A. & Tsai, L. H. 2018b. APOE4 Causes Widespread Molecular and Cellular Alterations Associated with Alzheimer's Disease Phenotypes in Human iPSC-Derived Brain Cell Types. *Neuron,* 98**,** 1141-1154.e7.

Lindhout, F. W., Krienen, F. M., Pollard, K. S. & Lancaster, M. A. 2024. A molecular and cellular perspective on human brain evolution and tempo. *Nature,* 630, 596-608.

Linville, R. M., Sklar, M. B., Grifno, G. N., Nerenberg, R. F., Zhou, J., Ye, R., Destefano, J. G., Guo, Z., Jha, R., Jamieson, J. J., Zhao, N. & Searson, P. C. 2022. Three-dimensional microenvironment regulates gene expression, function, and tight junction dynamics of iPSC-derived blood-brain barrier microvessels. *Fluids Barriers CNS,* 19, 87.

Lippmann, E. S., Al-Ahmad, A., Azarin, S. M., Palecek, S. P. & Shusta, E. V. 2014a. A retinoic acid-enhanced, multicellular human blood-brain barrier model derived from stem cell sources. *Sci Rep,* 4, 4160.

Lippmann, E. S., Al-Ahmad, A., Azarin, S. M., Palecek, S. P. & Shusta, E. V. 2014b. A retinoic acid-enhanced, multicellular human blood-brain barrier model derived from stem cell sources. *Scientific Reports,* 4, 4160.

Lippmann, E. S., Azarin, S. M., Kay, J. E., Nessler, R. A., Wilson, H. K., Al-Ahmad, A., Palecek, S. P. & Shusta, E. V. 2012a. Derivation of blood-brain barrier endothelial cells from human pluripotent stem cells. *Nature Biotechnology,* 30, 783-791.

Lippmann, E. S., Azarin, S. M., Kay, J. E., Nessler, R. A., Wilson, H. K., Al-Ahmad, A., Palecek, S. P. & Shusta, E. V. 2012b. Derivation of blood-brain barrier endothelial cells from human pluripotent stem cells. *Nat Biotechnol,* 30, 783-91.

Liu, B., Zhang, B., Wang, T., Liang, Q. C., Jing, X., Zheng, J., Wang, C., Meng, Q., Wang, L., Wang, W., Guo, H., You, Y., Zhang, H. & Gao, G. 2010. Increased Expression of Urokinase-type Plasminogen Activator Receptor in the Frontal Cortex of Patients With Intractable Frontal Lobe Epilepsy. *Journal of Neuroscience Research,* 88, 2747-2754.

Liu, C., Kang, C.-Y., Lu, Y., Fang, Z. & Yu, G. 2018. Catalpol Provides a Protective Effect on Fibrillary Aβ_{1–42}-induced Barrier Disruption in an in Vitro Model of the Blood–brain Barrier. *Phytotherapy Research,* 32, 1047-1055.

Liu, C. C., Wang, N., Chen, Y., Inoue, Y., Shue, F., Ren, Y., Wang, M., Qiao, W., Ikezu, T. C., Li, Z., Zhao, J., Martens, Y., Doss, S. V., Rosenberg, C. L., Jeevaratnam, S., Jia, L., Raulin, A. C., Qi, F., Zhu, Y., Alnobani, A., Knight, J., Chen, Y., Linares, C., Kurti, A., Fryer, J. D., Zhang, B., Wu, L. J., Kim, B. Y. S. & Bu, G. 2023. Cell-autonomous effects of APOE4 in restricting microglial response in brain homeostasis and Alzheimer's disease. *Nat Immunol,* 24, 1854-1866.

Liu, P. P., Xie, Y., Meng, X. Y. & Kang, J. S. 2019. History and progress of hypotheses and clinical trials for Alzheimer's disease. *Signal Transduct Target Ther,* 4, 29.

Liu, S., Butler, C. A., Ayton, S., Reynolds, E. C. & Dashper, S. G. 2024. Porphyromonas gingivalis and the pathogenesis of Alzheimer's disease. *Crit Rev Microbiol,* 50, 127-137.

Livingston, G., Sommerlad, A., Orgeta, V., Costafreda, S. G., Huntley, J., Ames, D., Ballard, C., Banerjee, S., Burns, A., Cohen-Mansfield, J., Cooper, C., Fox, N., Gitlin, L. N., Howard, R., Kales, H. C., Larson, E. B., Ritchie, K., Rockwood, K., Sampson, E. L., Samus, Q., Schneider, L. S., Selbæk, G., Teri, L. & Mukadam, N. 2017. Dementia prevention, intervention, and care. *The Lancet,* 390, 2673-2734.

Lok, Z. S. Y. & Lyle, A. N. 2019. Osteopontin in vascular disease: Friend or foe? *Arteriosclerosis, thrombosis, and vascular biology,* 39, 613-622.

López-Teros, M., Alarcón-Aguilar, A., Castillo-Aragón, A., Königsberg, M. & Luna-López, A. 2024. Cytokine profiling in senescent and reactive astrocytes: A systematic review. *Neurobiology of Aging,* 138, 28-35.

Lu, T.-Y., Lu, R.-M., Liao, M.-Y., Yu, J., Chung, C.-H., Kao, C.-F. & Wu, H.-C. 2010. Epithelial cell adhesion molecule regulation is associated with the maintenance of the undifferentiated phenotype of human embryonic stem cells. *The Journal of biological chemistry,* 285, 8719-8732.

Lu, T. M., Houghton, S., Magdeldin, T., Durán, J. G. B., Minotti, A. P., Snead, A., Sproul, A., Nguyen, D.-H. T., Xiang, J., Fine, H. A., Rosenwaks, Z., Studer, L., Rafii, S., Agalliu, D., Redmond, D. & Lis, R. 2021. Pluripotent stem cell-derived epithelium misidentified as brain microvascular endothelium requires ETS factors to acquire vascular fate. *Proceedings of the National Academy of Sciences,* 118**,** e2016950118.

Lutz, S. E., Smith, J. T., Kim, D. H., Cv, O., Ellefsen, K. L., Bates, J., Gandhi, S. & Agalliu, D. 2017. Caveolin1 Is Required for Th1 Cell Infiltration, but Not Tight Junction Remodeling, at the Blood-Brain Barrier in Autoimmune Neuroinflammation. *Cell Reports,* 21**,** 2104-2117.

Lv, Z., Chen, L., Chen, P., Peng, H., Rong, Y., Hong, W., Zhou, Q., Li, N., Li, B., Paolicelli, R. C. & Zhan, Y. 2024. Clearance of β-amyloid and synapses by the optogenetic depolarization of microglia is complement selective. *Neuron,* 112**,** 740-754.e7.

Ma, Q., Zhao, Z., Sagare, A. P., Wu, Y., Wang, M., Owens, N. C., Verghese, P. B., Herz, J., Holtzman, D. M. & Zlokovic, B. V. 2018. Blood-brain barrier-associated pericytes internalize and clear aggregated amyloid-β42 by LRP1-dependent apolipoprotein E isoform-specific mechanism. *Molecular Neurodegeneration,* 13**,** 57.

Maarouf, C. L., Kokjohn, T. A., Whiteside, C. M., Macias, M. P., Kalback, W. M., Sabbagh, M. N., Beach, T. G., Vassar, R. & Roher, A. E. 2013. Molecular Differences and Similarities Between Alzheimer's Disease and the 5XFAD Transgenic Mouse Model of Amyloidosis. *Biochem Insights,* 6**,** 1-10.

Mahley, R. W., Innerarity, T. L., Rall, S. C., Jr. & Weisgraber, K. H. 1984. Plasma lipoproteins: apolipoprotein structure and function. *J Lipid Res,* 25**,** 1277-94.

Mahmoud, S., Gharagozloo, M., Simard, C. & Gris, D. 2019. Astrocytes Maintain Glutamate Homeostasis in the CNS by Controlling the Balance Between Glutamate Uptake and Release. *Cells,* 8**,** 184.

Majumder, J., Torr, E. E., Aisenbrey, E. A., Lebakken, C. S., Favreau, P. F., Richards, W. D., Yin, Y., Chang, Q. & Murphy, W. L. 2024. Human induced pluripotent stem cell-derived planar neural organoids assembled on synthetic hydrogels. *J Tissue Eng,* 15**,** 20417314241230633.

Maki, T., Hayakawa, K., Pham, L. D., Xing, C., Lo, E. H. & Arai, K. 2013. Biphasic mechanisms of neurovascular unit injury and protection in CNS diseases. *CNS Neurol Disord Drug Targets,* 12**,** 302-15.

Mancha Sánchez, E., Gómez-Blanco, J. C., López Nieto, E., Casado, J. G., Macías-García, A., Díaz Díez, M. A., Carrasco-Amador, J. P., Torrejón Martín, D., Sánchez-Margallo, F. M. & Pagador, J. B. 2020. Hydrogels for Bioprinting: A Systematic Review of Hydrogels Synthesis, Bioprinting Parameters, and Bioprinted Structures Behavior. *Front Bioeng Biotechnol,* 8**,** 776.

Mancini, M., Terzic, A., Conley, B. A., Oxburgh, L., Nicola, T. & Vary, C. 2009. Endoglin Plays Distinct Roles in Vascular Smooth Muscle Cell Recruitment and Regulation of Arteriovenous Identity During Angiogenesis. *Developmental Dynamics,* 238**,** 2479-2493.

Mandelkow, E. M. & Mandelkow, E. 2012. Biochemistry and cell biology of tau protein in neurofibrillary degeneration. *Cold Spring Harb Perspect Med,* 2**,** a006247.

Mandybur, T. I. 1986. Cerebral amyloid angiopathy: the vascular pathology and complications. *J Neuropathol Exp Neurol,* 45**,** 79-90.

Marco, S. & Skaper, S. D. 2006. Amyloid beta-peptide1-42 alters tight junction protein distribution and expression in brain microvessel endothelial cells. *Neurosci Lett,* 401**,** 219-24.

Marin, E. P., Derakhshan, B., Lam, T. T., Dávalos, A. & Sessa, W. C. 2012. Endothelial Cell Palmitoylproteomic Identifies Novel Lipid-Modified Targets and Potential Substrates for Protein Acyl Transferases. *Circulation Research,* 110**,** 1336-1344.

Maruyama, T., Dougan, S. K., Truttmann, M. C., Bilate, A. M., Ingram, J. R. & Ploegh, H. L. 2015. Increasing the efficiency of precise genome editing with CRISPR-Cas9 by inhibition of nonhomologous end joining. *Nat Biotechnol,* 33**,** 538-42.

Masters, C. L., Bateman, R., Blennow, K., Rowe, C. C., Sperling, R. A. & Cummings, J. L. 2015. Alzheimer's disease. *Nat Rev Dis Primers,* 1**,** 15056.

Mathiisen, T. M., Lehre, K. P., Danbolt, N. C. & Ottersen, O. P. 2010. The perivascular astroglial sheath provides a complete covering of the brain microvessels: an electron microscopic 3D reconstruction. *Glia,* 58**,** 1094-103.

Matsunaga, S., Kishi, T. & Iwata, N. 2015. Memantine monotherapy for Alzheimer's disease: a systematic review and meta-analysis. *PLoS One,* 10**,** e0123289.

Mattson, M. P., Gary, D. S., Chan, S. L. & Duan, W. 2001. Perturbed endoplasmic reticulum function, synaptic apoptosis and the pathogenesis of Alzheimer's disease. *Biochem Soc Symp***,** 151-62.

Mcgonigle, P. 2014. Animal models of CNS disorders. *Biochem Pharmacol,* 87**,** 140-9.

Mcgowan, E., Pickford, F., Kim, J.-S., Onstead, L., Eriksen, J. L., Yu, C., Skipper, L., Murphy, M. P., Beard, J. D., Das, P., Jansen, K., Delucia, M. W., Lin, W., Dolios, G., Wang, R., Eckman, C. B., Dickson, D. W., Hutton, M., Hardy, J. & Golde, T. E. 2005. Aβ42 Is Essential for Parenchymal and Vascular Amyloid Deposition in Mice. *Neuron,* 47**,** 191-199.

Mcgraw, C. M., Ward, C. S. & Samaco, R. C. 2017. Genetic rodent models of brain disorders: Perspectives on experimental approaches and therapeutic strategies. *Am J Med Genet C Semin Med Genet,* 175**,** 368-379.

Mckhann, G. M., Knopman, D. S., Chertkow, H., Hyman, B. T., Jack, C. R., Jr., Kawas, C. H., Klunk, W. E., Koroshetz, W. J., Manly, J. J., Mayeux, R., Mohs, R. C., Morris, J. C., Rossor, M. N., Scheltens, P., Carrillo, M. C., Thies, B., Weintraub, S. & Phelps, C. H. 2011. The diagnosis of dementia due to Alzheimer's disease: recommendations from the National Institute on Aging-Alzheimer's Association workgroups on diagnostic guidelines for Alzheimer's disease. *Alzheimers Dement,* 7**,** 263-9.

Merlini, M., Meyer, E. P., Ulmann-Schuler, A. & Nitsch, R. M. 2011. Vascular β-amyloid and early astrocyte alterations impair cerebrovascular function and cerebral metabolism in transgenic arcAβ mice. *Acta neuropathologica,* 122**,** 293-311.

Mertens, J., Herdy, J. R., Traxler, L., Schafer, S. T., Schlachetzki, J. C. M., Böhnke, L., Reid, D. A., Lee, H., Zangwill, D., Fernandes, D. P., Agarwal, R. K., Lucciola, R., Zhou-Yang, L., Karbacher, L., Edenhofer, F., Stern, S., Horvath, S., Paquola, A. C. M., Glass, C. K., Yuan, S. H., Ku, M., Szücs, A., Goldstein, L. S. B., Galasko, D. & Gage, F. H. 2021. Age-dependent instability of mature neuronal fate in induced neurons from Alzheimer's patients. *Cell Stem Cell,* 28**,** 1533-1548.e6.

Mestre, H., Hablitz, L. M., Xavier, A. L. R., Feng, W., Zou, W., Pu, T., Monai, H., Murlidharan, G., Rivera, R. M. C., Simon, M., Pike, M. M., Plá, V., Du, T., Kress, B. T., Wang, X., Plog, B. A., Thrane, A. S., Lundgaard, I., Abe, Y., Yasui, M., Thomas, J. H., Xiao, M., Hirase, H., Asokan, A., Iliff, J. J. & Nedergaard, M. 2018. Aquaporin-4-Dependent Glymphatic Solute Transport in the Rodent Brain. *Elife,* 7.

Miao, Z., Chen, X., Yin, H., Huang, Z., Xu, L., Huang, L. F., Ye, M., You, R. & Zhang, X. 2023. Brain Cell Atlas: An Integrative Ensemble of Cell Transcriptomes Across Human Brain Regions.

Mihara, H., Kugawa, M., Sayo, K., Tao, F., Shinohara, M., Nishikawa, M., Sakai, Y., Akama, T. & Kojima, N. 2019. Improved Oxygen Supply to Multicellular Spheroids Using a Gas-Permeable Plate and Embedded Hydrogel Beads. *Cells,* 8**,** 525.

Miners, S., Schulz, I. & Love, S. 2017. Differing Associations Between Aβ Accumulation, Hypoperfusion, Blood–brain Barrier Dysfunction and Loss of PDGFRB Pericyte Marker in the Precuneus and Parietal White Matter in Alzheimer's Disease. *Journal of Cerebral Blood Flow & Metabolism,* 38**,** 103-115.

Mitroshina, E., Kalinina, E. & Vedunova, M. 2023. Optogenetics in Alzheimer's Disease: Focus on Astrocytes. *Antioxidants* [Online], 12.

Mizee, M. R., Nijland, P. G., Van Der Pol, S. M., Drexhage, J. A., Van Het Hof, B., Mebius, R., Van Der Valk, P., Van Horssen, J., Reijerkerk, A. & De Vries, H. E. 2014. Astrocyte-derived retinoic acid: a novel regulator of blood-brain barrier function in multiple sclerosis. *Acta Neuropathol,* 128**,** 691-703.

Mok, K. K., Yeung, S. H., Cheng, G. W., Ma, I. W., Lee, R. H., Herrup, K. & Tse, K. H. 2023. Apolipoprotein E ε4 disrupts oligodendrocyte differentiation by interfering with astrocyte-derived lipid transport. *J Neurochem,* 165**,** 55-75.

Monickaraj, F., Mcguire, P. & Das, A. 2018. Cathepsin D plays a role in endothelial-pericyte interactions during alteration of the blood-retinal barrier in diabetic retinopathy. *Faseb j,* 32**,** 2539-2548.

Montagne, A., Barnes, S. R., Sweeney, M. D., Halliday, M. R., Sagare, A. P., Zhao, Z., Toga, A. W., Jacobs, R. E., Liu, C. Y., Amezcua, L., Harrington, M. G., Chui, H. C., Law, M. & Zlokovic, B. V. 2015. Blood-brain barrier breakdown in the aging human hippocampus. *Neuron,* 85**,** 296-302.

Montagne, A., Zhao, Z. & Zlokovic, B. V. 2017. Alzheimer's disease: A matter of blood-brain barrier dysfunction? *J Exp Med,* 214**,** 3151-3169.

Montalbano, M., Majmundar, L., Sengupta, U., Fung, L. & Kayed, R. 2022. Pathological Tau Signatures and Nuclear Alterations in Neurons, Astrocytes and Microglia in Alzheimer's Disease, Progressive Supranuclear Palsy, and Dementia With Lewy Bodies. *Brain Pathology,* 33.

Monzel, A. S., Smits, L. M., Hemmer, K., Hachi, S., Moreno, E. L., Van Wuellen, T., Jarazo, J., Walter, J., Brüggemann, I., Boussaad, I., Berger, E., Fleming, R. M. T., Bolognin, S. & Schwamborn, J. C. 2017. Derivation of Human Midbrain-Specific Organoids from Neuroepithelial Stem Cells. *Stem Cell Reports,* 8**,** 1144-1154.

Mooradian, A. D., Chung, H. C. & Shah, G. N. 1997. GLUT-1 expression in the cerebra of patients with Alzheimer's disease. *Neurobiol Aging,* 18**,** 469-74.

Mori, M., Matsubara, K., Matsubara, Y., Uchikura, Y., Hashimoto, H., Fujioka, T. & Matsumoto, T. 2015. Stromal Cell-Derived Factor-1α Plays a Crucial Role Based on Neuroprotective Role in Neonatal Brain Injury in Rats. *International Journal of Molecular Sciences,* 16**,** 18018-18032.

Morita, W., Snelling, S., Wheway, K., Watkins, B., Appleton, L., Carr, A. & Dakin, S. G. 2019. ERK1/2 Drives IL-1β-induced Expression of TGF-β1 and BMP-2 in Torn Tendons. *Scientific Reports,* 9.

Morrissette, D. A., Parachikova, A., Green, K. N. & Laferla, F. M. 2009. Relevance of transgenic mouse models to human Alzheimer disease. *J Biol Chem,* 284**,** 6033-7.

Mungenast, A. E., Siegert, S. & Tsai, L. H. 2016. Modeling Alzheimer's disease with human induced pluripotent stem (iPS) cells. *Mol Cell Neurosci,* 73**,** 13-31.

Muñoz, S. S., Garner, B. & Ooi, L. 2021. Generation of APOE knock-down SK-N-SH human neuroblastoma cells using CRISPR/Cas9: a novel cellular model relevant to Alzheimer's disease research. *Biosci Rep,* 41.

Na, R., Yang, J. H., Yeom, Y., Kim, Y. J., Byun, S., Kim, K. & Kim, K. W. 2019. A Systematic Review and Meta-Analysis of Nonpharmacological Interventions for Moderate to Severe Dementia. *Psychiatry Investig,* 16**,** 325-335.

Nachman, E., Wentink, A. S., Madiona, K., Bousset, L., Katsinelos, T., Allinson, K., Kampinga, H., Mcewan, W. A., Jahn, T. R., Melki, R., Mogk, A., Bukau, B. & Nussbaum-Krammer, C. 2020. Disassembly of Tau fibrils by the human Hsp70 disaggregation machinery generates small seeding-competent species. *J Biol Chem,* 295**,** 9676-9690.

Nagy, J. I. & Rash, J. E. 2000. Connexins and gap junctions of astrocytes and oligodendrocytes in the CNS. *Brain Res Brain Res Rev,* 32**,** 29-44.

Nasiri, E., Sankowski, R., Dietrich, H., Oikonomidi, A., Huerta, P. T., Popp, J., Al-Abed, Y. & Bacher, M. 2020. Key role of MIF-related neuroinflammation in neurodegeneration and cognitive impairment in Alzheimer's disease. *Mol Med,* 26**,** 34.

Navarro-Guerrero, E., Tay, C., Whalley, J. P., Cowley, S. A., Davies, B., Knight, J. C. & Ebner, D. 2021. Genome-Wide CRISPR/Cas9-knockout in Human Induced Pluripotent Stem Cell (iPSC)-derived Macrophages. *Scientific Reports,* 11.

Nave, K. A. & Werner, H. B. 2014. Myelination of the nervous system: mechanisms and functions. *Annu Rev Cell Dev Biol,* 30**,** 503-33.

Neal, E. H., Marinelli, N. A., Shi, Y., Mcclatchey, P. M., Balotin, K. M., Gullett, D. R., Hagerla, K. A., Bowman, A. B., Ess, K. C., Wikswo, J. P. & Lippmann, E. S. 2019. A Simplified, Fully Defined Differentiation Scheme for Producing Blood-Brain Barrier Endothelial Cells from Human iPSCs. *Stem Cell Reports,* 12**,** 1380-1388.

Neuropathology Group of the Mrc Cfas 2001. Pathological correlates of late-onset dementia in a multicentre, community-based population in England and Wales. *Lancet,* 357**,** 169-75.

Ng, B., Vowles, J., Beccano-Kelly, D., Stefana, M. I., O'brien, D. P., Bengoa-Vergniory, N., Betherat, F., Abey, A., Carling, P., Kilfeather, P., Todd, J., Caffrey, T. M., Connor-Robson, N., Cowley, S. A. & Wade-Martins, R. 2022. Tau Depletion in Human Neurons Mitigates Aβ-Driven Toxicity.

Ng, V. Y., Ang, S. N., Chan, J. X. & Choo, A. B. 2010. Characterization of epithelial cell adhesion molecule as a surface marker on undifferentiated human embryonic stem cells. *Stem Cells,* 28**,** 29-35.

Ngandu, T., Von Strauss, E., Helkala, E. L., Winblad, B., Nissinen, A., Tuomilehto, J., Soininen, H. & Kivipelto, M. 2007. Education and dementia: what lies behind the association? *Neurology,* 69**,** 1442-50.

Nguyen, K. T. & West, J. L. 2002. Photopolymerizable hydrogels for tissue engineering applications. *Biomaterials,* 23**,** 4307-4314.

Ni, Y., Teng, T., Li, R., Simonyi, A., Sun, G. Y. & Lee, J. C. 2017. TNFα alters occludin and cerebral endothelial permeability: Role of p38MAPK. *PLOS ONE,* 12**,** e0170346.

Niego, B., Lee, N., Larsson, P., De Silva, T. M., Au, A. E., Mccutcheon, F. & Medcalf, R. L. 2017. Selective inhibition of brain endothelial Rho-kinase-2 provides optimal protection of an in vitro blood-brain barrier from tissue-type plasminogen activator and plasmin. *PLoS One,* 12**,** e0177332.

Nijhuis, C. S. M. O., Vellenga, E., Daenen, S., Kamps, W. A. & Bont, E. S. J. M. D. 2003. Endothelial Cells Are Main Producers of Interleukin 8 Through Toll-Like Receptor 2 and 4 Signaling During Bacterial Infection in Leukopenic Cancer Patients. *Clinical and Vaccine Immunology,* 10**,** 558-563.

Nikolakopoulou, A. M., Montagne, A., Kisler, K., Dai, Z., Wang, Y., Huuskonen, M. T., Sagare, A. P., Lazić, D., Sweeney, M. D., Kong, P., Wang, M., Owens, N. C., Lawson, E. J., Xie, X., Zhao, Z. & Zloković, B. V. 2019. Pericyte Loss Leads to Circulatory

Failure and Pleiotrophin Depletion Causing Neuron Loss. *Nature Neuroscience,* 22**,** 1089-1098.

Nikolakopoulou, A. M., Wang, Y., Ma, Q., Sagare, A. P., Montagne, A., Huuskonen, M. T., Rege, S. V., Kisler, K., Dai, Z., Körbelin, J., Herz, J., Zhao, Z. & Zlokovic, B. V. 2021. Endothelial LRP1 protects against neurodegeneration by blocking cyclophilin A. *J Exp Med,* 218.

Nortley, R., Korte, N., Izquierdo, P., Hirunpattarasilp, C., Mishra, A., Jaunmuktane, Z., Kyrargyri, V., Pfeiffer, T., Khennouf, L., Madry, C., Gong, H., Richard-Loendt, A., Huang, W., Saito, T., Saido, T. C., Brandner, S., Sethi, H. & Attwell, D. 2019. Amyloid B Oligomers Constrict Human Capillaries in Alzheimer's Disease via Signaling to Pericytes. *Science,* 365.

Nune, K. C., Misra, R. D. K., Gaytan, S. M. & Murr, L. E. 2014. Interplay Between Cellular Activity and Three-dimensional Scaffold-cell Constructs With Different Foam Structure Processed by Electron Beam Melting. *Journal of Biomedical Materials Research Part A,* 103**,** 1677-1692.

Nürnberg, E., Vitacolonna, M., Klicks, J., Von Molitor, E., Cesetti, T., Keller, F., Bruch, R., Ertongur-Fauth, T., Riedel, K., Scholz, P., Lau, T., Schneider, R., Meier, J., Hafner, M. & Rudolf, R. 2020. Routine Optical Clearing of 3D-Cell Cultures: Simplicity Forward. *Frontiers in Molecular Biosciences,* 7.

Nwokoye, P. N. & Abilez, O. J. 2024. Bioengineering methods for vascularizing organoids. *Cell Rep Methods,* 4**,** 100779.

Nzou, G., Wicks, R. T., Vanostrand, N. R., Mekky, G. A., Seale, S. A., El-Taibany, A., Wicks, E. E., Nechtman, C. M., Marotte, E. J., Makani, V. S., Murphy, S. V., Seeds, M. C., Jackson, J. D. & Atala, A. J. 2020a. Multicellular 3D Neurovascular Unit Model for Assessing Hypoxia and Neuroinflammation Induced Blood-Brain Barrier Dysfunction. *Sci Rep,* 10**,** 9766.

Nzou, G., Wicks, R. T., Vanostrand, N. R., Mekky, G. A., Seale, S. A., El-Taibany, A., Wicks, E. E., Nechtman, C. M., Marrotte, E. J., Makani, V. S., Murphy, S. V., Seeds, M. C., Jackson, J. D. & Atala, A. J. 2020b. Author Correction: Multicellular 3D Neurovascular Unit Model for Assessing Hypoxia and Neuroinflammation Induced Blood-Brain Barrier Dysfunction. *Scientific Reports,* 10**,** 20384.

Nzou, G., Wicks, R. T., Wicks, E. E., Seale, S. A., Sane, C. H., Chen, A., Murphy, S. V., Jackson, J. D. & Atala, A. J. 2018. Human Cortex Spheroid with a Functional Blood Brain Barrier for High-Throughput Neurotoxicity Screening and Disease Modeling. *Sci Rep,* 8**,** 7413.

Oakley, H., Cole, S. L., Logan, S., Maus, E., Shao, P., Craft, J., Guillozet-Bongaarts, A., Ohno, M., Disterhoft, J., Van Eldik, L., Berry, R. & Vassar, R. 2006. Intraneuronal β-Amyloid Aggregates, Neurodegeneration, and Neuron Loss in Transgenic Mice with Five Familial Alzheimer's Disease Mutations: Potential Factors in Amyloid Plaque Formation. *The Journal of Neuroscience,* 26**,** 10129.

Oddo, S., Caccamo, A., Shepherd, J. D., Murphy, M. P., Golde, T. E., Kayed, R., Metherate, R., Mattson, M. P., Akbari, Y. & Laferla, F. M. 2003. Triple-transgenic model of Alzheimer's disease with plaques and tangles: intracellular Abeta and synaptic dysfunction. *Neuron,* 39**,** 409-21.

Orihuela, R., Mcpherson, C. A. & Harry, G. J. 2016. Microglial M1/M2 polarization and metabolic states. *Br J Pharmacol,* 173**,** 649-65.

Orlova, V. V., Van Den Hil, F. E., Petrus-Reurer, S., Drabsch, Y., Ten Dijke, P. & Mummery, C. L. 2014. Generation, expansion and functional analysis of endothelial cells and pericytes derived from human pluripotent stem cells. *Nature Protocols,* 9**,** 1514-1531.

Oyama, F., Sawamura, N., Kobayashi, K., Morishima-Kawashima, M., Kuramochi, T., Ito, M., Tomita, T., Maruyama, K., Saido, T. C., Iwatsubo, T., Capell, A., Walter, J., Grünberg, J., Ueyama, Y., Haass, C. & Ihara, Y. 1998. Mutant presenilin 2 transgenic mouse: effect on an age-dependent increase of amyloid beta-protein 42 in the brain. *J Neurochem,* 71**,** 313-22.

Özen, I., Deierborg, T., Miharada, K., Padel, T., Englund, E., Genové, G. & Paul, G. 2014. Brain Pericytes Acquire a Microglial Phenotype After Stroke. *Acta Neuropathologica,* 128**,** 381-396.

Ozerdem, U., Grako, K. A., Dahlin-Huppe, K., Monosov, E. & Stallcup, W. B. 2001. NG2 proteoglycan is expressed exclusively by mural cells during vascular morphogenesis. *Developmental dynamics: an official publication of the American Association of Anatomists,* 222**,** 218-227.

Paik, S., Somvanshi, R. K. & Kumar, U. 2019. Somatostatin Maintains Permeability and Integrity of Blood-Brain Barrier in β-Amyloid Induced Toxicity. *Molecular Neurobiology,* 56**,** 292-306.

Pantazis, C. B., Yang, A., Lara, E., Mcdonough, J. A., Blauwendraat, C., Peng, L., Oguro, H., Kanaujiya, J., Zou, J., Sebesta, D., Pratt, G., Cross, E., Blockwick, J., Buxton, P., Kinner-Bibeau, L., Medura, C., Tompkins, C., Hughes, S., Santiana, M., Faghri, F., Nalls, M. A., Vitale, D., Ballard, S., Qi, Y. A., Ramos, D. M., Anderson, K. M., Stadler, J., Narayan, P., Papademetriou, J., Reilly, L., Nelson, M. P., Aggarwal, S., Rosen, L. U., Kirwan, P., Pisupati, V., Coon, S. L., Scholz, S. W., Priebe, T., Öttl, M., Dong, J., Meijer, M., Janssen, L. J. M., Lourenco, V. S., Van Der Kant, R., Crusius, D., Paquet, D., Raulin, A. C., Bu, G., Held, A., Wainger, B. J., Gabriele, R. M. C., Casey, J. M., Wray, S., Abu-Bonsrah, D., Parish, C. L., Beccari, M. S., Cleveland, D. W., Li, E., Rose, I. V. L., Kampmann, M., Calatayud Aristoy, C., Verstreken, P., Heinrich, L., Chen, M. Y., Schüle, B., Dou, D., Holzbaur, E. L. F., Zanellati, M. C., Basundra, R., Deshmukh, M., Cohen, S., Khanna, R., Raman, M., Nevin, Z. S., Matia, M., Van Lent, J., Timmerman, V., Conklin, B. R., Johnson Chase, K., Zhang, K., Funes, S., Bosco, D. A., Erlebach, L., Welzer, M., Kronenberg-Versteeg, D., Lyu, G., Arenas, E., Coccia, E., Sarrafha, L., Ahfeldt, T., Marioni, J. C., Skarnes, W. C., Cookson, M. R., Ward, M. E. & Merkle, F. T. 2022. A reference human induced pluripotent stem cell line for large-scale collaborative studies. *Cell Stem Cell,* 29**,** 1685-1702.e22.

Pantelakis, S. 1954. [A particular type of senile angiopathy of the central nervous system: congophilic angiopathy, topography and frequency]. *Monatsschr Psychiatr Neurol,* 128**,** 219-56.

Paolillo, E. W., Saloner, R., Vandebunte, A., Lee, S., Bennett, D. A. & Casaletto, K. B. 2023. Multimodal Lifestyle Engagement Patterns Support Cognitive Stability Beyond Neuropathological Burden. *Alzheimer S Research & Therapy,* 15.

Papadimitriou, C., Celikkaya, H., Cosacak, M. I., Mashkaryan, V., Bray, L., Bhattarai, P., Brandt, K., Hollak, H., Chen, X., He, S., Antos, C. L., Lin, W., Thomas, A. K., Dahl, A., Kurth, T., Friedrichs, J., Zhang, Y., Freudenberg, U., Werner, C. & Kizil, C. 2018. 3D Culture Method for Alzheimer's Disease Modeling Reveals Interleukin-4 Rescues Aβ42-Induced Loss of Human Neural Stem Cell Plasticity. *Dev Cell,* 46**,** 85-101.e8.

Park, H.-J., Zhang, Y., Georgescu, S. P., Johnson, K. L., Kong, D. & Galper, J. B. 2006. Human umbilical vein endothelial cells and human dermal microvascular endothelial cells offer new insights into the relationship between lipid metabolism and angiogenesis. *Stem Cell Reviews,* 2**,** 93-101.

Park, J. C., Baik, S.-H., Han, S. H., Cho, H. J., Choi, H., Kim, H. J., Choi, H., Lee, W., Kim, D. K. & Mook-Jung, I. 2016. Annexin A1 Restores Aβ₁₋₄₂-induced

Blood–brain Barrier Disruption Through the Inhibition of RhoA-<scp>ROCK</scp> Signaling Pathway. *Aging Cell,* 16**,** 149-161.

Park, L., Hochrainer, K., Hattori, Y., Ahn, S. J., Anfray, A., Wang, G., Uekawa, K., Seo, J., Palfini, V., Blanco, I., Acosta, D., Eliezer, D., Zhou, P., Anrather, J. & Iadecola, C. 2020. Tau induces PSD95-neuronal NOS uncoupling and neurovascular dysfunction independent of neurodegeneration. *Nat Neurosci,* 23**,** 1079-1089.

Park, R., Kook, S. Y., Park, J. C. & Mook-Jung, I. 2014. Aβ1-42 reduces P-glycoprotein in the blood-brain barrier through RAGE-NF-κB signaling. *Cell Death Dis,* 5**,** e1299.

Paşca, A. M., Sloan, S. A., Clarke, L., Tian, Y., Makinson, C. D., Huber, N., Kim, C. H., Park, J. Y., O'rourke, N. A., Nguyen, K. D., Smith, S. J., Huguenard, J. R., Geschwind, D. H., Barres, B. A. & Paşca, S. P. 2015. Functional Cortical Neurons and Astrocytes From Human Pluripotent Stem Cells in 3D Culture. *Nature Chemical Biology,* 12**,** 671-678.

Patel, A., Iannello, G., Diaz, A. G., Sirabella, D., Thaker, V. & Corneo, B. 2022. Efficient Cas9-based Genome Editing Using CRISPR Analysis Webtools in Severe Early-onset-obesity Patient-derived iPSCs. *Curr Protoc,* 2**,** e519.

Patel, R., Page, S. & Al-Ahmad, A. J. 2017. Isogenic blood–brain barrier models based on patient-derived stem cells display inter-individual differences in cell maturation and functionality. *Journal of neurochemistry,* 142**,** 74-88.

Pathak, A. & Kumar, S. 2011. From Molecular Signal Activation to Locomotion: An Integrated, Multiscale Analysis of Cell Motility on Defined Matrices. *Plos One,* 6**,** e18423.

Patterson, J. & Hubbell, J. A. 2010. Enhanced proteolytic degradation of molecularly engineered PEG hydrogels in response to MMP-1 and MMP-2. *Biomaterials,* 31**,** 7836-7845.

Pellegrini, L., Bonfio, C., Chadwick, J., Begum, F., Skehel, M. & Lancaster, M. A. 2020. Human CNS barrier-forming organoids with cerebrospinal fluid production. *Science,* 369**,** eaaz5626.

Peltonen, S., Sonninen, T.-M., Niskanen, J., Koistinaho, J., Ruponen, M. & Lehtonen, Š. 2024. Mutated LRRK2 induces a reactive phenotype and alters migration in human iPSC-derived pericyte-like cells. *Fluids and Barriers of the CNS,* 21**,** 92.

Penninkilampi, R., Casey, A. N., Singh, M. F. & Brodaty, H. 2018. The Association between Social Engagement, Loneliness, and Risk of Dementia: A Systematic Review and Meta-Analysis. *J Alzheimers Dis,* 66**,** 1619-1633.

Peppiatt, C. M., Howarth, C., Mobbs, P. & Attwell, D. 2006. Bidirectional control of CNS capillary diameter by pericytes. *Nature,* 443**,** 700-4.

Pfeifer, L. A., White, L. R., Ross, G. W., Petrovitch, H. & Launer, L. J. 2002. Cerebral amyloid angiopathy and cognitive function: the HAAS autopsy study. *Neurology,* 58**,** 1629-34.

Pflanzner, T., Janko, M. C., André-Dohmen, B., Reuss, S., Weggen, S., Roebroek, A. J., Kuhlmann, C. R. & Pietrzik, C. U. 2011. LRP1 mediates bidirectional transcytosis of amyloid-β across the blood-brain barrier. *Neurobiol Aging,* 32**,** 2323.e1-11.

Piccio, L., Rossi, B., Scarpini, E., Laudanna, C., Giagulli, C., Issekutz, A. C., Vestweber, D., Butcher, E. C. & Constantin, G. 2002. Molecular mechanisms involved in lymphocyte recruitment in inflamed brain microvessels: critical roles for P-selectin glycoprotein ligand-1 and heterotrimeric G(i)-linked receptors. *J Immunol,* 168**,** 1940-9.

Piergiovanni, M., Leite, S. B., Corvi, R. & Whelan, M. 2021. Standardisation needs for organ on chip devices. *Lab on a Chip,* 21**,** 2857-2868.

Pillai, J. A., Bena, J., Bonner-Jackson, A. & Leverenz, J. B. 2021. Impact of APOE ε4 genotype on initial cognitive symptoms differs for Alzheimer's and Lewy body neuropathology. *Alzheimer's Research & Therapy,* 13**,** 31.

Pinals, R. L. & Tsai, L. H. 2022. Building in vitro models of the brain to understand the role of APOE in Alzheimer's disease. *Life Sci Alliance,* 5.

Poole, S., Singhrao, S. K., Kesavalu, L., Curtis, M. A. & Crean, S. 2013. Determining the presence of periodontopathic virulence factors in short-term postmortem Alzheimer's disease brain tissue. *J Alzheimers Dis,* 36**,** 665-77.

Pound, P. & Ritskes-Hoitinga, M. 2018. Is it possible to overcome issues of external validity in preclinical animal research? Why most animal models are bound to fail. *J Transl Med,* 16**,** 304.

Privratsky, J. R. & Newman, P. J. 2014. PECAM-1: regulator of endothelial junctional integrity. *Cell Tissue Res,* 355**,** 607-19.

Qiu, C., Yuan, Z., He, Z., Chen, H., Liao, Y., Li, S., Wei, Z. & Zhang, S. 2021. Lipopolysaccharide Preparation Derived From Porphyromonas Gingivalis Induces a Weaker Immuno-Inflammatory Response in BV-2 Microglial Cells Than Escherichia Coli by Differentially Activating TLR2/4-Mediated NF-κB/STAT3 Signaling Pathways. *Frontiers in Cellular and Infection Microbiology,* 11.

Qosa, H., Levine, H., Keller, J. N. & Kaddoumi, A. 2014. Mixed Oligomers and Monomeric Amyloid-B Disrupts Endothelial Cells Integrity and Reduces Monomeric Amyloid-B Transport Across hCMEC/D3 Cell Line as an in Vitro Blood–brain Barrier Model. *Biochimica Et Biophysica Acta (Bba) - Molecular Basis of Disease,* 1842**,** 1806-1815.

Quadrato, G., Nguyen, T., Macosko, E. Z., Sherwood, J. L., Min Yang, S., Berger, D. R., Maria, N., Scholvin, J., Goldman, M., Kinney, J. P., Boyden, E. S., Lichtman, J. W., Williams, Z. M., Mccarroll, S. A. & Arlotta, P. 2017. Cell diversity and network dynamics in photosensitive human brain organoids. *Nature,* 545**,** 48-53.

Raber, J., Huang, Y. & Ashford, J. W. 2004. ApoE genotype accounts for the vast majority of AD risk and AD pathology. *Neurobiology of Aging,* 25**,** 641-650.

Ramanan, V. K. & Day, G. S. 2023. Anti-amyloid therapies for Alzheimer disease: finally, good news for patients. *Mol Neurodegener,* 18**,** 42.

Ransohoff, R. M., Kivisäkk, P. & Kidd, G. 2003. Three or more routes for leukocyte migration into the central nervous system. *Nat Rev Immunol,* 3**,** 569-81.

Raulin, A.-C., Doss, S. V., Trottier, Z. A., Ikezu, T. C., Bu, G. & Liu, C.-C. 2022. ApoE in Alzheimer’s disease: pathophysiology and therapeutic strategies. *Molecular Neurodegeneration,* 17**,** 72.

Raut, S., Patel, R. & Al-Ahmad, A. J. 2021a. Presence of a mutation in PSEN1 or PSEN2 gene is associated with an impaired brain endothelial cell phenotype in vitro. *Fluids and Barriers of the CNS,* 18**,** 3.

Raut, S., Patel, R. & Al-Ahmad, A. J. 2021b. Presence of a mutation in PSEN1 or PSEN2 gene is associated with an impaired brain endothelial cell phenotype in vitro. *Fluids Barriers CNS,* 18**,** 3.

Raz, L., Knoefel, J. & Bhaskar, K. 2016. The neuropathology and cerebrovascular mechanisms of dementia. *J Cereb Blood Flow Metab,* 36**,** 172-86.

Rensink, A. A., Otte-Höller, I., Ten Donkelaar, H. J., De Waal, R. M., Kremer, B. & Verbeek, M. M. 2004. Differential gene expression in human brain pericytes induced by amyloid-beta protein. *Neuropathol Appl Neurobiol,* 30**,** 279-91.

Riedel, B. C., Thompson, P. M. & Brinton, R. D. 2016a. Age, APOE and sex: Triad of risk of Alzheimer's disease. *J Steroid Biochem Mol Biol,* 160**,** 134-47.

Riedel, B. C., Thompson, P. M. & Brinton, R. D. 2016b. Age, APOE and sex: Triad of risk of Alzheimer’s disease. *The Journal of Steroid Biochemistry and Molecular Biology,* 160**,** 134-147.

Rieker, C., Migliavacca, E., Vaucher, A., Mayer, F. C., Baud, G., Marquis, J., Charpagne, A., Hegde, N., Guignard, L., Mclachlan, M. & Pooler, A. M. 2019. Apolipoprotein E4

Expression Causes Gain of Toxic Function in Isogenic Human Induced Pluripotent Stem Cell-Derived Endothelial Cells. *Arteriosclerosis, Thrombosis, and Vascular Biology,* 39**,** e195-e207.

Ringland, C., Schweig, J. E., Paris, D., Shackleton, B., Lynch, C., Eisenbaum, M., Mullan, M., Crawford, F., Abdullah, L. & Bachmeier, C. 2020. Apolipoprotein E Isoforms Differentially Regulate Matrix Metallopeptidase 9 Function in Alzheimer's Disease. *Neurobiology of Aging,* 95**,** 56-68.

Rivera-Torres, N., Banas, K., Bialk, P., Bloh, K. & Kmiec, E. B. 2017. Insertional Mutagenesis by CRISPR/Cas9 Ribonucleoprotein Gene Editing in Cells Targeted for Point Mutation Repair Directed by Short Single-Stranded DNA Oligonucleotides. *Plos One,* 12**,** e0169350.

Robert, J., Button, E. B., Yuen, B., Gilmour, M., Kang, K., Bahrabadi, A., Stukas, S., Zhao, W., Kulic, I. & Wellington, C. L. 2017. Clearance of Beta-Amyloid Is Facilitated by Apolipoprotein E and Circulating High-Density Lipoproteins in Bioengineered Human Vessels. *Elife,* 6.

Ruggieri, S., Giorgis, M. D., Annese, T., Tamma, R., Notarangelo, A., Marzullo, A., Senetta, R., Cassoni, P., Notarangelo, M. & Ribatti, D. 2019. Dp71 Expression in Human Glioblastoma. *International Journal of Molecular Sciences,* 20**,** 5429.

Russell, T., Dirar, Q., Li, Y., Chiang, C., Laskowitz, D. T. & Yun, Y. 2023. Cortical spheroid on perfusable microvascular network in a microfluidic device. *PLoS One,* 18**,** e0288025.

Ryman, D. C., Acosta-Baena, N., Aisen, P. S., Bird, T., Danek, A., Fox, N. C., Goate, A., Frommelt, P., Ghetti, B., Langbaum, J. B., Lopera, F., Martins, R., Masters, C. L., Mayeux, R. P., Mcdade, E., Moreno, S., Reiman, E. M., Ringman, J. M., Salloway, S., Schofield, P. R., Sperling, R., Tariot, P. N., Xiong, C., Morris, J. C. & Bateman, R. J. 2014. Symptom onset in autosomal dominant Alzheimer disease: a systematic review and meta-analysis. *Neurology,* 83**,** 253-60.

Sadagopan, S., Veettil, M. V., Chakraborty, S., Sharma-Walia, N., Paudel, N., Bottero, V. & Chandran, B. 2012. Angiogenin Functionally Interacts With P53 and Regulates P53-Mediated Apoptosis and Cell Survival. *Oncogene,* 31**,** 4835-4847.

Sagare, A. P., Bell, R. D., Zhao, Z., Ma, Q., Winkler, E. A., Ramanathan, A. & Zlokovic, B. V. 2013. Pericyte loss influences Alzheimer-like neurodegeneration in mice. *Nat Commun,* 4**,** 2932.

Saito, T., Suemoto, T., Brouwers, N., Sleegers, K., Funamoto, S., Mihira, N., Matsuba, Y., Yamada, K., Nilsson, P., Takano, J., Nishimura, M., Iwata, N., Van Broeckhoven, C., Ihara, Y. & Saido, T. C. 2011. Potent amyloidogenicity and pathogenicity of Aβ43. *Nature Neuroscience,* 14**,** 1023-1032.

Saitou, M., Furuse, M., Sasaki, H., Schulzke, J. D., Fromm, M., Takano, H., Noda, T. & Tsukita, S. 2000. Complex Phenotype of Mice Lacking Occludin, a Component of Tight Junction Strands. *Molecular Biology of the Cell,* 11**,** 4131-4142.

Sakhneny, L., Epshtein, A. & Landsman, L. 2021. Pericytes Contribute to the Islet Basement Membranes to Promote Beta-Cell Gene Expression. *Scientific Reports,* 11.

Salvarani, C., Morris, J. M., Giannini, C., Brown, R. D., Christianson, T. J. H. & Hunder, G. G. 2016. Imaging Findings of Cerebral Amyloid Angiopathy, Aβ-Related Angiitis (ABRA), and Cerebral Amyloid Angiopathy–Related Inflammation. *Medicine,* 95**,** e3613.

Sanjana, N. E., Shalem, O. & Zhang, F. 2014. Improved vectors and genome-wide libraries for CRISPR screening. *Nat Methods,* 11**,** 783-784.

Sato, N., Matsumoto, T., Kawaguchi, S., Seya, K., Matsumiya, T., Ding, J., Aizawa, T. & Imaizumi, T. 2021. <i>Porphyromonas Gingivalis</I> Lipopolysaccharide Induces

Interleukin-6 and C-c Motif Chemokine Ligand 2 Expression in Cultured hCMEC/D3 Human Brain Microvascular Endothelial Cells. *Gerodontology,* 39**,** 139-147.

Sawamura, N., Morishima-Kawashima, M., Waki, H., Kobayashi, K., Kuramochi, T., Frosch, M. P., Ding, K., Ito, M., Kim, T. W., Tanzi, R. E., Oyama, F., Tabira, T., Ando, S. & Ihara, Y. 2000. Mutant presenilin 2 transgenic mice. A large increase in the levels of Abeta 42 is presumably associated with the low density membrane domain that contains decreased levels of glycerophospholipids and sphingomyelin. *J Biol Chem,* 275**,** 27901-8.

Schaeffer, E. L., Figueiro, M. & Gattaz, W. F. 2011. Insights into Alzheimer disease pathogenesis from studies in transgenic animal models. *Clinics (Sao Paulo),* 66 Suppl 1**,** 45-54.

Schindelin, J., Arganda-Carreras, I., Frise, E., Kaynig, V., Longair, M., Pietzsch, T., Preibisch, S., Rueden, C., Saalfeld, S., Schmid, B., Tinevez, J.-Y., White, D. J., Hartenstein, V., Eliceiri, K., Tomancak, P. & Cardona, A. 2012. Fiji: an open-source platform for biological-image analysis. *Nature Methods,* 9**,** 676-682.

Schmidt, N. O., Koeder, D., Messing, M., Mueller, F.-J., Aboody, K. S., Kim, S. U., Black, P. M., Carroll, R. S., Westphal, M. & Lamszus, K. 2009. Vascular endothelial growth factor-stimulated cerebral microvascular endothelial cells mediate the recruitment of neural stem cells to the neurovascular niche. *Brain Research,* 1268**,** 24-37.

Schreier, B., Gekle, M. & Grossmann, C. 2014. Role of epidermal growth factor receptor in vascular structure and function. *Current opinion in nephrology and hypertension,* 23**,** 113-121.

Schuetz, A. N., Rubin, B. P., Goldblum, J. R., Shehata, B. M., Weiss, S. W., Liu, W., Wick, M. R. & Folpe, A. L. 2005. Intercellular Junctions in Ewing Sarcoma/Primitive Neuroectodermal Tumor: Additional Evidence of Epithelial Differentiation. *Modern Pathology,* 18**,** 1403-1410.

Schwartz, M. P., Hou, Z., Propson, N. E., Zhang, J., Engstrom, C. J., Santos Costa, V., Jiang, P., Nguyen, B. K., Bolin, J. M., Daly, W., Wang, Y., Stewart, R., Page, C. D., Murphy, W. L. & Thomson, J. A. 2015. Human pluripotent stem cell-derived neural constructs for predicting neural toxicity. *Proc Natl Acad Sci U S A,* 112**,** 12516-21.

Seghezzi, G., Patel, S., Ren, C., Gualandris, A., Pintucci, G., Robbins, E., Shapiro, R. L., Galloway, A. C., Rifkin, D. B. & Mignatti, P. 1998. Fibroblast Growth Factor-2 (FGF-2) Induces Vascular Endothelial Growth Factor (VEGF) Expression in the Endothelial Cells of Forming Capillaries: An Autocrine Mechanism Contributing to Angiogenesis. *The Journal of Cell Biology,* 141**,** 1659-1673.

Selkoe, D. J. & Hardy, J. 2016. The amyloid hypothesis of Alzheimer's disease at 25 years. *EMBO molecular medicine,* 8**,** 595-608.

Sengillo, J. D., Winkler, E. A., Walker, C. T., Sullivan, J. S., Johnson, M. & Zlokovic, B. V. 2013a. Deficiency in mural vascular cells coincides with blood-brain barrier disruption in Alzheimer's disease. *Brain Pathol,* 23**,** 303-10.

Sengillo, J. D., Winkler, E. A., Walker, C. T., Sullivan, J. S., Johnson, M. & Zlokovic, B. V. 2013b. Deficiency in Mural Vascular Cells Coincides with Blood–Brain Barrier Disruption in Alzheimer's Disease. *Brain Pathology,* 23**,** 303-310.

Sengupta, U., Nilson, A. N. & Kayed, R. 2016. The Role of Amyloid-β Oligomers in Toxicity, Propagation, and Immunotherapy. *EBioMedicine,* 6**,** 42-49.

Shahryari, A., Moya, N., Siehler, J., Wang, X., Burtscher, I. & Lickert, H. 2021. Increasing Gene Editing Efficiency for CRISPR-Cas9 by Small RNAs in Pluripotent Stem Cells. *Crispr j,* 4**,** 491-501.

Shi, Y., Manis, M., Long, J. M., Wang, K., Sullivan, P. M., Serrano, J. R., Hoyle, R. & Holtzman, D. M. 2019. Microglia Drive APOE-dependent Neurodegeneration in a Tauopathy Mouse Model. *The Journal of Experimental Medicine,* 216**,** 2546-2561.

Shibata, M., Yamada, S., Kumar, S. R., Calero, M., Bading, J., Frangione, B., Holtzman, D. M., Miller, C. A., Strickland, D. K., Ghiso, J. & Zlokovic, B. V. 2000. Clearance of Alzheimer's amyloid-ss(1-40) peptide from brain by LDL receptor-related protein-1 at the blood-brain barrier. *J Clin Invest,* 106**,** 1489-99.

Shimizu, F., Sano, Y., Haruki, H. & Kanda, T. 2011. Advanced Glycation End-Products Induce Basement Membrane Hypertrophy in Endoneurial Microvessels and Disrupt the Blood–nerve Barrier by Stimulating the Release of TGF-β and Vascular Endothelial Growth Factor (VEGF) by Pericytes. *Diabetologia,* 54**,** 1517-1526.

Shin, Y., Choi, S. H., Kim, E., Bylykbashi, E., Kim, J. A., Chung, S., Kim, D. Y., Kamm, R. D. & Tanzi, R. E. 2019. Blood-Brain Barrier Dysfunction in a 3D In Vitro Model of Alzheimer's Disease. *Adv Sci (Weinh),* 6**,** 1900962.

Shoemaker, A. R., Jones, I. E., Jeffris, K., Gabrielli, G., Togliatti, A. G., Pichika, R., Martin, É., Kiskinis, E., Franz, C. K. & Finan, J. D. 2021. Biofidelic Dynamic Compression of Human Cortical Spheroids Reproduces Neurotrauma Phenotypes. *Disease Models & Mechanisms,* 14.

Siddiqui, M. R., Mayanil, C. S., Kim, K. S. & Tomita, T. 2015. Angiopoietin-1 Regulates Brain Endothelial Permeability Through PTPN-2 Mediated Tyrosine Dephosphorylation of Occludin. *Plos One,* 10**,** e0130857.

Simon, M., Wang, M. X., Ismail, O., Braun, M., Schindler, A. G., Reemmer, J., Wang, Z., Haveliwala, M. A., O'boyle, R. P., Han, W., Roese, N., Grafe, M. R., Woltjer, R. L., Boison, D. & Iliff, J. J. 2022. Loss of Perivascular Aquaporin-4 Localization Impairs Glymphatic Exchange and Promotes Amyloid Β Plaque Formation in Mice. *Alzheimer S Research & Therapy,* 14.

Sims, D. E. 1986. The pericyte--a review. *Tissue Cell,* 18**,** 153-74.

Sims, J. R., Zimmer, J. A., Evans, C. D., Lu, M., Ardayfio, P., Sparks, J., Wessels, A. M., Shcherbinin, S., Wang, H., Monkul Nery, E. S., Collins, E. C., Solomon, P., Salloway, S., Apostolova, L. G., Hansson, O., Ritchie, C., Brooks, D. A., Mintun, M. & Skovronsky, D. M. 2023. Donanemab in Early Symptomatic Alzheimer Disease: The TRAILBLAZER-ALZ 2 Randomized Clinical Trial. *Jama,* 330**,** 512-527.

Sixt, M., Engelhardt, B., Pausch, F., Hallmann, R., Wendler, O. & Sorokin, L. M. 2001. Endothelial cell laminin isoforms, laminins 8 and 10, play decisive roles in T cell recruitment across the blood-brain barrier in experimental autoimmune encephalomyelitis. *J Cell Biol,* 153**,** 933-46.

Smith, Q. R. & Rapoport, S. I. 1986. Cerebrovascular Permeability Coefficients to Sodium, Potassium, and Chloride. *Journal of Neurochemistry,* 46**,** 1732-1742.

Smyth, L., Rustenhoven, J., Park, T. I. H., Schweder, P., Jansson, D., Heppner, P., O'carroll, S. J., Mee, E., Faull, R. L. M., Curtis, M. A. & Dragunow, M. 2018. Unique and Shared Inflammatory Profiles of Human Brain Endothelia and Pericytes. *Journal of Neuroinflammation,* 15.

Song, H., Foreman, K. L., Gastfriend, B. D., Kuo, J. S., Palecek, S. P. & Shusta, E. V. 2020. Transcriptomic Comparison of Human and Mouse Brain Microvessels. *Scientific Reports,* 10.

Song, L., Yuan, X., Jones, Z., Griffin, K., Zhou, Y., Ma, T. & Li, Y. 2019. Assembly of Human Stem Cell-Derived Cortical Spheroids and Vascular Spheroids to Model 3-D Brain-like Tissues. *Sci Rep,* 9**,** 5977.

Sosa, M. a. G., Gasperi, R. D. & Elder, G. A. 2011. Modeling Human Neurodegenerative Diseases in Transgenic Systems. *Human Genetics,* 131**,** 535-563.

Spampinato, S. F., Obermeier, B., Cotleur, A., Love, A., Takeshita, Y., Sano, Y., Kanda, T. & Ransohoff, R. M. 2015. Sphingosine 1 Phosphate at the Blood Brain Barrier: Can the Modulation of S1P Receptor 1 Influence the Response of Endothelial Cells and Astrocytes to Inflammatory Stimuli? *PLoS One,* 10**,** e0133392.

Spence, J. R., Mayhew, C. N., Rankin, S. A., Kuhar, M. F., Vallance, J. E., Tolle, K., Hoskins, E. E., Kalinichenko, V. V., Wells, S. I., Zorn, A. M., Shroyer, N. F. & Wells, J. M. 2011. Directed differentiation of human pluripotent stem cells into intestinal tissue in vitro. *Nature,* 470**,** 105-9.

Srinivasan, B., Kolli, A. R., Esch, M. B., Abaci, H. E., Shuler, M. L. & Hickman, J. J. 2015. TEER Measurement Techniques for in Vitro Barrier Model Systems. *Slas Technology,* 20**,** 107-126.

Staerk, J., Dawlaty, M. M., Gao, Q., Maetzel, D., Hanna, J., Sommer, C. A., Mostoslavsky, G. & Jaenisch, R. 2010. Reprogramming of human peripheral blood cells to induced pluripotent stem cells. *Cell Stem Cell,* 7**,** 20-4.

Stankovic, I., Notaras, M., Wolujewicz, P., Lu, T., Lis, R., Ross, M. E. & Colak, D. 2024. Schizophrenia endothelial cells exhibit higher permeability and altered angiogenesis patterns in patient-derived organoids. *Transl Psychiatry,* 14**,** 53.

Stebbins, M. J., Wilson, H. K., Canfield, S. G., Qian, T., Palecek, S. P. & Shusta, E. V. 2016. Differentiation and characterization of human pluripotent stem cell-derived brain microvascular endothelial cells. *Methods,* 101**,** 93-102.

Štěpanovská, J., Šupová, M., Hanzalek, K., Brož, A. & Matějka, R. 2021. Collagen Bioinks for Bioprinting: A Systematic Review of Hydrogel Properties, Bioprinting Parameters, Protocols, and Bioprinted Structure Characteristics. *Biomedicines,* 9**,** 1137.

Stewart, K. L. & Radford, S. E. 2017. Amyloid plaques beyond Abeta: a survey of the diverse modulators of amyloid aggregation. *Biophys Rev,* 9**,** 405-419.

Storck, S. E., Meister, S., Nahrath, J., Meißner, J. N., Schubert, N., Di Spiezio, A., Baches, S., Vandenbroucke, R. E., Bouter, Y., Prikulis, I., Korth, C., Weggen, S., Heimann, A., Schwaninger, M., Bayer, T. A. & Pietrzik, C. U. 2016. Endothelial LRP1 transports amyloid-β(1-42) across the blood-brain barrier. *J Clin Invest,* 126**,** 123-36.

Suffee, N., Visage, C. L., Hlawaty, H., Aid, R., Vanneaux, V., Larghero, J., Haddad, O., Oudar, O., Charnaux, N. & Sutton, A. 2017. Pro-Angiogenic Effect of RANTES-loaded Polysaccharide-Based Microparticles for a Mouse Ischemia Therapy. *Scientific Reports,* 7.

Sullivan, M. A., Lane, S., Volkerling, A., Engel, M., Werry, E. L. & Kassiou, M. 2023. Three-dimensional bioprinting of stem cell-derived central nervous system cells enables astrocyte growth, vasculogenesis, and enhances neural differentiation/function. *Biotechnol Bioeng,* 120**,** 3079-3091.

Sullivan, M. A., Lane, S. D., Mckenzie, A. D. J., Ball, S. R., Sunde, M., Neely, G. G., Moreno, C. L., Maximova, A., Werry, E. L. & Kassiou, M. 2024. iPSC-derived PSEN2 (N141I) astrocytes and microglia exhibit a primed inflammatory phenotype. *J Neuroinflammation,* 21**,** 7.

Suls, A., Dedeken, P., Goffin, K., Esch, H. V., Dupont, P., Cassiman, D., Kempfle, J. S., Wuttke, T. V., Weber, Y. G., Lerche, H., Afawi, Z., Vandenberghe, W., Korczyn, A. D., Berkovic, S. F., Ekstein, D., Kivity, S., Ryvlin, P., Claes, L., Deprez, L., Maljevic, S., Vargas, A. M., Dyck, T. V., Goossens, D., Del-Favero, J., Laere, K. V., Jonghe, P. D. & Paesschen, W. V. 2008. Paroxysmal Exercise-Induced Dyskinesia and Epilepsy Is Due to Mutations in SLC2A1, Encoding the Glucose Transporter GLUT1. *Brain,* 131**,** 1831-1844.

Sultan, A., Nesslany, F., Violet, M., Bégard, S., Loyens, A., Talahari, S., Mansuroglu, Z., Marzin, D., Sergeant, N., Humez, S., Colin, M., Bonnefoy, E., Buée, L. & Galas, M.-

C. 2011. Nuclear Tau, a Key Player in Neuronal DNA Protection*. *Journal of Biological Chemistry,* 286**,** 4566-4575.

Sun, T., Jackson, S., Haycock, J. W. & Macneil, S. 2006. Culture of skin cells in 3D rather than 2D improves their ability to survive exposure to cytotoxic agents. *J Biotechnol,* 122**,** 372-81.

Sun, X., Kofman, S., Ogbolu, V. C., Karch, C. M., Ibric, L. & Qiang, L. 2024. Vascularized Brain Assembloids With Enhanced Cellular Complexity Provide Insights Into the Cellular Deficits of Tauopathy. *Stem Cells,* 42**,** 107-115.

Sunde, M., Serpell, L. C., Bartlam, M., Fraser, P. E., Pepys, M. B. & Blake, C. C. F. 1997. Common core structure of amyloid fibrils by synchrotron X-ray diffraction11Edited by F. E. Cohen. *Journal of Molecular Biology,* 273**,** 729-739.

Sweeney, M. D., Sagare, A. P. & Zlokovic, B. V. 2018. Blood–brain barrier breakdown in Alzheimer disease and other neurodegenerative disorders. *Nature Reviews Neurology,* 14**,** 133-150.

Syková, E. & Nicholson, C. 2008. Diffusion in brain extracellular space. *Physiol Rev,* 88**,** 1277-340.

Szepes, M., Melchert, A., Dahlmann, J., Hegermann, J., Werlein, C., Jonigk, D., Haverich, A., Martin, U., Olmer, R. & Gruh, I. 2020. Dual Function of iPSC-Derived Pericyte-Like Cells in Vascularization and Fibrosis-Related Cardiac Tissue Remodeling In Vitro. *International Journal of Molecular Sciences* [Online], 21.

Tai, H. C., Wang, B. Y., Serrano-Pozo, A., Frosch, M. P., Spires-Jones, T. L. & Hyman, B. T. 2014. Frequent and symmetric deposition of misfolded tau oligomers within presynaptic and postsynaptic terminals in Alzheimer's disease. *Acta Neuropathol Commun,* 2**,** 146.

Takahashi, K., Tanabe, K., Ohnuki, M., Narita, M., Ichisaka, T., Tomoda, K. & Yamanaka, S. 2007a. Induction of pluripotent stem cells from adult human fibroblasts by defined factors. *Cell,* 131**,** 861-72.

Takahashi, K. & Yamanaka, S. 2006. Induction of pluripotent stem cells from mouse embryonic and adult fibroblast cultures by defined factors. *Cell,* 126**,** 663-76.

Takahashi, S., Leiß, M., Moser, M., Ohashi, T., Kitao, T., Heckmann, D., Pfeifer, A., Kessler, H., Takagi, J., Erickson, H. P. & Fässler, R. 2007b. The RGD Motif in Fibronectin Is Essential for Development but Dispensable for Fibril Assembly. *The Journal of Cell Biology,* 178**,** 167-178.

Takei, Y., Teng, J., Harada, A. & Hirokawa, N. 2000. Defects in axonal elongation and neuronal migration in mice with disrupted tau and map1b genes. *J Cell Biol,* 150**,** 989-1000.

Tcw, J., Wang, M., Pimenova, A. A., Bowles, K. R., Hartley, B. J., Lacin, E., Machlovi, S. I., Abdelaal, R., Karch, C. M., Phatnani, H., Slesinger, P. A., Zhang, B., Goate, A. M. & Brennand, K. J. 2017. An Efficient Platform for Astrocyte Differentiation from Human Induced Pluripotent Stem Cells. *Stem Cell Reports,* 9**,** 600-614.

Thakur, S., Dhapola, R., Sarma, P., Medhi, B. & Reddy, D. H. 2023. Neuroinflammation in Alzheimer's Disease: Current Progress in Molecular Signaling and Therapeutics. *Inflammation,* 46**,** 1-17.

Thomsen, M. S., Routhe, L. J. & Moos, T. 2017. The Vascular Basement Membrane in the Healthy and Pathological Brain. *Journal of Cerebral Blood Flow & Metabolism,* 37**,** 3300-3317.

Torok, O., Schreiner, B., Schaffenrath, J., Tsai, H.-C., Maheshwari, U., Stifter, S. A., Welsh, C. A., Amorim, A., Sridhar, S., Utz, S. G., Mildenberger, W., Nassiri, S., Delorenzi, M., Aguzzi, A., Han, M., Greter, M., Becher, B. & Keller, A. 2021. Pericytes Regulate

Vascular Immune Homeostasis in the CNS. *Proceedings of the National Academy of Sciences,* 118.

Tricco, A. C., Ashoor, H. M., Soobiah, C., Rios, P., Veroniki, A. A., Hamid, J. S., Ivory, J. D., Khan, P. A., Yazdi, F., Ghassemi, M., Blondal, E., Ho, J. M., Ng, C. H., Hemmelgarn, B., Majumdar, S. R., Perrier, L. & Straus, S. E. 2018. Comparative Effectiveness and Safety of Cognitive Enhancers for Treating Alzheimer's Disease: Systematic Review and Network Metaanalysis. *J Am Geriatr Soc,* 66**,** 170-178.

Trujillo, C. A., Gao, R., Negraes, P. D., Gu, J., Buchanan, J., Preissl, S., Wang, A., Wu, W., Haddad, G. G., Chaim, I. A., Domissy, A., Vandenberghe, M., Devor, A., Yeo, G. W., Voytek, B. & Muotri, A. R. 2019. Complex Oscillatory Waves Emerging from Cortical Organoids Model Early Human Brain Network Development. *Cell Stem Cell,* 25**,** 558-569.e7.

Tsioti, I., Steiner, B. L., Escher, P., Zinkernagel, M. S., Benz, P. M. & Kokona, D. 2023. Endothelial Toll-like receptor 4 is required for microglia activation in the murine retina after systemic lipopolysaccharide exposure. *Journal of Neuroinflammation,* 20**,** 25.

Uemura, M., Maki, T., Ihara, M., Lee, V. & Jq, T. 2020. Brain Microvascular Pericytes in Vascular Cognitive Impairment and Dementia. *Frontiers in Aging Neuroscience,* 12.

Ueno, M., Chiba, Y., Murakami, R., Miyai, Y., Matsumoto, K., Wakamatsu, K., Nakagawa, T., Takebayashi, G., Uemura, N., Yanase, K. & Ogino, Y. 2024. Transporters, Ion Channels, and Junctional Proteins in Choroid Plexus Epithelial Cells. *Biomedicines,* 12**,** 708.

Urich, E., Patsch, C., Aigner, S., Graf, M., Iacone, R. & Freskgård, P.-O. 2013. Multicellular Self-Assembled Spheroidal Model of the Blood Brain Barrier. *Scientific Reports,* 3**,** 1500.

Utama, R. H., Atapattu, L., O'mahony, A. P., Fife, C. M., Baek, J., Allard, T., O'mahony, K. J., Ribeiro, J. C. C., Gaus, K., Kavallaris, M. & Gooding, J. J. 2020. A 3D Bioprinter Specifically Designed for the High-Throughput Production of Matrix-Embedded Multicellular Spheroids. *iScience,* 23.

Utama, R. H., Tan, V. T. G., Tjandra, K. C., Sexton, A., Nguyen, D. H. T., O'mahony, A. P., Du, E. Y., Tian, P., Ribeiro, J. C. C., Kavallaris, M. & Gooding, J. J. 2021. A Covalently Crosslinked Ink for Multimaterials Drop-on-Demand 3D Bioprinting of 3D Cell Cultures. *Macromolecular Bioscience,* 21**,** 2100125.

Vadukul, D. M., Gbajumo, O., Marshall, K. E. & Serpell, L. C. 2017. Amyloidogenicity and toxicity of the reverse and scrambled variants of amyloid-β 1-42. *FEBS Lett,* 591**,** 822-830.

Velasco, S., Kedaigle, A. J., Simmons, S. K., Nash, A., Rocha, M., Quadrato, G., Paulsen, B., Nguyen, L., Adiconis, X., Regev, A., Levin, J. Z. & Arlotta, P. 2019. Individual brain organoids reproducibly form cell diversity of the human cerebral cortex. *Nature,* 570**,** 523-527.

Villabona-Rueda, A. F., Erice, C., Pardo, C. A. & Stins, M. F. 2019. The Evolving Concept of the Blood Brain Barrier (BBB): From a Single Static Barrier to a Heterogeneous and Dynamic Relay Center. *Frontiers in Cellular Neuroscience,* 13.

Vinters, H. V. 1987. Cerebral amyloid angiopathy. A critical review. *Stroke,* 18**,** 311-24.

Vinters, H. V., Secor, D. L., Read, S. L., Frazee, J. G., Tomiyasu, U., Stanley, T. M., Ferreiro, J. A. & Akers, M. A. 1994. Microvasculature in brain biopsy specimens from patients with Alzheimer's disease: an immunohistochemical and ultrastructural study. *Ultrastruct Pathol,* 18**,** 333-48.

Von Bergen, M., Friedhoff, P., Biernat, J., Heberle, J., Mandelkow, E. M. & Mandelkow, E. 2000. Assembly of τ protein into Alzheimer paired helical filaments depends on a local sequence motif (<sup>306</sup>VQIVYK<sup>311</sup>) forming β structure. *Proceedings of the National Academy of Sciences,* 97**,** 5129.

Walhovd, K. B., Fjell, A. M., Brewer, J., Mcevoy, L. K., Fennema-Notestine, C., Hagler, D. J., Jr., Jennings, R. G., Karow, D. & Dale, A. M. 2010. Combining MR imaging, positron-emission tomography, and CSF biomarkers in the diagnosis and prognosis of Alzheimer disease. *AJNR Am J Neuroradiol,* 31**,** 347-54.

Walsh, D. M. & Selkoe, D. J. 2007. A beta oligomers - a decade of discovery. *J Neurochem,* 101**,** 1172-84.

Wang, H. & Eckel, R. H. 2014. What are lipoproteins doing in the brain? *Trends Endocrinol Metab,* 25**,** 8-14.

Wang, X., Louden, C., Yue, T., Ellison, J. A., Barone, F. C., Solleveld, H. A. & Feuerstein, G. 1998. Delayed Expression of Osteopontin After Focal Stroke in the Rat. *Journal of Neuroscience,* 18**,** 2075-2083.

Wang, Y. & Mandelkow, E. 2016. Tau in physiology and pathology. *Nature Reviews Neuroscience,* 17**,** 22-35.

Wanleenuwat, P., Iwanowski, P. & Kozubski, W. 2019. Alzheimer's dementia: pathogenesis and impact of cardiovascular risk factors on cognitive decline. *Postgrad Med,* 131**,** 415-422.

Warboys, C. M., Berson, R. E., Mann, G. E., Pearson, J. D. & Weinberg, P. D. 2010. Acute and Chronic Exposure to Shear Stress Have Opposite Effects on Endothelial Permeability to Macromolecules. *Ajp Heart and Circulatory Physiology,* 298**,** H1850-H1856.

Watson, P. M. D., Kavanagh, E., Allenby, G. & Vassey, M. 2017. Bioengineered 3D Glial Cell Culture Systems and Applications for Neurodegeneration and Neuroinflammation. *SLAS Discov,* 22**,** 583-601.

Weickenmeier, J., De Rooij, R., Budday, S., Steinmann, P., Ovaert, T. C. & Kuhl, E. 2016. Brain stiffness increases with myelin content. *Acta Biomater,* 42**,** 265-272.

Weingarten, M. D., Lockwood, A. H., Hwo, S. Y. & Kirschner, M. W. 1975. A protein factor essential for microtubule assembly. *Proc Natl Acad Sci U S A,* 72**,** 1858-62.

Weksler, B., Romero, I. A. & Couraud, P. O. 2013. The hCMEC/D3 cell line as a model of the human blood brain barrier. *Fluids Barriers CNS,* 10**,** 16.

Weksler, B. B., Subileau, E. A., Perrière, N., Charneau, P., Holloway, K., Leveque, M., Tricoire-Leignel, H., Nicotra, A., Bourdoulous, S., Turowski, P., Male, D. K., Roux, F., Greenwood, J., Romero, I. A. & Couraud, P. O. 2005. Blood-brain barrier-specific properties of a human adult brain endothelial cell line. *Faseb j,* 19**,** 1872-4.

Wewer, C., Seibt, A., Wolburg, H., Greune, L., Schmidt, M. A., Berger, J., Galla, H. J., Quitsch, U., Schwerk, C., Schroten, H. & Tenenbaum, T. 2011. Transcellular Migration of Neutrophil Granulocytes Through the Blood-Cerebrospinal Fluid Barrier After Infection With Streptococcus Suis. *Journal of Neuroinflammation,* 8.

Weygant, J., Koch, F., Adam, K., Troendle, K., Zengerle, R., Finkenzeller, G., Kartmann, S., Koltay, P. & Zimmermann, S. 2022. A Drop-on-Demand Bioprinting Approach to Spatially Arrange Multiple Cell Types and Monitor Their Cell-Cell Interactions Towards Vascularization Based on Endothelial Cells and Mesenchymal Stem Cells.

Who. 2015. *The Epidemiology and Impact of Dementia. Current State and Future Trends.* [Online]. Available: https://www.who.int/mental_health/neurology/dementia/dementia_thematicbrief_epidemiology.pdf [Accessed].

Wilcock, D. M., Vitek, M. P. & Colton, C. A. 2009. Vascular amyloid alters astrocytic water and potassium channels in mouse models and humans with Alzheimer's disease. *Neuroscience,* 159**,** 1055-69.

Wilson, H. K., Canfield, S. G., Hjortness, M. K., Palecek, S. P. & Shusta, E. V. 2015. Exploring the effects of cell seeding density on the differentiation of human pluripotent stem cells to brain microvascular endothelial cells. *Fluids Barriers CNS,* 12**,** 13.

Wimmer, I., Tietz, S., Nishihara, H., Deutsch, U., Sallusto, F., Gosselet, F., Lyck, R., Müller, W. A., Lassmann, H. & Engelhardt, B. 2019. PECAM-1 Stabilizes Blood-Brain Barrier Integrity and Favors Paracellular T-Cell Diapedesis Across the Blood-Brain Barrier During Neuroinflammation. *Frontiers in Immunology,* 10.

Winkler, E. A., Bell, R. D. & Zloković, B. V. 2010. Pericyte-Specific Expression of PDGF Beta Receptor in Mouse Models With Normal and Deficient PDGF Beta Receptor Signaling. *Molecular Neurodegeneration,* 5.

Winkler, E. A., Nishida, Y., Sagare, A. P., Rege, S. V., Bell, R. D., Perlmutter, D., Sengillo, J. D., Hillman, S., Kong, P., Nelson, A. R., Sullivan, J. S., Zhao, Z., Meiselman, H. J., Wendy, R. B., Soto, J., Abel, E. D., Makshanoff, J., Zuniga, E., De Vivo, D. C. & Zlokovic, B. V. 2015. GLUT1 reductions exacerbate Alzheimer's disease vasculo-neuronal dysfunction and degeneration. *Nat Neurosci,* 18**,** 521-530.

Wisniewski, H. M. & Kozlowski, P. B. 1982. Evidence for blood-brain barrier changes in senile dementia of the Alzheimer type (SDAT). *Ann N Y Acad Sci,* 396**,** 119-29.

Wisniewski, H. M., Vorbrodt, A. W. & Wegiel, J. 1997. Amyloid angiopathy and blood-brain barrier changes in Alzheimer's disease. *Ann N Y Acad Sci,* 826**,** 161-72.

Wright, K. M., Lyon, K. A., Leung, H. C., Leahy, D. J., Ma, L. & Ginty, D. D. 2012. Dystroglycan Organizes Axon Guidance Cue Localization and Axonal Pathfinding. *Neuron,* 76**,** 931-944.

Wu, T., Zhang, B., Ye, F. & Xiao, Z. 2013. A Potential Role for Caveolin-1 in VEGF-induced Fibronectin Upregulation in Mesangial Cells: Involvement of VEGFR2 and SRC. *Ajp Renal Physiology,* 304**,** F820-F830.

Wurm, J., Behringer, S. P., Ravi, V. M., Joseph, K., Neidert, N., Maier, J. P., Doria-Medina, R., Follo, M., Delev, D., Pfeifer, D., Beck, J., Sankowski, R., Schnell, O. & Heiland, D. H. 2019. Astrogliosis Releases Pro-Oncogenic Chitinase 3-Like 1 Causing MAPK Signaling in Glioblastoma. *Cancers,* 11**,** 1437.

Xiao, D. & Zhang, C. 2024. Current therapeutics for Alzheimer ' s disease and clinical trials. *Exploration of Neuroscience,* 3**,** 255-271.

Xie, L., Mao, M., Zhou, L., Zhang, L. & Jiang, B. 2017. Signal Factors Secreted by 2D and Spheroid Mesenchymal Stem Cells and by Cocultures of Mesenchymal Stem Cells Derived Microvesicles and Retinal Photoreceptor Neurons. *Stem Cells International,* 2017**,** 1-13.

Xie, M., Tang, Q., Yu, S., Sun, J., Feng, M., Zhao, J. & Chen, L. 2020. Porphyromonas Gingivalis Disrupts Vascular Endothelial Homeostasis in a TLR-NF-κB Axis Dependent Manner. *International Journal of Oral Science,* 12.

Xiong, R., Zhang, Z., Chai, W., Chrisey, D. B. & Huang, Y. 2017. Study of Gelatin as an Effective Energy Absorbing Layer for Laser Bioprinting. *Biofabrication,* 9**,** 024103.

Xu, H., Wang, B., Ono, M., Kagita, A., Fujii, K., Sasakawa, N., Ueda, T., Gee, P., Nishikawa, M., Nomura, M., Kitaoka, F., Takahashi, T., Okita, K., Yoshida, Y., Kaneko, S. & Hotta, A. 2019. Targeted Disruption of HLA Genes via CRISPR-Cas9 Generates iPSCs With Enhanced Immune Compatibility. *Cell Stem Cell,* 24**,** 566-578.e7.

Xu, X., Gao, D., Wang, P., Chen, J., Ruan, J., Xu, J. & Xia, X. 2018. Efficient Homology-Directed Gene Editing by CRISPR/Cas9 in Human Stem and Primary Cells Using Tube Electroporation. *Scientific Reports,* 8.

Yamazaki, T. & Mukouyama, Y.-S. 2018. Tissue Specific Origin, Development, and Pathological Perspectives of Pericytes. *Frontiers in Cardiovascular Medicine,* 5.

Yan, Y., Jiang, F., Lai, Y., Wang, H., Liu, A., Wang, C., Zhang, Y., Teng, W. & Shan, Z. 2016. Effect of Thyrotropin on Osteopontin, Integrin αvβ3, and VCAM-1 in the Endothelium via Activation of Akt. *International Journal of Molecular Sciences,* 17**,** 1484.

Yang, J., Lunde, L. K., Nuntagij, P., Oguchi, T., Camassa, L. M., Nilsson, L. N., Lannfelt, L., Xu, Y., Amiry-Moghaddam, M., Ottersen, O. P. & Torp, R. 2011. Loss of astrocyte polarization in the tg-ArcSwe mouse model of Alzheimer's disease. *J Alzheimers Dis,* 27**,** 711-22.

Yee, C., Chan, Y. L., Utama, R., Besnier, M., Engel, M. & Belfiore, L. 2024. Protocol to create phenotypic primary human hepatocyte cultures using the RASTRUM 3D cell model platform. *STAR Protocols,* 5**,** 103234.

Yiannopoulou, K. G. & Papageorgiou, S. G. 2020. Current and Future Treatments in Alzheimer Disease: An Update. *J Cent Nerv Syst Dis,* 12**,** 1179573520907397.

Zekry, D., Duyckaerts, C., Belmin, J., Geoffre, C., Moulias, R. & Hauw, J. J. 2003. Cerebral amyloid angiopathy in the elderly: vessel walls changes and relationship with dementia. *Acta Neuropathol,* 106**,** 367-73.

Zempel, H., Thies, E., Mandelkow, E. & Mandelkow, E. M. 2010. Aβ Oligomers Cause Localized Ca²⁺Elevation, Missorting of Endogenous Tau Into Dendrites, Tau Phosphorylation, and Destruction of Microtubules and Spines. *Journal of Neuroscience,* 30**,** 11938-11950.

Zenaro, E., Piacentino, G. & Constantin, G. 2017. The blood-brain barrier in Alzheimer's disease. *Neurobiology of Disease,* 107**,** 41-56.

Zeng, F., Liu, Y., Huang, W., Qing, H., Kadowaki, T., Kashiwazaki, H., Ni, J. & Wu, Z. 2020. Receptor for Advanced Glycation End Products Up-regulation in Cerebral Endothelial Cells Mediates Cerebrovascular-related Amyloid Β Accumulation After <i>Porphyromonas Gingivalis</I> Infection. *Journal of Neurochemistry,* 158**,** 724-736.

Zeng, X., Hunsberger, J. G., Simeonov, A., Malik, N., Pei, Y. & Rao, M. 2014. Concise review: modeling central nervous system diseases using induced pluripotent stem cells. *Stem cells translational medicine,* 3**,** 1418-1428.

Zeppenfeld, D. M., Simon, M., Haswell, J. D., D'abreo, D., Murchison, C., Quinn, J. F., Grafe, M. R., Woltjer, R. L., Kaye, J. & Iliff, J. J. 2017. Association of Perivascular Localization of Aquaporin-4 With Cognition and Alzheimer Disease in Aging Brains. *JAMA Neurol,* 74**,** 91-99.

Zhan, X., Stamova, B., Jin, L. W., Decarli, C., Phinney, B. S. & Sharp, F. R. 2016. Gram-Negative Bacterial Molecules Associate With Alzheimer Disease Pathology. *Neurology,* 87**,** 2324-2332.

Zhang, J., Chu, L. F., Hou, Z., Schwartz, M. P., Hacker, T., Vickerman, V., Swanson, S., Leng, N., Nguyen, B. K., Elwell, A., Bolin, J., Brown, M. E., Stewart, R., Burlingham, W. J., Murphy, W. L. & Thomson, J. A. 2017a. Functional characterization of human pluripotent stem cell-derived arterial endothelial cells. *Proc Natl Acad Sci U S A,* 114**,** E6072-e6078.

Zhang, J., Schwartz, M. P., Hou, Z., Bai, Y., Ardalani, H., Swanson, S., Steill, J., Ruotti, V., Elwell, A. L., Nguyen, B. K., Bolin, J. M., Stewart, R., Thomson, J. A. & Murphy, W. L. 2017b. A Genome-Wide Analysis of Human Pluripotent Stem Cell-Derived Endothelial Cells in 2D or 3D Culture. *Stem Cell Reports,* 8**,** 907-918.

Zhang, J. P., Yang, Z. X., Zhang, F., Fu, Y. W., Dai, X. Y., Wen, W., Zhang, B., Choi, H., Chen, W., Brown, M., Baylink, D., Zhang, L., Qiu, H., Wang, C., Cheng, T. & Zhang, X. B. 2021. HDAC inhibitors improve CRISPR-mediated HDR editing efficiency in iPSCs. *Sci China Life Sci,* 64**,** 1449-1462.

Zhang, X., Wang, T., Gui, P., Yao, C., Sun, W., Wang, L., Wang, H., Xie, W., Yao, S., Lin, Y. & Wu, Q. 2013. Resolvin D1 Reverts Lipopolysaccharide-Induced TJ Proteins Disruption and the Increase of Cellular Permeability by Regulating I<i>κ</I>B<i>α</I>Signaling in Human Vascular Endothelial Cells. *Oxidative Medicine and Cellular Longevity,* 2013**,** 1-8.

Zhang, Y., Sloan, S. A., Clarke, L., Caneda, C., Plaza, C. A., Blumenthal, P. D., Vogel, H., Steinberg, G. K., Edwards, M. S. B., Li, G., Duncan, J. A., Cheshier, S., Shuer, L. M., Chang, E. F., Grant, G. A., Gephart, M. H. & Barres, B. A. 2016. Purification and Characterization of Progenitor and Mature Human Astrocytes Reveals Transcriptional and Functional Differences With Mouse. *Neuron,* 89**,** 37-53.

Zhang, Z., Mcgoron, A. J., Crumpler, E. T. & Li, C. Z. 2011. Co-culture based blood-brain barrier in vitro model, a tissue engineering approach using immortalized cell lines for drug transport study. *Appl Biochem Biotechnol,* 163**,** 278-95.

Zhao, H., Zheng, T., Yang, X., Fan, M., Zhu, L. L., Liu, S., Wu, L. & Sun, C. 2019. Cryptotanshinone Attenuates Oxygen-Glucose Deprivation/ Recovery-Induced Injury in an in Vitro Model of Neurovascular Unit. *Frontiers in Neurology,* 10.

Zhao, L., Li, Z., Vong, J. S. L., Chen, X., Lai, H. M., Yan, L. Y. C., Huang, J., Sy, S. K. H., Tian, X., Huang, Y., Chan, H. Y. E., So, H. C., Ng, W.-L., Tang, Y., Lin, W.-J., Mok, V. C. T. & Ko, H. 2020. Pharmacologically Reversible Zonation-Dependent Endothelial Cell Transcriptomic Changes With Neurodegenerative Disease Associations in the Aged Brain. *Nature Communications,* 11.

Zhao, L., Yang, Z., Liu, Y., Ying, H., Zhang, H. & Xue, Y. 2010. Vascular Endothelial Growth Factor Increases Permeability of the Blood–Tumor Barrier via Caveolae-Mediated Transcellular Pathway. *Journal of Molecular Neuroscience,* 44**,** 122-129.

Zhao, N., Kulkarni, S., Zhang, S., Linville, R. M., Chung, T. D., Guo, Z., Jamieson, J. J., Norman, D., Liang, L., Pessell, A. F. & Searson, P. 2023. Modeling angiogenesis in the human brain in a tissue-engineered post-capillary venule. *Angiogenesis,* 26**,** 203-216.

Zhao, Y., Jaber, V., Pogue, A. I., Sharfman, N. M., Taylor, C. E. & Lukiw, W. J. 2022. Lipopolysaccharides (LPSs) as Potent Neurotoxic Glycolipids in Alzheimer's Disease (AD). *International Journal of Molecular Sciences,* 23**,** 12671.

Zhao, Z., Nelson, A. R., Betsholtz, C. & Zlokovic, B. V. 2015. Establishment and Dysfunction of the Blood-Brain Barrier. *Cell,* 163**,** 1064-1078.

Zheng, H., Jiang, M., Trumbauer, M. E., Hopkins, R., Sirinathsinghji, D. J., Stevens, K. A., Conner, M. W., Slunt, H. H., Sisodia, S. S., Chen, H. Y. & Van Der Ploeg, L. H. 1996. Mice deficient for the amyloid precursor protein gene. *Ann N Y Acad Sci,* 777**,** 421-6.

Zhong, M. Z., Peng, T., Duarte, M. L., Wang, M. & Cai, D. 2024. Updates on mouse models of Alzheimer's disease. *Mol Neurodegener,* 19**,** 23.

Zhou, R., Chen, L. L., Yang, H., Li, L., Liu, J., Chen, L., Hong, W. J., Wang, C. G., Ma, J. J., Huang, J., Zhou, X. F., Liu, D. & Zhou, H. D. 2021. Effect of High Cholesterol Regulation of LRP1 and RAGE on Aβ Transport Across the Blood-Brain Barrier in Alzheimer's Disease. *Curr Alzheimer Res,* 18**,** 428-442.

Zhou, T., Benda, C., Dunzinger, S., Huang, Y., Ho, J. C., Yang, J., Wang, Y., Zhang, Y., Zhuang, Q., Li, Y., Bao, X., Tse, H.-F., Grillari, J., Grillari-Voglauer, R., Pei, D. & Esteban, M. A. 2012. Generation of human induced pluripotent stem cells from urine samples. *Nature Protocols,* 7**,** 2080-2089.

Zhu, J. 2010. Bioactive modification of poly(ethylene glycol) hydrogels for tissue engineering. *Biomaterials,* 31**,** 4639-56.

Zhu, J., Song, W., Lin, L. & Fan, X. 2016. Endothelial Nitric Oxide Synthase: A Potential Therapeutic Target for Cerebrovascular Diseases. *Molecular Brain,* 9.

Zipser, B. D., Johanson, C. E., Gonzalez, L., Berzin, T. M., Tavares, R., Hulette, C. M., Vitek, M. P., Hovanesian, V. & Stopa, E. G. 2007. Microvascular injury and blood-brain barrier leakage in Alzheimer's disease. *Neurobiol Aging,* 28**,** 977-86.

Zlokovic, B. V. 2011a. Neurovascular pathways to neurodegeneration in Alzheimer's disease and other disorders. *Nature Reviews Neuroscience,* 12**,** 723-738.

Zlokovic, B. V. 2011b. Neurovascular pathways to neurodegeneration in Alzheimer's disease and other disorders. *Nat Rev Neurosci,* 12**,** 723-38.

Zlokovic, B. V. & Apuzzo, M. L. 1998. Strategies to circumvent vascular barriers of the central nervous system. *Neurosurgery,* 43**,** 877-8.

Zrzavy, T., Hametner, S., Wimmer, I., Butovsky, O., Weiner, H. L. & Lassmann, H. 2017. Loss of 'homeostatic' microglia and patterns of their activation in active multiple sclerosis. *Brain,* 140**,** 1900-1913.

Zullo, J., Fan, J., Azar, T., Yen, W.-Y., Zeng, M., Ratliff, B. B., Song, J., Tarbell, J. M., Goligorsky, M. S. & Fu, B. M. 2016. Exocytosis of Endothelial Lysosome-Related Organelles Hair-Triggers a Patchy Loss of Glycocalyx at the Onset of Sepsis. *American Journal of Pathology,* 186**,** 248-258.